UNIVERSITY OF SOUTHAMPTON
Faculty of Engineering and the Environment
Institute of Sound and Vibration Research

# AN EXPERIMENTAL INVESTIGATION OF LEAK NOISE FROM WATER FILLED PLASTIC PIPES

by

Anastasia Papastefanou

Thesis for the degree of Doctor of Philosophy

April 2011

UNIVERSITY OF SOUTHAMPTON

ABSTRACT

FACULTY OF ENGINEERING AND THE ENVIRONMENT

INSTITUTE OF SOUND AND VIBRATION RESEARCH

Doctor of Philosophy

# AN EXPERIMENTAL INVESTIGATION OF LEAK NOISE FROM WATER FILLED PLASTIC PIPES

by Anastasia Papastefanou

This thesis is concerned with the investigation of the characteristics of leak noise and is mainly based on experimental work. Knowledge of these characteristics may help in predicting the performance of different leak detection algorithms.

There are two main objectives of this thesis. The first is to identify the physical mechanisms of leak noise generation which has not received much attention in the past. Possible mechanisms include cavitation and turbulence. An experimental set-up is designed to aid this investigation. The experiments show that cavitation is not responsible for leak noise generation and clearly indicate that turbulent flow is the main mechanism, at least in our experiment. The second objective of this thesis is to identify the characteristics of leak noise spectra and to investigate how the spectra are affected by the leak size and the leak flow velocity. An alternative experimental set-up is designed and a number of different leak sizes between 1 mm and 4 mm diameter are tested for different jet velocities. Conclusions are drawn for the general trend of the shape of leak noise spectrum. It is found that the leak noise spectrum follows a $\omega^{-1}$ frequency power law until a specific frequency which varies with leak size and flow velocity.

In the theoretical part of this thesis, a linear matched field processor, which is widely used in underwater acoustics for source localization, is applied to the leak detection problem. The results are compared with those from the Basic Cross Correlator (BCC) and Phase Transform correlator (PHAT). It is found that the matched field processor gives better performance than the BCC when applied to experimental data and similar

performance when compared to the PHAT processor. However, specific features of the matched field processor make it more useful in practical applications than the PHAT processor.

# TABLE OF CONTENTS

# LIST OF FIGURES

# ACADEMIC THESIS: DECLARATION OF AUTHORSHIP

I, Anastasia Papastefanou declare that this thesis titled, ‘An experimental investigation of leak noise from water filled plastic pipes’ and the work presented in it are my own and have been generated by me as the result of my own original research. I confirm that:

1. This work was done wholly or mainly while in candidature for a research degree at this University.
2. Where any part of this thesis has previously been submitted for a degree or any other qualification at this University or any other institution, this has been clearly stated.
3. Where I have consulted the published work of others, this is always clearly attributed.
4. Where I have quoted from the work of others, the source is always given. With the exception of such quotations, this thesis is entirely my own work.
5. I have acknowledged all main sources of help.
6. Where the thesis is based on work done by myself jointly with others, I have made clear exactly what was done by others and what I have contributed myself.
7. None of this work has been published before submission.

Signed:

________________________________________

Date:

________________________________________

# AKNOWLEDGEMENTS

I would like to acknowledge and thank my supervisors, Professor Phillip Joseph and Professor Mike Brennan for their valuable academic guidance and understanding throughout the project. I would like to specially thank Professor Phillip Joseph for his support and encouragement during the writing of the thesis. My thanks also go to Professor Paul White and Professor Victor Humphrey for their useful suggestions at each review meeting.

Grateful thanks are also due to the ISVR technicians, for their help and support in making the experimental rig.

Finally, I would like to thank my parents and my sister for their understanding and encouragement all these years of my studies and all my friends, in both UK and Greece, who have supported me in any respect during the completion of the project.

*To Efi, Stergios and Maria who make my*
*world a better place and to everyone who*
*fights nowadays to change this world*

# LIST OF SYMBOLS

| | |
|---|---|
| ABP | Alternative Bartlett processor |
| $A_f$ | Cross-sectional area of the pipe |
| $A_l$ | Area of the leak |
| $A_c$ | Vena contracta area |
| BCC | Basic cross-correlation |
| CSD | Cross-spectral density |
| $C_d$ | Discharge coefficient |
| $C_v$ | Velocity coefficient |
| $C_c$ | Contraction coefficient |
| $c, c_f$ | Wavespeed and fluid wavespeed |
| $d_1, d_2$ | Distances of sensors relative to leak position |
| $d_t$ | Distance of sensor from the tap |
| $\hat{d}_1, \hat{d}_2$ | Assumed trial distances |
| $d^{'}, \Delta d$ | $d^{'} = d_1 + \ d_2$ and $\Delta d = d_2 - d_1$ |
| $d$ | Leak diameter |
| $D$ | Pipe diameter |
| E{ } | Expectation operator |

| | |
|---|---|
| $F^{-1}\{\quad\}$ | Inverse Fourier transform |
| FFT | Fast Fourier Transform |
| $f_{s,}\ \omega_s$ | Critical frequencies |
| $H(\omega, x)$ | Frequency response function |
| K | Covariance matrix |
| $k$ | wavenumber |
| $\hat{k}$ | Assumed wavenumber |
| $L$ | Characteristic length |
| $l(t)$ | Leak signal |
| $l_1, l_2$ | Distance of discontinuities from the sensor positiom |
| $l$ | $l = l_1 + \ l_2$ |
| MFP | Matched Field Processing |
| $M_{c,}$ | Mach number |
| N | Number of sensors |
| $n(t), n_2(t)$ | Background noise |
| p | Pressure measured |
| $\hat{p}$ | Modelled pressure |
| $\mathrm{P_B}$ | Bartlett processor |
| $\mathrm{P_B'}$ | Bartlett processor integrated over frequency |
| $\hat{\mathbf{p}}(\omega, \mathbf{d})^{+}$ | Conjugate transpose of $\hat{\mathbf{p}}(\omega, \mathbf{d})$ |

| | |
|---|---|
| PSD | Power-spectral density |
| PHAT | Phase transform |
| $P_c$ | Collapse pressure of the bubble |
| $Q$ | Flow rate |
| $Q_\mathrm{i}$ | Ideal flow rate |
| $R_{x_1 x_2}(\tau)$ | BCC function of $x_1(t), x_2(t)$ |
| $Re$ | Reynolds number |
| $r_1, r_2$ | Reflection coefficients |
| $S_{ll}(\omega)$ | PSD of leak noise spectrum |
| $S_{tt}(\omega)$ | PSD of the tap signal |
| $S_{ff}(\omega)$ | PSD of flow noise |
| SNR | Signal to Noise ratio |
| $s_1(t), s_2(t)$ | Random processes |
| $St$ | Strouhal number |
| $St_c$ | Critical Strouhal number of the characteristic frequency $f_{s,}$ |
| $St_g$ | Critical Strouhal number above which remains some pressure fluctuation |
| $\mathrm{T}_0 = -(d_2 - d_1)/c$ | Time delay |
| $t, \tau$ | Time and lag of time |

| | |
|---|---|
| $V$ | Jet-leak flow velocity |
| $V_f$ | Flow velocity inside the pipe |
| $V_i$ | Ideal leak flow velocity |
| $x_1(t), x_2(t)$ | Measured signals |
| $\sigma_{n_1}^2, \sigma_{n_2}^2, \sigma_{s_1}^2, \sigma_{s_2}^2$ | Variances of the signals $n_1(t), n_2(t), s_1(t), s_2(t)$ |
| $\rho_{x_1x_2}(\tau)$ | Cross-correlation coefficient of $x_1(t), x_2(t)$ |
| $\rho_{peak}$ | Peak value of the cross-correlation coefficient |
| $\Delta\omega$ | Frequency bandwidth |
| $\alpha_o$ | Radius of the maximum bubble |
| $\beta$ | A measure of the loss within the pipe wall |
| $\hat{\beta}$ | Assumed attenuation factor |
| $\eta$ | Loss factor |
| $\theta$ | Observer angle |
| $\lambda$ | wavelength |
| $\rho$ | Fluid density |
| $\rho_o$ | Water density |
| $\Psi_p(\omega)$ | PHAT frequency weighting function |
| $\omega_o, \omega_1$ | Lower and higher frequency of the band-pass filter |
| * | Complex conjugate |

# CHAPTER 1

# THEORETICAL BACKGROUND

## 1.1 Introduction

In many water distribution systems a significant percentage of water is lost due to leakage from distribution pipes while in transit from treatment plants to consumers. In 1991, the International Water Supply Association (IWSA) made an inquiry concerning the amount of lost or ‘unaccounted for’ water which was found to be in the range of 20 to 30% of production. In some cases, where the water distribution systems were older this percentage could be as high as 50% [1].

Water leakage is a major problem, not only in environmental terms, because of wasting an important natural source, but also in economic and health terms. The cost of pumping and treatment production, the damage of the pipe network due to erosion of pipe bedding and major pipe breaks can inevitably result in significant economic and energy loss. Furthermore, a leaky pipe creates a public health risk as every leak is a potential entry point for contaminants if a pressure drop occurs in the system. For all the above reasons, in recent years, significant efforts have been made to develop water audit procedures and leak detection methods. As a result, several leak detection techniques are now well-established and modern equipment is often used to help control water loss.

## 1.2 Acoustic and non-acoustic leak detection techniques

A leak from a water supply pipe generates noise which can be used to detect and locate the leak. Acoustic leak detection techniques have been shown to be effective [2-4] and are in common use in the water industry. Alternative, non-acoustic methods of leak detection have been also developed and are used with varying degrees of success. These, include methods of tracer gas [1], thermography [1,5], flow and pressure modelling [6], and ground-penetrating radar (GPR) [1, 7-8].

The method of tracer gas works simply by isolating a suspected leak zone, removing water from the pipe and then pressurizing it with a mixture of air and tracer gas. The most commonly used tracer gases are helium and hydrogen which are both non-toxic. The tracer gas escapes under pressure through leaks in the pipe and rises through the surrounding soil to the ground surface. The location of the leak is determined by scanning the ground surface with a portable gas sensor [1]. The disadvantage of this method is that it requires removing water from the pipe, something that is usually inconvenient and therefore this method is rarely used by the water industry.

The method of thermography involves the detection and display of infrared (IR) radiation in the form of visible images. Thermography could be suitable for leak detection if the surface temperature of the ground is affected by leaking water. Depending on the temperature of the water relative to the surrounding soil, the ground surface area above a leak may appear cooler or warmer than the surrounding areas. This thermal effect could take place if there is significant heat transfer between the leaking water and the surface soil [1].

Ground-penetrating radar works by transmitting a short duration pulse of high-frequency electromagnetic energy into the ground by means of a transmitting antenna. The transmitted pulse signal is partially reflected back to the ground surface by buried objects or voids in the ground or by boundaries between soil layers that have different dielectric properties. Reflected radar signals are captured by a receiving antenna and then digitized and stored for processing. Time traces of radar signals captured along the surface of the ground are normally displayed vertically (side by side) to form a vertical cross-section of the ground with position being along the horizontal axis and time (or depth if the velocity in the ground is known) along the vertical axis. Reflection patterns in the resulting radar images are then used to delineate information about buried objects. Ground penetrating radar could be used to locate leaks in water pipes by either detecting underground voids created by leaking water as it circulates near the pipe or by detecting anomalies in the pipe depth as measured by radar. Saturation of soil by leaking water slows down radar waves and makes the pipe appear deeper than it really is [1].

Although the non-acoustic methods described above prove to be more complex and time consuming in their present form compared to acoustic techniques, experiments have been conducted to further investigate further the various parameters that affect their performance [1].

## 1.3 Procedure and equipment for leak detection using acoustic techniques

There are two major steps in any systematic leakage control program. These are: (i) water audits, and (ii) leak detection surveys [1]. Water audits involve detailed accounting of water flow into and out of the distribution system or parts of it. The audits help to identify parts of the distribution system that have excessive leakage but unfortunately they do not provide information about the precise location of leaks. In order to locate leaks in areas that have been identified by water audits as suffering from leakage, leak detection surveys must be undertaken. In leak surveys, the water distribution system is systematically checked for leaks by using acoustic equipment which detects the sound or vibration induced by water as it escapes from pipes under pressure [1]. Listening rods or hydrophones (underwater microphones) are used at all accessible contact points within the water distribution system like fire hydrants or valves. In the second phase, when a sound is detected and a leak is suspected, a more accurate investigation takes place, in the specific position, using ground microphones (geophones) to listen for leak sounds on the ground directly above the pipe at very close intervals or by using leak noise correlators [1].

Acoustic devices include sensitive mechanisms or materials such as piezo-electric elements for sensing leak-induced sound and vibration. Their use is usually straightforward but their effectiveness depends on the experience of the user. They could be either mechanical or electronic. Modern electronic devices may include signal amplifiers and noise filters which may be very helpful in an environment where ambient noise exists and dominates [1].

Leak noise correlators have proved to be very effective in locating leaks in either automatic or manual modes based on the cross-correlation method. They are portable, state-of-the-art computer-based devices which work by measuring sound or vibration signals at two points that include the location of a suspected leak. Vibration sensors, usually accelerometers, are attached to fire hydrants, valves or other contact points with water pipes or alternatively, hydrophones are used and are inserted into fire hydrants through modified hydrant caps. The two vibration or sound signals are transmitted to the correlators usually through wireless radio transmitters. The cross-correlation operation produces an output that indicates how similar the two signals are as they are shifted in time with respect to each other. If, for example, there is a leak at the mid-point between the two sensors the leak sound will reach these sensors at the same time and so the correlation function will have a single central peak. If the leak is located asymmetrically between the two sensors the signals do not reach the sensors at the same time. The peak of the cross-correlation will be offset from the centre by this difference in arrival times of the leak noise at the two sensors. The location of the leak, relative to one of the measurement points can be easily calculated afterwards using a simple algebraic relationship between the time lag, the distance between the two measurement points and the sound propagation velocity in the pipe.

Generally, acoustic methods are considered to be satisfactory by most professional users for use with metallic pipes. For plastic pipes the effectiveness of existing equipment is still not well established due to the high levels of attenuation in those pipes.

## 1.4 Leak detection using the correlation technique

With the correlation technique, if a leak is suspected, acoustic sensors such as accelerometers or hydrophones are placed at either side of the leak at convenient access points such as hydrants or valves in order to determine the position of the leak. A typical measurement layout to determine the location of a leak in a buried plastic pipe is presented in Figure 1.1. An access point, where a sensor can be attached, is located at each side of the leak at distances $d_1$ and $d_2$. The assumption made here is that the pipe is of infinite length without reflecting discontinuities for the predominantly fluid-borne wave at all frequencies of interest [9].

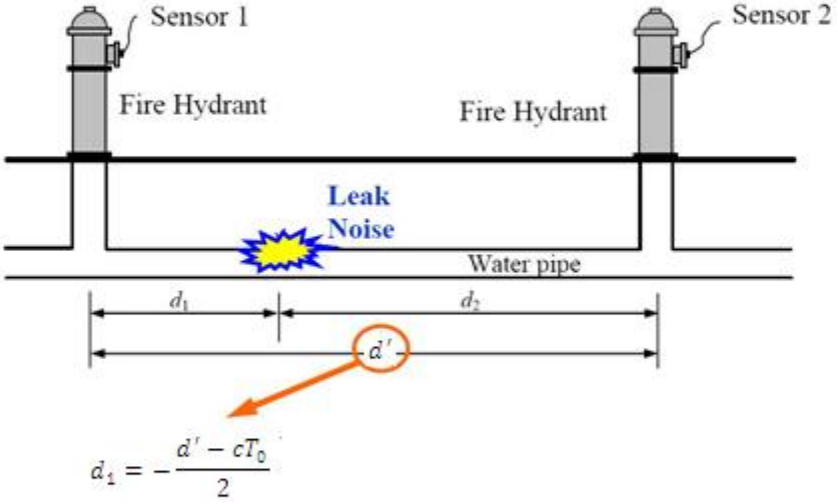

Figure 1.1. A typical measurement layout to determine the location of a leak from a buried water distribution pipe [9].

Considering the situation where the measured data are two continuous random signals $x_1(t)$ and $x_2(t)$ which are assumed to be stationary (ergodic), and setting the mean value of each signal equal to zero, the cross-correlation function (BCC) is defined by [10],

$$R_{x_1x_2}(\tau) = \mathrm{E}\{x_1(t)x_2(t+\tau)\} \tag{1.1}$$

where $\tau$ is the lag of time and $\mathrm{E}\{\quad\}$ is the expectation operator. The argument $T_0$ that maximizes Eq.(1.1) provides an estimate of the delay. In many cases, it is useful to express the cross-correlation function with the cross-correlation coefficient which is a normalized form with scale between -1 to +1 and is defined as [10],

$$\rho_{x_1x_2}(\tau) = \frac{R_{x_1x_2}(\tau)}{\sqrt{R_{x_1x_1}(0)R_{x_2x_2}(0)}} \tag{1.2}$$

where $R_{x_1x_1}(0)$ and $R_{x_2x_2}(0)$ are the values of auto-correlation function $R_{x_1x_1}(\tau)$ and $R_{x_2x_2}(\tau)$ at $\tau = 0$.

In the case where a leak exists, the cross-correlation function will have a distinct peak at the time delay $T_0$ that corresponds to the difference in arrival times of the leak noise at the two sensors. With reference to Figure 1.1 the time delay $T_0$ is related to the location of the sensors and the propagation wavespeed $c$ by the simple algebraic relationship,

$$T_0 = \frac{d_1 - d_2}{c} \tag{1.3}$$

By substituting $d_2 = d^{'} - d_1$ into Eq.(1.3) the position of the leak relative to sensor 1 is found to be,

$$d_1 = -\frac{d^{'} - cT_0}{2} \tag{1.4}$$

From the above variables, $d^{'}$ can be measured reasonably accurately using a variety of methods, for example GPS. The wavespeed $c$ is generally difficult to measure. It has been observed in practice that the wavespeed (speed of leak noise propagation through the pipe) varies considerably from case to case and that leak noise does not propagate long distances in plastic pipes. An experiment which was carried out at the University of East Anglia [11], showed that the wave speed is highly dependent upon the pipe thickness, diameter and material properties [11,12]. Furthermore, the material properties of the pipe are dependent upon temperature so the wave speed can change from day to day and from season to season [13]. If the geometry and material properties of the pipe and also the soil properties are known the wavespeed can be predicted accurately. However, these data are often not available so an estimate has to be made.

### 1.4.1 Development of an analytical model for prediction of the cross-correlation function

In recent work, Gao *et al.* [9] showed that, assuming a flat leak spectrum, the cross-correlation function only depends upon the attenuation of signal in the plastic pipe with frequency and the distance between the two sensors. Applying a band-pass filter to the signals of the sensors the cross-correlation and auto-correlation functions become [9],

$$R_{x_1x_2}(\tau) = \frac{S_0 e^{-\omega_0 \beta d'}}{\pi\sqrt{(\beta d')^2 + (\tau + T_0)^2}}\left[\cos(\omega_0(\tau + T_0) + \theta) - e^{-\Delta\omega\beta d'}\cos(\omega_1(\tau + T_0) + \theta)\right] \tag{1.5}$$

and

$$R_{xx}(\tau) = \frac{S_0 e^{-2\omega_0 \beta x}}{\pi\sqrt{(2\beta x)^2 + \tau^2}}\left[\cos(\omega_0 \tau + \theta) - e^{-2\Delta\omega\beta x}\cos(\omega_1 \tau + \theta)\right] \tag{1.6}$$

where $S_0$ is the leak noise spectral density $\mathrm{Pa}^2/\mathrm{Hz}$, $\beta$ is a measure of the loss within the pipe wall, $d'$ is the distance between the sensors, $\omega_0$, $\omega_1$ are the cut-off frequencies of the band-pass filter, $\Delta\omega = \omega_1 - \omega_0$ is the bandwidth of the band-pass filter, $T_0$ is the time shift and $\theta = \tan^{-1}(\tau/\beta d')$. If the frequency bandwidth satisfies $e^{-\Delta\omega\beta d'} \ll 1$, Eq.(1.5) can be approximated by,

$$R_{x_1x_2}(\tau) \approx \frac{S_0 e^{-\omega_0 \beta d'}}{\pi\sqrt{(\beta d')^2 + (\tau + T_0)^2}}\left[\cos(\omega_0(\tau + T_0) + \theta)\right] \tag{1.7}$$

Comparing Eq.(1.5) with Eq.(1.7) it can be seen that the upper cut-off frequency $\omega_1$ does not appear in the latter equation which means that when the frequency bandwidth is relatively broad the cross-correlation function is mainly dominated by the lower cut-off frequency $\omega_0$. This happens because the pipe acts as a low-pass filter because of damping in the pipe wall [9].

After substituting the cross and auto-correlation functions into Eq.(1.2) the peak value of the cross-correlation coefficient is found to be,

$$\rho_{x_1x_2}(-T_0) = \frac{2\sqrt{d_1 d_2}}{d'} \frac{1 - e^{-\Delta\omega\beta d'}}{(1 - e^{-2\Delta\omega\beta d_1})^{1/2}(1 - e^{-2\Delta\omega\beta d_2})^{1/2}} \tag{1.8}$$

where $T_0$ is given by Eq.(1.3).

Assuming that $d_1 \approx d_2 \neq 0$ and $e^{-\Delta\omega\beta d_1} \ll 1$ (or $e^{-\Delta\omega\beta d_2} \ll 1$), Eq.(1.8) reduces to,

$$\rho_{x_1 x_2}(-T_0) = \frac{2\sqrt{d_1 d_2}}{d'} \tag{1.9}$$

In Figure 1.2 a comparison of the peak cross-correlation coefficient given by Eq.(1.8) and its approximation given by Eq.(1.9) is shown.

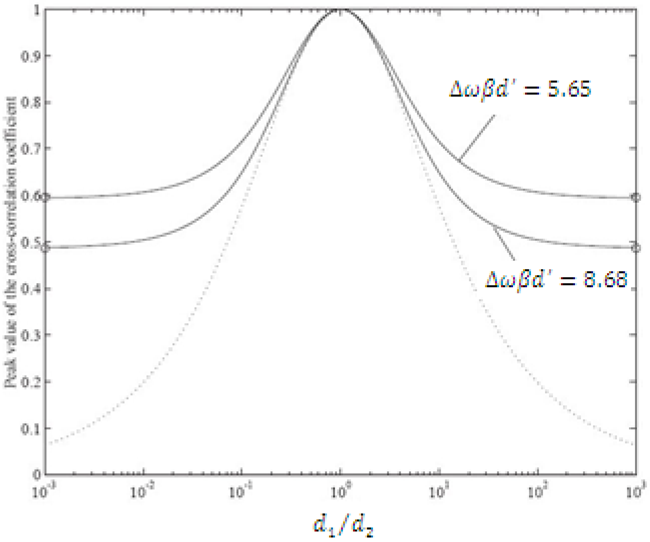

Figure 1.2. Peak value of the cross-correlation coefficient as a function of the ratio of the distances $d_1$ and $d_2$: ———, theoretical values, ……, approximation [9].

Figure 1.2 suggests that when the product $\Delta\omega\beta d$ increases, the approximation given in Eq.(1.9) approaches the solution given in Eq.(1.8). Also, for two sensors spaced eually either side of the leak, $d_1/d_2 = 1$, the peak cross-correlation coefficient is found to be unity which means that there is a perfect linear relationship between the two sensor signals.

The above theoretical model has assumed a flat leak spectrum. In reality, little is known about its real shape and so more experiments have to be conducted in order to determine it with accuracy. This is the main objective of this thesis.

### 1.4.2 Effect of the background noise on the correlation technique

In the same work [9], Gao *et al.* quantified the effect of background noise on the correlation technique. The noise was included into the analytical model mentioned above. Assuming that the leak signals measured by the two acoustic sensors are in the presence of additive background noise, the measured signals are of the form,

$$\begin{aligned} x_1(t) &= s_1(t) + n_1(t) \\ x_2(t) &= s_2(t) + n_2(t) \end{aligned} \tag{1.10}$$

where $s_1(t), s_2(t)$ are random signals due to the leak and $n_1(t)$, $n_2(t)$ are stationary random signals due to the background noise. Assuming that the noise at each sensor is uncorrelated with each other and with the signals $s_1(t), s_2(t)$, the cross-correlation function between $x_1(t)$ and $x_2(t)$ is given by,

$$R_{x_1x_2}(\tau) = R_{s_1s_2}(\tau) \tag{1.11}$$

which means that the effect of uncorrelated background noise can be removed when correlating the two sensor signals.

After substitution of $R_{x_1x_2}(0) = \sigma_x^2$, the cross-correlation coefficient including the noise effects is given by [9],

$$\rho_{x_1x_2}(\tau) = \frac{R_{x_1x_2}(\tau)}{\sqrt{R_{x_1x_1}(0)R_{x_2x_2}(0)}} = \frac{\rho_{s_1s_2}(\tau)}{\sqrt{\left(1 + \frac{\sigma_{n_1}^2}{\sigma_{s_1}^2}\right)\left(1 + \frac{\sigma_{n_2}^2}{\sigma_{s_2}^2}\right)}} \tag{1.12}$$

where $\sigma_{n_1}^2, \sigma_{n_2}^2$ , $\sigma_{s_1}^2, \sigma_{s_2}^2$ are the variances of the signals $n_1(t), n_2(t), s_1(t), s_2(t)$ respectively and $\rho_{s_1s_2}(\tau)$ is the theoretical prediction of the cross-correlation coefficient in the absence of noise. From Eq.(1.12) it can be seen that the correlation coefficient is strongly affected by the signal to noise ratios (SNR) at the two measurement positions.

Assuming that the noise levels at the two measurement positions are the same ($\sigma_{n_1}^2 = \sigma_{n_2}^2$) Gao *et al.* also showed that [9],

$$\left[\frac{\rho_{s_1s_2}(\tau)}{\rho_{x_1x_2}(\tau)}\right]^2 = \left(1 + \frac{\sigma_{n_1}^2}{\sigma_{s_1}^2}\right)\left(1 + \frac{\sigma_{n_1}^2}{\sigma_{s_2}^2}\right) \tag{1.13}$$

Using the ratio of the peak cross-correlation coefficients $\rho_{s_1 s_2}(T_0)/\rho_{x_1 x_2}(T_0)$ the ratio $\sigma_{n_1}^2/\sigma_{s_1}^2$ can be determined from Eq.(1.13). Therefore, taking into account that the correlation technique is affected by the selection of the cut-off frequencies of the band-pass filter the SNR can therefore be enhanced using carefully selected frequency information.

### 1.4.3 Selection of acoustic/vibration sensors for leak detection

In a recent study Gao *et al.* [14] evaluated the effect of the selection of acoustic and vibration sensors on the correlation technique by investigating the peak cross-correlation coefficient. They found that when the two sensors are not equidistant from the leak source ($d_1 \neq d_2$), which occurs in most practical situations, the signals measured with hydrophones (acoustic signals) give the highest peak cross-correlation coefficient. Therefore, in cases of a small SNR environment it is better to use hydrophones instead of accelerometers. On the other hand, it was found that the peak of the cross-correlation coefficient between accelerometer-measured signals is sharper than that between hydrophone-measured signals. This suggests that accelerometers are most suitable in multi-leak and coherent noise situations [14].

## 1.5 Acoustical characteristics of leak signals in plastic water pipes

As mentioned above the effectiveness of existing acoustic leak detection methods and equipment has been demonstrated in the past and are considered to be satisfactory for use in metallic pipes. For plastic pipes, the propagation characteristics change due to the different properties of plastic materials. Therefore, it is important to conduct a study to investigate the acoustical characteristics of leak signals in plastic pipes to determine the frequency content of leak signals, the attenuation rate and the variation of propagation velocity with frequency.

### 1.5.1 Wave propagation in plastic pipes

For the correlation technique to be effective, the propagation wavespeed and wave attenuation must be known *a priori*. For plastic pipes, the wave propagation behaviour becomes highly coupled between the pipe wall, the contained fluid and the surrounding medium [15], which means that the wavespeed and losses in water pipes are highly dependent on the pipe wall properties and the surrounding medium.

A Canadian study was carried out [13] for investigating the acoustical characteristics of leak signals in plastic water pipes and experiments were conducted on a 200m long buried plastic pipe of 150 mm diameter. Results showed that most leak noise energy is concentrated at frequencies below 100 Hz [13]. Therefore, studies for wave propagation have been focused on frequencies well below the pipe ring frequency where four wave types are responsible for most of the energy transfer: three axisymmetric waves ($n$=0) and the $n$=1 wave related to beam bending [16,17]. The first $n$=0 wave, termed $s$=1, is a predominantly fluid-borne wave which is strongly influenced by the flexibility of the wall. The second wave termed, $s$=2, is predominantly the compressional wave in the shell with some associated radial wall motion influenced by the contained fluid. The third wave, $s$=0, is a torsional wave in the shell uncoupled from the contained fluid.

Muggleton *et al.* [12], solved the pipe equations for $n$=0 axisymmetric wave motion for a fluid-filled pipe surrounded by an infinite elastic medium which can sustain both longitudinal and shear waves for two wave types $s$=1, 2. These wave types correspond to a fluid dominated wave and an axial shell dominated wave and both involve motion of the shell and the fluid. Solutions were expressed in terms of a complex wavenumber for each wave, the real part of which gives the wavespeed and the imaginary part of which gives the wave attenuation. It was found that, for the fluid-borne $s$=1 wave, the wavespeed is reduced by the presence of the pipe wall from the free field value and it is further reduced by the presence of the surrounding medium. However, the latter effect is small compared with the effect of the pipe wall. Furthermore, it was found that the wave may or may not radiate into the external medium depending on its wavespeed compared with that of the surrounding medium. In the case that it radiates, at low frequencies, losses within the shell wall will dominate. For the $s$=2 wave the effect of both the contained fluid and the surrounding medium on the wavespeed was found to be small. The wave always radiates into the surrounding medium but at the frequencies of interest (low frequencies) the radiation losses are small compared with the losses within the shell wall.

Extending the above work, Muggleton *et al.* [11] validated experimentally the theoretical model for predicting both the wavespeed and wave attenuation of the fluid-borne axisymmetric wave for a buried fluid-filled pipe [11]. Wavenumber measurements were carried out in *in vacuo* and buried pipes and the results showed good agreement with theoretical predictions. In Figures 1.3(a) and (b), the real and the imaginary components of the measured and predicted wavenumbers of *in vacuo* pipe are presented whereas in Figures 1.4(a) and (b) the real and the imaginary components of the measured wavenumbers of the buried and of the *in vacuo* pipes are shown to allow easier comparison.

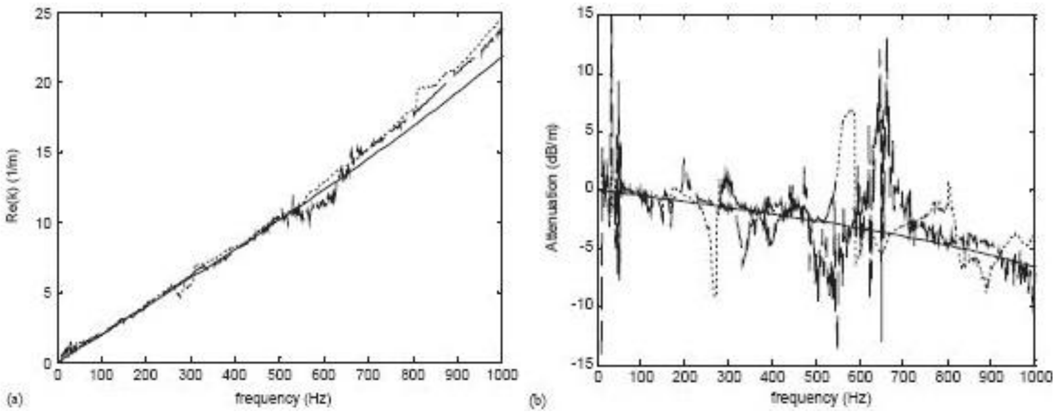

Figure 1.3. Wavenumber for the axisymmetric fluid-borne wave in *in vacuo* pipe: (a) real part; (b) imaginary part; ─── predicted; …… measured [11].

Figure 1.3 suggests good agreement between the measured and predicted values for the real part of the wavenumber especially at low frequencies where the wavenumber varies approximately linearly with frequency, implying a frequency-independent wavespeed. When the frequency increases and approaches the pipe ring frequency (~ 2 kHz in that case) the results deviate from the theoretical values. From Figure 1.3(a) the wavespeed was deduced to be around 300 m/s. From Figure 1.3(b) it can be seen that deviations exist between the theoretical and measured values of attenuation. However, at low frequencies the mean values for the measured data show good agreement. The attenuation at 400 Hz is around 2 dB/m indicating that in the absence of reflected waves the pressure amplitude would halve approximately every 3 m [11].

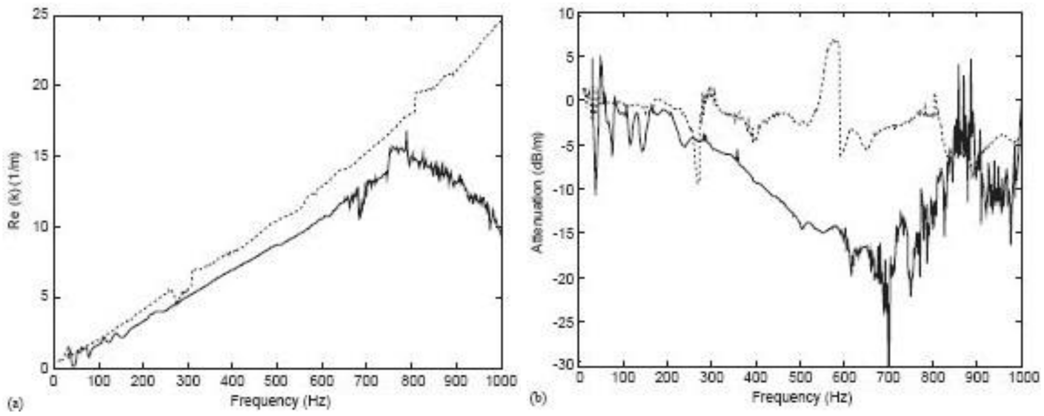

Figure 1.4. Measured wavenumber for the axisymmetric fluid-borne wave: (a) real part; (b) imaginary part; ——, buried pipe; ……, *in vacuo* pipe [11].

Figure 1.4(a) suggests that the real part of the wavenumber for the buried pipe increases with frequency until around 750 Hz where it starts to drop off. Similarly, in Figure 1.4(b), the magnitude of the imaginary part for the buried pipe increases also with frequency until around 700 Hz. Comparing with the *in vacuo* data both the wavespeed and the measured attenuation are greater for the buried pipe. The fact that the attenuation is greater (~ 10 dB/m compared with ~ 2 dB/m at 400 Hz) is expected because of the radiation into the surrounding ground. The increase in wavespeed (to around 350-400 m/s compared with 300 m/s) may be due to an increase in stiffness and this is most likely to be in the pipe wall itself [11]. Therefore, for detecting leaks in plastic pipes the pipe’s environment must be taken into consideration as it can affect the estimation of the wavespeed which is vital for the correct estimation of the leak position. This is essential because the properties of the pipe wall are temperature dependent and so may vary considerably depending on the pipe’s environment. Also the finding that the surrounding soil increases the wave attenuation compared with the *in vacuo* case suggests an additional difficulty.

In a different study [18], Muggleton and Brennan investigated theoretically the wave transmission and reflection characteristics of the $s$=1 and $s$=2 waves at an axisymmetric pipe wall discontinuity for a soft-walled pipe, taking into account the coupled nature of the two wave types. The discontinuities considered were: a change in wall thickness, a change in pipe wall material elastic modulus and a change of internal fluid cross-section. It was found that in the case where the fluid cross-section remains the same, changing the wall thickness or the wall elasticity causes negligible mode conversion at the discontinuity. Also, the wave transmission and reflection coefficients can be determined by considering each wavetype separately. For the $s=1$ fluid-dominated wave the reflection and transmission coefficient can be found by taking into account only the wavenumber change at the discontinuity whereas for the $s=2$ shell-dominated wave the coefficients can be found assuming that the pipe is empty and considering the thickness or the elasticity change only. When there is a change in fluid cross-section it was found that mode conversion occurs between the two wave types. That means that the waves cannot be treated separately and must be considered together.

## 1.5.2 Experimental leak detection facility

Tests have been carried out at a leak detection facility at an experimental site located at the National Research Council (NRC) campus in Ottawa, Canada in order to evaluate the acoustical characteristics of leak signals in buried plastic pipes [1,13]. The facility consisted of a 150 mm diameter PVC pipe that was about 200 m long and was buried in soft clay soil at a depth of 2.4 m. The following acoustical characteristics were evaluated:

- ➢ Frequency content of sound or vibration signals as a function of sensor attachment, leak type, flow rate, pipe pressure and season
- ➢ Attenuation rate
- ➢ Variation of propagation velocity with frequency

The leak types included those from faulty joints and service connections. Leak detection sensors, like accelerometers and hydrophones, were attached at various contact points of the test pipe including two fire hydrants that were about 100 m apart as well as several 19 mm copper pipe service connections [1,13].

### Frequency content of sound and vibration signals

#### *Comparison of fire hydrants with service connections*

In the Canadian study, in order to investigate the suitability of signals measured at service connections for use in evaluating the attenuation characteristics of leak signals, the frequency content of leak signals measured with hydrophones attached to copper service connections was compared with that of a hydrophone attached to fire hydrants [13]. The results showed that the amplitudes at frequency components above 20 Hz at the service connection were significantly lower than those at the fire hydrant. Another significant observation was that the results obtained for leak signals measured at service connections were not reproducible. That means that when the hydrophone was removed and attached again different results were produced. One possible reason for this is that the soil around the service connection was not well compacted and the coupling between the vertical service connection pipe and the soil was easily changed. For all those reasons the leak signals were measured only at the fire hydrants.

### *Leak type effect*

In the Canadian study, two leak types were taken into consideration and were compared with ambient noise. A joint leak and a service connection leak. The measurements were made with both accelerometers and hydrophones and are presented in Figure 1.5 [13].

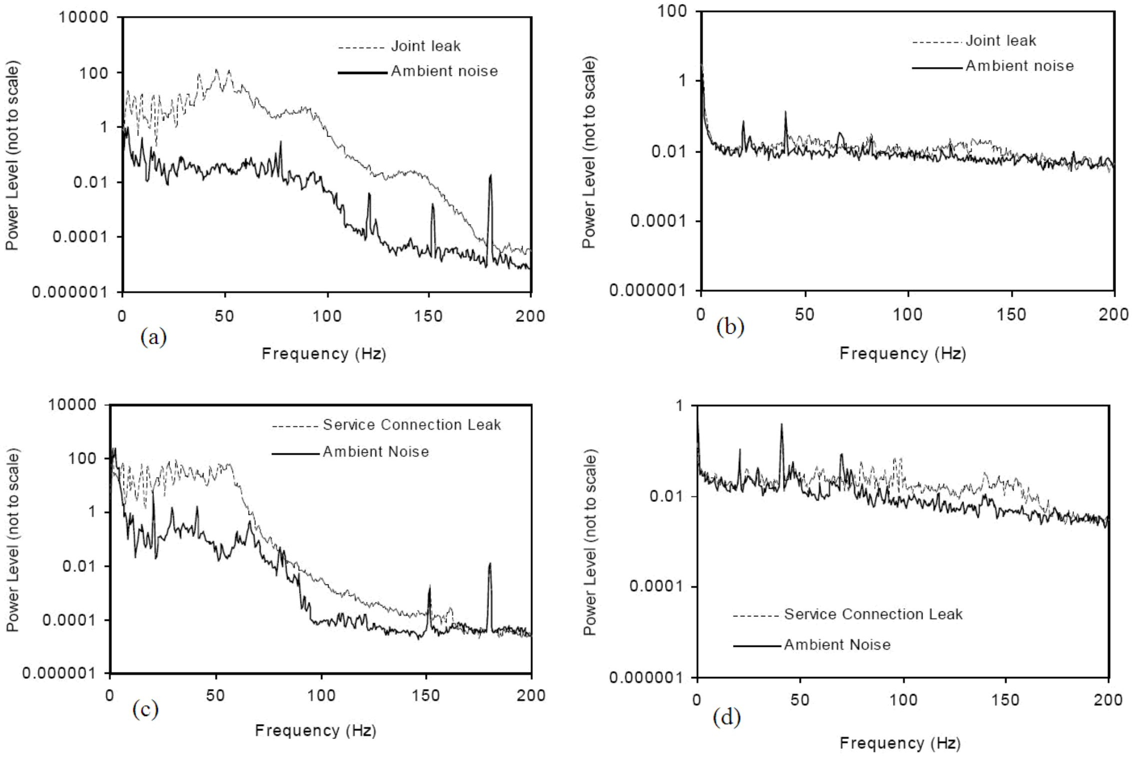

Figure 1.5. Comparison of frequency spectra of joint leak and ambient noise and service connection leak and ambient noise measured by two different sensors; (a),(c) using a hydrophone; (b),(d) using an accelerometer [13].

Figure 1.5 suggests that the frequency content of the signals induced by the joint leak is higher compared to the frequency content of the signals induced by a service connection leak. Also, the signals measured with hydrophones are significantly higher than the ambient noise compared with the leak signals measured with accelerometers. One possible reason for this is that the accelerometers are able to detect the ground-borne ambient noise whereas the hydrophones are not. Also, for signals from the service connection leak measured with hydrophones most of the frequency content was below 50 Hz whereas at higher frequencies the signal amplitudes were extremely small. Accelerometer measured signals had higher levels at high frequencies.

***Pipe pressure and flow rate effect***

It is known from the theory [19] that at higher pressure the flow rate from a fixed size opening in the pipe is higher which then leads to signals that have a greater high-frequency content. This agrees with the measurement results obtained in the Canadian study, presented in Figure 1.6. It can be seen that at low frequencies there is a small difference between the signals with low and high pressure whereas at higher frequencies this difference increases [13].

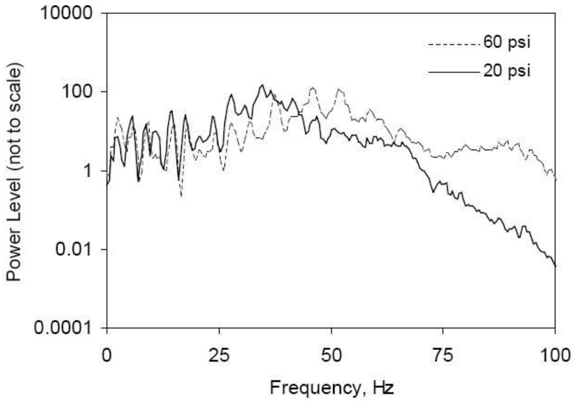

Figure 1.6. Frequency spectrum of leak signals induced by fully open joint leak at pipe pressures of 1.38 bar and 4.14 bar (20 and 60 psi) [13].

Figure 1.7 suggests that for a particular pressure, the flow rate of the leak signal has a significant impact on the amplitude of measured signals but has a negligible impact on their frequency content as the shape of the frequency spectrum does not change [13]. This is not in agreement with the results that will be presented in Chapter 5 according to which both the frequency content and the amplitude of the signals decrease as flow velocity (flow rate) decreases.

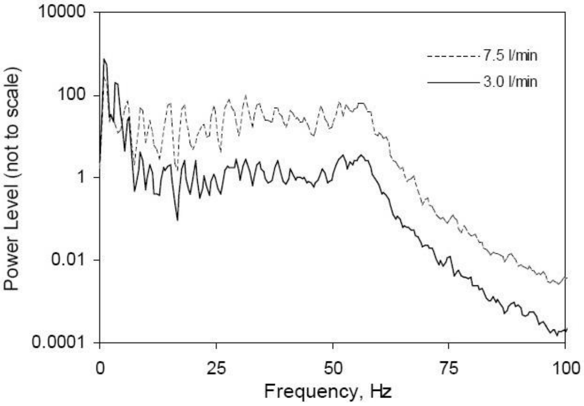

Figure 1.7. Frequency spectrum of signals induced by 0.64 cm underground nozzle open at flow rate of 3 L/min ($\approx V = 1.25$ m/s) and 7.5 L/min ($\approx V = 4$ m/s) [13].

### *Effect of season*

The same study, showed that seasonal effects play a major role on the frequency content of leak signals. This can be seen in Figure 1.8 where for frequencies below 10 Hz the amplitude of the signals in winter is slightly higher than those in summer whereas at higher frequencies the opposite happens but with a large difference in the signal amplitudes between the two seasons. [13].

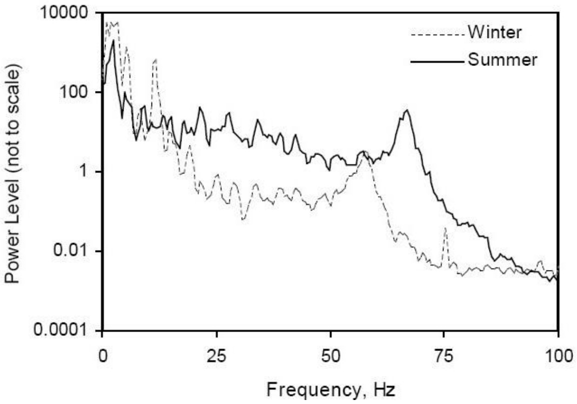

Figure 1.8. Frequency spectrum of joint leak signals measured in summer and winter [13].

## Attenuation rate

The attenuation rate of leak signals between two hydrophones was also evaluated in the same study by measurements at two fire hydrants. Signals were induced by two leak sources. One joint leak that was in the pipe segment between the two fire hydrants (in-bracket source) and an open valve which was in the pipe segment outside the fire hydrants (out-of-bracket source). In the first case (in-bracket source) the distance between the two receivers was 44.4 m whereas in the second case (out-of-bracket source) the corresponding distance was 102.6 m [13]. The attenuation rate was evaluated from the transfer function between the leak signals. Figure 1.9 suggests an overall attenuation rate at 0.25 dB/m at 15 Hz. For winter the corresponding attenuation rate was found to be 0.33 dB/m at 15 Hz [12].

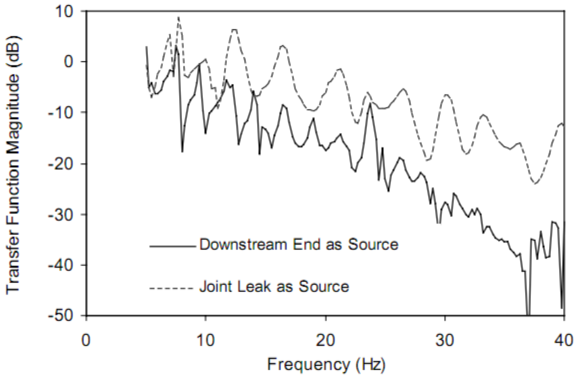

Figure 1.9. Transfer function obtained by a joint leak and an open valve at the downstream end of the test pipe for signals measured at the upstream and downstream hydrants [13].

## Propagation velocity

### *Effect of source position relatively to the leak*

Using the cross-correlation method the propagation velocity can be estimated using the time lag between coherent continuous signals measured at two points at a known distance apart. The signals are generated using a source at a known location. In the Canadian study [13], the signals were induced by either the in-bracket source or the out-of-bracket source. In Figure 1.10 the cross-correlation of the measured signal is presented. The cross-correlation peak for the out-of-bracket source is seen to be less definite than that for the in-bracket source. This was expected because, for the out-of-bracket source, the distance between the two measured points is greater and therefore the signals are less similar compared with the in-bracket source. The calculated velocities were 482 m/s and 466 m/s for the in-bracket and out-of-bracket source respectively [13].

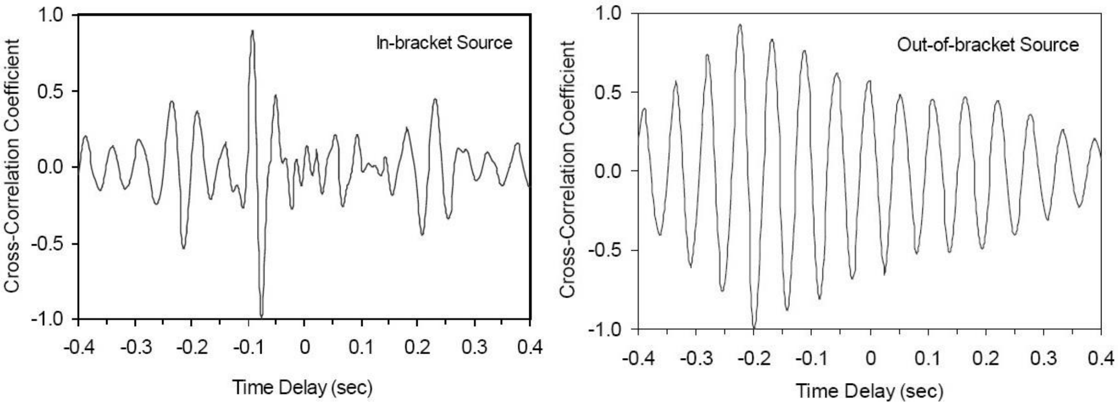

Figure 1.10. Cross-correlation of signals induced by two different sources [13].

### *Sensor type effect (hydrophones /accelerometers)*

The effect of sensor type (hydrophones and accelerometers) in the propagation velocity was also evaluated by Hunaidi *et al*. Based on the slope of the unwrapped phase angle presented in Figure 1.11 the wavespeed was calculated to be 482 m/s for hydrophone-measured signals and 492 m/s for accelerometer-measured signals at the frequency range of 10 Hz- 150 Hz [13]. These results match well with theoretical estimations obtained from an analytical model developed by Gao *et al.* to predict the cross-correlation function using pressure velocity and acceleration sensors [14]. From this theoretical model, the wavespeed was calculated to be 479 m/s for hydrophone-measured signals and 484 m/s for accelerometer measured signals which are in good agreement with the results obtained by Hunaidi *et al.* [13].

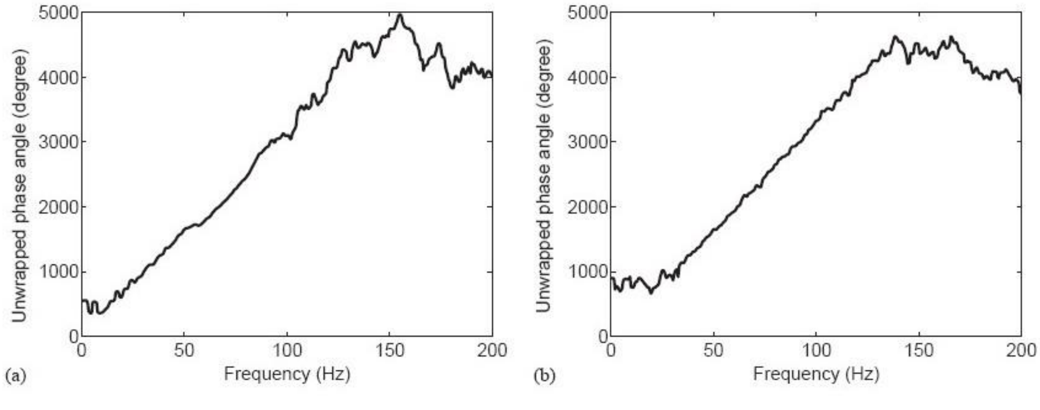

Figure 1.11. Unwrapped phase angle for (a) hydrophone-measured signals; (b) accelerometer-measured signals.

### *Effect of season*

Finally, the effect of season on the propagation velocity was examined at the same study and it was found that the propagation velocity measured during winter was 515 m/s compared with 482 m/s during summer, which suggests a difference of 7% [13]. This may be explained by the fact that in winter the stiffness of the pipe may increase and also the density of the water core may increase due to lower water temperature in winter.

## Analysis of sensor signals using cross-correlation

In the same study, the leak signals from the sensors were recorded simultaneously on a 16-bit digital tape recorder. The signals were first passed through anti-aliasing filters with 200 Hz cut-off frequency. The sampling frequency was 500 Hz. Spectral analysis was performed on the digitized signals using a 1024-point fast Fourier transform (FFT), Hanning window, and power spectrum averaging. For computing the cross-correlation function via FFT the digitized signals were passed through a band-pass filter with cut-off frequencies 10 and 100 Hz. A rectangular 512-point force window with 50% overlap was also employed to eliminate the circular effect implicit in the discrete Fourier transform [13].

The measurements from the above experiment (hydrophone measured signals) were also used by Gao *et al.* in order to evaluate the effect of the cut-off frequencies of the band-pass filters [9]. For the comparison of the experimental results with the corresponding theoretical predictions the effect of the background noise on the theoretical predictions was taken into account by setting the peak values of correlation coefficient to be the same as those of the experimental results [9]. In the same work it was theoretically shown that the cross-correlation coefficient is mainly determined by the lower cut-off frequency provided that the bandwidth of the leak noise is relatively broad. This effect can be seen by comparing Figures 1.12(d), (f), (h) which are very similar to each other. A slight difference can be seen in Figure 1.12(b) as in this case the theoretical correlation coefficient is governed by both the lower and the upper cut-off frequencies as the bandwidth is small. In the experimental results there is a small difference in the correlation coefficient when the cut-off frequency of the low pass filter is set to 30 and 50 Hz (Figures 1.12 (a) and (c)). For values above 50 Hz the correlation coefficient does not change [9]. This indicates that the most information about the leak signal is concentrated below 50 Hz which is in agreement with the conclusion of Hunaidi *et al.* [1,13].

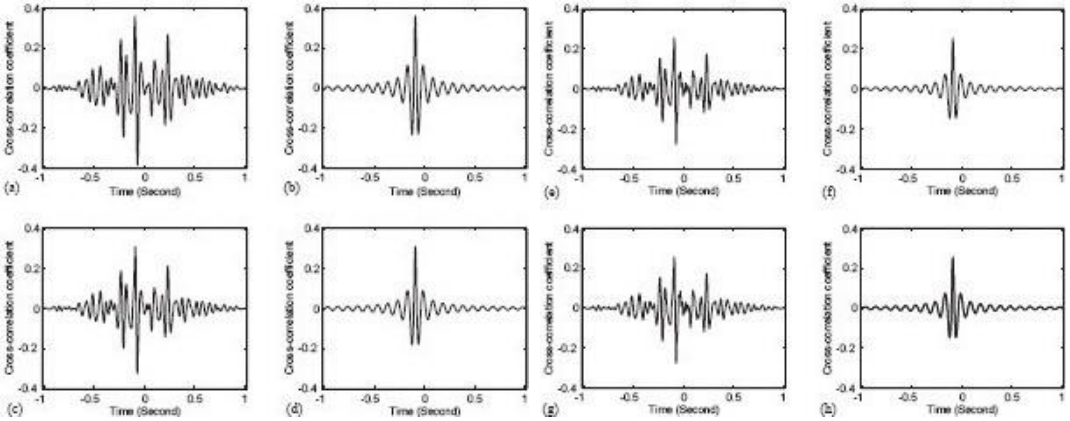

Figure 1.12. Effect of the low-pass filter cut-off frequency on the cross-correlation coefficient. The cut-off frequencies of the high-pass filters are set at 10 Hz. The low-pass filter cut-off frequencies are: (a) 30 Hz; (c) 50 Hz; (e) 100 Hz; (g) 200 Hz. Comparison with the corresponding theoretical values when the low-pass filter cut-off frequencies are set at: (b) 30 Hz; (d) 50 Hz; (f) 100 Hz; (h) 200 Hz [9].

Figure 1.13 shows the effect of the high-pass filter cut-off frequency for both experimental results and predictions. It can be seen that when the cut-off frequency is below 10 Hz a definite peak cannot always be obtained. Thus, the high-pass filter can be set at 10 Hz.

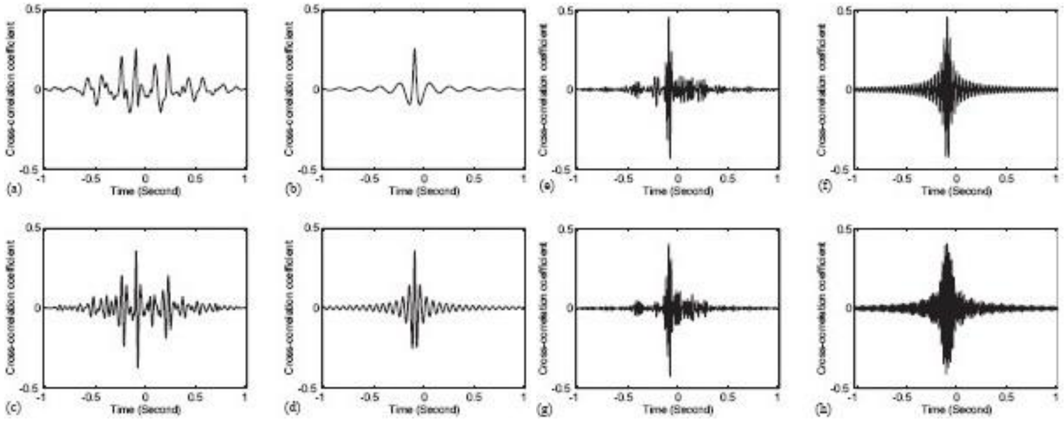

Figure 1.13. Effect of the high-pass filter cut-off frequency on the cross-correlation coefficient. The cut-off frequencies of the low-pass filters are set at 50 Hz. The high-pass filter cut-off frequencies are: (a) 5 Hz; (c) 15 Hz; (e) 30 Hz; (g) 40 Hz. Comparison with the corresponding theoretical values when the high-pass filter cut-off frequencies are set at: (b) 5 Hz; (d) 15 Hz; (f) 30 Hz; (h) 40 Hz [9].

## 1.6 Current problems of detecting leaks in plastic water pipes

The effectiveness of leak detection techniques depends on a number of factors including the characteristics of the pipe, the leak size, the pipe pressure and the background noise.

The material, the diameter and the wall thickness of the pipe have a significant effect on the wavespeed and the attenuation of the leak signals. The larger the ratio of the diameter to the thickness, the greater attenuation and the harder it is to detect the leak. Furthermore, leak signals are highly attenuated in plastic pipes and travel furthest in metallic ones.

The larger the leak, the larger the leak signal but this may not be the case for very large leaks [1]. As far as the pressure is concerned the higher the pipe pressure the stronger the leak signals (Figure 1.6). It is difficult to detect small leaks in pipes having pressures less that 1 bar [1]. Also, background noise may mask the leak signals especially when the latter are weak.

## 1.7 Research Objectives

This research work has two main objectives. The first is to determine and characterize the physical mechanisms of leak noise generation. Although water flow through pipe orifices has been studied in the past, as seen in the previous sections, and the frequency content of leak signals has been investigated to some extent for different kinds of leaks, pipe pressure, flow rate and season, there have been no firm conclusions about the mechanism of leak noise generation.

The second main objective is to investigate the shape of the leak noise spectrum and the factors that influence it such as leak size and jet flow velocity. This information is used to develop an empirical model that describes this behaviour. Work, carried out in the past for developing an analytical model to predict the Basic Cross Correlation (BCC) function (and so the cross-correlation coefficient) of leak signals in plastic pipes has assumed a flat leak spectrum over the frequency bandwidth of interest. How the real spectral shape affects the peak of cross-correlation coefficient is investigated.

Finally a matched field processor that is widely used in underwater acoustics for source localization is applied to the leak detection problem. Its performance is compared with that of the Basic Cross-Correlator (BCC) and Phase Transform correlator (PHAT).

The research objectives are therefore to,

1 Investigate the physical mechanisms of leak noise generation.

2 Derive the spectral shape of leak noise and investigate experimentally how it is affected by leak size and jet flow velocity.

3 Derive an empirical model that describes this behaviour.

4 Investigate how this model for the leak noise spectrum affects the peak of the cross-correlation coefficient for leak signals in plastic water pipes and compare it with the results obtained from previous work that assumes a flat leak spectrum.

5 Apply a matched field processor used for source localization in underwater acoustics to the leak detection problem and compare its performance with that of the BCC and PHAT.

## 1.8 Contributions of the Thesis

In the accomplishment of the research objectives, the following contributions have been made:

1 Turbulence in the water jet has been identified as the mechanism of leak noise generation, at least in our experimental rig.

2 Measurements revealed that the leak noise spectrum followed a general well defined shape. The effect of jet velocity and leak size to the general spectral shape was quantified.

3 An empirical model that describes this behaviour has been established.

4 The effect of the model of the leak noise spectrum on the peak of the cross-correlation coefficient has been determined.

5 A matched field processor has been applied to the leak detection problem and to real experimental data and found to give much better performance compared to the BCC and a similar one compared to the PHAT. However, some advantages of the matched processor make it more useful in practical situations.

## 1.9 Thesis outline

The main body of this thesis consists of eight chapters. **Chapter 2** reviews some basic theory of noise generation through fluid flow. **Chapter 3** describes the preliminary rig that was designed to characterize leak noise and presents some initial results. **Chapter 4** presents an improved rig that was designed and focuses on the investigation of the mechanisms of leak noise generation. **Chapter 5** examines the characteristics of leak noise spectrum and how it is affected by leak size and flow velocity by using a different experimental set-up designed for this reason. An empirical model that describes this behaviour is proposed. **Chapter 6** applies a matched field processor to the leak detection problem and to experimental data and it compares its performance with the BCC and PHAT. **Chapter 7** investigates how the shape of the leak noise spectrum affects the peak of the cross-correlation coefficient and comparison is made for the case of a flat leak spectrum. **Chapter 8** concludes the thesis and avenues for future investigation are given.

# CHAPTER 2

# BASIC THEORY OF NOISE GENERATION THROUGH FLUID FLOW

## 2.1 Introduction

In this chapter some fundamental principles of fluid noise theory are presented that are later used in the following chapters of this thesis. Bernoulli’s principle is initially presented and information about the types of flow through a circular pipe is given. Reynolds and Strouhal numbers, are defined. The flow through different kinds of circular orifices is examined and different parameters that affect it are presented. Information about the structure of water jets discharging into air and the waves that are created is also given. Finally, possible mechanisms of leak noise such as cavitation and turbulence in the water jet are investigated. This information will be later used to draw conclusions about the nature of leak noise in our test rig.

## 2.2 Bernoulli’s principle

Bernoulli’s principle states that for an inviscid steady flow an increase in the speed of the fluid occurs simultaneously with a decrease in pressure or a decrease in the fluid's potential energy. Bernoulli equation can be derived from the equation of motion which due to its complexity is not capable of solution except in special cases [20]. For a two-dimensional flow of an incompressible, inviscid fluid in the absence of body forces the relationship between flow velocity and pressure described by the Bernoulli’s equation is given by [20],

$$\frac{V_1^2}{2}+\frac{p_1}{\rho}=\frac{V_2^2}{2}+\frac{p_2}{\rho} \tag{2.1}$$

where $V$ is the fluid velocity, $p$ is the fluid pressure, $\rho$ is the fluid density and the subscripts 1 and 2 refer to two points on the same streamline. Eq. (2.1) is the simplest form of Bernoulli equation and shows that the flow velocity is greatest where the pressure is least. In the case where we consider a flow of a liquid through a tube, as shown in Figure 2.1 and assuming constant density the continuity equation requires that [20],

$$Q = V_1 A_1 = V_2 A_2 \tag{2.2}$$

where $Q$ is the volume flow rate. Substituting Eq.(2.2) into Eq.(2.1) the pressure difference between points 1 and 2 is given by,

$$p_1 - p_2 = \frac{\rho}{2}\left(\frac{Q}{A_2}\right)^2\left[1-\left(\frac{A_2}{A_1}\right)^2\right] \tag{2.3}$$

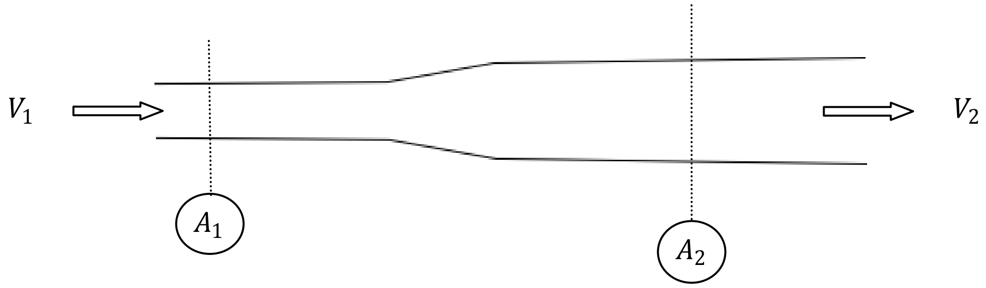

Figure 2.1. Tube with different cross-section areas $A_1$ and $A_2$.

## 2.3 Flow in circular pipes

Flow in circular pipes for Newtonian fluids has been extensively studied due to the practical interest the problem is relevant to [20-25]. Experiments have been conducted by various researchers using clear pipes where dye was injected for detecting whether the flow is laminar or turbulent and when transition occurs. It was found that at a very slow flow rate, the dye stream follows a well-defined straight line parallel to the pipe axis and remains straight as the flow rate is slowly increased. This flow is a laminar flow. Increasing the flow rate, it was found that above a certain point the streamlines becomes wavy and if the flow is increased still further, the distinct line will disappear completely and the dye will spread uniformly throughout the pipe. This flow is a turbulent flow [20-25]. The change from laminar to turbulent flow is accompanied by a large change in flow-related processes such as mixing, heat transfer and drag which all increase significantly [24].

A phenomenon that can be also observed in the flow in circular pipes is the reverse transition from turbulent to laminar flow. This is known as relaminarization [26-29]. Reverse transition is essentially due to the domination of pressure forces over the slowly responding Reynolds stresses in an original turbulent flow accompanied by the generation of a new laminar boundary layer stabilized by a favourable pressure gradient [29].

## 2.3.1 Reynolds number

The transition from laminar to turbulent flow is a function of a dimensionless quantity known as Reynolds number following Osborne Reynolds who was the first to demonstrate the two possible modes of flow in pipes. The Reynolds number is given by,

$$Re = \frac{Vd}{\nu} \tag{2.4}$$

where $V$ is the average fluid velocity in the pipe, $d$ is the pipe diameter and $\nu$ is the kinematic viscosity which for water at $20^{o}$C is approximately $10^{-6}$ $\mathrm{m^2/s}$ [20-25,30].

The transition occurs because above a certain Reynolds number the laminar flow becomes unstable. If small disturbances are imposed on the fluid these disturbances are damped out for the case of laminar flow. As the Reynolds number is increased, laminar pipe flow becomes unstable for a disturbance of a certain frequency and for all small disturbances. For these higher Reynolds numbers the disturbances grow and interact with each other to result in the irregular, fluctuating characteristic motion of turbulent flow [20]. Increasing more the value of disturbance it can return back to laminar (relaminarization) and at still larger disturbances the flow again becomes turbulent. Because the transition depends on disturbances either imposed externally or from roughness elements in the surface it may occur in a wide range of Reynolds numbers. In very carefully controlled experiments it has been possible to maintain laminar flow in smooth pipes up to *Re*=40000 based on pipe's diameter [20].

### 2.3.2 Strouhal number

Strouhal number is another important dimensionless quantity in fluid dynamics which remains constant for dynamically similar flow and is given by [30],

$$St = \frac{fd}{V} \tag{2.5}$$

where $f$ is the frequency, $d$ is the characteristic transverse dimension of the body (diameter for circular pipes) and $V$ is the average fluid velocity of the pipe.

The frequency content of noise sources is determined by the 'length-scale' and 'velocity' of hydrodynamic disturbances as shown in Figure 2.2.

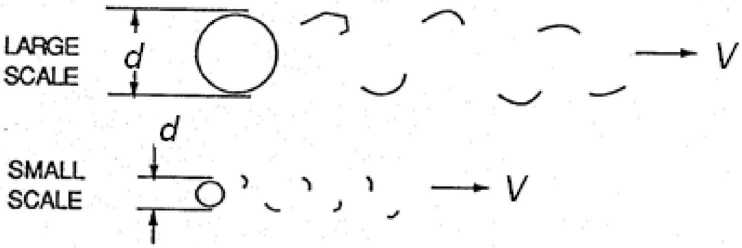

Figure 2.2. Proportionality of the 'wavelength' of disturbance with *d*.

## 2.4 Flow through orifices

The flow through orifices has been studied extensively in the past. Johansen has investigated the flow of water up-stream and down-stream of a sharp-edged circular orifice mounted concentrically in a glass pipe by injecting colouring matter into the stream over a range of low Reynolds number [23]. Photographs show the gradual transition from steady to turbulent flow. Nevertheless, the exact flow through or about these orifices is quite complicated. For this reason, simplifying assumptions are made, such as an absence of friction and one-dimensional flow. Idealized solutions are computed, which afterwards are corrected by coefficients which either are determined experimentally or from theoretical expressions. For an ideal jet through a small sharp-edge orifice of diameter $d$ the appearance of the flow would be as shown in Figure 2.3 [21].

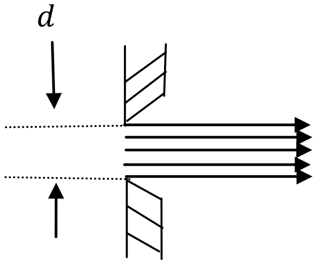

Figure 2.3. Ideal flow through a small orifice of diameter $d$ and area $A_l$.

The flow rate from this ideal jet is equal to the ideal velocity, which is the velocity assuming no losses, multiplied by the area of the jet. In reality, the appearance of the actual jets will differ from the one showed above since the jet, due to the friction effect, will be slowed in the surrounding medium and will have a tendency to spread out. The appearance of a real jet through a sharp-edge orifice can be seen in Figure 2.4 [22].

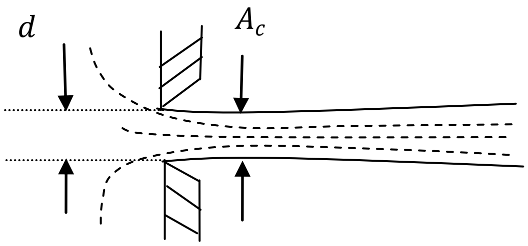

Figure 2.4. Real flow through small orifice of diameter $d$.

The streamlines converge while approaching the orifice and they continue to converge beyond the upstream section of the orifice until they reach a section where they become parallel [20,22]. This section is called *vena contracta* and is a section of minimum area $A_c$ at a position of about 0.5 $d$ from the upstream edge of the opening [22].

## 2.4.1 Coefficient of contraction, velocity and discharge

The ratio $A_c$ of the jet area to the area $A_l$ of the orifice is called the coefficient of contraction $C_c = A_c/A_l$. If $V_i$ is the velocity that would be attained in the jet if friction did not exist (ideal situation) and $V$ the actual average velocity, always smaller than the ideal velocity, then the ratio $V/V_i$ is called the coefficient of velocity $C_v$. The ratio of the actual rate of discharge $Q$ to the ideal rate of discharge $Q_i$ (that would occur if no friction and contraction existed) is defined as discharge coefficient $C_d$. Knowing that $Q_i = V_i A_l$ and $Q = VA_c$ it can be seen that $C_d = C_c C_v$ [20,22].

The coefficient of contraction can be determined by measuring the jet diameter at the vena contracta and then comparing the jet area with the orifice area. Small variation in the edge of the orifice can significantly alter its value [20,22].

The average velocity $V$ can be determined by measuring the flow rate and dividing by the cross-sectional area of the jet whereas the ideal velocity $V_i$ can be determined by Bernoulli's equation. Dividing these two values gives the velocity coefficient.

The coefficient of discharge is the easiest to obtain with a high degree of accuracy and it has most practical value. For a fluid the real $Q$ can be determined by measuring the volume or weight over a known time. Thus, for a circular orifice of area $A_l$ the contraction coefficient will be given by

$$C_d = \frac{Q}{Q_i} = \frac{Q}{A_l\sqrt{\dfrac{2\Delta p/\rho}{1-\left(\dfrac{A_l}{A_{pipe}}\right)^2}}} \tag{2.6}$$

where, $\Delta p$ is the pressure difference between the pipe and the jet and $A_{pipe}$ is the cross-sectional area of the pipe.

Therefore, in practical situations, where the discharge coefficient of the orifices has to be taken into account, Bernoulli's equation will be given by,

$$p_1 - p_2 = \frac{\rho}{2}\left(\frac{Q}{C_d A_2}\right)^2\left[1-\left(\frac{A_2}{A_1}\right)^2\right] \tag{2.7}$$

In Figure 2.5, four different types of orifices are sketched and the approximate values of the coefficients of contraction, velocity and discharge are shown [22].

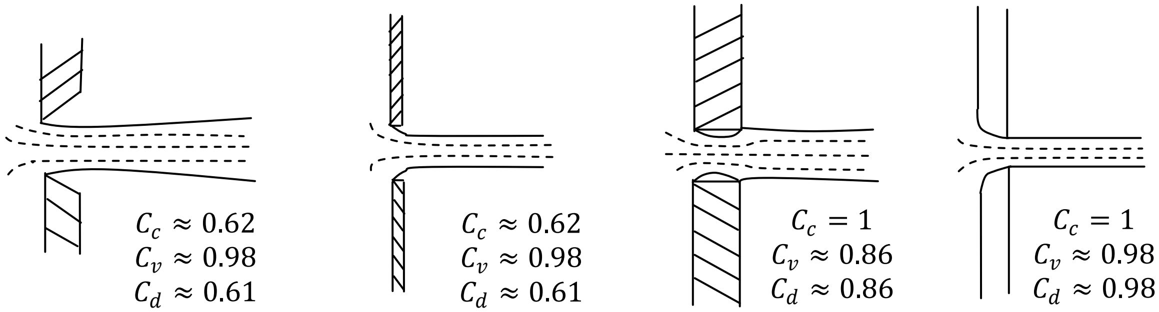

(a) (b) (c) (d)

Figure 2.5. Different kind of orifices; (a) Sharp-edge; (b) Square shoulder; (c) Thick-plate; square edge; (d) Rounded.

## 2.4.2 Structure in water jets

A significant amount of theoretical and experimental work has been undertaken in the past about the structure of water jets in air [31-36]. Landahl, [31] used the kinematic wave theory to determine the conditions under which the laminar flow breaks into turbulent flow. In this work primary and secondary waves corresponding to primary and secondary instabilities of the jet were described theoretically. Amplification of the secondary waves and their interaction with the primary wave were believed to result in flow breakdown into turbulence and subsequent amplified disturbances. The important role of these instability waves in predicting jet noise and constructing a proper casual solution to the jet noise problem has been recently investigated [37].

Very important contributions to the study of waves in water jets has been made by Hoyt *et al.* who made visible, by the use of high-speed photography, instabilities occurring in high Reynolds number of water jets discharging into air [32-34]. These instabilities include the axisymmetric mode accompanying the transition from laminar to turbulent flow at the nozzle exit, spray formation and further downstream helical disturbances which result in the entire jet assuming a helical form. Figure 2.6 shows a water jet emerging from the nozzle and the initial few diameters of travel [33]. Initially, the jet is laminar due to the strong pressure gradient in the nozzle [32,33]. Axisymmetric instability waves are immediately apparent after less than one diameter of air travel [33]. As many as six to eight discrete waves may be identified before they merge into a less well-defined flow. These instabilities are further amplified in the next, rather chaotic region, and culminate in the ejection of spray droplets.

Figure 2.6. Water jet emerging from 0.635 cm diameter nozzle into stagnant air. Jet velocity=25.3 m/s [32].

Figure 2.7 shows the jet path by means of photos taken every 24 nozzle diameters. Axisymemtric instabilities are not obvious on the jet surface after the initial spray formation zone. Instead, instabilities begin to bend the jet into a helical path, first perceptible at about 70 diameters and clearly evident by 100 diameters and further downstream.

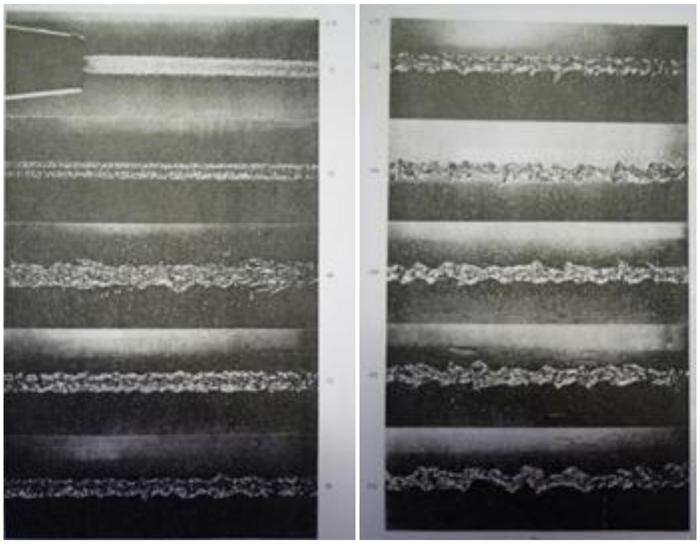

Figure 2.7. Photos of a water jet of 0.635 cm diameter nozzle taken every 24 nozzle diameters apart [32].

As the jet moves through the air, viscous forces and large-scale instabilities cause the jet to break-up [32]. Figure 2.8 shows the nature of the jet just before complete break-up into drops. These larger-scale motions appear to be helical-type instabilities in contrasted to the axisymmetric instabilities near the nozzle exit [32].

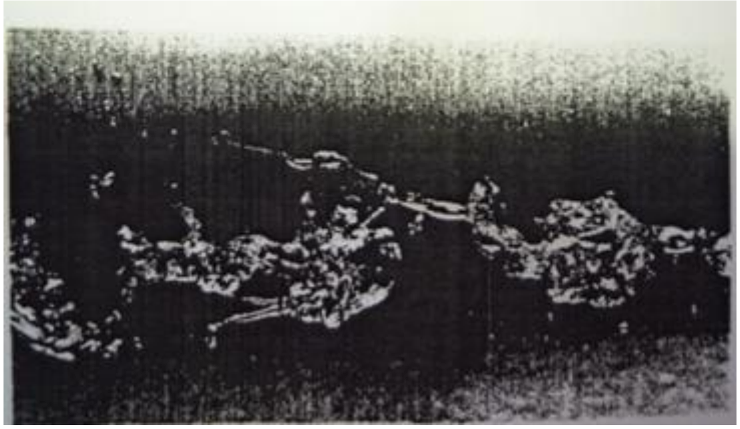

Figure 2.8. Jet about to break into droplets [32].

It was concluded in the same work that the initial system of waves which accomplish the transition from laminar to turbulent flow on the surface of the jet can be regarded as almost axisymmetric. This conclusion is in good agreement with work done by Mattingly *et al.* where the growth of infinitesimal disturbances on an axisymmetric jet column was investigated theoretically and experimentally [36]. It was found that initially in the jet there exists an axisymmetric disturbance which dominates the other modes considered, namely the helical and double helical modes. Further, with downstream distance it was found that the helical mode of instability becomes the most highly amplified.

## 2.5 Possible sound mechanisms responsible for leak noise

### 2.5.1 Cavitation

Cavitation is an especially important noise source in underwater acoustics. In 2001 a study group carried out experimental work to investigate the processes generating leak noise. They proposed that cavitation is the mechanism of leak noise generation at high frequencies [38]. Cavitation is defined as the rupture of a liquid or of a liquid-solid interface caused by reduction of local static pressure [30]. A rupture is the formation of a macroscopic or visible bubble. Liquids contain many microscopic or submicroscopic voids which act as nuclei for cavitation. However, cavitation is only said to occur when these voids grow to significant size [30]. The bubbles may contain gas or vapour or a mixture of both gas and vapour. There are four ways of inducing bubble growth [39]:

1 For a gas-filled bubble, by pressure reduction or an increase in temperature. This is called gaseous cavitation.

2 For a vapour-filled bubble, by pressure reduction. This is called vaporous cavitation.

3 For a gas-filled bubble, by diffusion. This is called degassing as gas comes out of the liquid.

4 For a vapour-filled bubble, by sufficient temperature rising (boiling).

Cavitation is described by the cause of the static pressure drop, the location of the rupture and the contents of the bubble [30]. There are two locations where cavitation occurs: at a liquid-solid interface or within the volume of the liquid [30]. In calculating the total energy radiated by the collapse of a partially gas-filled vapour bubble the energy for initial collapse and subsequent rebounds should be summed. In Figure 2.9 the growth and collapse of a cavitation bubble is shown whereas in Figure 2.10 the acoustic pressure pulses from a collapsing cavity is depicted [30]. Because cavitation involves volume changing it is basically a monopole sound source [30].

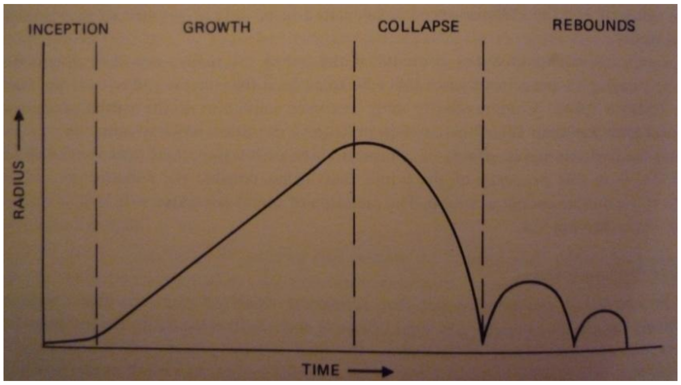

Figure 2.9. Growth and collapse of a cavitation bubble having finite gas content [30].

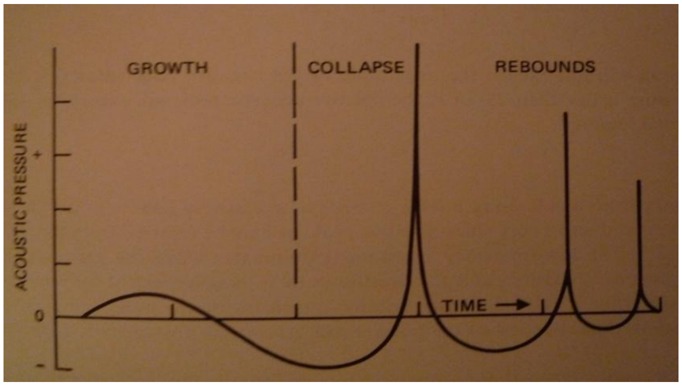

Figure 2.10. Pressure pulses from collapsing cavity [30].

## Broadband cavitation noise

The resultant spectrum of cavitation noise covers a wide frequency range because of the pulse nature of the individual bubble collapses and the random sequence of occurrence [30]. In Figure 2.11. an idealized cavitation noise spectrum is shown.

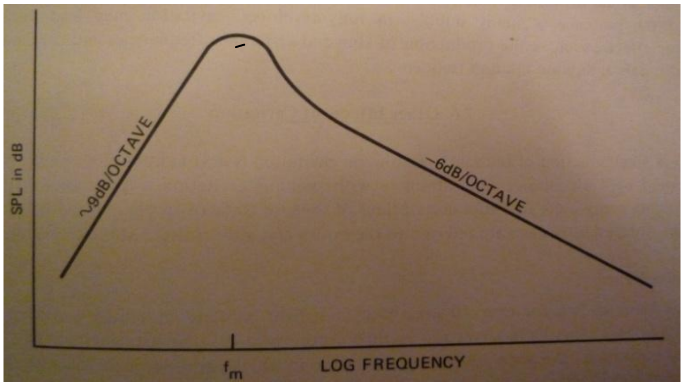

Figure 2.11. Idealized cavitation spectrum [30].

It can be seen that the spectrum rises sharply to a peak and then decreases at a rate of 6 dB/octave over a wide frequency band. Measured cavitation spectra show spectral peaks at frequencies related to the collapse time of the largest bubbles,

$$f_m = \frac{1}{2\alpha_o}\sqrt{\frac{P_c}{\rho_o}} \tag{2.8}$$

where $\alpha_o$ is the radius of the maximum bubble, $\rho_o$ is the water density and $P_c$ is the collapse pressure. The peak frequency is therefore lower for larger bubbles but it increases with collapse pressure. Below the peak, the spectrum increases at a rate of 6 to 12 dB/octave. At high frequencies, an octave or more above the peak, it decreases at a rate close to 6 dB/octave.

### 2.5.2 Noise from oscillating bubbles

Another common noise source that can be present in pipe flows is bubbles oscillating at their natural frequencies and radiating as monopoles [30]. Pumphrey *et al.* [40] showed that the averaged power spectra of bubbles leaving a needle (small jet) and passing through turbulence without breaking up is described by Figure 2.12 [40]. Both spectra show a peak at approximately 1.5 kHz.

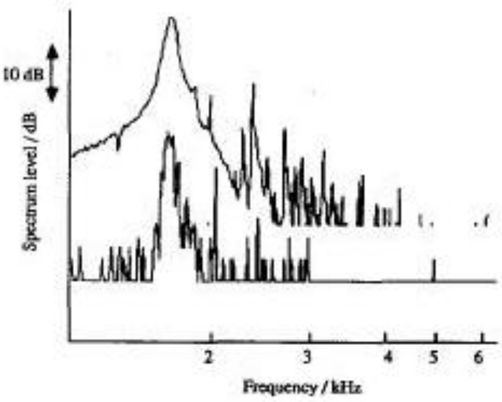

Figure 2.12. Acoustic intensity spectra of bubbles leaving a nozzle (above) and passing through turbulence but not breaking up (below) [40].

### 2.5.3 Turbulent flow noise

Turbulent flow represents the irregular motion of a large number of particles and is characterized by fluctuations in velocity at all points of the flow field [22,41]. These fluctuations arise due to the presence of eddies in the turbulent flow superimposed on the general mean flow pattern [22]. These eddies interact with one another and with the general flow and they change shape and size with time as they move along with the flow. In this type of flow an individual particle will follow a very irregular and erratic path and no two particles may have identical or even similar motion [20,22,41]. Turbulent fluid motions involve distortion without net volume changes or net forces and radiate as quadrupoles (Figure 2.13). Quadrupoles can occur within the fluid itself away from fluid boundaries in regions of free turbulence where they are associated with fluctuating turbulent shear stresses [30].

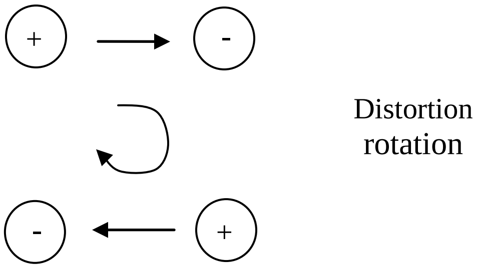

Figure 2.13. Quadrupole sound source.

## Acoustic analogy

Lighthill [42] first showed that the exact mass and momentum conservation equations could be rearranged exactly to give an inhomogeneous wave equation for the fluctuating density with a right hand side which could be interpreted as a distribution of quadrupole sources. The strength of the quadrupole sources was determined exactly by the properties of the real flow and the sources were assumed to radiate as if embedded in an equivalent acoustic medium at rest [42]. Using this theory the dependence of far-field intensity was predicted to be [43];

$$I(r,\theta)\sim\frac{\rho_s^2V^8d^2}{\rho_0c_0^5r^2}(1-M_c cos\theta)^{-5} \tag{2.9}$$

where $\theta$ is the observer polar angle measured from the jet downstream axis, $V$ is the jet velocity, $\rho_s$ is the density appropriate to the most intense source region and $M_c$ is the Mach number, normally taken to be of order $0.7V/c_0$. From Eq.(2.9) it can be seen that for each doubling of velocity $V$ there is a 24 dB increase in noise intensity.

In Figure 2.14 a single jet noise spectrum is shown [44] for a jet nozzle diameter *d*=0.0254 m. The solid line shown is the predicted far-field acoustic spectrum using the acoustic analogy of Lighthill whereas the dashed line is the spectrum obtained using the ESDU database [44]. The estimates are in good agreement.

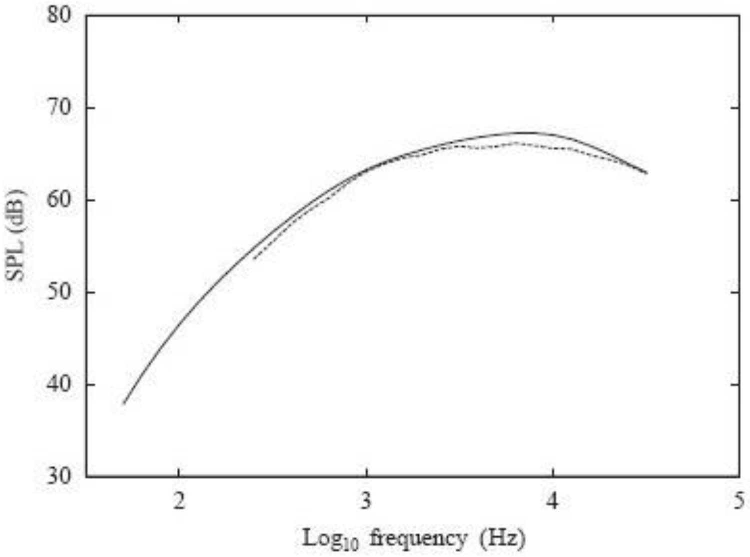

Figure 2.14. Predicted far-field acoustic spectrum at the jet axis obtained using the model (solid line —) compared with that obtained using the ESDU scheme (dashed line - - -). Jet nozzle diameter $d$=0.0254 m, jet exit Mach number is $M_j$=0.67 [44]. Mach number is a dimensionless measure of relative speed. It is defined as the speed of an object relative to a fluid medium, divided by the speed of sound in that medium.

## 2.6 Summary

In this chapter some basic theory of noise generation through fluid flow was given which will be found to be useful in the rest of this thesis. Flow in circular pipes was examined and dimensionless quantities like Reynolds and Strouhal number were introduced. These quantities will be extensively used in Chapters 4 and 5. Also information about laminar, turbulent and re-laminar flow was included. Furthermore, the flow through different kinds of orifices was examined and information for the structure in water jets was given. Finally, possible sound mechanisms responsible for leak noise were discussed. This part will be found useful in Chapter 4 when the mechanism of leak noise generation will be examined.

# CHAPTER 3

# A PRELIMINARY RIG FOR CHARACTERIZING LEAK NOISE

## 3.1 Introduction

In this chapter the first attempt at designing an experimental rig aimed at characterizing leak noise is described and some initial measurement results of leak noise spectra are presented. The main disadvantage of this rig is that the leak noise measurements *may* be contaminated by tap noise and flow noise. For this reason, measurements are reported here for different lengths of pipe sections to estimate the level of each different noise source and thus their contribution to the overall acoustic pressure measured signal.

The objective of this rig was to obtain an estimate of the leak noise spectra and determine how this is affected by leak size and flow velocity. However, a number of problems with this rig that were not foreseen at the start of the project, created doubts about the validity of the results. It was therefore necessary to design an alternative rig for the measurement of leak noise that could validate these results. The new rig and results will be presented in Chapters 4 and 5. Nevertheless, as we shall show, the leak noise measurements made in this rig have a number of important similarities to those measured in the rig described in Chapters 4 and 5.

## 3.2 Description of the experimental rig

A schematic of the experimental rig that was used to characterize leak noise is shown in Figure 3.1.

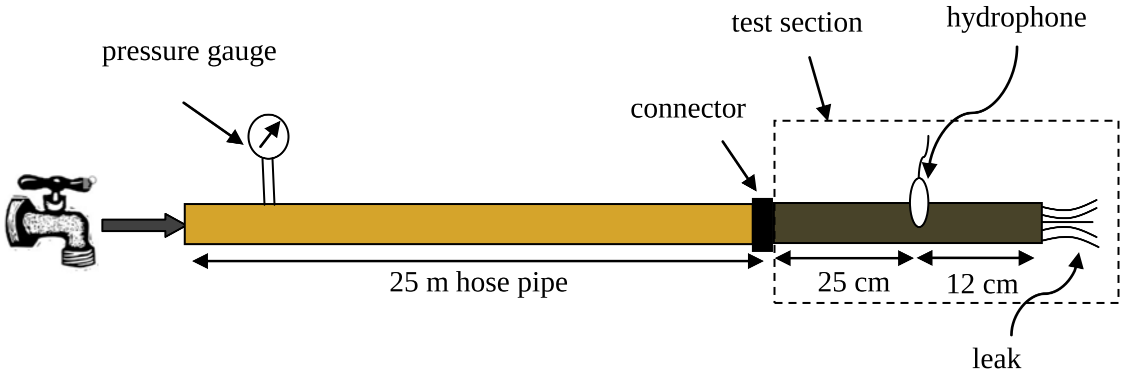

Figure 3.1. Schematic of the experimental set-up.

A 25 m long rubber garden hose pipe with 15 mm external diameter and 1 mm wall thickness was connected to a water tap at mains pressure, as shown in Figure 3.2a. The other end of the pipe, was connected to a copper test section which was constructed in order to support the hydrophone and the different leak holes. A pressure gauge, shown in Figure 3.2b, was connected just after the water tap to monitor the static water pressure. The copper test section and the different leak holes are shown in Figures 3.3 and 3.4 respectively.

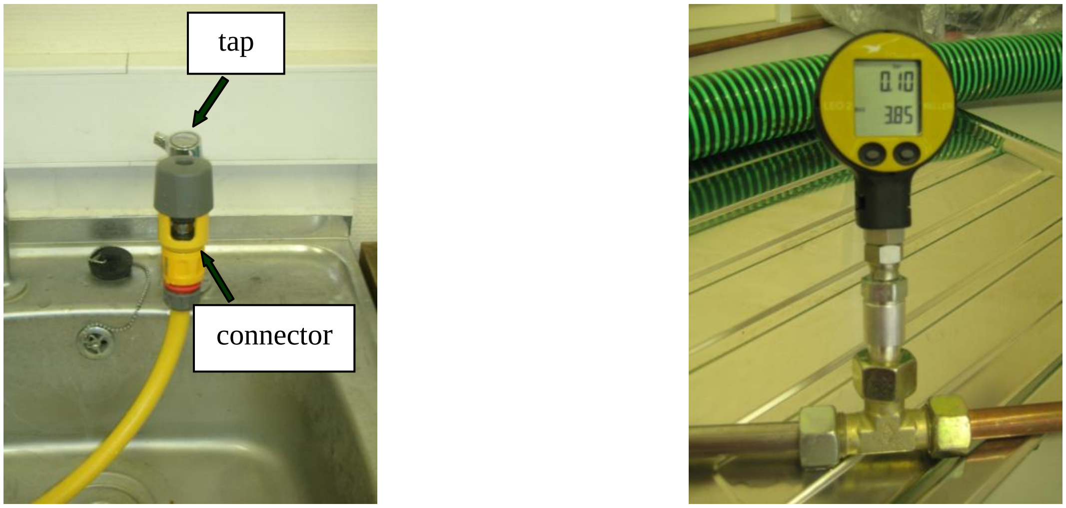

(a) (b)

Figure 3.2. (a) Hose pipe connected to a standard domestic tap with main pressure; (b) Pressure gauge connected close to the tap to monitor static pressure inside the pipe.

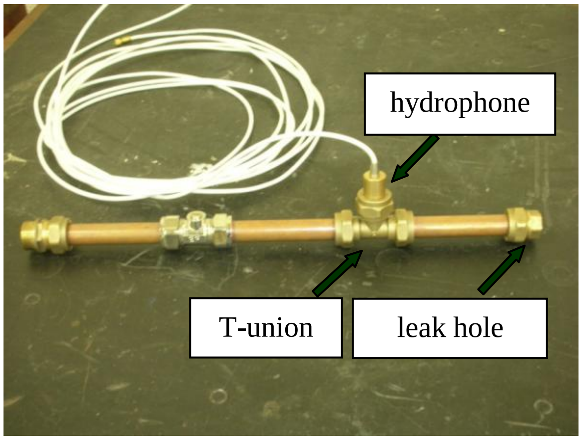

Figure 3.3. Copper test section to support the hydrophone and the different leak holes.

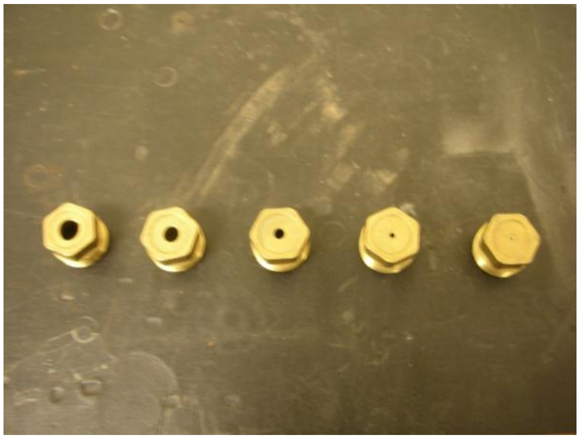

Figure 3.4. Circular leak holes of 8 mm, 6 mm, 4 mm, 2 mm, 1 mm diameter.

The copper test section, shown in Figure 3.3, in which the hydrophone and leak holes were located, consisted of a 15 mm diameter copper pipe, a T-union in which the hydrophone was inserted, and a number of different leak holes shown in Figure 3.4, which were attached alternatively. The distance between the hydrophone and the test sections was approximately 12 cm in an attempt to minimize the effect of the attenuation of the pipe on the measured acoustic pressure signal. Measurements of the acoustic pressure were made at different static pressures inside the pipe between 0.2 bar, corresponding to a range of leak flow velocities between 1 m/s (for the 8 mm leak hole) to 6.5 m/s (for the 1 mm leak hole), and the maximum possible static pressure for each orifice, which was of 2 to 3 bar corresponding to a range of leak flow velocities between 4 m/s (for the 8 mm leak hole) to 19 m/s (for the 1 mm leak hole). The velocity of the water discharging from each different leak hole was estimated by measuring the weight of water from each leak over a specific time interval at a known static pressure.

## 3.3 Data acquisition and analysis

The acoustic pressure was measured with a B&K Type 8103 hydrophone with a sensitivity of 0.162 pC/Pa, using the P5650 Data Acquisition System, which is an 8-channel, 16-bit data acquisition unit. The hydrophone was connected to a B&K Type 2635 charge amplifier. The signals were acquired for a time duration of 30 seconds at the sampling rate of 20 kHz. The time history was exported into Matlab and spectral analysis was performed on the sensor signals using a 8192 (or 16384) point FFT, with a Hanning window and 50% overlap. This gives approximately 150 (or 75) averages for the 30 s length measured signals and 2.4 (or 1.2 Hz) frequency resolution.

## 3.4 Extraneous noise sources on the experimental rig

The signals captured by the hydrophone were the sum of three noise sources; leak noise source, tap noise source and flow noise. Therefore, the spectral density $S_{x_1x_1}(\omega)$ of a signal $x_1(t)$ measured at a distance $d_l$ from the leak and at a distance $d_t$ from the tap, can by obtained from the sum of contribution from the leak, tap and flow noise.

$$S_{x_1x_1}(\omega) = S_{ll}(\omega)|H(\omega, d_l)|^2 + S_{tt}(\omega)|H(\omega, d_t)|^2 + S_{ff}(\omega) \tag{3.1}$$

In Eq.(3.1) $S_{ll}(\omega)$ is the power spectral density (PSD) of the plane wave at the leak location due to the leak, that is consistent with the pressure radiated to a point along the pipe whose transfer function between the leak and the observer is given by $H$. Note that this is not the same as the exact pressure measurement at the leak location due to the presence of the non-radiating hydrodynamic near field. Therefore, the measurement should be made at many source diameters from the source. In the same equation $H(\omega, d_l)$ is the transfer function between the leak and the sensor, $S_{tt}(\omega)$ is the PSD of the tap signal as discussed above for the $S_{ll}(\omega)$, $H(\omega, d_t)$ is the transfer function between the tap and the sensor and $S_{ff}(\omega)$ is the PSD of the flow noise.

It was important therefore to qualify these three different noise sources, $S_{ll}(\omega)$, $S_{tt}(\omega)$ and $\mathrm{S}_{ff}(\omega)$ and determine their level at the sensor position in order to ensure that the leak noise estimate is not dominated by tap and flow noise.

### 3.4.1 Tap noise source investigation

The contribution of tap noise to the measured signal can be considered negligible if by increasing the distance between the tap and the hydrophone (with the leak at fixed distance from the hydrophone) the measured noise remains unchanged. This test was performed by increasing this distance from 25 m to 50 m and observing the change in noise level. The set-up that was used is shown in Figures 3.5(a) and (b).

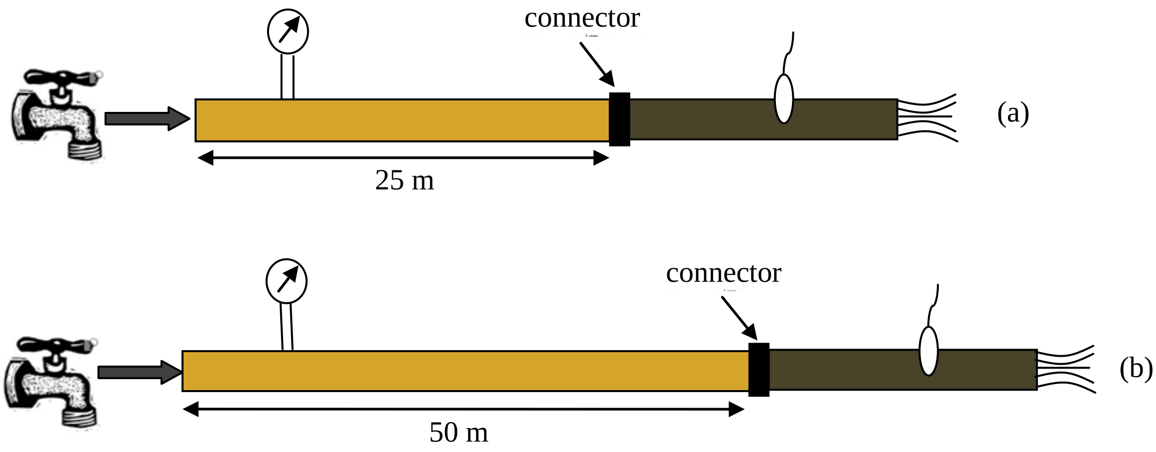

Figure 3.5. Experimental set-up to investigate the contribution of tap noise to the measured pressure signal. The hydrophone is:(a) 25 m far from the tap; (b) 50 m far from the tap.

In Figures 3.6(a) and (b) the PSD of the noise due to the 4 mm orifice is shown for a lower leak flow velocity equal to 4.6 m/s and a higher one equal to 10.3 m/s respectively.

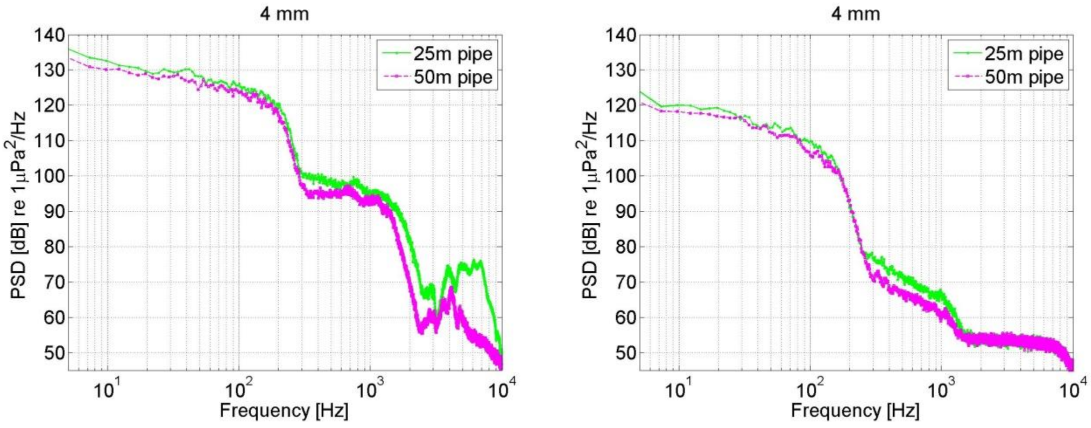

(a)

(b)

Figure 3.6. PSD of the noise signal for the 4 mm orifice and for two different leak flow velocities; a) 4.6 m/s; b) 10.3 m/s.

The spectra shown in Figures 3.6(a) and (b) for the two lengths of pipe are within 1 dB over most of the frequency range. This means, therefore, that there is no further attenuation of the tap noise possibly, indicating that 25 m of rubber hose is sufficient to eliminate the tap noise from the measured pressure signal.

### 3.4.2 Leak noise investigation

To quantify the leak noise source level the hydrophone was placed at different positions from the leak by using the set-up arrangements shown in Figures 3.7, 3.8 and 3.9. These configurations of the rig were implemented to assign the relative contribution of the three noise sources to the total noise of the measured signal. The water tap was placed close to the hydrophone through a 2 m length hose pipe. Initially, the leak hole was positioned close to the hydrophone through the copper test section as sketched in Figure 3.7 so that all the noise sources contributed significantly to the measured acoustic pressure signal.

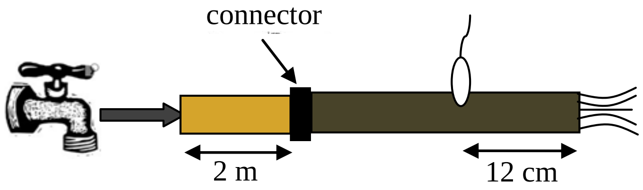

Figure 3.7. Configuration of the experimental rig; The leak is 12 cm away from the hydrophone.

The leak hole was then moved further away from the hydrophone at distance of 25 m as shown in Figure 3.8 to investigate the difference in the noise measured signal.

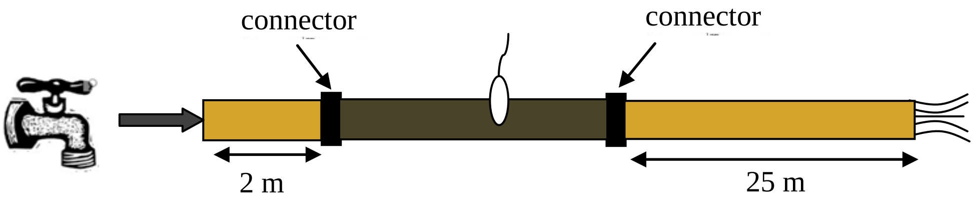

Figure 3.8. Configuration of the experimental rig; The leak is 25 m away from the hydrophone.

Finally, the leak hole was moved away from the hydrophone at distance of 50 m as shown in Figure 3.9 to investigate any additional difference in the measured pressure signal.

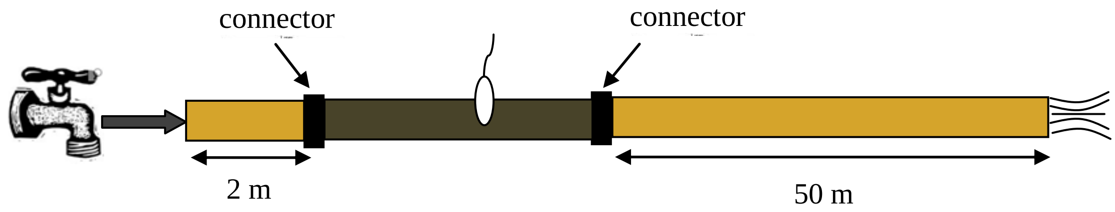

Figure 3.9. Configuration of the experimental rig; The leak is 50 m away from the hydrophone.

In Figure 3.10 examples of the measured PSD due to the 8, 6 and 4 mm diameter leaks are shown for the three lengths of hose shown in Figures 3.7, 3.8 and 3.9.

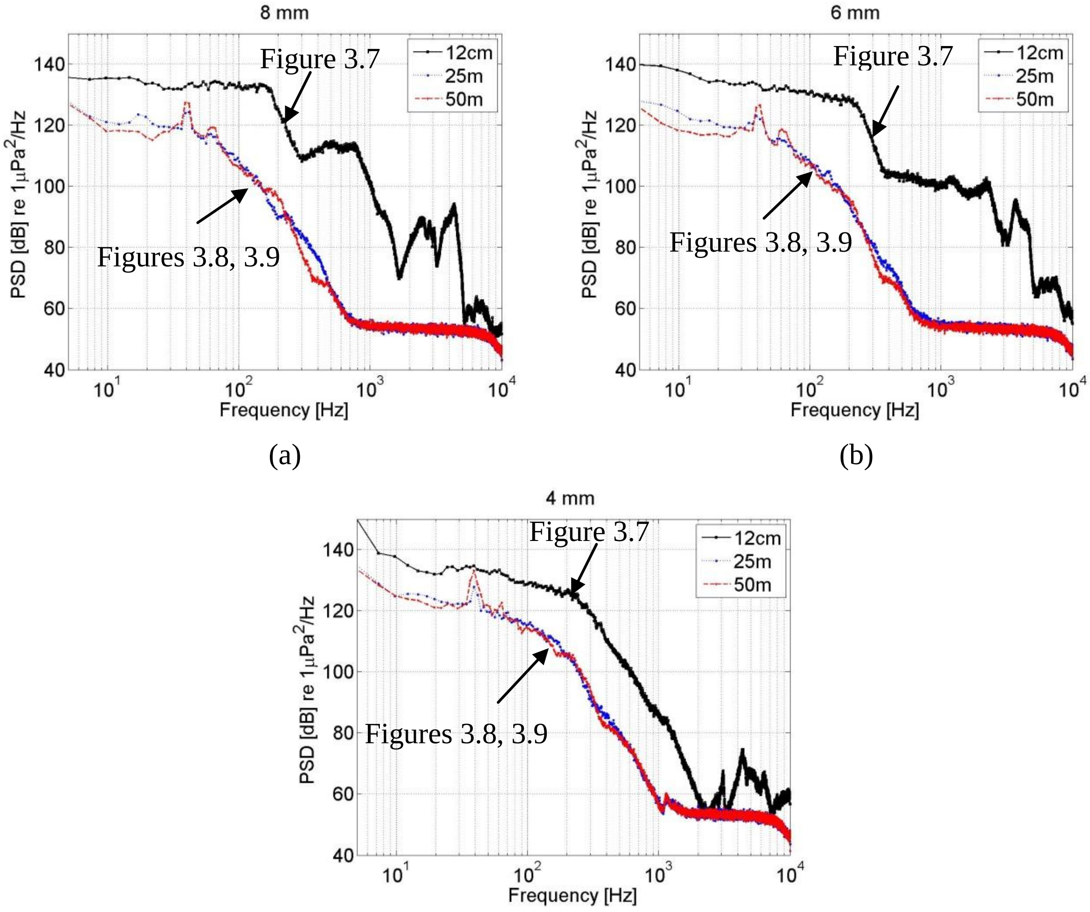

(a) (b)

(c)

Figure 3.10. PSD of the noise signal when the leak is 12 cm, 25 m, 50 m away from the hydrophone; a) 8 mm, $V = 1.7$ m/s; b) 6 mm, $V = 3$ m/s; c) 4 mm, $V = 4.6$ m/s.

Figure 3.10 suggests that the leak noise makes a dominant contribution to the measured acoustic pressure and can vary as much as 10 to 50 dB depending on frequency and leak size. Furthermore, this investigation shows that 25 m of hose is sufficient to attenuate the leak noise as no further attenuation is observed by doubling the length of the hose.

### 3.4.3 Flow noise investigation

Finally, the level of flow noise due to turbulent flow over the hydrophone was investigated, by increasing the distance by 25 m between the tap and the leak from the hydrophone so they both are well attenuated before they reach the hydrophone. Thus, only the flow noise now contributes to the measured acoustic pressure. The set-up used in this investigation is shown in Figure 3.11.

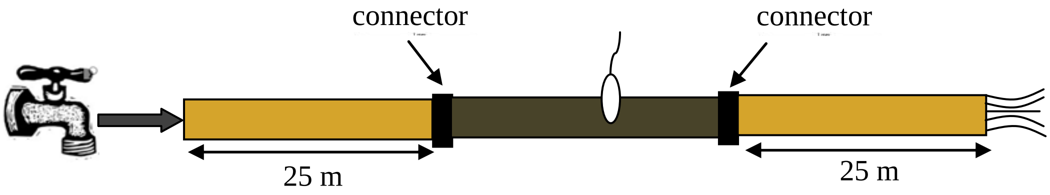

Figure 3.11. Experimental set-up to investigate the level of flow noise, eliminating both the leak and tap noise sources.

The velocity of the water discharging from the 8, 6, 4, 2 and 1 mm diameter leak holes was estimated by measuring the weight of water discharged by each leak over a specific time interval at a known static pressure. From continuity, the flow velocity inside the pipe can be found by,

$$V_f = \frac{VA_l}{A_f} \tag{3.2}$$

where $V_f$ is the flow velocity inside the pipe, $V$ is the measured leak flow velocity, $A_f$ is the cross-sectional area of the pipe and $A_l$ is the area of the leak.

In Figure 3.12 the PSD of the measured signal is shown for a lower $V_f$=0.43 m/s and a higher $V_f$=0.98 m/s flow velocity inside the hose pipe.

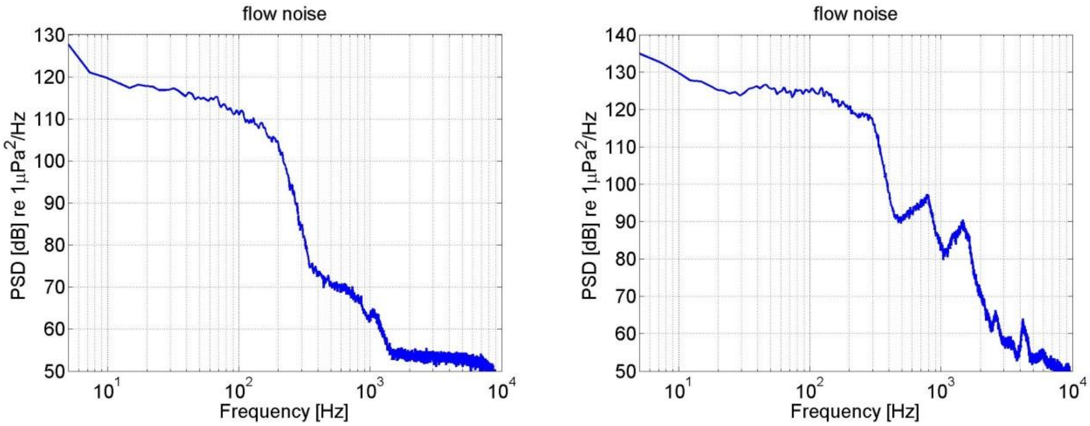

(a) (b)

Figure 3.12. PSD of the noise signal for two different flow velocities inside the pipe; a) $V_f$=0.43 m/s; b) $V_f$=0.98 m/s.

Figure 3.12 shows a measurement of the flow noise level and suggests that its level increases approximately by 10 to 20 dB depending on the frequency for doubling the flow velocity inside the pipe. Thus, it is possible that this noise source has a significant effect on the measurements of leak noise, especially for high flow velocities inside the pipe.

## 3.5 PSD of the measured acoustic pressure signals for different leak sizes

Measurements were made using the experimental set-up shown in Figure 3.1 for the 8, 6, 4, 2 and 1 mm diameter leaks and for different leak flow velocities. In Figure 3.13 the PSD of the hydrophone signal for all the different cases is shown. Note that the velocities indicated in Figure 3.13 refer to the leak flow velocities of the water discharged from each leak hole and not to the flow velocity inside the hose pipe.

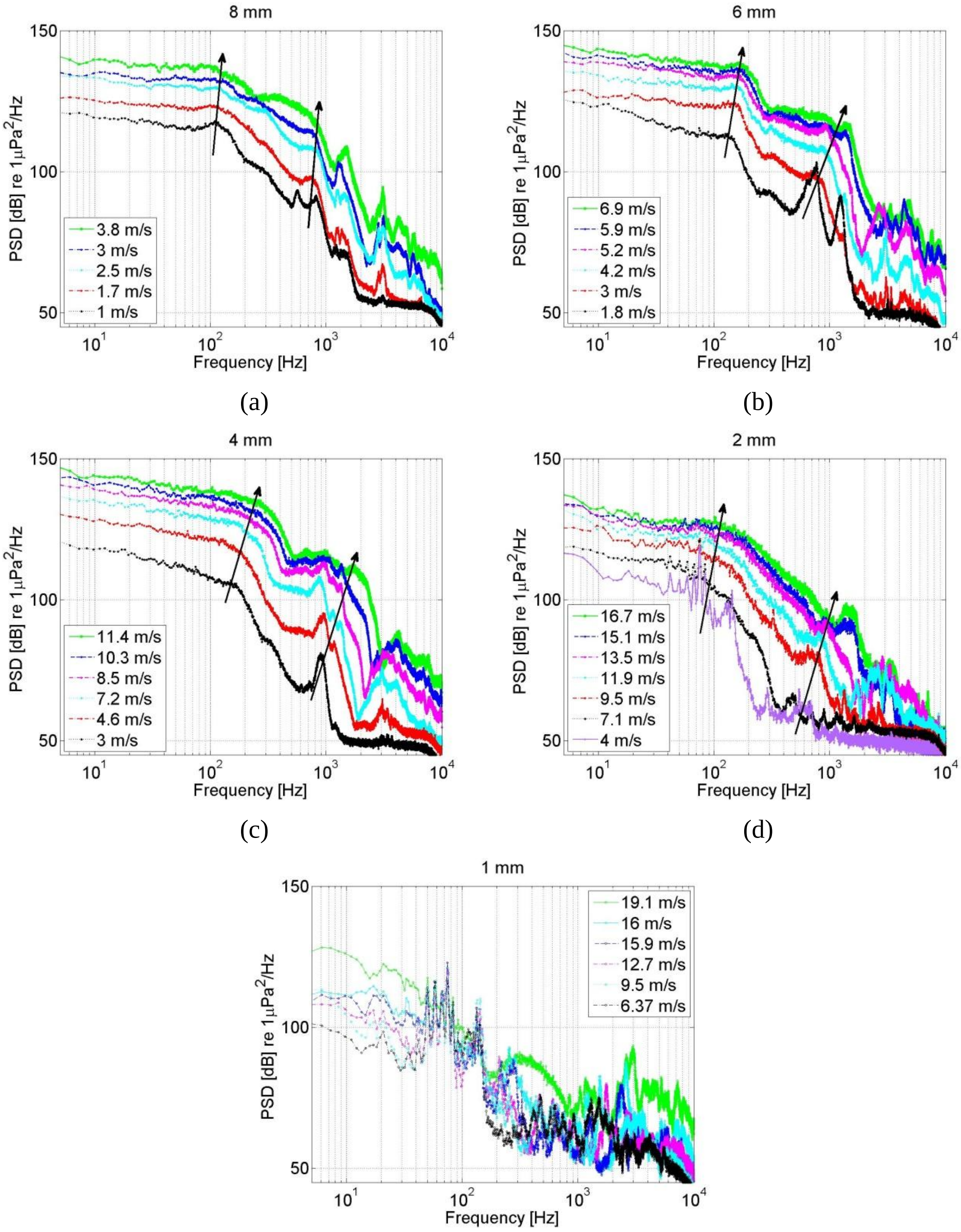

(a)

(b)

(c)

(d)

(e)

Figure 3.13. PSD of the noise signals for different leak sizes and flow velocities; a) 8 mm; b) 6 mm; c) 4 mm; d) 2 mm; e) 1 mm.

Figure 3.13 suggests that for all the leak sizes apart from the 1 mm leak the PSD decays with frequency. This decay does not follow a single frequency power law. Two critical frequencies can be distinguished to represent the onset where the slope of the PSD changes. These frequencies vary with leak size and flow velocity. The arrows in Figure

3.13 show roughly the variation of these frequencies with velocity and leak hole diameter. It can be seen that the critical frequencies increase roughly linearly with an increase in flow velocity for a constant leak size and with a decrease of leak hole size for a constant flow velocity. This variation roughly indicates a Strouhal number dependency whereby these frequencies occur at constant Strouhal numbers. In each frequency region separated by the two critical frequencies the PSD of the measured signals decays with a different frequency power law $1/\omega^n$. Until the first critical frequency $n \leq 1$ but its value increases significantly at higher frequencies.

The results for the 1 mm leak do not follow the same trend. A possible reason is that the level of the signals from this small leak is quite low and may be masked by background noise.

## 3.6 Noise measurements using two hydrophones

Measurements were then conducted using the experimental set-up shown in Figure 3.14 now, with two hydrophones being used instead of one. This allowed the calculation of the cross correlation of the two signals between the two hydrophones to provide an estimate of the time delay between them and hence provide an estimate of the wavespeed and coherence for signal to noise ratio. The attenuation rate of the pipe versus frequency could also be estimated from the amplitude decay of the transfer function.

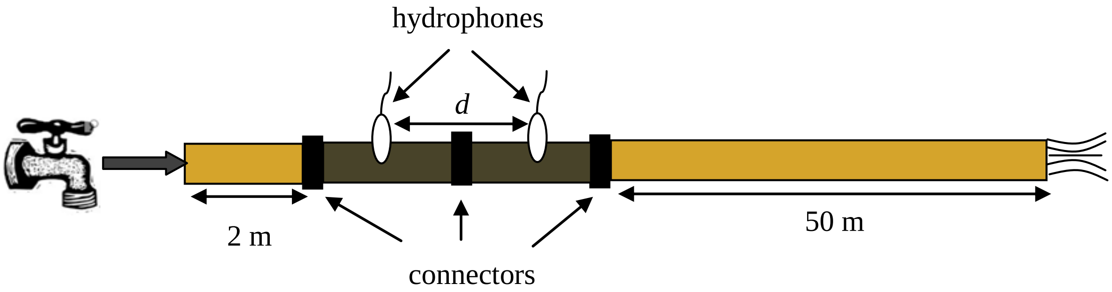

Figure 3.14. Experimental set-up using two hydrophones to obtain an estimate of the attenuation rate of the hose pipe.

Figures 3.15 and 3.16 show the coherence between the two hydrophone signals for two different distances between the hydrophones; very close to each other at a distance $d = 5$ cm and much further apart at a distance $d = 1$ m.

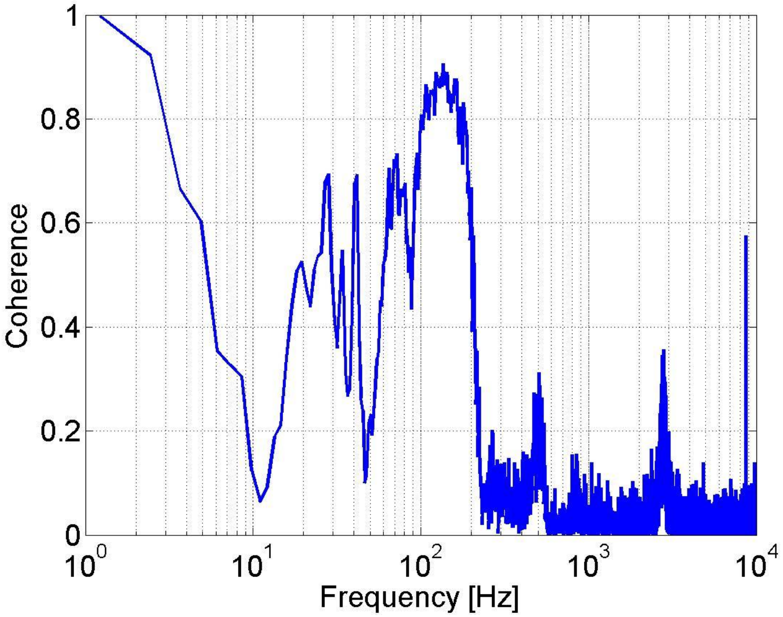

Figure 3.15. Coherence of the noise signals measured by the two hydrophones when the distance between them is 5 cm.

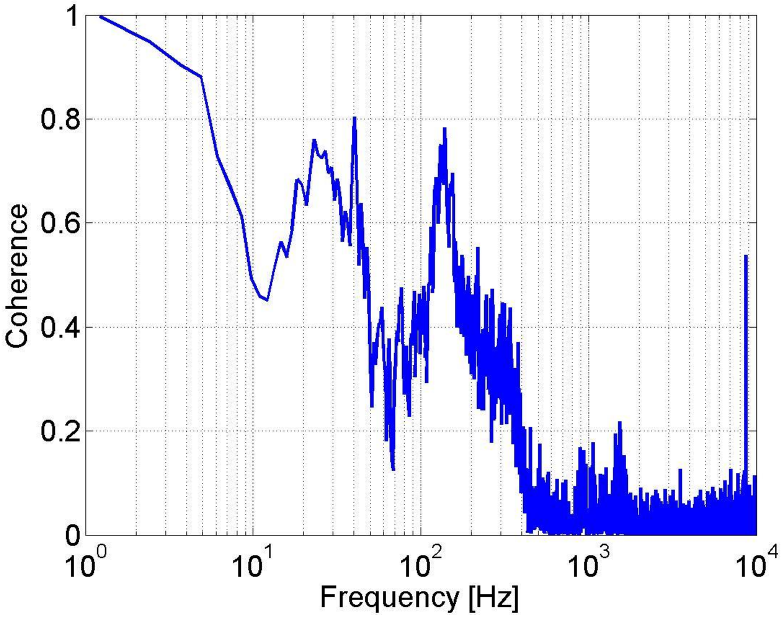

Figure 3.16. Coherence of the pressure signals measured by the two hydrophones when the distance between them is 1 m.

Figures 3.15 and 3.16 both show generally poor coherence between the signals on the two hydrophones. This was probably due to the connectors between them and on their either side which could disturb the flow and hence create additional flow noise thereby masking the noise signals received by the two hydrophones. Therefore the leak noise measurements may be susceptible to flow noise and thus a different test rig was required for the characterization of leak noise that could validate these results.

## 3.7 Discussion

An experimental rig was designed for the characterization of leak noise for different leak sizes and flow velocities. Due to possible contamination of leak noise signals by tap and flow noise a set of initial measurements was conducted to identify the level of each noise source. The results showed that measuring the leak noise 25 m from tap was sufficient to attenuate tap noise (Figure 3.6). However, flow noise due to the small diameter of the hose pipe could not be eliminated and may make a significant contribution to the measured acoustic pressure signal (Figure 3.12). Measurements were conducted for different leak sizes and flow velocities and a general trend of the spectrum shape was observed. However, measurements conducted with two hydrophones gave poor coherence between the signals even when placed close to each other. A possible reason for this is that the flow was disturbed by the connectors that were connecting the different sections of the test rig and this could create additional noise and signal masking. For these reasons, it was important for the results obtained from this rig to be validated against another rig.

## 3.8 Conclusions

The measurement results presented in this chapter represent the first attempt at measuring leak noise. However, due to poor coherence between the measured signals and the high level of flow noise, the results obtained from this rig were not convincing and need to be validated using a different rig. Thus, a new experimental rig was designed for characterizing leak noise using a pipe with a larger diameter to eliminate flow noise and using different connectors that could allow a smooth and undisturbed water flow between the connecting sections. The new experimental rig and its results obtained are presented in Chapters 4 and 5.

# CHAPTER 4

# AN IMPROVED EXPERIMENTAL RIG FOR CHARACTERIZING LEAK NOISE

## 4.1 Introduction

In this chapter a rig for characterizing leak noise is described, that has improved characteristics compared to the preliminary rig described in Chapter 3. The problem of flow noise was overcome by using a pipe of a larger diameter to reduce the flow speed. Different connectors between the different pipe sections were also used to ensure smoother water flow between them. In Section 4.2 a detailed description of the test rig is given and in Section 4.4 measurement results are presented. Technical problems encountered during the rig design are also described. The objective of this rig was to investigate the physical mechanisms of leak noise generation and also to investigate how leak size and leak flow velocity affect the leak noise spectra. The first set of measurements were conducted for a 2 mm leak hole diameter. Results gave significant information regarding the mechanism of leak noise generation. Broadband leak noise is shown to be related to the onset of turbulence in the water jet while at lower pressures, narrow band noise is present in the spectrum. These can be related to instability waves in the jet. However, firm conclusions could not be made for the effect of leak size and leak velocity on the measured spectra due to a broad resonant peak that existed centred on 750 Hz due to the dynamics of one of the pipe sections.

## 4.2 Description of the Experimental Rig

The rig consists of a 50 m long, medium density plastic pipe (MDPE) of external diameter 50 mm and wall thickness 5 mm. The pipe was cut into two sections, one of length 10 m and another of 40 m. A schematic of the test rig is shown in Figure 4.1 and these sections are labelled Section 1 and Section 3 respectively. Between the two sections another section of clear plastic pipe of 0.3 m length was inserted in which a cylindrical hole of 2 mm diameter was drilled; this is referred to as Section 2 in Figure 4.1. This section of clear pipe allows for the flow to be observed while the water escapes from the leak. Thus, it could be seen whether large-bubble cavitation was present and was therefore a possible cause of leak noise. Two hydrophones were inserted into the pipe on either side of the leak at a distance of 50 cm from the leak. Connectors of 0.22 m length, to allow the different pipe sections to be connected together without water leakage are shown schematically in Figure 4.1 as black rectangular boxes. Use of these connectors allowed the internal bores of the two pipe sections to be aligned precisely.

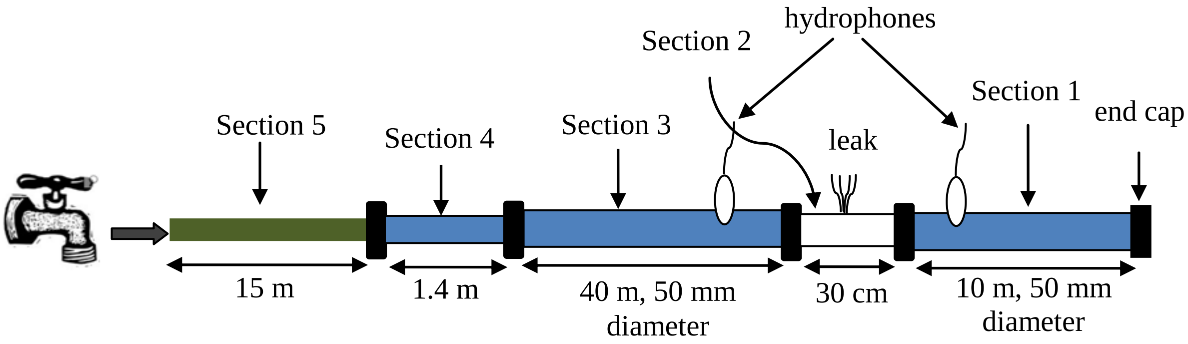

Figure 4.1 Schematic of the test rig.

The pipe section is terminated at the end furthest from the tap by an end-cap, as shown in Figure 4.2.

Figure 4.2. End cap sealing the end of Section 1.

Section 2 of the pipe rig is shown in Figure 4.3 in more detail. It comprises a clear plastic section in which a hole was drilled to simulate the leak. Although the length of that section is 0.3 m only 0.12 m are visible in Figure 4.3 as the rest of the clear pipe is inside the connectors.

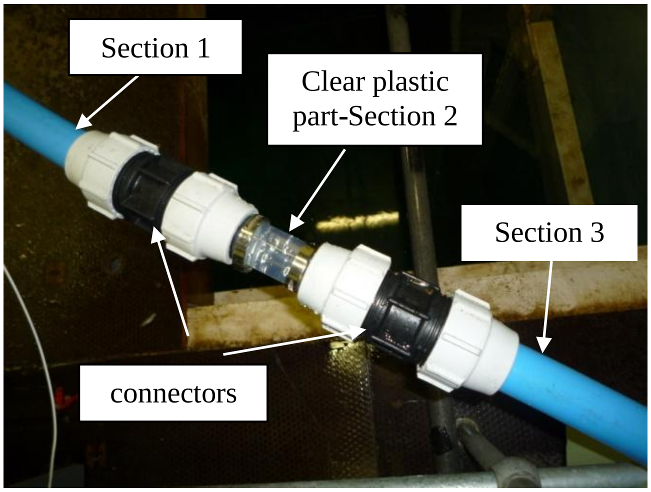

Figure 4.3. Section 2 of the experimental rig and connectors which connects it with Sections 1 and 2.

The clear plastic pipe is of 46 mm external diameter and 3 mm wall thickness. Although the pipes were of slightly different external diameter and wall thickness, the internal diameter for both pipes was identical and equal to 40 mm. The connectors, therefore, maintained firm contact between the internal bore of the two pipe sections and allowed a good connection without discontinuities, which could disturb the flow and hence generate flow noise.

Photographs of Sections 3, 4 and 5 are shown in Figure 4.4. Section 4 is a 1.4 m long MDPE pipe of external diameter of 25 mm. Section 5 is a 15 mm diameter hose of length 15 m. This was introduced between the tap and the main pipe section to reduce the level of tap noise at the measurement locations as a result of the high attenuation in the soft plastic material of the hose.

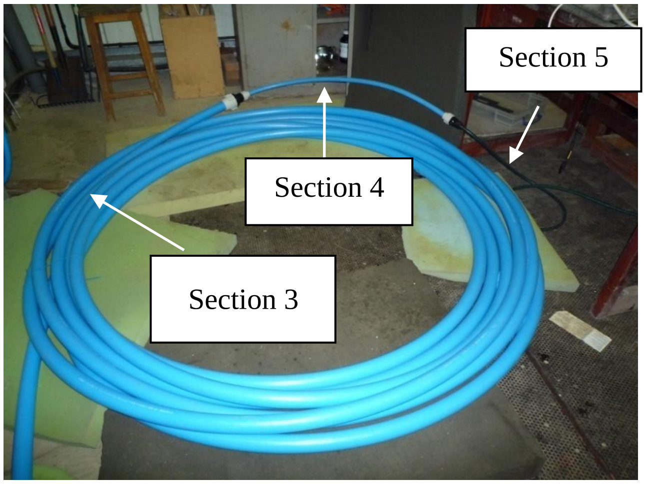

Figure 4.4. Sections 3, 4, 5 of the experimental rig.

The hose pipe, Section 5, was connected to a water tap at mains pressure with a conventional tap connector as shown in Figure 4.5. A pressure gauge was connected between them to measure the static pressure within the pipe.

Figure 4.5. Hose pipe connected to the water tap.

The reason for using the 1.4 m long MDPE pipe was to connect the main pipe section of 50 mm diameter to the hose pipe of 15 mm diameter through available diameter reduction connectors.

Two identical B&K omnidirectional hydrophones, of Type 8103 were used to measure the sound field in the pipe. A schematic of this hydrophone is shown in Figure 4.6. It has dimensions of 50 x 9.5 mm and double-shielded, low-noise integral cable of 6 m length. The hydrophone’s frequency responses are flat from 3 Hz up to 20 kHz.

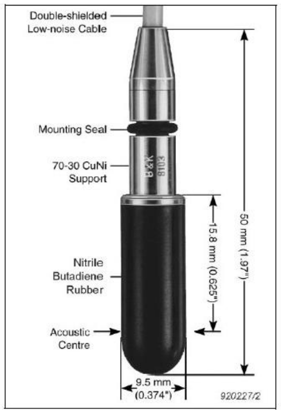

Figure 4.6. Hydrophone that was used for the experimental measurements. B&K Type 8103.

The hydrophones were located 0.5 m either side of the leak in the main pipe section. They were inserted into the pipe through holes of 9.5 mm diameter which were drilled into the Sections 1 and 3. To ensure a good seal, rubber ‘O’ rings were used around each hydrophone, as seen in Figure 4.7.

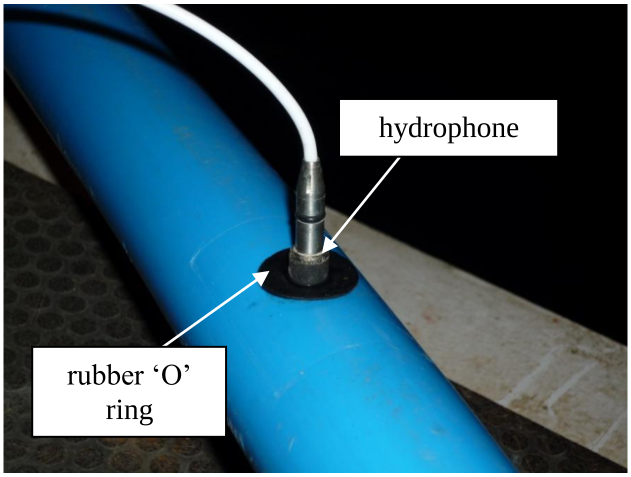

Figure 4.7. Hydrophone placement in the pipe.

Two holders, made from Perspex, were used to support the two hydrophones in the pipe as shown in Figure 4.8. The two separate pieces of the holder were firmly screwed together by four bolts to prevent water leakage. Figure 4.9 shows Sections 1,2 and 3 and the hydrophone and leak positions.

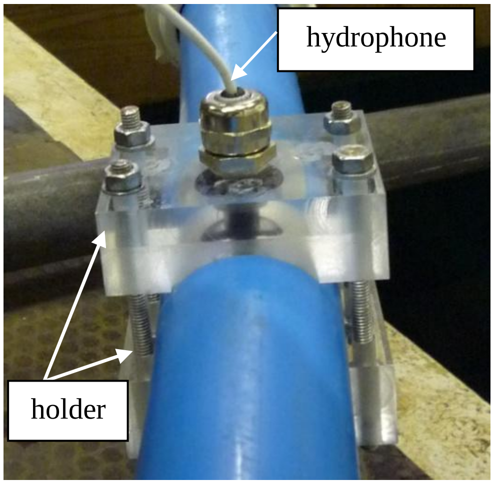

Figure 4.8. Hydrophone fittings.

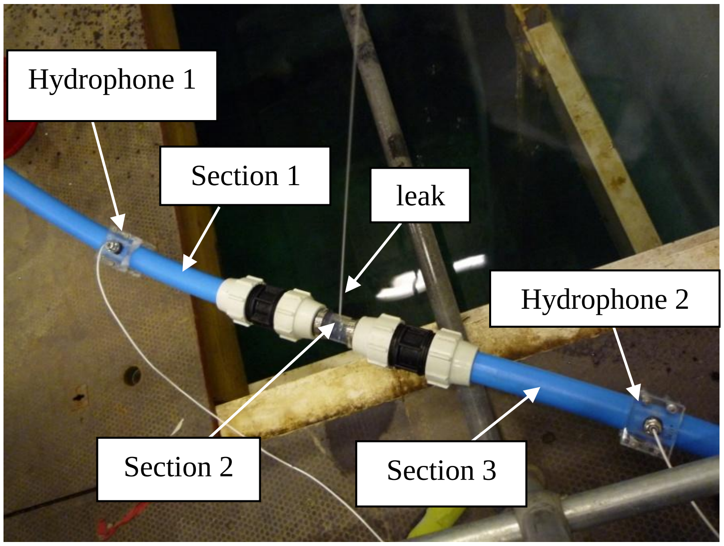

Figure 4.9. Overview of Sections 1, 2, 3 and hydrophone positions.

The experiment was performed in the A. B. Wood laboratory at the ISVR. The water that escaped from the leak then drained into an underground water tank, with dimensions of 8 m × 8 m × 5 m.

Thus, this rig is fundamentally different from the one presented in Chapter 3 as now a pipe with bigger diameter is used to attenuate the flow noise and also the leak hole is on the side of the pipe and not on the end.

## 4.3 Data acquisition and analysis

The signals from the two hydrophones were input into two separate B&K charge amplifiers, of Type 2635. The outputs of the charge amplifiers were connected to a two channel, 16-bit Analogue to Digital converter (ADC), UCA202. The hydrophone signals were acquired using the Audacity software, for a time duration of about 30s or longer in some specific cases, with a sampling rate of 44100 samples/second. A band pass anti-alias filter was used with cut-off frequencies at 5 Hz and 22 kHz to encompass a sufficiently large frequency range. A schematic of the acquisition system is shown in Figure 4.10.

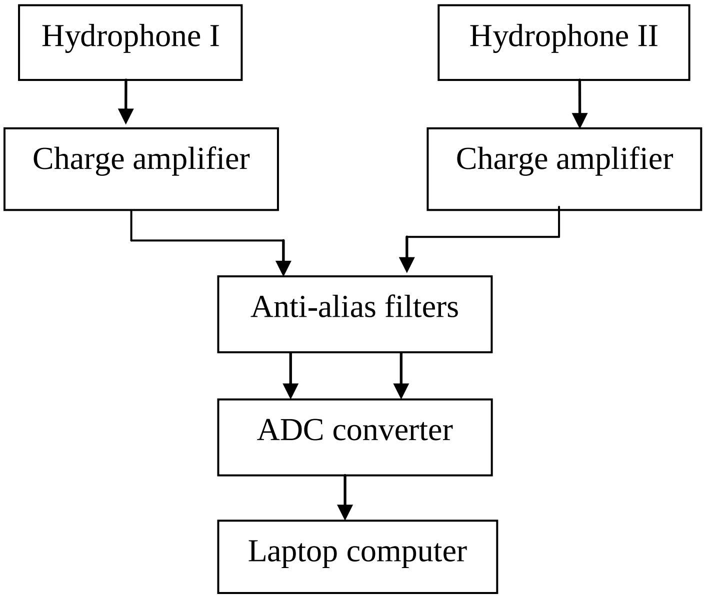

Figure 4.10. Schematic of the hardware used.

Spectral analysis was performed on the hydrophone signals using a 32,768-points FFT, unless otherwise stated. A Hanning window was used together with power spectrum averaging with 50% overlap.

## 4.4 Measurement Results

### 4.4.1 Preliminary Results: Coherence of the signals

Initial noise measurements for the 2 mm leak at all flow velocities gave poor coherence between the two hydrophone signals as shown in Figure 4.11. This suggests excessive background levels compared to the leak signals. This was unexpected as the two sensors were located a short distance apart compared to the wavelength $\lambda$ up to 70 Hz which arises following a general rule of $d < \lambda/6$ where $d$ is the distance between the sensors. This general rule arises from the spatial correlation function $\rho(\Delta x) = cos(k\Delta x)$ of the plane wave sound field.

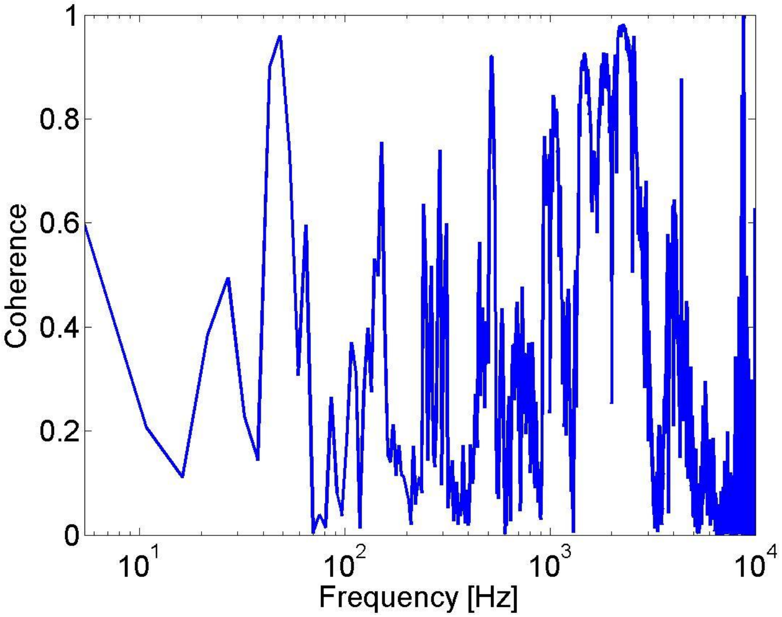

Figure 4.11. Initial coherence of the signals on the two hydrophones for the 2 mm leak size.

One possible reason for the poor coherence was the presence of structural vibrations transmitted through the floor and walls on which the pipe was situated. Therefore, it was important to isolate as much as possible the entire length of the pipe. To isolate the pipe from the floor, foam was placed under all the sections of the pipe rig. Another possible reason could have been the presence of trapped air inside the pipe, which could cause reflections and significantly affect the signals. Air was removed from the pipe by introducing a small hole in Section 1 of the pipe located at the point of maximum elevation of the pipe as shown in Figure 4.12. After bleeding the air from the pipe rig the small hole was then sealed. This procedure was followed at the start of each day of testing.

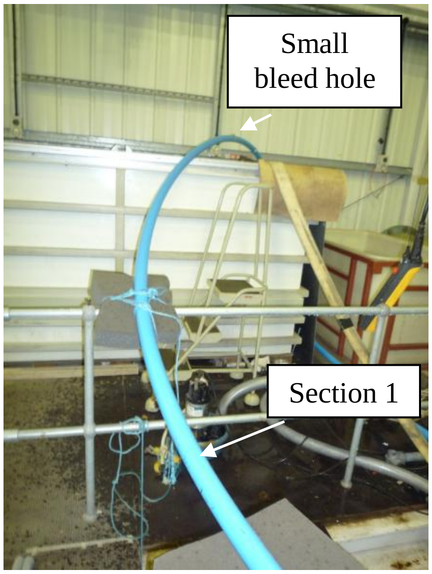

Figure 4.12. Position of the small hole drilled for bleeding the air.

After isolating the system and removing the air out of the pipe the coherence of the sensor signals was significantly improved up to about 4.5 kHz as shown in Figure 4.13 below. The reason for the poor coherence at frequencies higher than 4.5 kHz will be shown later in this chapter to be due to the low level of the signals at those frequencies.

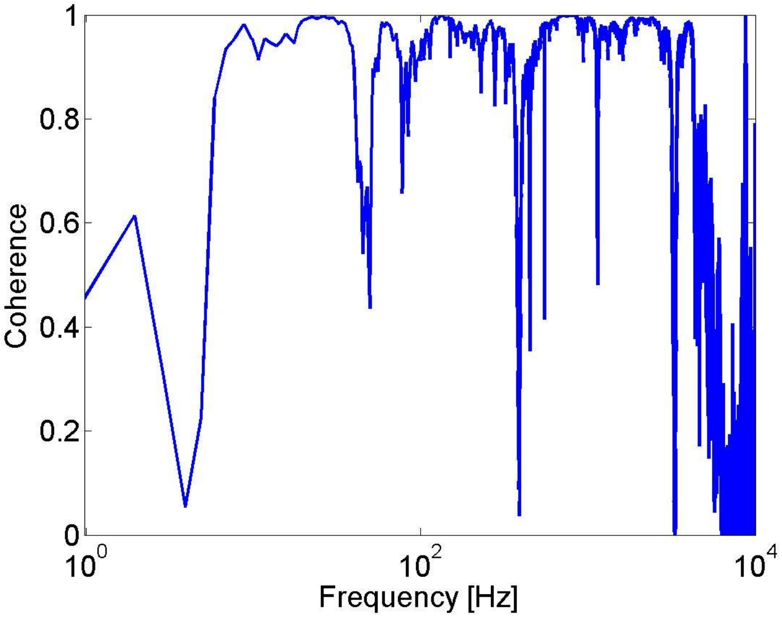

Figure 4.13. Coherence of the signals after isolating the system and bleeding the trapped air.

### 4.4.2 Background noise measurements

Background noise measurements were conducted with the leak hole sealed. This was done at different times of the same day and on different days in order to investigate the variability of background noise. Furthermore, contributions of the background noise to the overall measured sound pressure level was examined by measuring the background noise while the tap was turned on and then off. The background noise measurements were conducted by filling the pipe with water and then sealing the leak hole using a jubilee clip. In Figure 4.14 the PSD for hydrophones 1 and 2 at different times during the same day are shown. In Figure 4.15 background noise spectra measured at different days are shown.

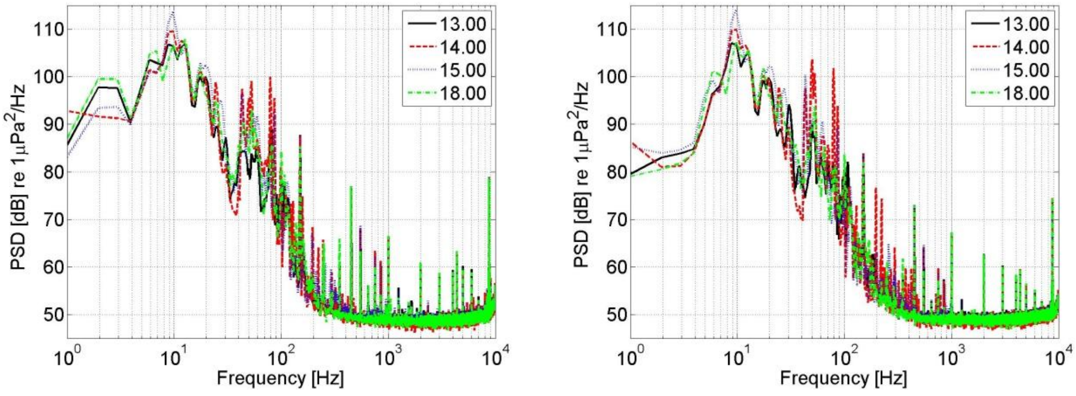

(a) (b)

Figure 4.14. Background noise measurements at different hours of the *same* day shown in the legend; (a) Hydrophone 1; (b) Hydrophone 2.

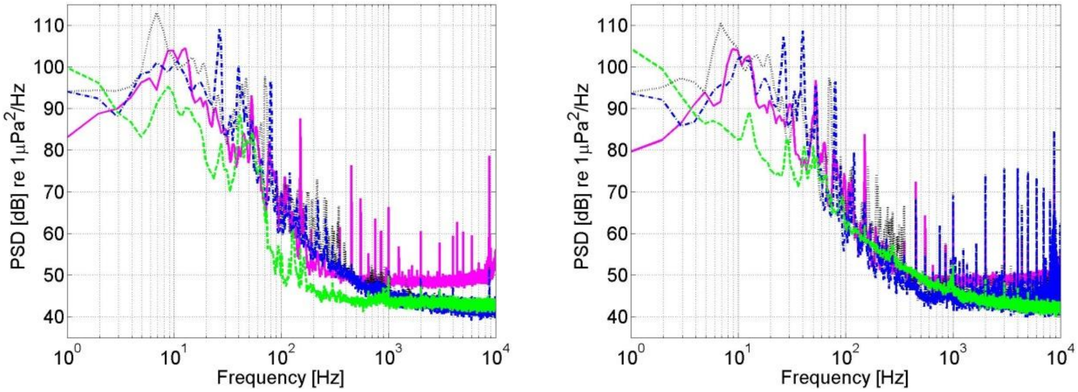

(a) (b)

Figure 4.15. Background noise measurements on *different* days; (a) Hydrophone 1; (b) Hydrophone 2.

It can be seen from Figure 4.14 (a-b) that the background noise spectra are very similar during the same day but there is a level difference of 10 to 15 dB in the low frequency range of 40-90 Hz. From Figure 4.15 it can be seen that there was a significant difference in the background noise level during different days, especially at low frequencies. A possible reason for this was that construction work was being undertaken a few hundred meters from the lab which might have affected the background noise measurements. Thus, no firm conclusions could be drawn about the exact level of background noise and for this reason it was measured frequently in each set of measurements.

In Figure 4.16 the background noise is shown when the water tap was switched on and allowed to reach steady state, and then off, to investigate whether there is any tap effect on the level of the signals. It can be seen that there is no significant difference in the level of the signals, which suggests that the tap noise is adequately attenuated.

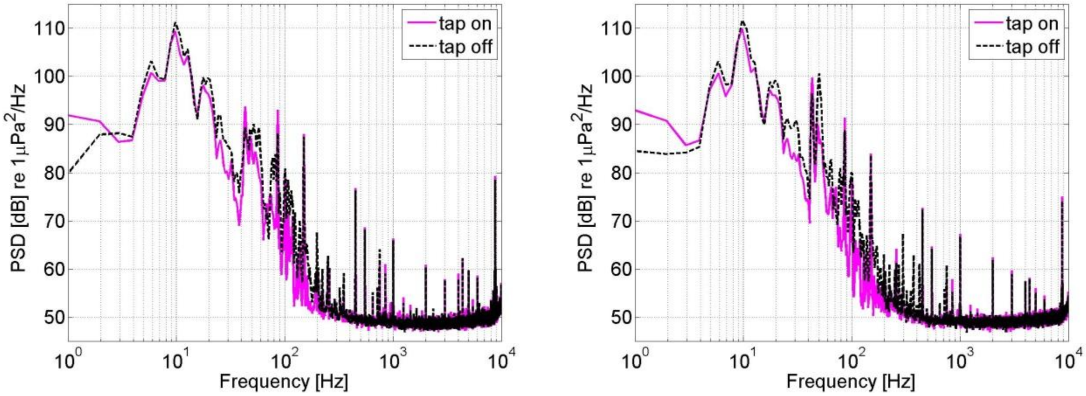

(a) (b)

Figure 4.16. Background noise measurements with the water tap turned on and off; (a) Hydrophone 1; (b) Hydrophone 2.

### 4.4.3 Flow velocity measurements versus pressure and time for the 2 mm diameter leak

The velocity of the water discharging from the 2 mm diameter leak was estimated by measuring the volume of water from each leak over a specific time interval at a known static pressure. The volume of the water was measured at various instants in time using measuring cylinders. These measurements allow the relationship between flow velocity and pressure to be deduced. The results are shown in Figure 4.17. The theoretical estimate given by Bernoulli’s equation presented in Chapter 2, is also shown for comparison for a discharge coefficient of 0.9, estimated by using Eq.(2.6). As mentioned in Chapter 2, Bernoulli’s equation in this simple form is valid only for steady (laminar) flow. Note that the flow velocity, at zero pressure, is not equal to zero because water still leaks from the pipe under the effect of gravity.

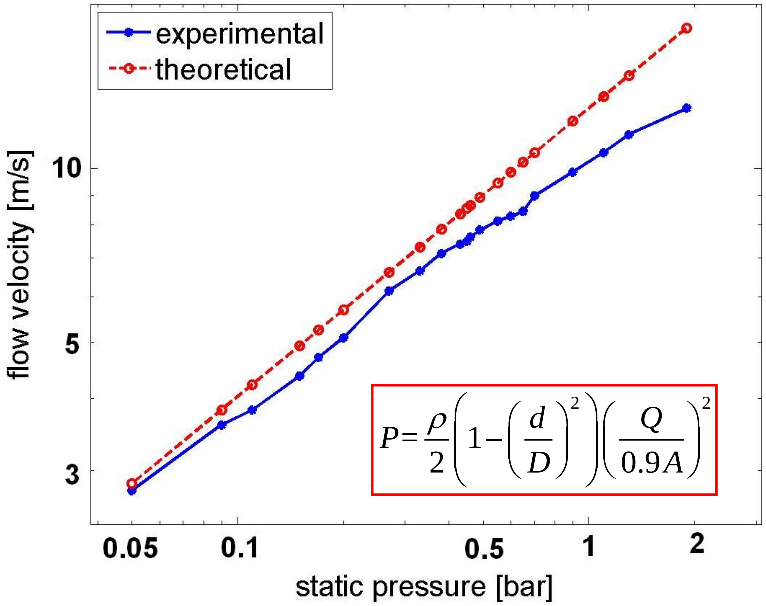

Figure 4.17. Flow velocity as a function of pressure gauge indication for the 2 mm diameter leak and theoretical estimation from Bernoulli equation [Eq.2.7].

Figure 4.17 shows that at low static pressures, and hence low flow velocities, there is a better agreement with theory. As flow velocity increases, the two lines start to increasingly diverge. This occurs because, as mentioned above, Bernoulli’s equation in this simple form is valid only for laminar flow and low Reynolds number and hence low flow velocities. Thus, as the flow undergoes transition to turbulence with increasing flow velocity the experimental results and theoretical estimates begin to diverge. Note that the transition from laminar to turbulent flow, for low flow velocities, was not sudden and occurred progressively. Hence, it was hard to determine the critical Reynolds number that the transition occurred.

## Static pressure decay as a function of time

With the pipe at a high pressure the tap was switched off to deduce the static pressure decay with time for the 2 mm leak. This information will be shown to be useful in Section 4.4.8. Starting from a high static pressure, the pressure gauge reading was recorded every 5 or 10 s until zero pressure was reached. This relationship is shown in Figure 4.18.

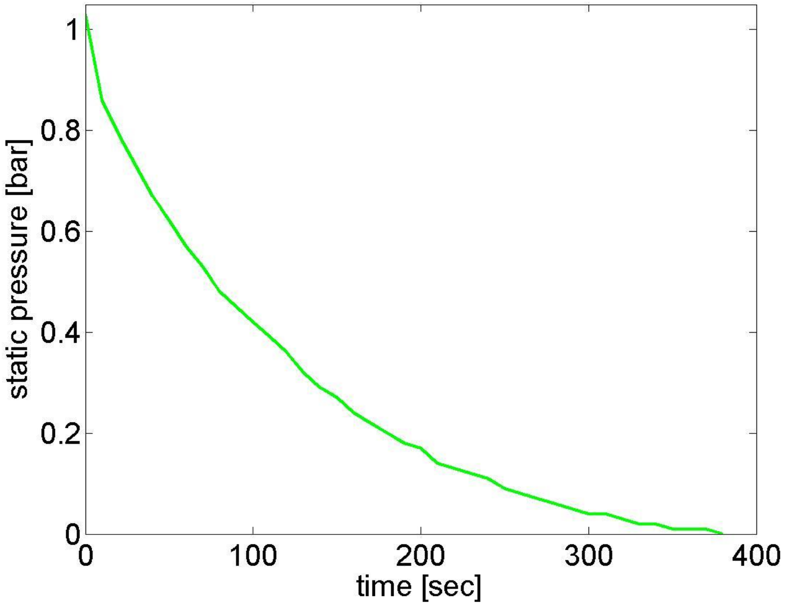

Figure 4.18. Static pressure variation with time for the 2 mm diameter leak.

From the relationship between flow velocity and pressure shown in Figure 4.17, and from the relationship between pressure and time shown in Figure 4.18, the relationship between flow velocity and time was estimated for the 2 mm leak by substituting the values of flow velocity that correspond to the specific pressure values. Knowing that water leaves the leak hole for 80 s from the moment that the pressure gauge indicates 0 bar, the relationship between flow velocity and time is shown in Figure 4.19.

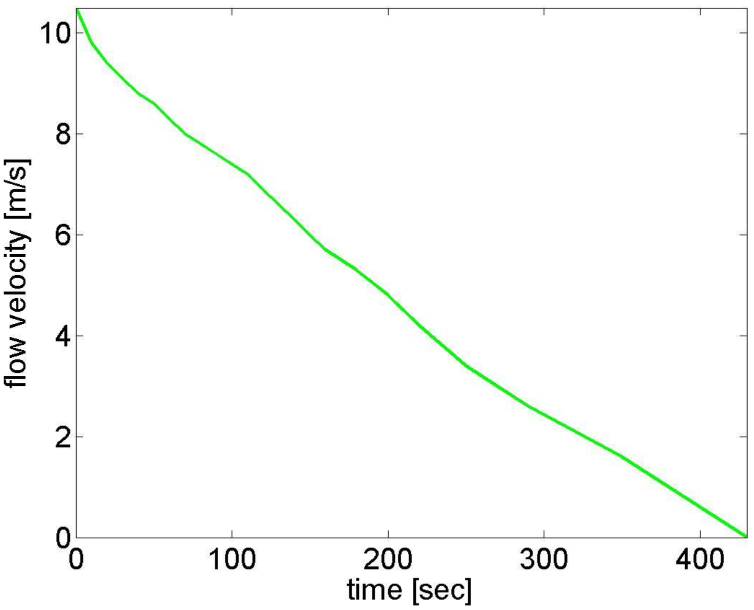

Figure 4.19. Estimation of flow velocity decay with time for the 2 mm leak.

Figure 4.19 suggests an almost linear relationship between flow velocity and time.

### 4.4.4 Leak flow observation for the 2 mm diameter leak size

As mentioned above, one of the main objectives for conducting this experiment was to identify the mechanism of leak noise generation. Observations of the flow while the water escaped from the 2 mm hole in the clear plastic section revealed no *visible* bubbles in the vicinity of the leak. Therefore, cavitation, as discussed in Chapter 2 was excluded as a possible mechanism of leak noise generation in this case. Although microbubbles could still be present, these are too small to generate the low frequency signals observed in the leak noise spectrum. This hypothesis will be further validated when the measured leak spectrum will be shown to be substantially different from the cavitation leak spectrum presented in Chapter 2.

Depending upon the flow velocity and pressure two different types of flow could be seen leaving the hole in the pipe, turbulent flow and laminar flow. Initially, when the tap was turned on, the flow of the water jet escaping from the leak was laminar near the leak hole but progressively developed into turbulent flow while the jet velocity was increasing. A phenomenon observed in the test rig for the 2 mm diameter leak was that the jet in the vicinity of the leak hole changed from appearing turbulent to laminar above a critical flow velocity. This phenomenon is referred to as relaminarization in fluid dynamics theory and is well known for rapidly accelerated flow [26-29]. It was found that in the test rig, relaminarization occurred when sudden pressure changes or a pressure increase occurred and was observed only for the 2 mm leak. It was also observed that when the turbulent flow from the 2 mm hole was sealed, which also resulted in an increase of static pressure inside the pipe, the flow was laminar when the seal was removed.

In Figure 4.20, photographs of the flow for the 2 mm leak size are shown at increasing specific static pressures. The velocity range was between 1 to 13 m/s. Initially, for a flow velocity of 1 m/s the flow is clearly laminar as can be seen in Figure 4.20(a). As the flow speed increases, and hence the Reynolds number increases, the flow gradually starts to become turbulent (Figures 4.20(b-f)). In studies of water jet flow from jet nozzles, and according to Hoyt *et al.* [33,34], when the jet leaves the nozzle the flow is laminar. In this laminar regime, instability waves related to axisymmetric modes appear on the surface of the jet and are seen after less than one diameter of air travel, before they merge into a less well defined flow (see Fig. 2.5 in Chapter 2). This laminar region is not clearly visible in the photographs of Figure 4.20, probably due to insufficient camera quality and due to the small leak diameter. Thus, instability waves could not be seen in the photographs although their effect can be seen in the noise measurements in Section 4.4.8. However, these instabilities, according to Hoyt *et al.*, are further amplified downstream and culminate in the ejection of spray droplets as can be seen in Figures 4.20(e-f). As the water jet moves through the air, viscous forces and large-scale instabilities cause the jet to break up [33,34]. Break-up of the water jet can be seen in Figure 4.20(e). In Figure 4.20(g) the flow has returned to laminar flow (relaminarization). The close-up photos in Figures 4.20(f-g) show in better detail the turbulent and the re-laminar flow in the vicinity of the leak hole.

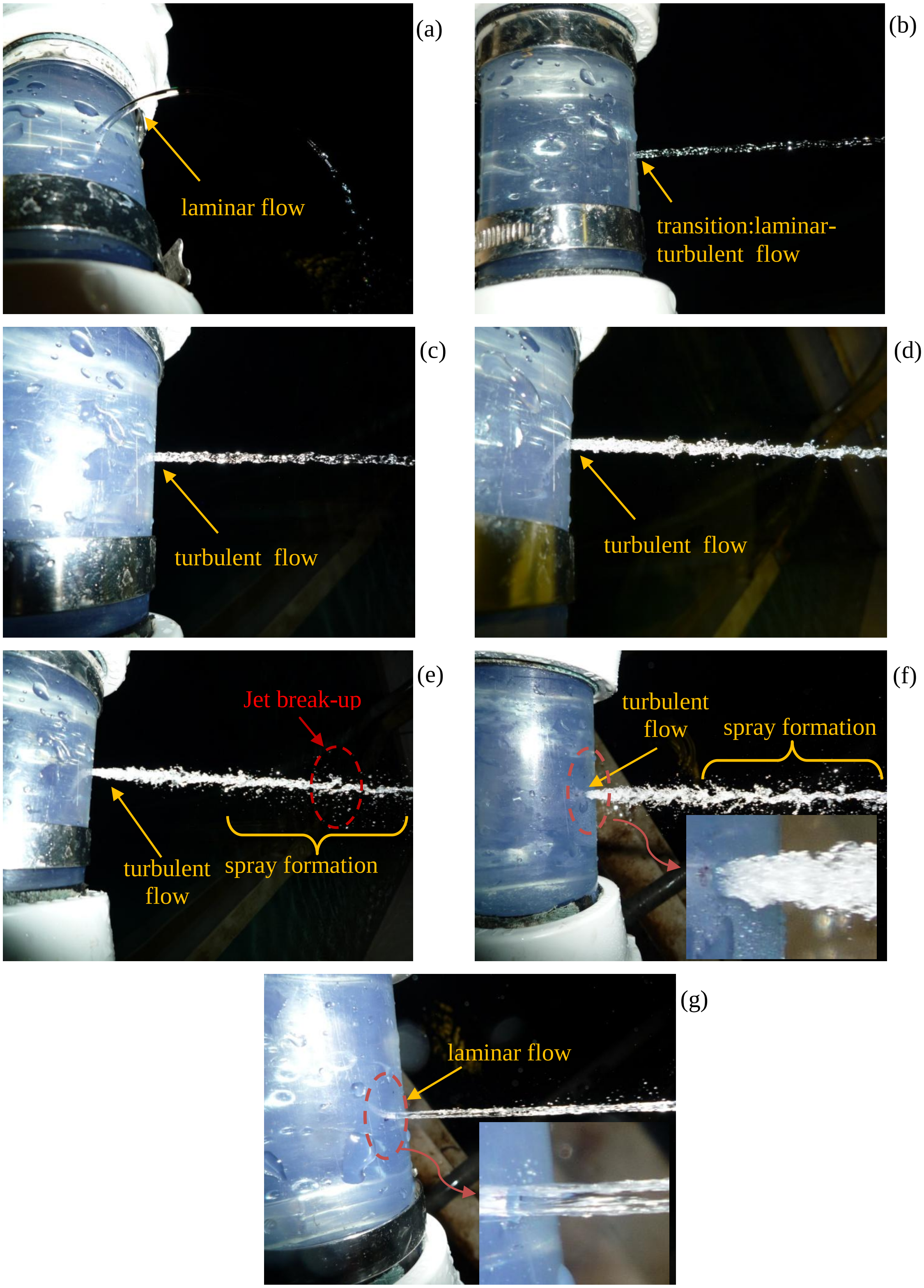

Figure 4.20. Flow observation for the 2 mm diameter leak for different flow velocities; (a) $V \approx 1\ \mathrm{m/s}$, $Re \approx 2000$; (b) $V \approx 3\ \mathrm{m/s}$ $Re \approx 6000$;(c) $V \approx 5\ \mathrm{m/s}$ $Re \approx 10000$; (d) $V \approx 8\ \mathrm{m/s}$ $Re \approx 16000$; (e) $V \approx 10\ \mathrm{m/s}$ $Re \approx 20000$; (f) $V \approx 12\ \mathrm{m/s}$ $Re \approx 24000$; (g) $V \approx 13\ \mathrm{m/s}$ $Re \approx 26000$.

## 4.4.5 Laminar and turbulent flow

It was mentioned in the previous section that for high static pressure, corresponding to a flow velocity of around 13 m/s, transition from turbulent to laminar flow occurred. This behaviour is shown clearly in Figure 4.21, which shows the instantaneous acoustic pressure as a function of jet velocity. Starting from a high flow velocity of 12 m/s, the flow was initially turbulent. The noise signal was captured while the static pressure inside the pipe was steadily increased. At a static pressure of around 1.6 bar the flow changed from turbulent to laminar. This corresponds to a flow velocity of around 13 m/s and Reynolds number of around 26000.

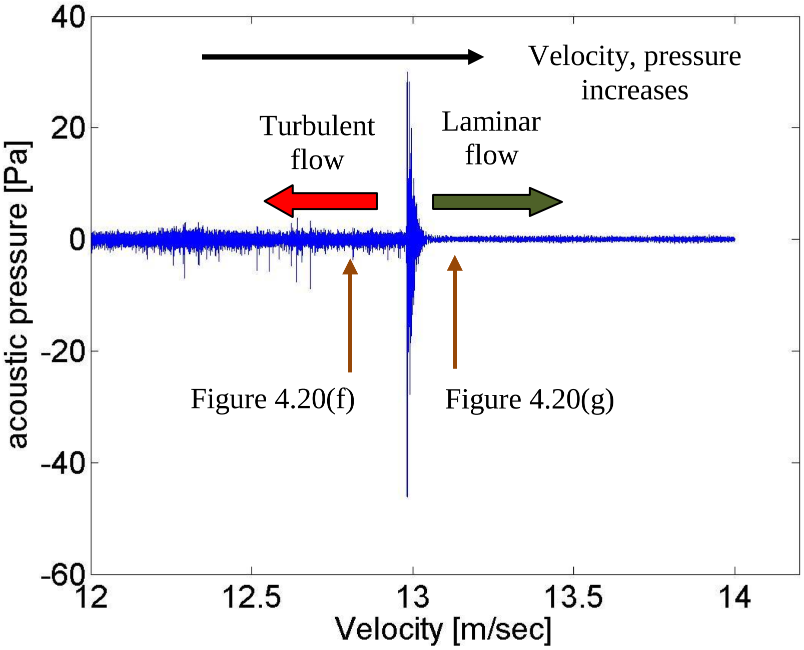

Figure 4.21. Transition from turbulent flow to laminar flow; acoustic pressure versus jet velocity. Initially the jet velocity is 12 m/s (Re=24000). The transition occurs at jet velocity equal to 13 m/s (Re=26000).

Figure 4.21 suggests that as the flow velocity increases, and hence Reynolds number increases, a sharp spike in the pressure is observed at the transition velocity above which the flow becomes laminar. It can also be seen that for laminar flow the rms pressure amplitude is significantly smaller compared with the amplitude of the turbulent flow. This is a strong evidence to suggest that the noise inside the pipe is caused by the turbulent jet outside the pipe.

Figure 4.22 shows the spectrogram of the signal shown in Figure 4.21. Initially, at *t* = 0, and for the following 6 seconds there is high level of noise energy due to the turbulent flow. As velocity increases and the flow becomes laminar the level of noise energy significantly drops.

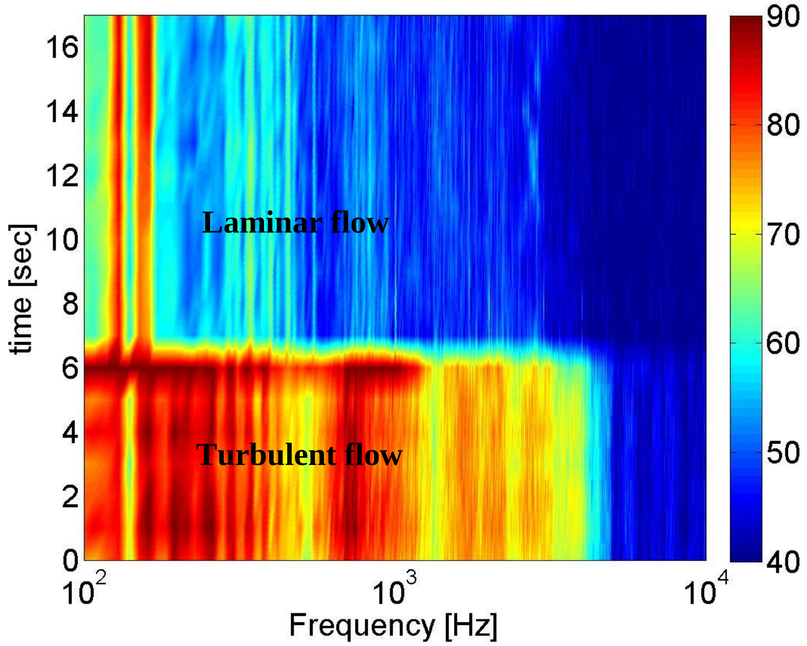

Figure 4.22. Spectrogram of the signal shown in Figure 4.21. Units of colorbar are in dB re 1 μPa$^2$/Hz.

Figure 4.22 shows also that for frequencies higher than 4.5 kHz the level of the PSD significantly drops independently of whether the flow is laminar or turbulent. It will be shown in Chapter 5 that this frequency varies with velocity and leak size.

In Figure 4.23 the PSD of noise due to turbulent and laminar flow is shown for a flow velocity of 12 m/s, at which the flow is turbulent, and at 13 m/s where the flow is laminar. The background noise is also shown for comparison. Details for the shape of the spectrum will be given in Section 4.4.6.

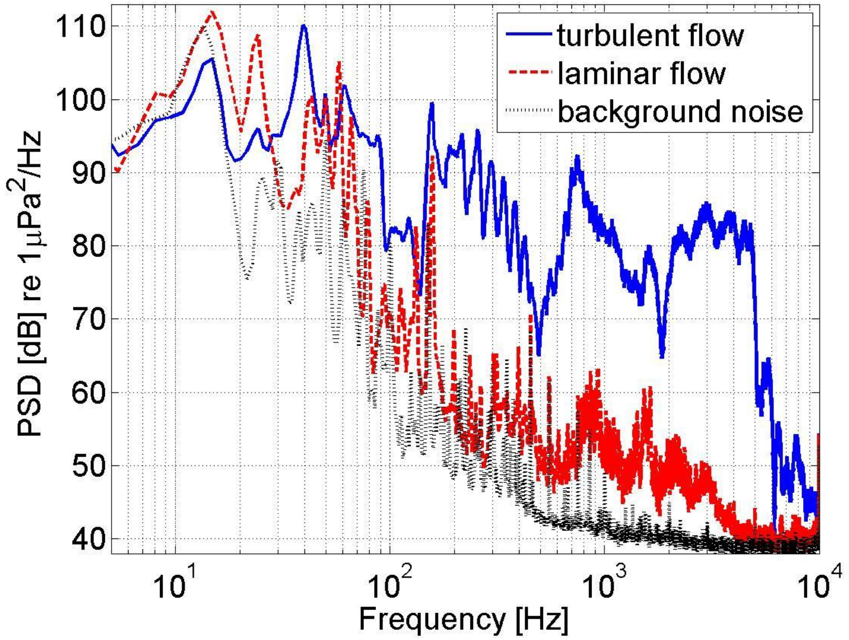

Figure 4.23. Power Spectral Density (PSD) for turbulent flow $V \approx 12$ m/s, laminar flow $V \approx 13$ m/s (relaminarization) and background noise for the 2 mm diameter leak size.

Figure 4.23 shows a significant difference in the PSD level between turbulent and laminar flow in the frequency range 70 Hz-10 kHz, with the latter having a level comparable to the level of the background noise. This is further evidence to suggest that leak noise is due to turbulent flow and not due cavitation or flow instabilities inside the pipe as speculated previously [34]. The PSD of the captured signals was calculated using a 32,768 point FFT and a Hanning window with 50% overlap. The sampling frequency here was 32 kHz and the signals were acquired for a time duration of approximately 30 s.

## 4.4.6 Spectral description of the leak noise

In this section PSDs of the measurements recorded at each hydrophone located either side of the leak are shown. The background noise is also shown for comparison. Figure 4.24(a) shows the measured PSD and Figure 4.24(b) the coherence between the two signals for a pressure of 1.3 bar corresponding to a flow velocity of around 12 m/s.

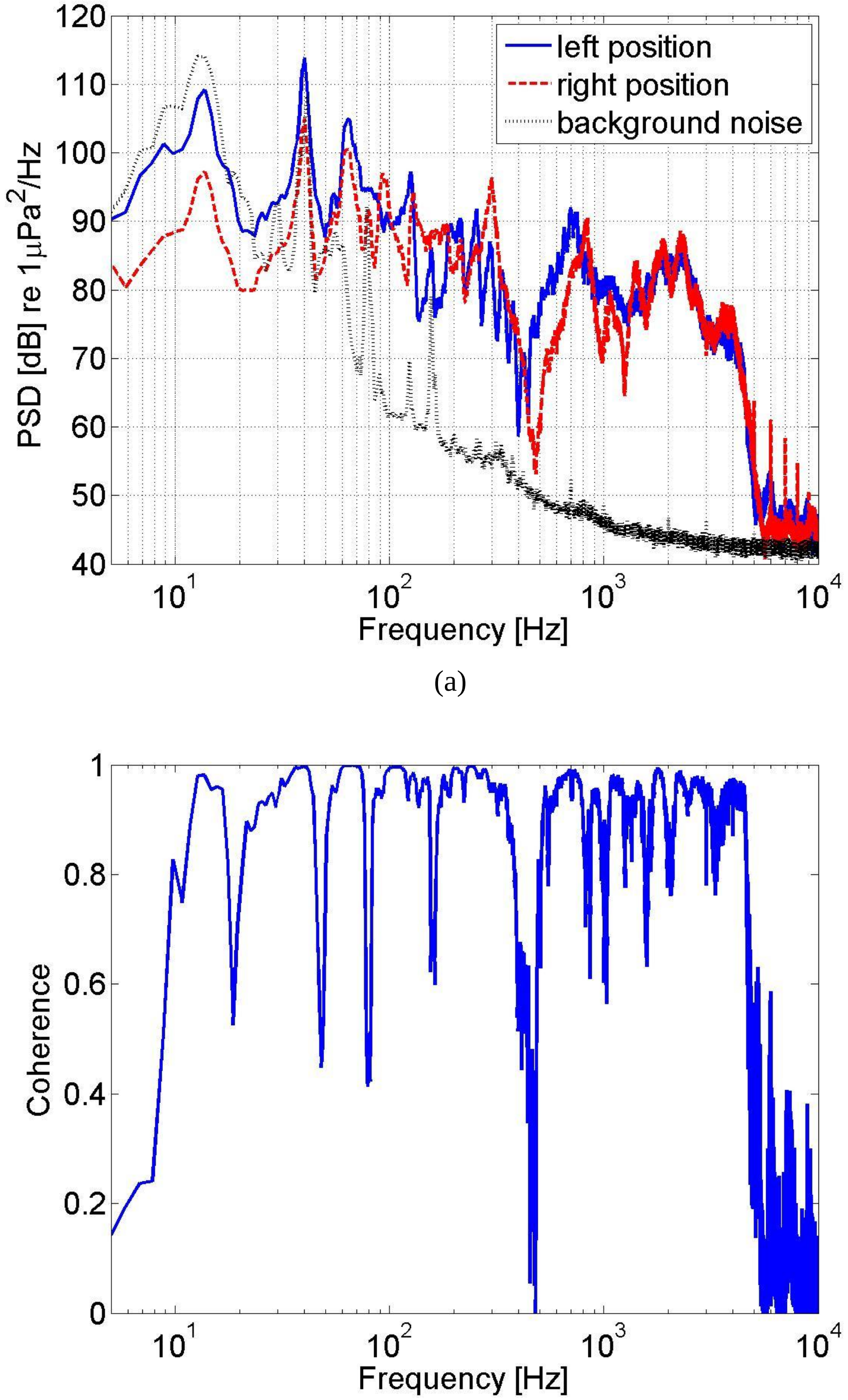

(a)

(b)

Figure 4.24. PSD and coherence between the hydrophone signals; (a) PSD for $P \approx 1.3$ bar and $V \approx 12$ m/s; (b) coherence when $P \approx 1.3$ bar and $V \approx 12$ m/s.

Figure 4.24(b) shows generally good coherence between the two hydrophone signals. Figure 4.24(a) shows that the background noise level is similar to the level of leak signals below about 50-60 Hz but at higher frequencies there is a significant difference between them. Resonance-like behaviour can be seen up to about 450 Hz, followed by a strong broad peak at around 750 Hz. Differences between the two signals are possibly due to different hydrophone position relative to the ends which could be close to nodes and anti-nodes of the standing waves. In Figure 4.25 the PSD of the hydrophone on the left side of the leak is now shown separately so that the spectrum can be described in more detail.

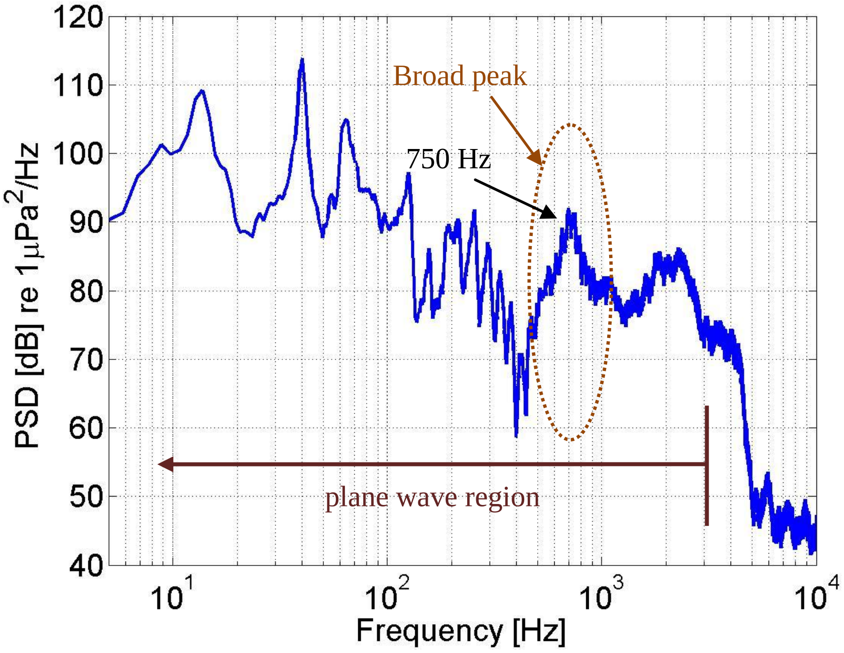

Figure 4.25. PSD of the noise signal measured on the left side of the leak for $P \approx 1.3$ bar and $V \approx 12\ \mathrm{m/s}$.

The peaks in the spectrum in the frequency range up to 450 Hz can be attributed to axial resonances of plane waves. These resonances are apparent due to the low damping of the plastic pipe, which from theoretical predictions was estimated to be around 0.4 dB/m at 100 Hz. At frequencies up to 450 Hz the spectrum decays gradually but at higher frequencies the behaviour of the pipe exhibits a different character. A significant feature in the spectrum is the appearance of a high-amplitude, broad peak at around 750 Hz. This will be further investigated in Section 4.4.7.

The sharp drop in the PSD at about 4.5 kHz will be shown in Chapter 5 to be connected to leak noise. Note, however, that this frequency also matches well with the cut on frequency of the 1st higher order spinning mode $m$=1, $n$=0 whose cut-on frequency is given by $ka$= 1.84, where $k = \omega/c$ and $a$ is the pipe radius, and whose mode shape is shown in Figure 4.26 with the arrow indicating the spin of the mode. Nevertheless, it will be shown that the frequency at which the pressure drops varies with flow velocity and is therefore not associated with the cut-on frequency of the 1st higher order spinning mode.

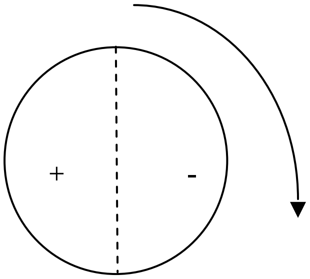

Figure 4.26. Mode shape of the first higher order spinning wave $m$=1, $n$=0 with $ka = 1.84$.

The position of the hydrophone in relation to the pipe is shown in Figure 4.27.

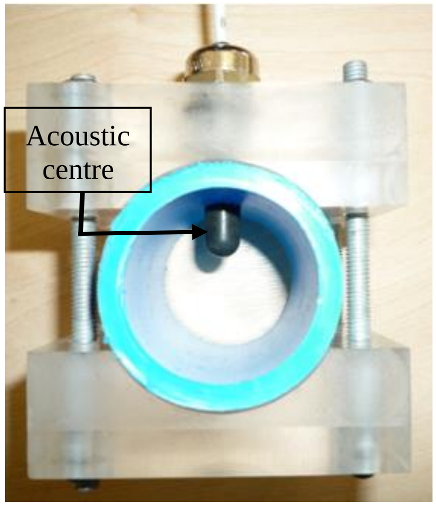

Figure 4.27. Exact hydrophone position inside the pipe. The acoustic centre of the hydrophone is also indicated.

### 4.4.7 Investigation of the broad peak at 750 Hz

In this section the experiments conducted to investigate the cause of the peak in the PSD of the noise signal at 750 Hz are described. The aim was to separate the contribution of the leak signal and the pipe response to the measured pressure signal. Initially, the fittings and hydrophone position were tested, to see whether their dynamics was the cause of this peak, by making small alterations to the tension of the bolts and by removing and replacing the hydrophones and repeating the measurement. However, none of these changes altered the peak at 750 Hz.

In order to establish whether the 750 Hz peak was due to the dynamic characteristics of the pipe or due to the leak noise a set of measurements were conducted using a shaker to excite the pipe while the leak was sealed. The shaker was connected to the end cap of the pipe as shown in Figure 4.28. The distance between the shaker and the closest hydrophone was 10 m.

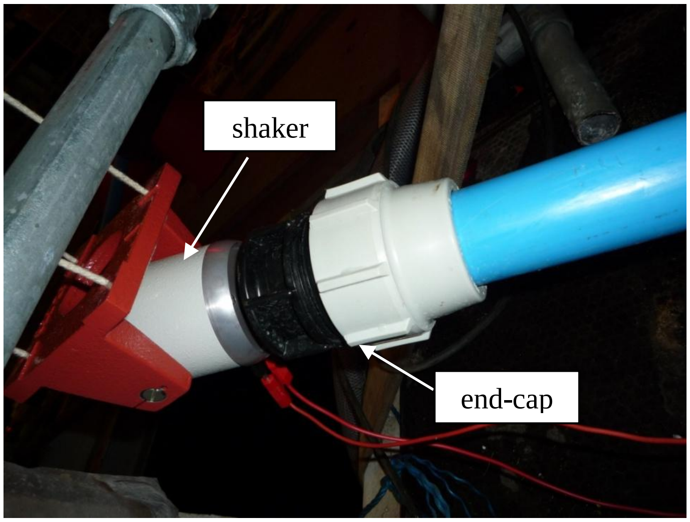

Figure 4.28. Shaker connected to the end-cap of the pipe.

While the leak was sealed the shaker was driven by a 20 kHz white noise generator and the signals from the two hydrophones and the output of the white noise generator were captured simultaneously. The transfer function (TF) between the input to the shaker and the two outputs from the two hydrophones are shown separately in Figures 4.29, together with the coherence. The static pressure inside the pipe was 1.2 bar.

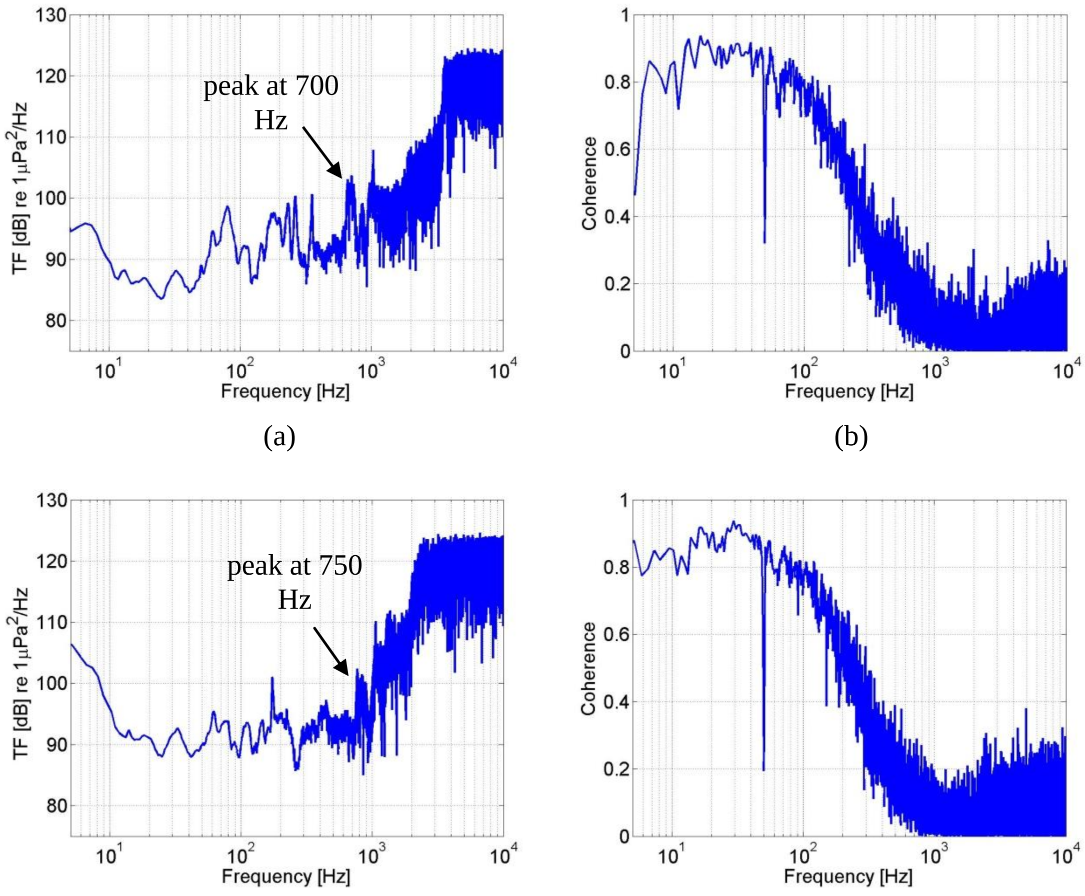

(a) (b)

(c) (d)

Figure 4.29. TF and coherence between the white noise generator and the hydrophone noise signals; (a) TF between the white noise generator and the left hydrophone signal; (b) coherence between the white noise generator and the left hydrophone signal; (c) TF the white noise generator and the right hydrophone signal; (d) coherence between the white noise generator and the right hydrophone signal.

Figures 4.29(b) and (d) suggest poor coherence between the signals in the frequency range of interest at 750 Hz (around 0.15). Nevertheless, a small peak is noticeable in that frequency range in Figures 4.29(a) and (c). This is an indication that the peak is probably related to pipe dynamics and not to leak noise.

The final experiment undertaken to investigate further the cause of the 750 Hz peak involved placing an accelerometer next to the hydrophone nearest to the end cap on the blue pipe and comparing the hydrophone and accelerometer captured signals. This would give some information about the radial motion of the pipe. The pipe was excited only by the leak. For this experiment the diameter of the leak hole in the pipe was 3 mm.

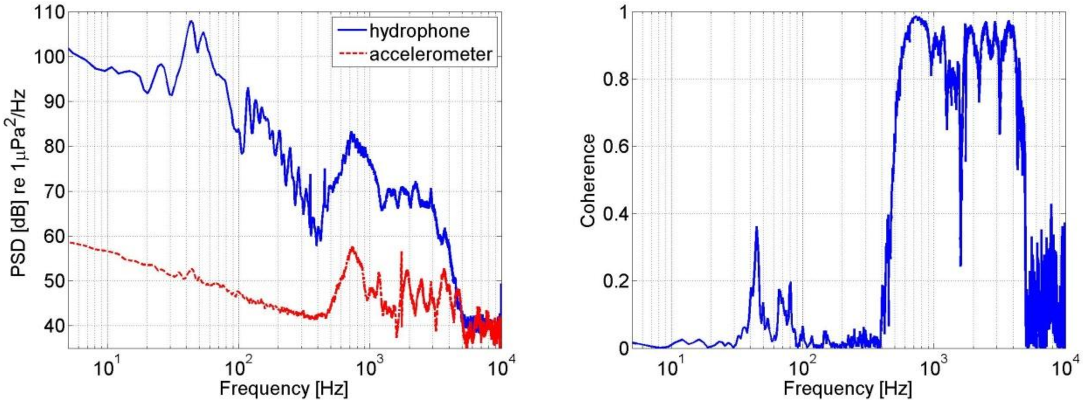

(a) (b)

Figure 4.30. (a) PSD and (b) coherence between the hydrophone and accelerometer measured signals.

From Figure 4.30, a clear peak at around 750 Hz can be seen in both the accelerometer and the hydrophone signals. This experiment provided clear evidence that the acoustic pressure in the pipe is well-coupled to the radial motion of the pipe at frequencies above 600 Hz where the coherence significantly increases.

The most likely cause of this 750 Hz resonance is standing waves in the 30 cm length of the clear plastic section due to the discontinuities between the clear and blue plastic sections. Assuming that resonant frequencies in this pipe section occur when half of wavelength equals the length of the section and a wavespeed of 385 m/s, the resonant frequency is predicted to be 650 Hz which is not far from the 750 Hz measured value.

## 4.4.8 Power Spectral Density variation for pressure decay for the 2 mm leak

Useful information about the leak noise characteristics can be obtained by studying the variation of leak signals as the tap is switched off from a high pressure while the pressure is allowed to decay slowly over many minutes. Therefore, starting from a high static pressure inside the pipe the leak noise signal was captured immediately after the tap was switched off until the moment when no water escaped from the leak. Thus the pressure, and hence flow velocity, was continuously decaying. The length of the time history varied according to the initial static pressure. An example of a time history is shown in Figure 4.31 for the 2 mm leak starting with initial pressure 0.85 bar which corresponds to a flow velocity of approximately 9 m/s. A high pass filter with cut-off frequency at 50 Hz was applied to that signal to remove the low frequency background noise. Note that in this case the flow was initially turbulent and became laminar while the flow velocity was steadily decreased. As mentioned in Section 4.4.3 the transition was not clear as in the case of relaminarization for high flow velocities (see Figure 4.21).

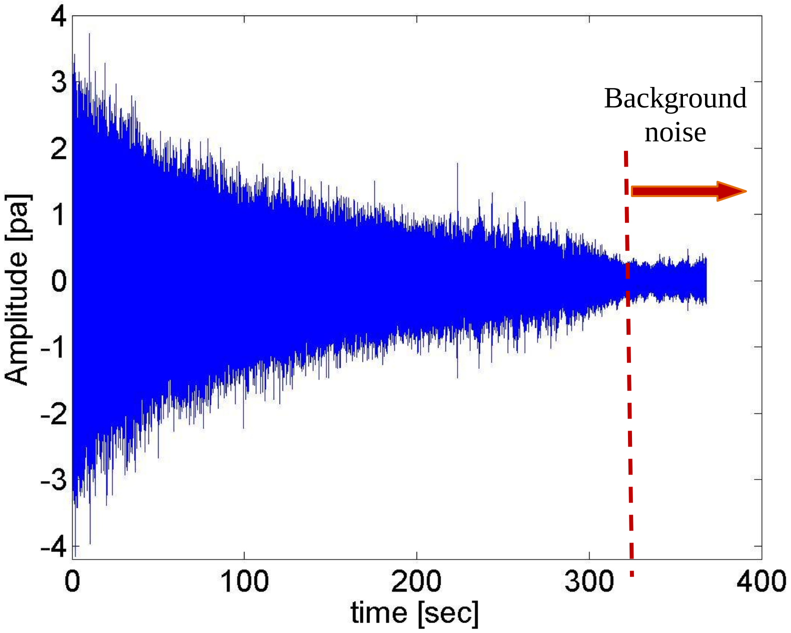

Figure 4.31. Time history for the 2 mm leak noise signal while the static pressure inside the pipe decays with time. Initial pressure 0.85 bar which corresponds to a flow velocity of around 9 m/s.

Figure 4.31 suggests that the pressure decays with time for approximately 300 s and then falls into the level of background noise. The flow velocity after 300 s is close to 1 m/s.

To obtain more information about how the PSD of the noise signal varies with time, the time history shown in Figure 4.31 was divided into segments of 1 s length. For each segment the PSD was calculated using a 4096 FFT, Hanning window and 50% overlap. The sampling frequency in this case was 32 kHz.

In Figure 4.32, the variation of PSD with time and frequency is shown with initial pressure equal to 0.85 bar at $t$=0. It can be seen that for higher pressures the pipe resonances, revealed as time-independent lines in Figure 4.32, dominate the PSD results up to approximately 1 kHz. As the pressure decays, three curves whose frequencies are time-dependent are visible in the frequency range of 500 Hz to 2.5 kHz, as Figure 4.32

suggests, which cannot therefore be related to pipe resonances. These curves are consistent with instability waves in the water jet, which according to previous work [1,2] appear after less than one diameter of air travel. At frequencies above the highest frequency of the instability waves the noise drops to a very low level similar to the level of the background noise.

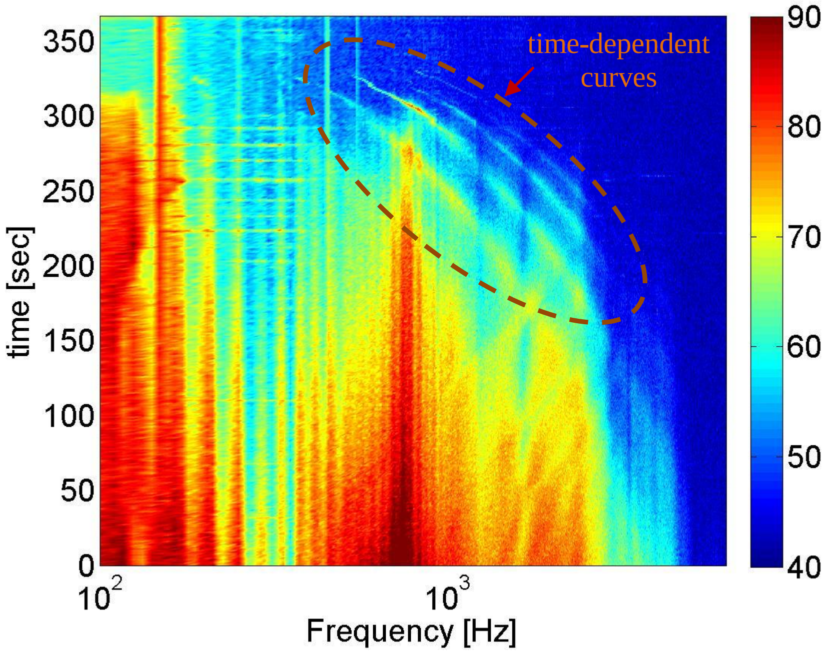

Figure 4.32. Spectrogram of the 2 mm leak; At $t$=0 the static pressure is 0.85 bar. Units of colorbar are in dB re 1 μPa$^2$/Hz.

In Figure 4.33 the PSD is now plotted versus flow velocity and frequency. It can be seen that the three curves have now become straight as indicated by the dashed lines suggesting a Strouhal number dependency.

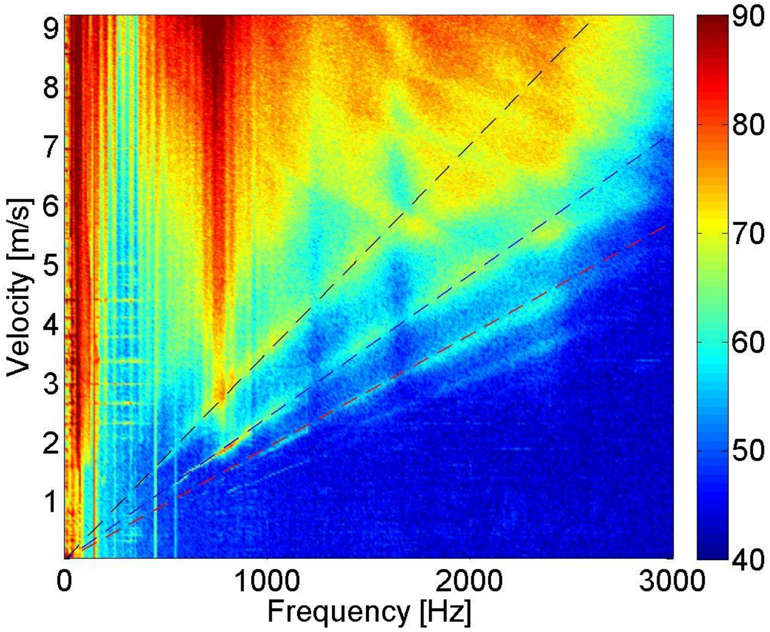

Figure 4.33. PSD of the noise signal versus flow velocity and frequency; At *t*=0 the static pressure is 0.85 bar. Units of colorbar are in dB re 1 μPa$^2$/Hz.

This dependency can be seen again in Figure 4.34 where the PSD is plotted versus Strouhal number, *St*=*fd*/*V*, and flow velocity when *d*=2 mm. Each curved line can be associated with a unique Strouhal number.

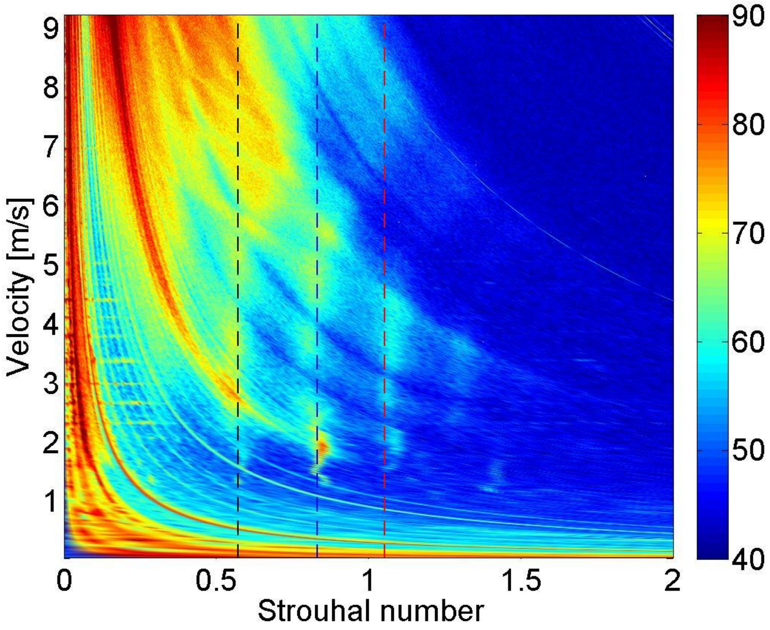

Figure 4.34. PSD of the noise signal versus Strouhal number and flow velocity; At *t*=0 the static pressure is 0.85 bar. Units of colorbar are in dB re 1 μPa$^2$/Hz.

# 4.5 Discussion

This rig was designed with the objective of obtaining information about the mechanism of leak noise generation by observing the flow in the vicinity of the leak as the water leaves the leak hole. Another objective was to derive information about the shape of leak noise spectrum and how it is affected by leak size and jet flow velocity. Problems encountered with the preliminary rig, such as flow noise and flow obstruction due to the various connectors, were overcome by using a pipe with a larger diameter and by using connectors that could connect the different pipe sections in a way to ensure smooth flow.

From the experiment it was shown that cavitation is not a mechanism of leak noise generation in this rig at least, as no bubbles were observed in the vicinity of the leak. Furthermore, the general shape of the measured leak spectrum had many differences from a typical cavitation spectrum shown in Chapter 2. Another finding from the experiment was that turbulence in the water jet is the main mechanism responsible for leak noise generation. Measurements conducted for turbulent and laminar flow showed that the pressure level in the case of laminar flow was comparable with the pressure level of background noise whereas for turbulent flow the difference is significant and can be around 30-40 dB greater for frequencies between 60 Hz and 8 kHz.

Noise measurements also revealed some information about the shape of leak noise spectra. The plane wave region was dominant by strong resonances, due to the finite length of the pipe, whose amplitudes were decaying with frequency until about 400-500 Hz. At higher frequencies, a broad resonance with a peak at around 750 Hz did not allow conclusions to be drawn about the behaviour of leak noise spectrum in this frequency region. The experiments conducted to investigate the reason of this peak provided evidence that this peak was not due to leak noise but due to the pipe dynamics. Possible reason for this could be standing waves created by the connectors between the 30cm length clear plastic section and the two sections of the blue pipe.

Finally, measurements on the 2 mm leak for low flow velocities revealed flow activity, with Strouhal number dependency. This flow activity is possibly related to axisymmetric instability waves which according to Hoyt *et al.*, appear after less than one diameter of air travel. For higher flow velocities instability waves were not visible, possibly due to masking by the strong pipe resonances. This result provides evidence that flow instabilities observed outside of the pipe in the water jet are observable as pressure fluctuations in the pipe.

## 4.6 Conclusions

The rig described in this chapter gave important information about the mechanism of leak noise generation which is associated with turbulent flow and not with cavitation. At lower pressures, noise due to flow activity was present which could be related to axisymmetric instability waves in the jet. However, firm conclusions about the leak noise spectrum and how it is influenced by leak size and flow velocity could not be made due to the presence of a broad peak in the frequency range close to 750 Hz. Shaker tests showed that these are possibly caused by resonances at the connectors between the clear and blue plastic section. Therefore, a different set-up of the existing rig had to be designed without discontinuities, that could allow information about the shape of the leak noise spectrum to be derived and also how the leak spectrum is affected by leak size and jet flow velocity to be investigated. This will be presented in Chapter 5.

# CHAPTER 5

# A FINAL RIG FOR CHARACTERIZING LEAK NOISE

## 5.1 Introduction

In this chapter the final rig for characterizing leak noise is described. Results are presented for the leak noise spectrum and its variation with leak flow velocity and leak hole size. The difference between this rig and the one presented in Chapter 4 is that the clear plastic section and the 10 m plastic pipe (Sections 1 and 2 in Figure 4.12) has now been removed. The connectors that were the main cause of additional reflections in the noise signal are now avoided. A different number of leak sizes were examined starting from 1 mm in diameter and increasing progressively every 0.5 mm until the size of 4 mm in diameter. The effect of leak size and water velocity to the leak spectrum is investigated and an empirical model for describing this behaviour is proposed.

## 5.2 Rig description

In this final rig the leak hole was directly drilled into the MDPE pipe. The two hydrophones were placed on either side of the leak at a distance of 0.7 m and 0.3 m. One end of the pipe was terminated by an end cap at a distance of 6m from the left hydrophone. Section 4 and Section 5 remained unaltered. A schematic of the experimental rig and a picture of the leak and hydrophones are shown in Figures 5.1 and 5.2 respectively.

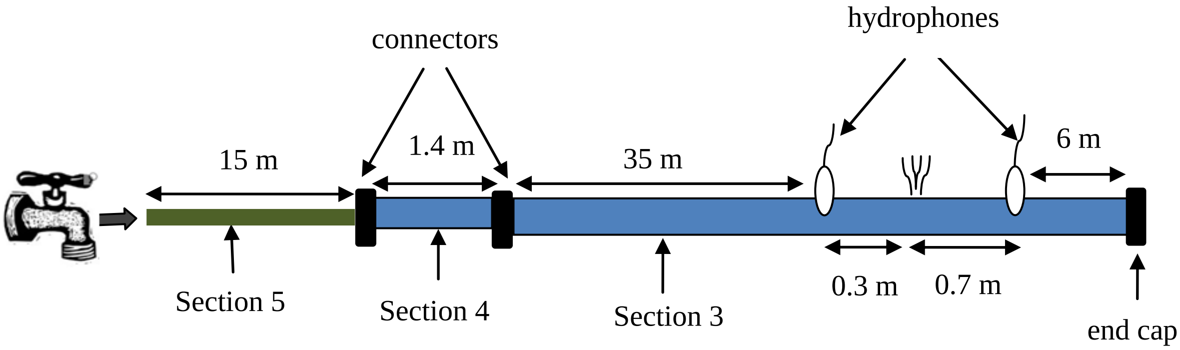

Figure 5.1. Final set-up of the experimental rig.

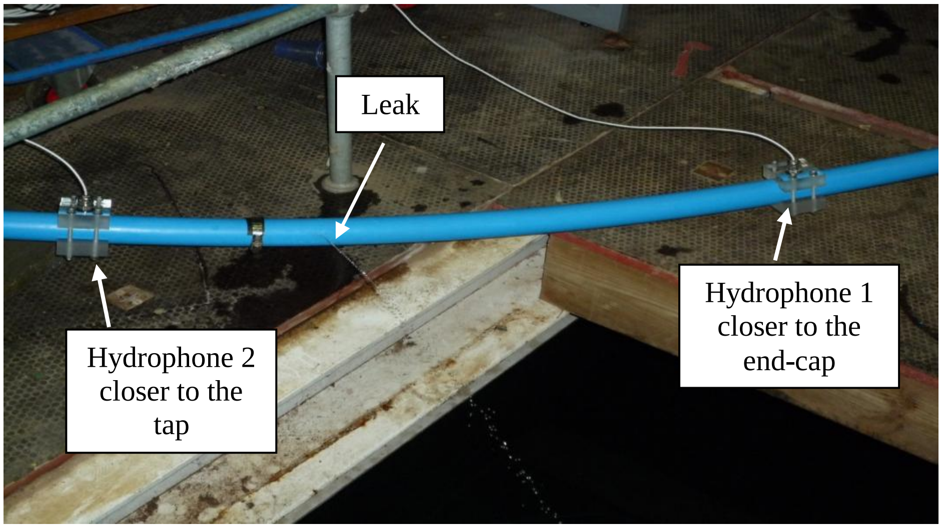

Figure 5.2.Hydrophones and leak position at the final rig.

## 5.3 Spectrum of the 1 mm diameter leak

In this section, measurements of the leak spectrum for the 1 mm diameter leak hole are presented. In Figure 5.3 the Power Spectral Density (PSD) is shown for the two hydrophone signals located left and right of the leak with the pipe at maximum pressure, corresponding to a jet velocity of 9.7 m/s. The background noise is also indicated for comparison. It can be seen that the broad peak at about 750 Hz is now absent in these results, which is further proof that this spectral peak was related to the dynamics of the clear pipe section and not to the leak noise. In Figure 5.4 the coherence between the hydrophone signals is shown, which is very close to unity at frequencies between 50 Hz and 4 kHz.

Strong resonant peaks in the PSD can be still seen in Figure 5.3 at frequencies below 1 kHz that are due to the finite length of the pipe. Their amplitudes decay with increasing frequency. Below about 50 Hz, the leak spectrum can be seen to be dominated by the background noise, indicated by the poor level of coherence below this frequency.

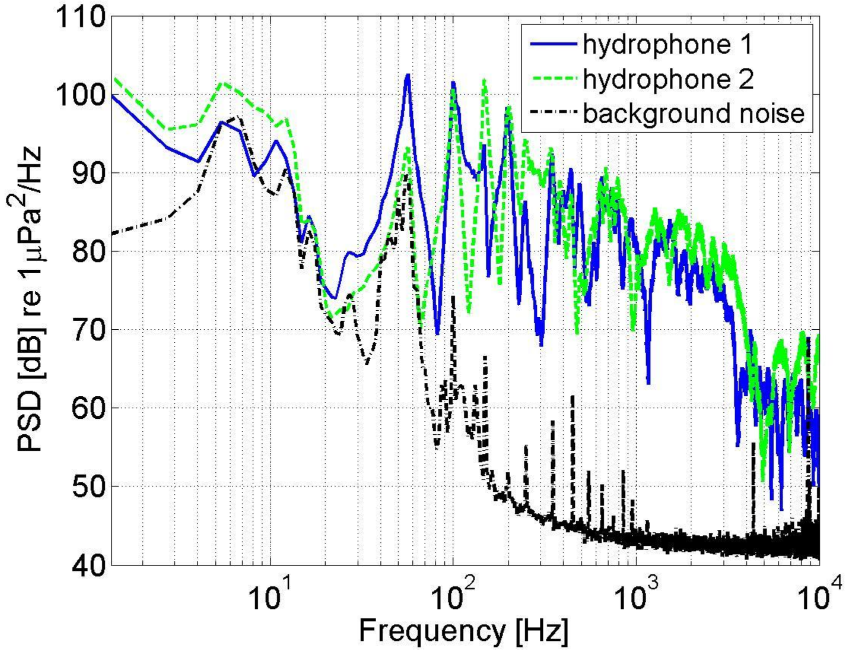

Figure 5.3. PSD of the noise signals for the maximum flow velocity $V = 9.7\ \mathrm{m/s}$.

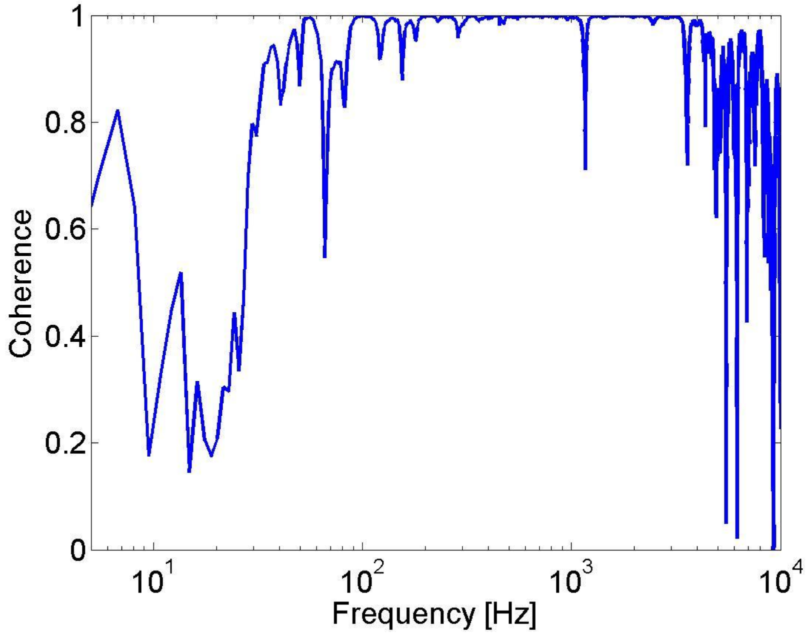

Figure 5.4. Coherence between the two hydrophone signals.

## 5.4 Wavespeed calculation

The acoustic wavespeed inside the pipe was calculated from the time delay of the leak signals between the two hydrophones. This was measured from the cross-correlation function and also from the slope of the phase spectrum of the transfer function between the two hydrophones. From the time delay $T_0$ of the peak in the cross-correlation function shown in Figure 5.5 the wavespeed can be calculated using [9]

$$c = \frac{d_1 - d_2}{T_0} \tag{5.1}$$

where $d_1$, and $d_2$ are the distances of hydrophone 1 and 2 from the leak.

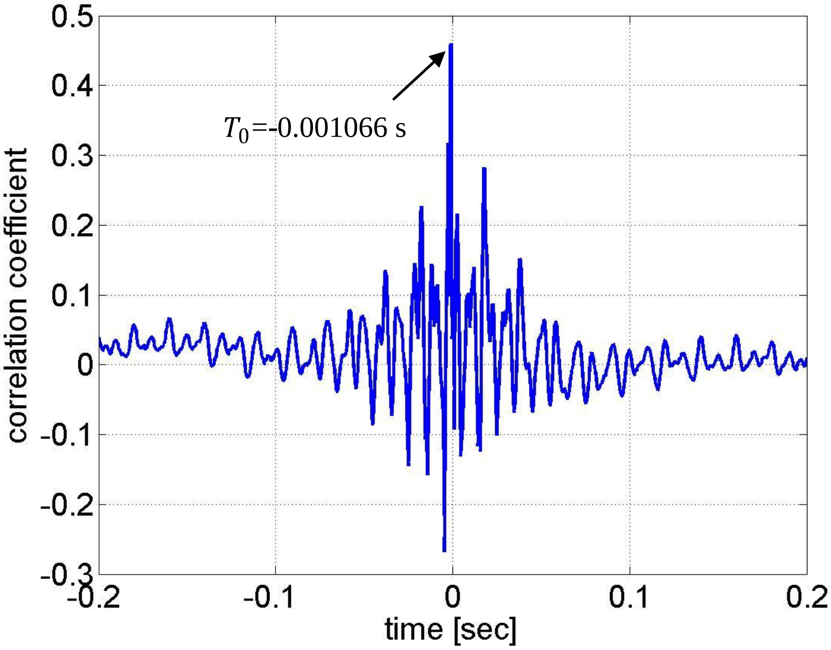

Figure 5.5. Cross-correlation coefficient between the two hydrophones

From the measured time delay $T_0$, and by using Eq.(5.1), the wavespeed $c$ was calculated to be 375 m/s, which matches well with the theoretical prediction of 385 m/s [9]. Assuming an error of 3 mm in measuring correctly the distances $d_1$ and $d_2$ the total error in calculating the wavespeed is approximately $\pm$ 3%. Note that the error arising from the sampling frequency $f_s$ is negligible of order $\approx 2.2 \cdot 10^{-5}$.

Figure 5.6 shows the unwrapped phase angle of the transfer function between the two signals. Note that the difference in the phase response between the two hydrophones is much smaller than the one due to the phase delay. Based on the slope of the line of least squares fit, also shown in Figure 5.6 as the red straight line, the wavespeed was calculated to be 312 m/s. This discrepancy between the wavespeed measured from the correlation function and those from the phase gradient cannot be explained at the present time. However, it will be shown in this chapter that the wavespeed does not affect the later results presented in this thesis and for this reason it is not investigated further.

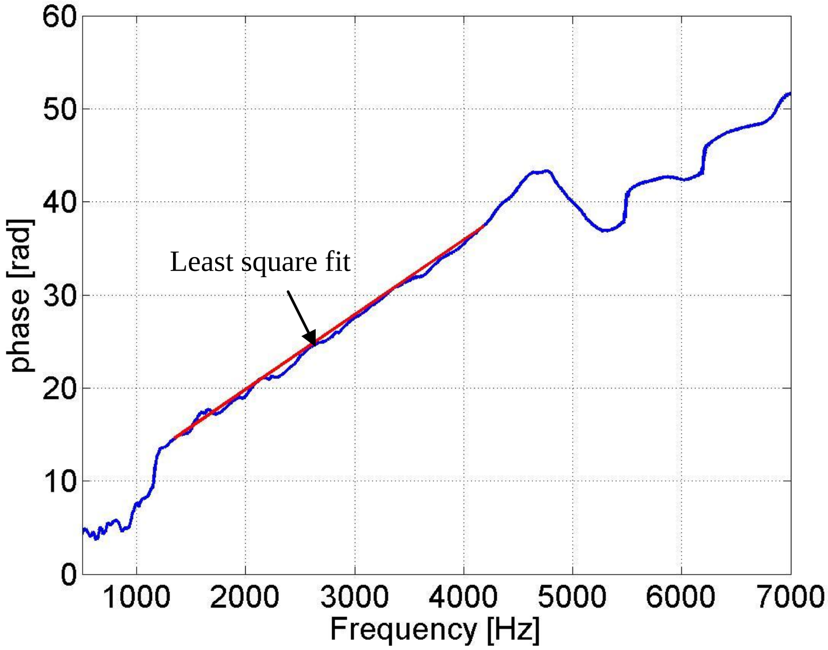

Figure 5.6. Unwrapped phase angle for the hydrophone-measured signals.

## 5.5 A theoretical model of the cross-spectrum including wave reflections

In previous work, Gao *et al.* developed an analytical model for the cross spectrum between two signals measured on either side of a leak, in a finite-length pipe [44].

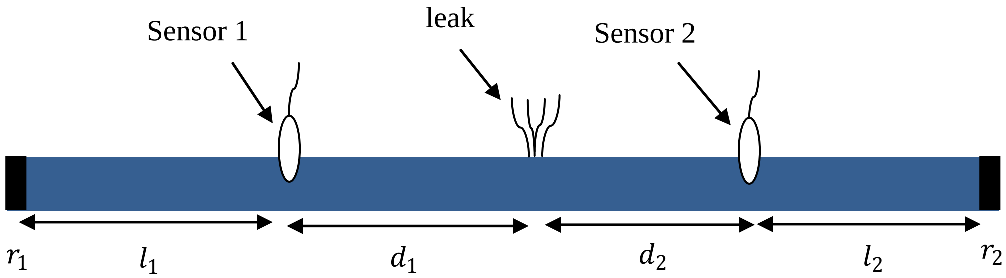

Figure 5.7. Schematic of a finite length pipe with pressure reflection coefficients $r_1$ and $r_2$ at the two ends. The sensors are in distances $d_1$ and $d_2$ from the leak.

With reference to Figure 5.7, the cross-spectral density (CSD) $S_{x_1x_2}(\omega)$ of two signals $x_1(t)$ and $x_2(t)$ measured at distances $d_1$ and $d_2$ from the leak, is given by [44],

$$S_{x_1x_2}(\omega) = H^*(\omega, d_1)H(\omega, d_2)S_{ll}(\omega) \tag{5.2}$$

where * denotes complex conjugation, $S_{ll}(\omega)$ is the effective PSD of the acoustic pressure generated by the leak signal as defined in Chapter 3, and $H(\omega, d_1)$ and $H(\omega, d_2)$ are the transfer functions between the signals at the leak and sensor position 1 and 2 respectively.

It has been shown that for the case where the reflections do not occur between the leak and the sensors (out of bracket discontinuities) the transfer functions between the leak and each sensor are given by [44],

$$H(\omega, d_1) = \frac{e^{-jk\,d_1}\left(1 + r_1 e^{-jk\,2l_1} + r_2 e^{-jk\,2(d_2+l_2)} + r_1 r_2 e^{-jk\,2(d_2+l)}\right)}{\left(1 - r_1 r_2 e^{-jk\,2(d_1+d_2+l)}\right)} \tag{5.3}$$

$$H(\omega, d_2) = \frac{e^{-jk\,d_2}\left(1 + r_2 e^{-jk\,2l_2} + r_1 e^{-jk\,2(d_1+l_1)} + r_1 r_2 e^{-jk\,2(d_1+l)}\right)}{\left(1 - r_1 r_2 e^{-jk\,2(d_1+d_2+l)}\right)} \tag{5.4}$$

where $k = \omega/c(1 - j\eta/2)$, $\eta$ is the loss factor of the pipe, $c$ is the acoustic wavespeed, $r_1, r_2$ are pressure reflection coefficients at the two ends, $l_1$, is the distance between sensor 1 and reflection point 1 and $l_2$ is the distance between sensor 2 and reflection point 2 as can be seen in Figure 5.7.

## 5.6 Procedure for estimating the leak noise spectrum

In this section a procedure for estimating the leak noise spectrum is shown based on the theoretical model presented in Section 5.5. This method is initially applied to a leak signal obtained from the 1 mm diameter leak and for a maximum flow velocity of 9.7 m/s.

From Eq.(5.2),

$$S_{ll}(\omega) = \frac{S_{x_1x_2}(\omega)}{H^*(\omega, d_1)H(\omega, d_2)} \tag{5.5}$$

This formulation is useful in the case of poor signal to noise ratio since $S_{x_1x_2}$ rejects noise that is uncorrelated between the two sensors. However, it will be shown that, because of good signal to noise ratio in our measurements above about 50 Hz, the PSD of the signal at a single hydrophone can be used to estimate the leak noise spectrum. Therefore, $S_{ll}(\omega)$ may be obtained from,

$$S_{ll}(\omega) = \frac{S_{x_1x_1}(\omega)}{H^*(\omega, d_1)H(\omega, d_1)} = \frac{S_{x_2x_2}(\omega)}{H^*(\omega, d_2)H(\omega, d_2)} \tag{5.6}$$

where $S_{x_1x_1}(\omega)$ and $S_{x_2x_2}(\omega)$ are the PSDs of the signals on hydrophone 1 and 2 respectively.

At low static pressures, approximately lower than 0.4 bar, it was observed that the hydrophone located closer to the tap produced a very low voltage signal similar to that produced by the background noise. An accurate CSD could not therefore be obtained at low pressures and Eq.(5.5) could lead to erroneous results for the leak noise spectrum. Problems associated with this hydrophone were therefore suspected. Hence, the leak noise spectrum was deduced from $S_{x_1x_1}(\omega)$ only.

To illustrate the consistency of Eqs.(5.5) and (5.6) in our experiment for static pressures above 0.4 bar two different measurement results are presented for a high and low static pressure. The PSDs and CSDs for the 1 mm leak at a high static pressure of 2.5 bar and for the 2 mm leak at a lower static pressure of 0.5 bar are shown in Figures 5.8 and 5.9 respectively.

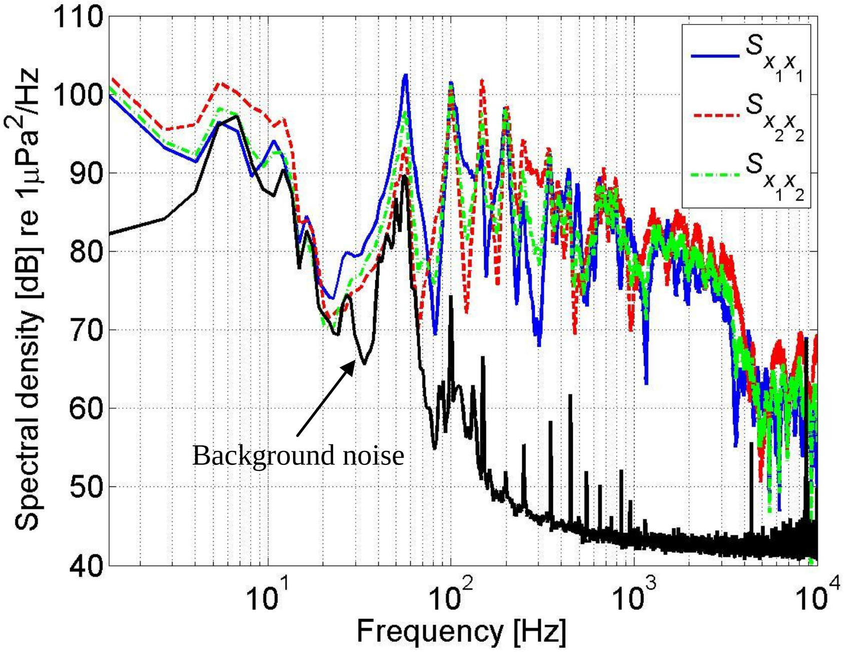

Figure 5.8. Comparison of the PSD and CSD of the 1 mm diameter leak; *P*=2.5 bar, *V*=8.5 m/s.

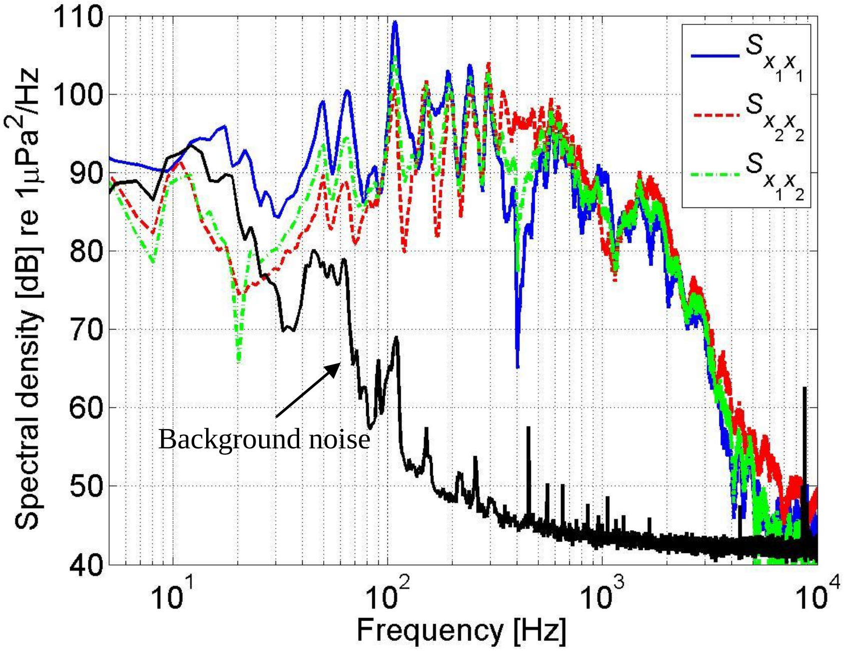

Figure 5.9. Comparison of the PSD and CSD of the 2 mm diameter leak; *P* = 0.5 bar, *V* = 4.5 m/s.

Figures 5.8 and 5.9 suggest that at frequencies higher than 50 Hz, the PSDs and CSDs are generally similar except near modal resonant and anti-resonant frequencies. Thus, the leak spectrum can be obtained by the PSD of the signal at a single hydrophone according to Eq.(5.6) without significant loss of accuracy.

Equations (5.5) and (5.6) suggest that the measured pressure signals at the hydrophones are a combination of the leak spectrum $S_{ll}$ and the pipe response $H$. Clearly the measurement of $S_{ll}$ is most accurate when the variation of $S_{ll}$ with frequency is much greater than that of the pipe response. In order to make this assessment the frequency variability of $S_{x_1x_1}$ and $|H|^2$ are now compared. This requires an estimate for $H$.

The estimation of $|H(\omega, d_1)|^2$ or $|H(\omega, d_2)|^2$ requires the estimate of the acoustic wavespeed $c$, the loss factor of the pipe $\eta$, and the reflection coefficient $r_1$ and $r_2$ at the two ends of the pipe as can be seen from Eqs.(5.3) and (5.4). The wavespeed, 375 m/s, was assumed to be correct calculated from the time delay of the cross-correlation coefficient of the measured signals as described in Section 5.4. The reflection coefficient $r_1$ at the end of the pipe terminated by the end cap was taken to equal to -1 due to the much higher acoustic impedance of water compared to that of air on the outside although the contribution from the rigid end cap is unknown. However, varying the sign of $r_2$ is found to have no significant effect on $H$. On the other end, the reflection coefficient $r_2$ was taken equal to 0.6, calculated from the cross sectional areas of the 50 mm diameter pipe $A_1$, and of the 25 mm diameter connecting pipe $A_2$ by using Eq.(5.7) [46].

$$r_2 = \frac{A_1 - A_2}{A_1 + A_2} \tag{5.7}$$

The value for the attenuation factor $\eta$, was taken from previously measured values of the MDPE pipe material properties equal to 0.06 [11]. In Figure 5.10 the PSD is compared with the $|H(\omega, d_1)|^2$ whereas in Figure 5.11 this comparison is shown for a 50% decrease of loss factor is order to investigate its effect on the theoretical pipe response and hence the estimate for $S_{ll}(\omega)$. Note that $|H(\omega, d_1)|^2$ has been adjusted in level to allow direct comparison with $S_{x_1x_1}$.

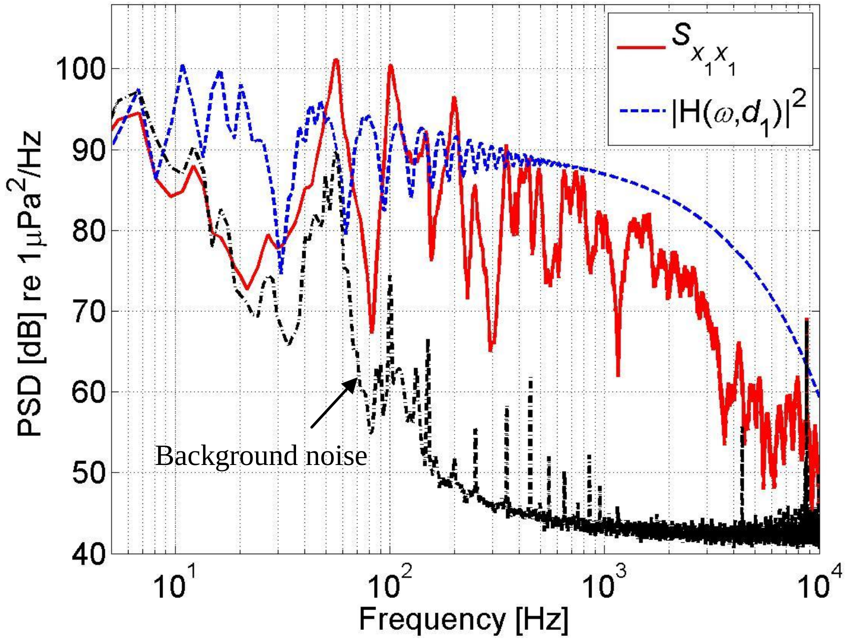

Figure 5.10. Comparison of the PSD of the signal on the one hydrophone and frequency response function between the signal and the leak for $\eta$ = 0.06, $r_1 = -1$, $r_2 = 0.6$, $c = 375$ m/s.

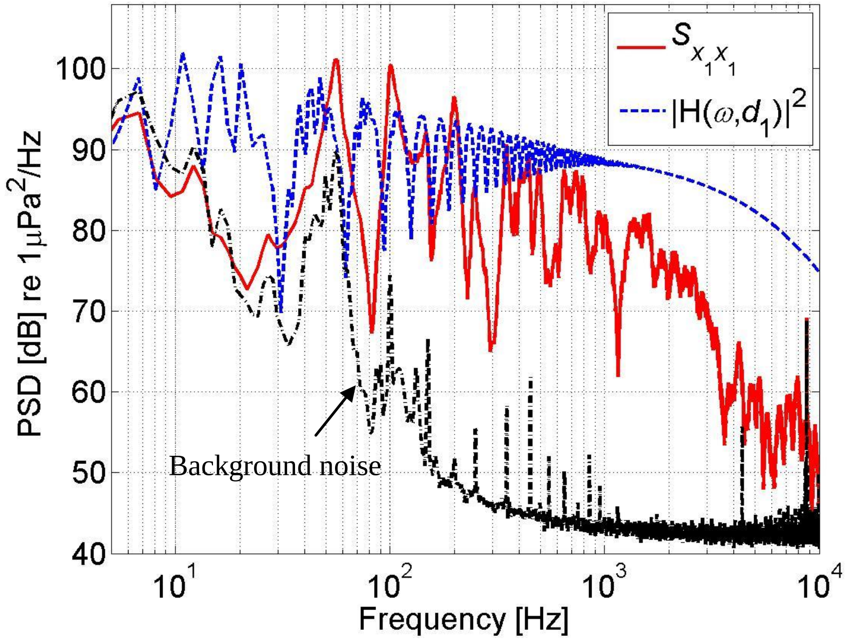

Figure 5.11. Comparison of the PSD of the signal on the one hydrophone and frequency response function between the signal and the leak for $\eta$ = 0.03, $r_1 = -1$, $r_2 = 0.6$, $c = 375$ m/s.

Figures 5.10 and 5.11 suggest that decreasing the loss factor has two effects on *H*. One is that it increases the amplitude of *H* at the resonant frequencies. The other is that it decreases the rate of decay at high frequencies. However, it can be seen in Figure 5.11 that even for the lower loss factor the amplitude at resonances of the PSD do not match in frequency with those of $|H(\omega, d_1)|^2$. Thus, the loss factor was adjusted to achieve a better match with the amplitude of the first few resonant peaks, as shown in Figure 5.12 by using a loss factor equal to 0.008. As before, $|H(\omega, d_1)|^2$ has been adjusted in level to allow direct comparison with $S_{x_1x_1}$.

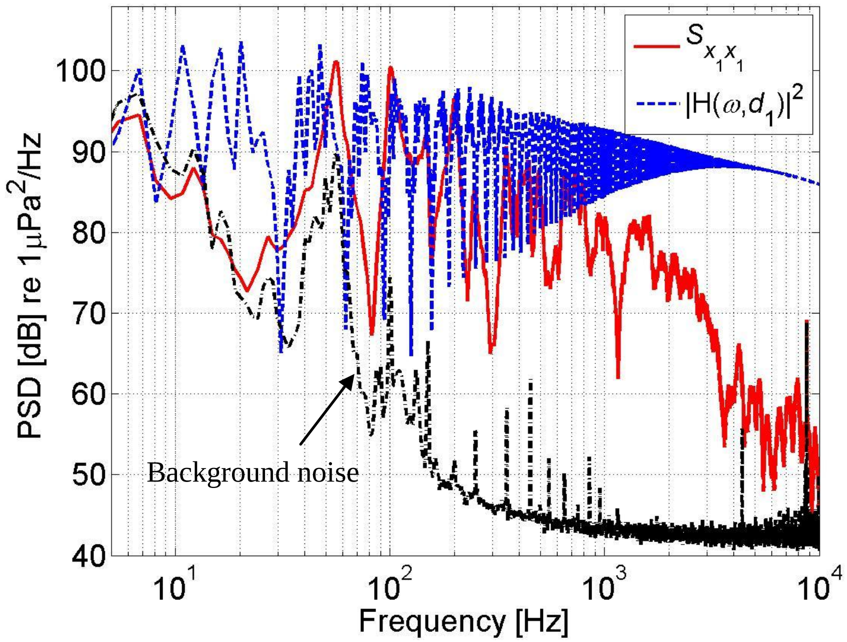

Figure 5.12. Comparison of the PSD of the signal on the one hydrophone and frequency response function between the signal and the leak for $\eta$ = 0.008, $r_1 = -1$, $r_2 = 0.6$, $c = 375$ m/s.

Figure 5.12 indicates that the peaks of the PSD and $|H(\omega, d_1)|^2$ still do not match. Altering the value of the wavespeed does not offer any improvement as it only shifts in frequency the resonant frequencies of $|H(\omega, d_1)|^2$. This is illustrated in Figure 5.13.

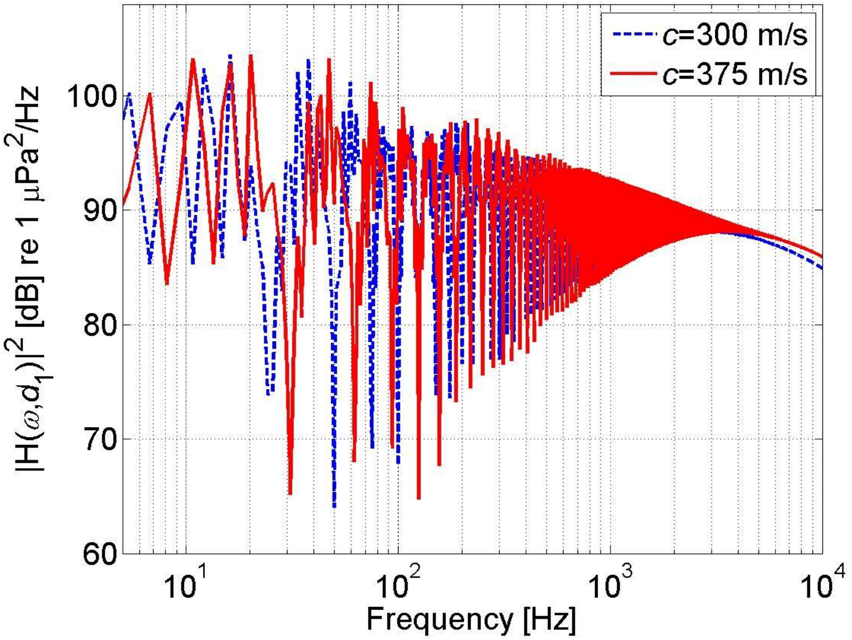

Figure 5.13. Effect of altering the value of the wavespeed on the $|H(\omega, d_1)|^2$ function. The value of loss factor is $\eta$ = 0.008, and $r_1 = -1$, $r_2 = 0.6$.

Thus, there is a discrepancy between the resonant frequencies in the noise spectra at the hydrophones and the pipe dynamics as predicted from $H$. The inversion of the pipe response using Eq.(5.5) or (5.6) is therefore imperfect and some residuals of the pipe response will remain in the leak noise estimate.

Possible explanation for this mismatch is that the theoretical model was developed for the case of a finite straight pipe whereas in our case, and for practical reasons, one part of the pipe was in a coil and another part inclined. The curved position of the pipe may introduce additional loss mechanisms but this is only a hypothesis as no literature could be found for this subject. Furthermore, the damping of the modes at higher frequencies appears to be higher in the measurements than that predicted by the theoretical damping model. Therefore, by dividing the power spectral density by $|H(\omega, d_1)|^2$ to estimate the leak spectrum will produce additional peaks. To avoid this, and because we are interested in how the pipe affects the *general* shape of the leak spectrum, $|H(\omega, d_1)|^2$ will be calculated without reflections, $r_1 = r_2 = 0$. In this case, the frequency response function between the leak and the two sensor signals will be given by:

$$H(\omega, d_1) = e^{-jk\,d_1} \tag{5.8}$$

$$H(\omega, d_2) = e^{-jk\,d_2} \tag{5.9}$$

By substituting Eqs.(5.8) and (5.9) to Eq.(5.6) therefore, the leak noise spectrum may be estimated from,

$$S_{ll}(\omega) = S_{x_1x_1}(\omega)e^{\frac{\omega\eta}{c}d_1} = S_{x_2x_2}(\omega)e^{\frac{\omega\eta}{c}d_2} \tag{5.10}$$

Figure 5.14 shows the general shape of the $|H(\omega, d_1)|^2$ for loss factors equal to 0.06, 0.03 and 0.008.

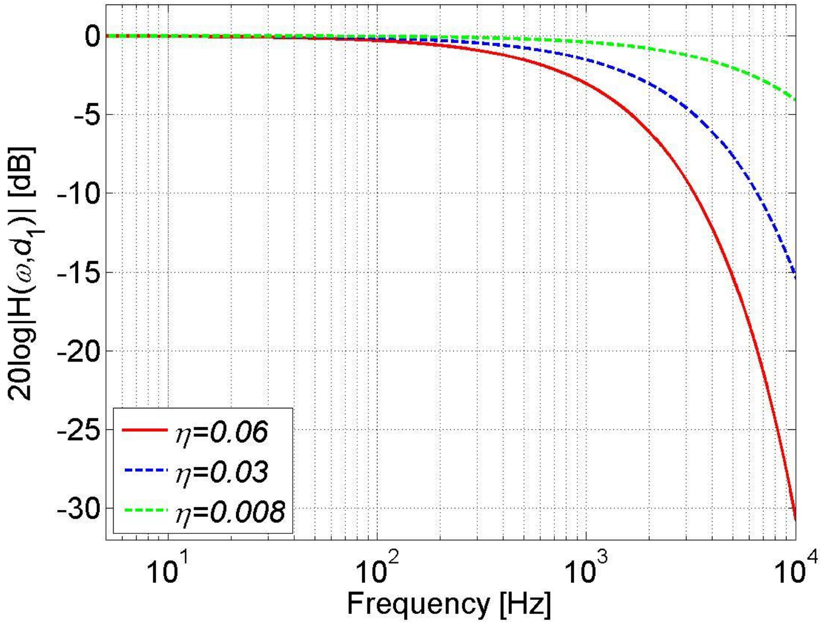

Figure 5.14. General shape of the pipe effect for three different values of loss factor.

Estimate of the leak noise spectrum obtained from Eq.(5.10) is shown in Figures 5.15 to 5.17 for the three values of loss factor. The straight dashed line represents a $1/\omega$ power law which describes the spectrum slope at frequencies approximately up to 3 kHz.

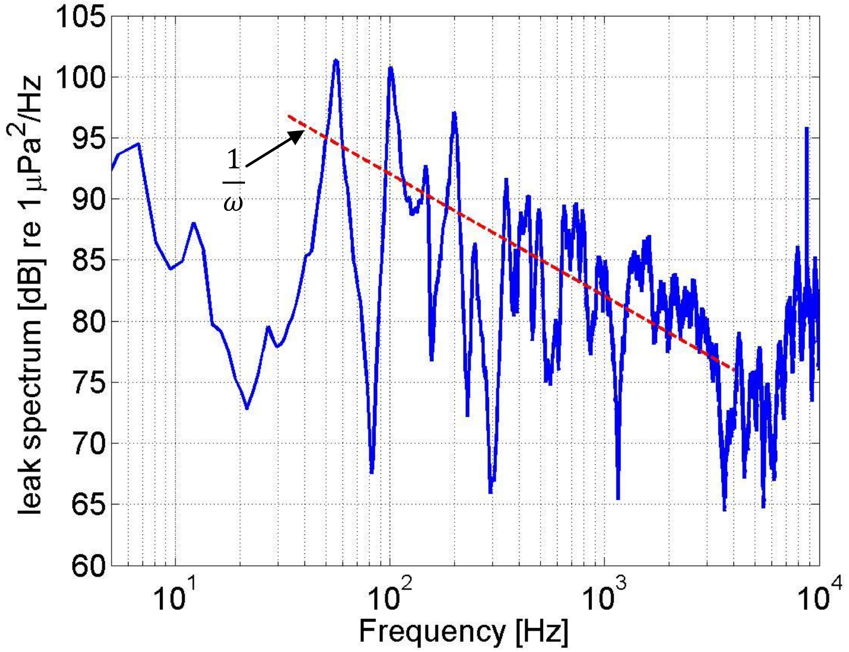

Figure 5.15. Leak spectrum; $\eta$ = 0.06.

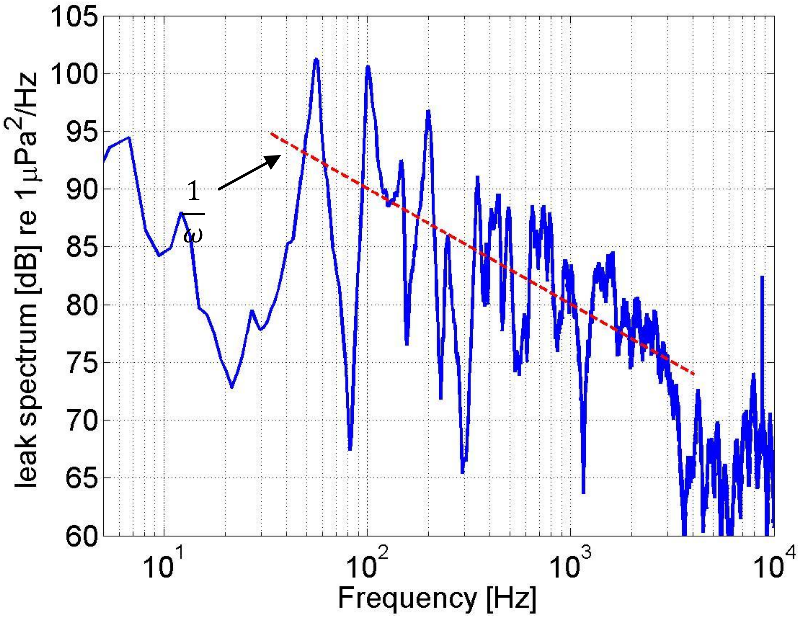

Figure 5.16. Leak spectrum; $\eta$ = 0.03.

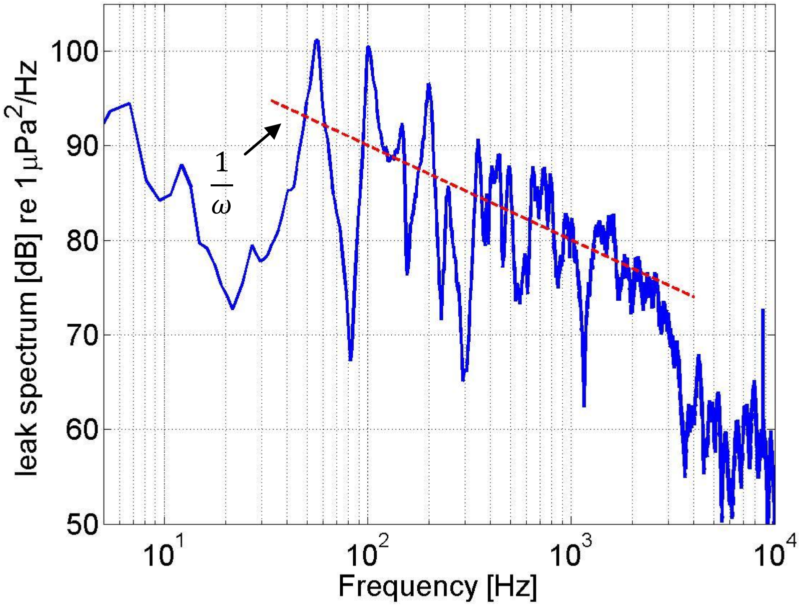

Figure 5.17. Leak spectrum; $\eta$ = 0.008.

Figures 5.15 to 5.17 suggest that the assumption of the different loss factor makes no appreciable difference to the estimate of the leak noise spectrum. The frequency dependence of the leak spectrum is therefore much greater than that due to the uncertainly in the loss factor. Assuming a power law of $1/\omega$ for the leak noise spectrum, the effect of $\eta$ on the measured noise spectrum can be deduced from Eq.(5.10).

$$S_{x_1x_1}(\omega) = S_{ll}(\omega)e^{-\frac{\omega\eta}{c}d_1} = \frac{A}{\omega}e^{-\frac{\omega\eta}{c}d_1} \tag{5.11}$$

where $A$ is the leak noise 'source level'. Taking the logarithm of both sides of Eq.(5.11)

$$10\log_{10}\left(S_{x_1x_1}(\omega)\right) = 10\log_{10}\left(\frac{A}{\omega}e^{-\frac{\omega\eta}{c}d_1}\right) \approx 10\log_{10}A - 10\log_{10}\omega - 4.3\frac{\omega\eta}{c}d_1 \text{ (dB)} \tag{5.12}$$

The reduction in the sound pressure level over one decade is therefore,

$$\Delta\left(10\log_{10}\left(S_{x_1x_1}(\omega)\right)\right) \approx 10 + 43\frac{\eta}{c}d_1 \text{ (dB)} \tag{5.13}$$

Equation (5.13) suggests that even a large value of loss factor (of the range of 0.06) has a small effect on the results compared to that due to the leak. For example, over a frequency decade the leak estimate decay due to the leak is 10 dB and due to the pipe 0.005 dB for $\eta$ = 0.06 and $d_1 = 0.7$ m. The reason for this is that in the current rig the hydrophones are placed close enough to the leak to prevent any significant attenuation of the leak signals at the hydrophones and therefore uncertainly in the loss factor cannot influence significantly the results. In the following section the value of loss factor that was used was chosen to be 0.008 to avoid any amplification of leak noise level at high frequencies.

## 5.7 Leak noise spectrum for different leak sizes and flow velocities

In this section the leak noise spectrum is presented for various combinations of leak hole size and flow velocity. Photographs of the water leak are also shown for each case. The background noise level is indicated for comparison. The red-dashed lines represent a frequency power law of $1/\omega^n$ where $n$ is a positive integer that closely matches the slope of each part of the leak spectrum. The characteristic frequency where the spectrum slope changes is also indicated for the different cases.

## • 1 mm diameter leak size

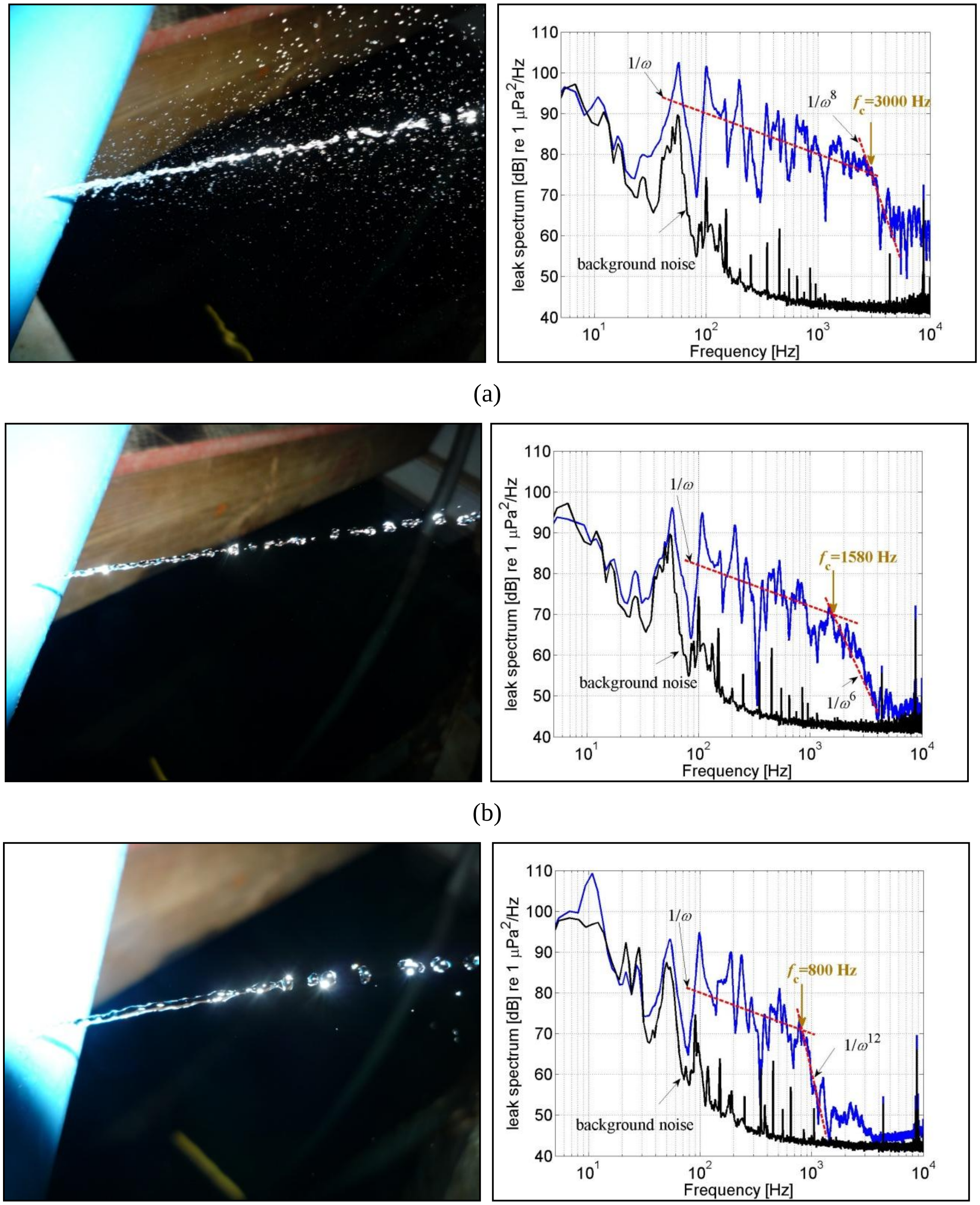

(a)

(b)

(c)

Figure 5.18. Photographs of water leak and the corresponding leak spectrum for the 1 mm diameter leak; (a) $V$ =9.75 m/s; (b) $V$ =4 m/s; (c) $V$ =1.85 m/s.

## • 1.5 mm diameter leak size

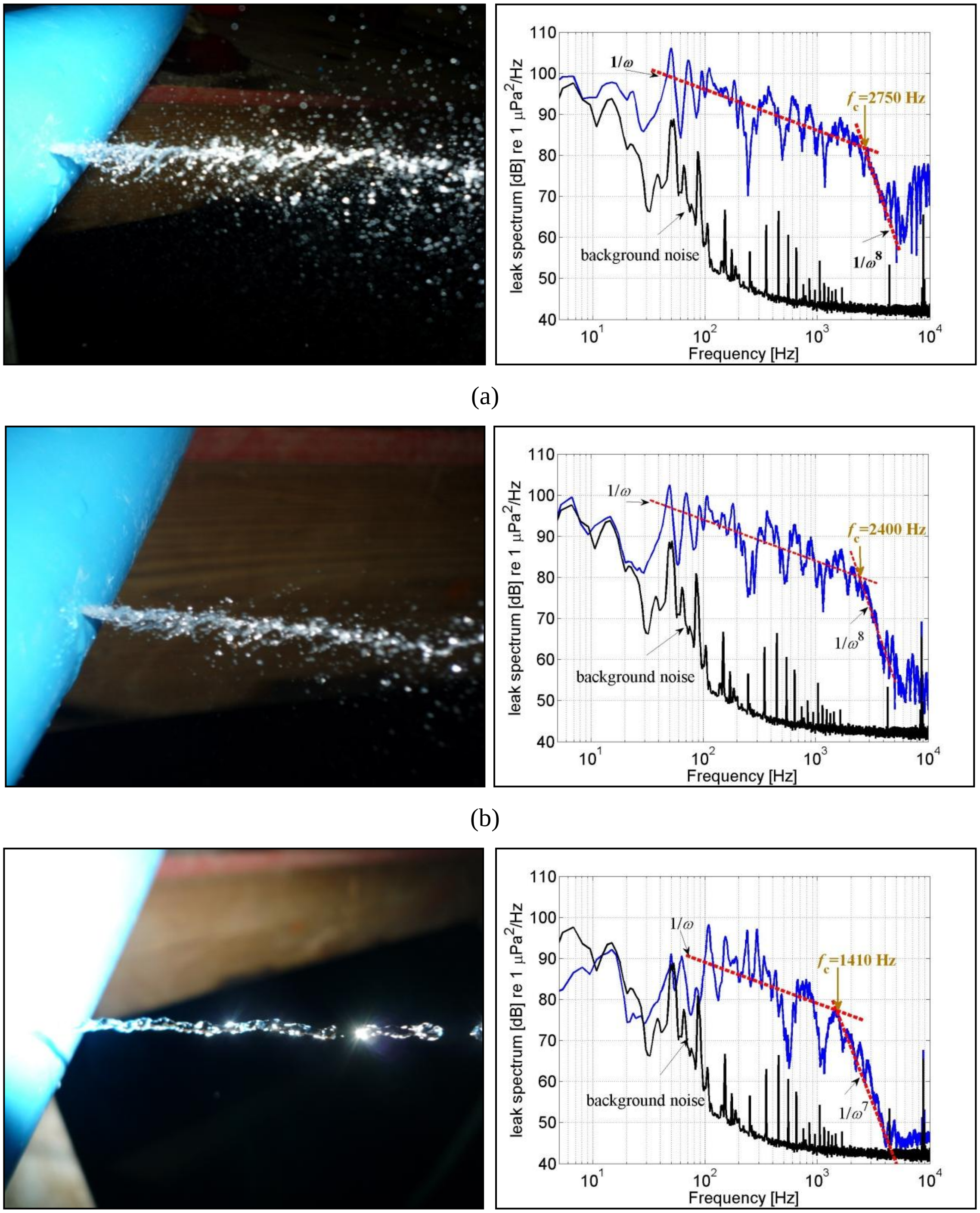

(a)

(b)

(c)

Figure 5.19. Photographs of water leak and the corresponding leak spectrum for the 1.5 mm diameter leak; (a) $V$ =8.5 m/s; (b) $V$ =6.5 m/s; (c) $V$ =2.9 m/s.

## • 2 mm diameter leak size

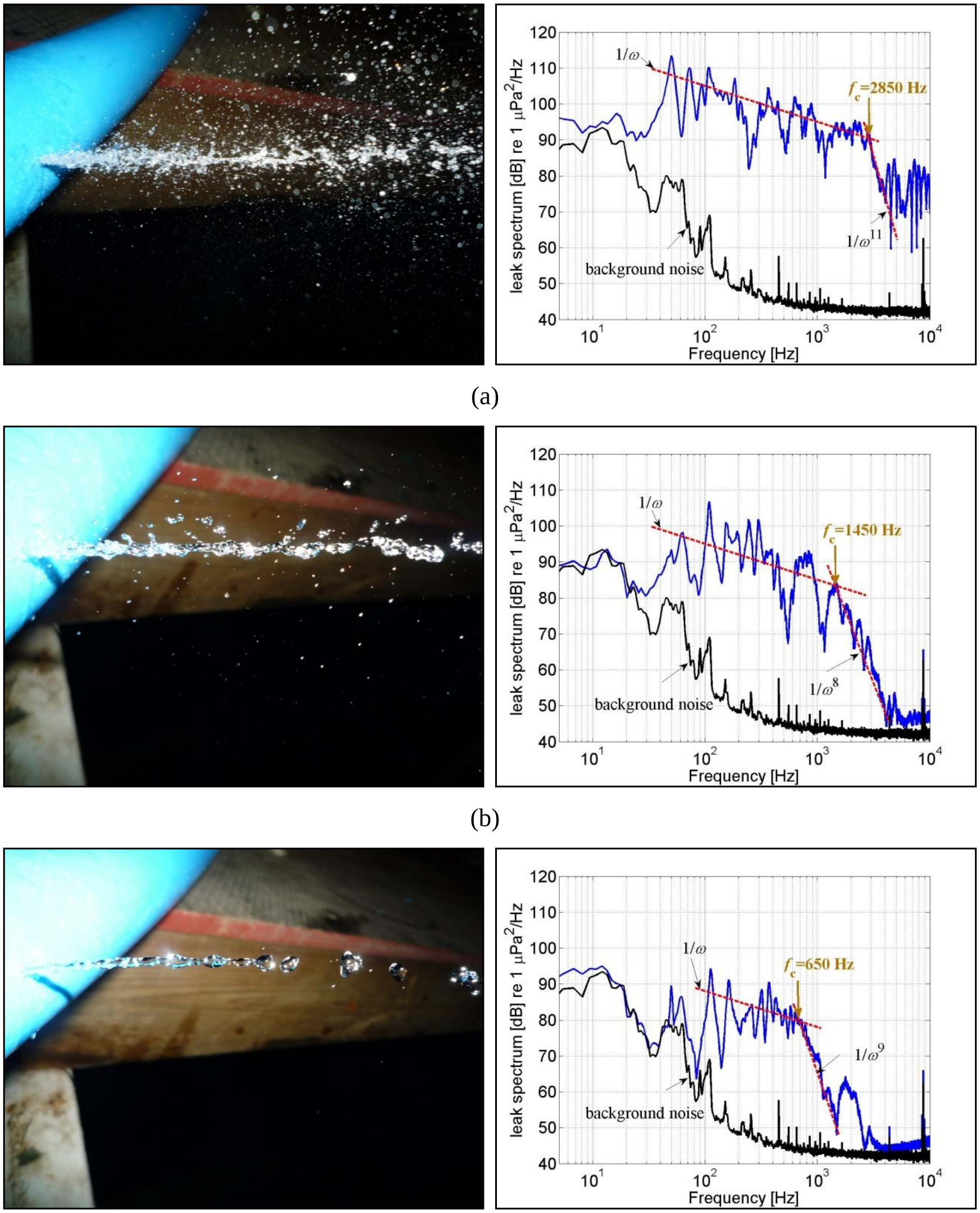

(a)

(b)

(c)

Figure 5.20. Photographs of water leak and the corresponding leak spectrum for the 2 mm diameter leak; (a) $V$ =9 m/s; (b) $V$ =3.5 m/s;(c) $V$ =1.3 m/s.

## • 2.5 mm diameter leak size

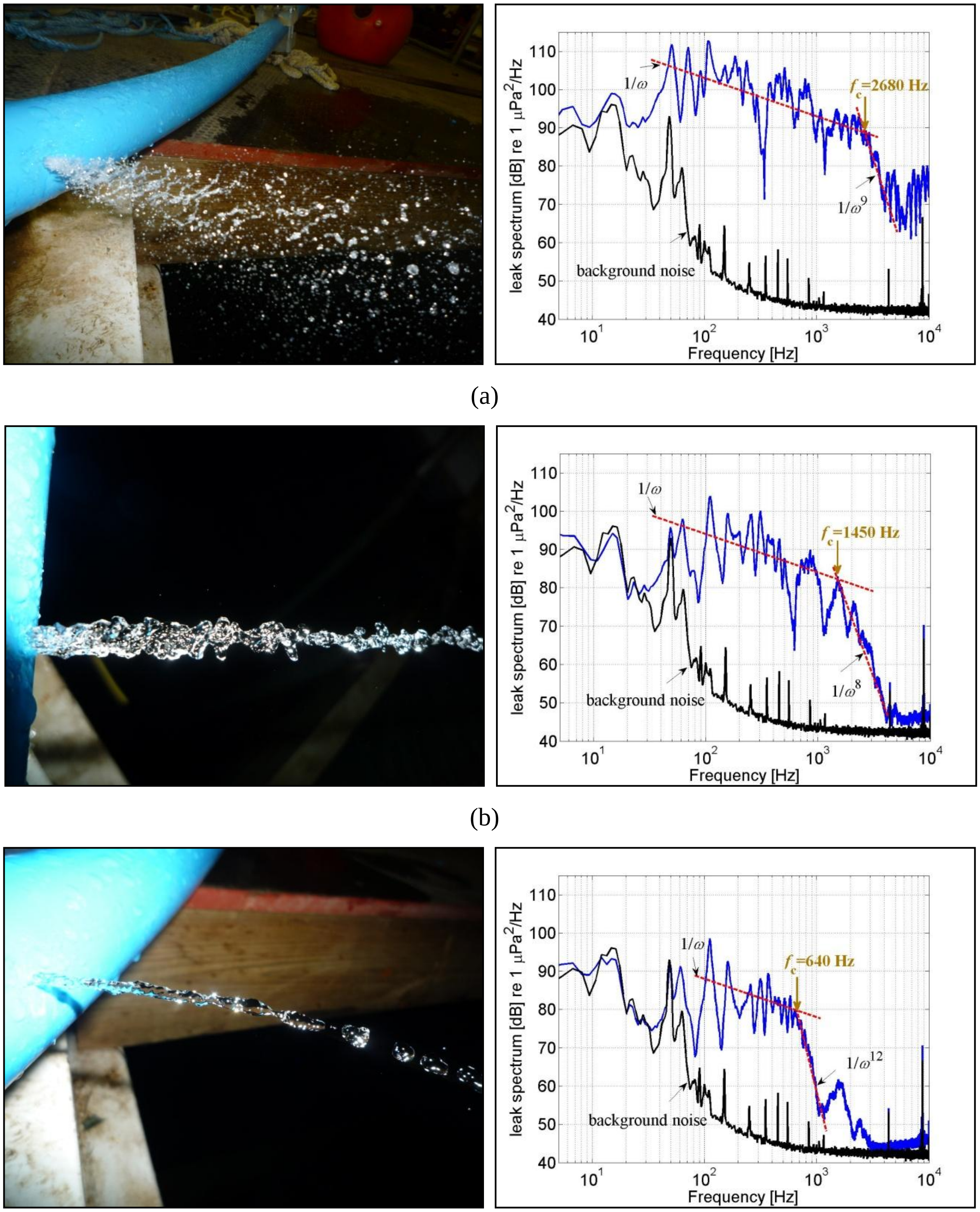

(a)

(b)

(c)

Figure 5.21. Photographs of water leak and the corresponding leak spectrum for the 2.5 mm diameter leak; (a) *V* =7.7 m/s; (b) *V* =3 m/s;(c) *V* =1.4 m/s.

## • 3 mm diameter leak size

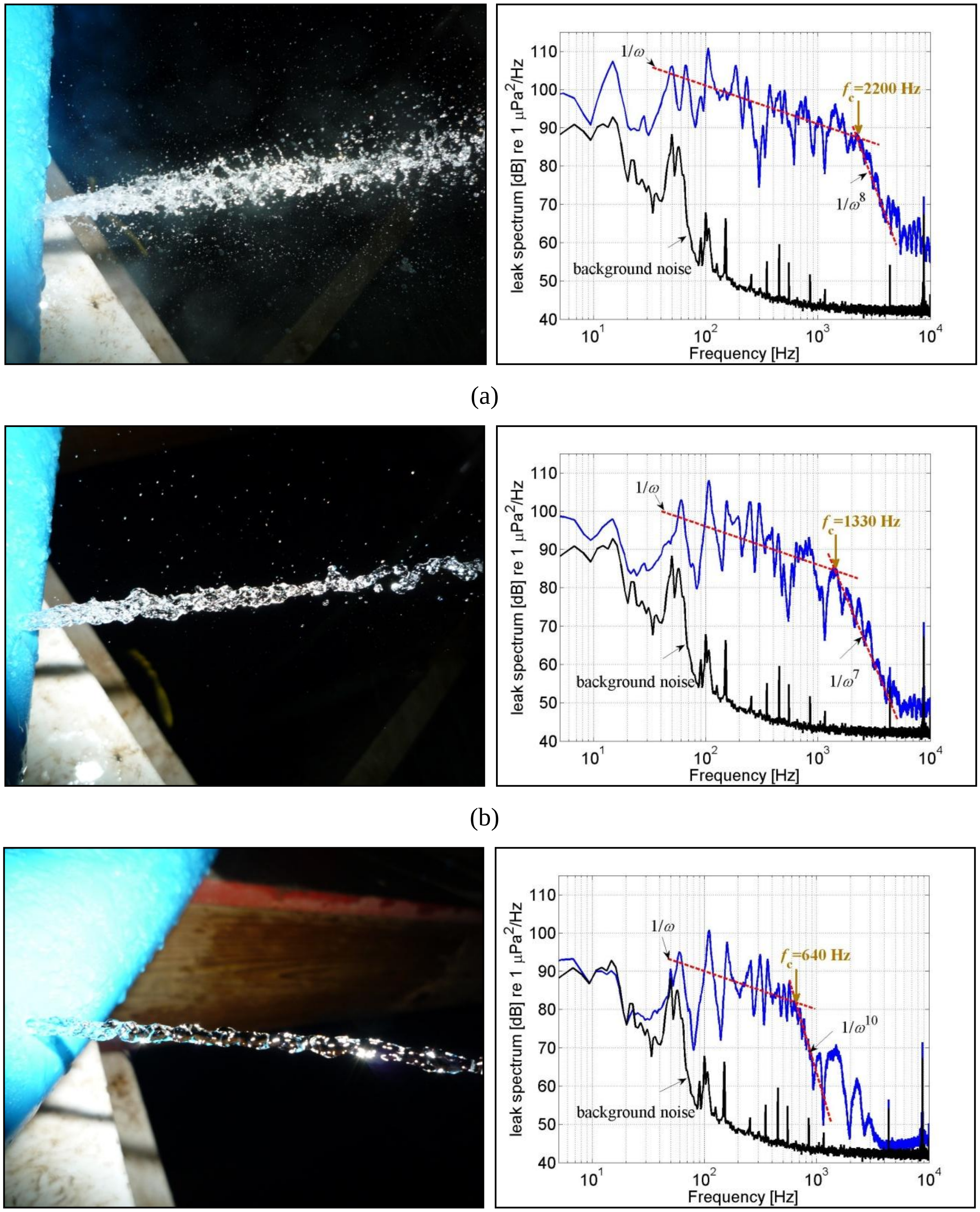

(a)

(b)

(c)

Figure 5.22. Photographs of water leak and the corresponding leak spectrum for the 3 mm diameter leak; (a) $V$ =7.5 m/s; (b) $V$ =3.7 m/s; (c) $V$ =1.6 m/s.

## • 3.5 mm diameter leak size

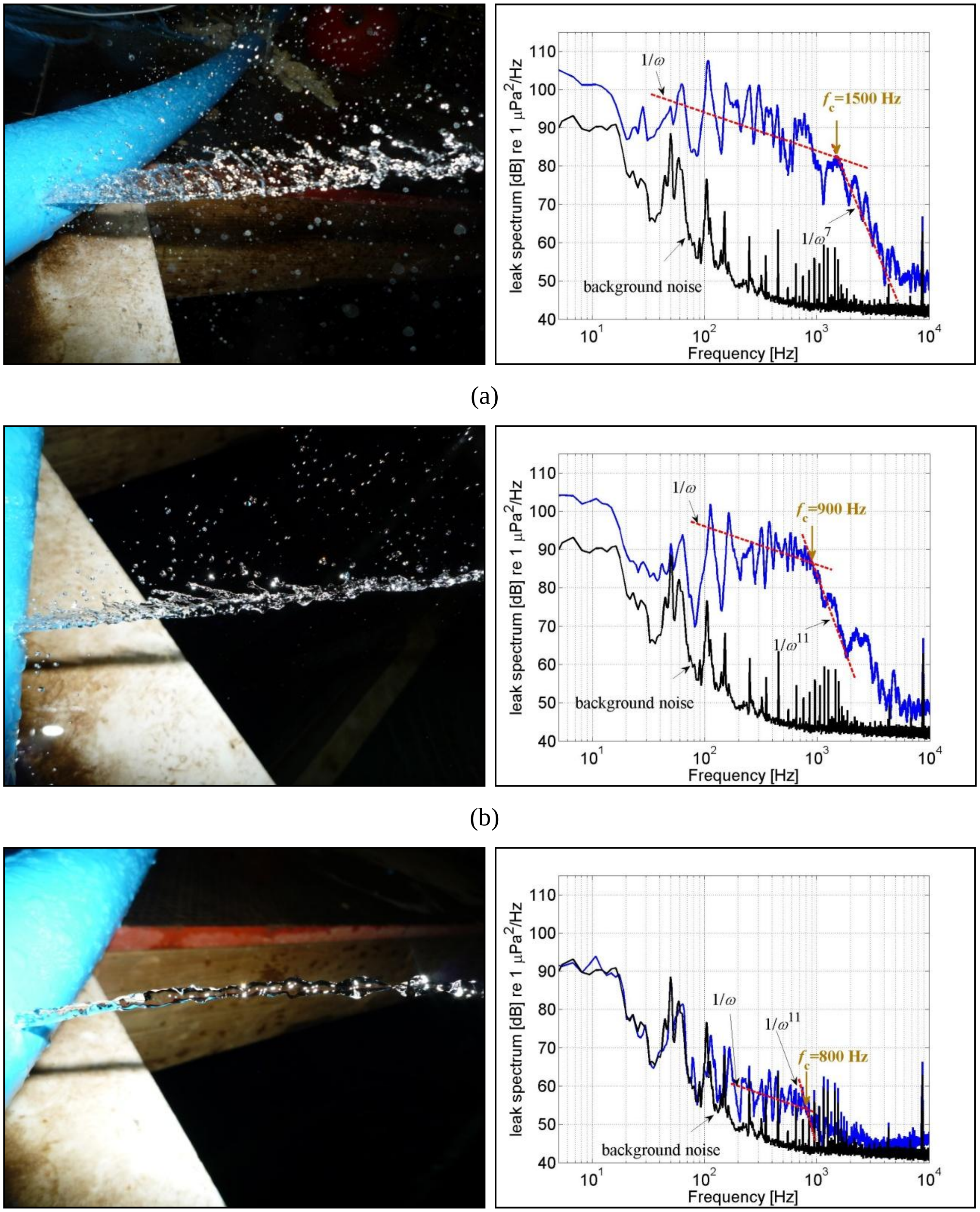

(a)

(b)

(c)

Figure 5.23. Photographs of water leak and the corresponding leak spectrum for the 3.5 mm diameter leak; (a) $V$ =5.5 m/s; (b) $V$ =3.5 m/s; (c) $V$ =1.3 m/s.

## • 4 mm diameter leak size

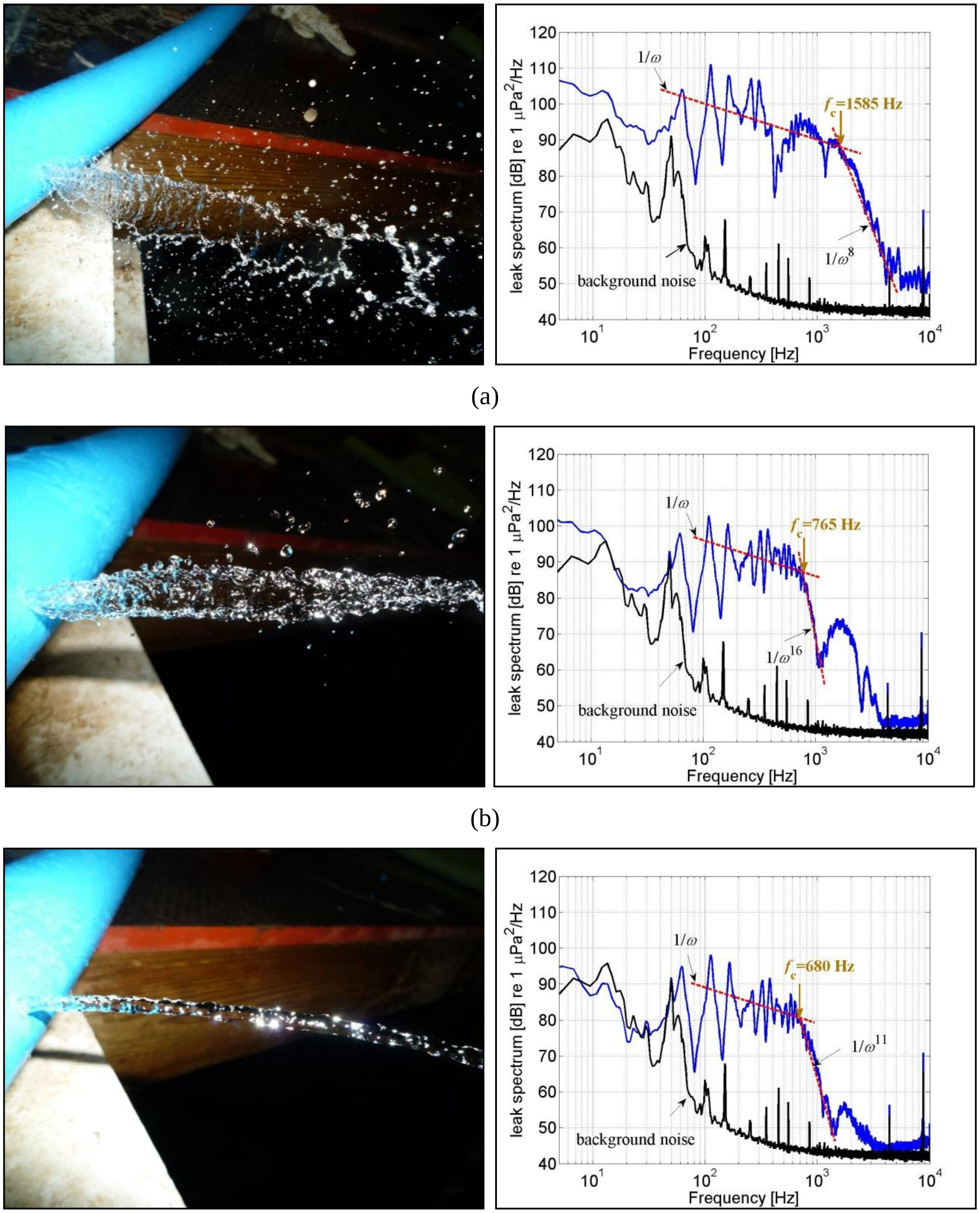

(a)

(b)

(c)

Figure 5.24. Photographs of water leak and the corresponding leak spectrum for the 4 mm diameter leak; (a) $V$ =5 m/s; (b) $V$ =2.5 m/s; (c) $V$ =1.5 m/s.

Figures 5.18 to 5.24 suggest that for all the different velocities and leak sizes the leak noise spectrum decays with a $1/\omega$ frequency power law up to a specific critical frequency $f_c$. Above this critical frequency the decay of the leak spectrum is much higher, following a frequency power law of $1/\omega^n$ where $n$ takes values between 6 and 16. However, for most of the cases, the value of $n$ is approximately equal to 8.

In Figure 5.25 the variation of the critical frequency with flow velocity is presented for each leak size.

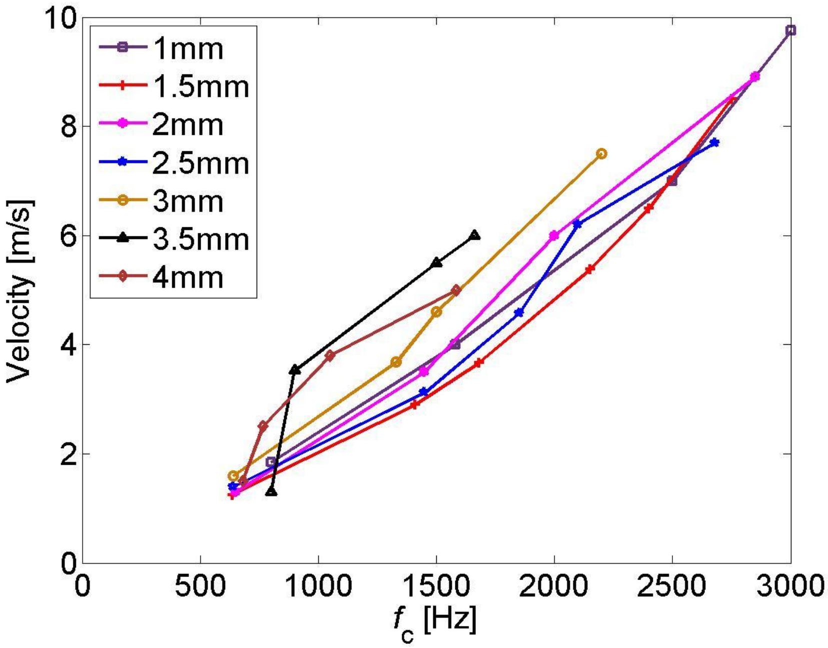

Figure 5.25. Critical frequency variation with flow velocity for the different leaks.

Figure 5.25 suggests that the critical frequency $f_c$ increases almost linearly with velocity for most of the leak sizes with only the 3.5 and 4 mm diameter leaks at low flow velocities diverting from this linear behaviour. This linear behaviour suggests that $f_c$ follows a Strouhal number relationship, whereby $f_c L/V$ is constant, where $L$ is some characteristic length-scale and $V$ is the leak flow velocity.

In Figure 5.26 the critical frequency is re-plotted in terms of the critical Strouhal number, $St_c = f_c L/V$ for all the different cases, where the characteristic length $L$ is chosen to be equal to the leak diameter $d$.

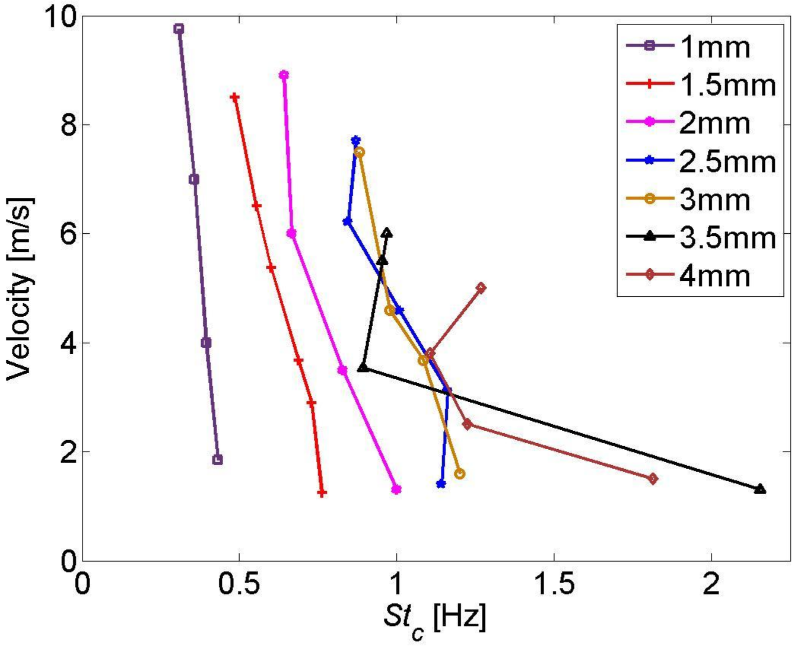

Figure 5.26. Critical Strouhal number variation with flow velocity for the different leaks.

Figure 5.26 shows that the critical Strouhal numbers defined with respect to leak hole diameters are weakly dependent upon velocity apart from the cases of the 3.5 and 4 mm leaks and for the lowest flow velocities, but are strongly dependent upon leak hole diameters. This suggests that the leak hole diameter is the incorrect ‘length-scale’ with which to establish a universal constant Strouhal number for collapsing the critical frequencies obtained at different velocities and leak hole diameters. This is not surprising as the characteristic length–scale must be related to a characteristic dimension of the water jet that is responsible for the generation of the turbulence in the water jet that generates the noise in the pipe. This is most likely to be related to the shear layer thickness of the water jet. This behaviour is investigated qualitatively in Section 5.8.

In Figure 5.27 the variation of Strouhal number $St_c$ with leak diameter is shown. It can be seen that the critical Strouhal number increases with an increase in leak diameter.

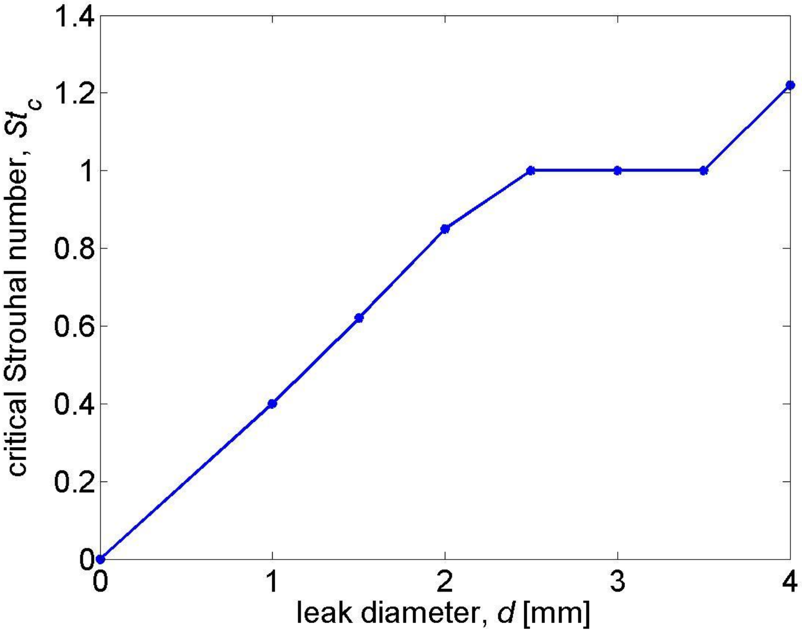

Figure 5.27. Critical Strouhal number variation for increasing leak diameter.

As stated earlier, $St_c$ varies with $d$, so that $d$ is clearly the incorrect length with which to define a universal Strouhal number.

## 5.8 Leak noise variation with continuously decaying velocity

In Section 5.7 the leak noise spectrum was presented for discrete values of velocities, and the variation of the critical frequency Strouhal number at each velocity with leak diameter was investigated. In this section we aim to investigate the overall trend of leak noise energy for a continuously decaying velocity using the procedure described in Chapter 4. Although, above the critical frequency $f_c$ the spectrum level decays with a much higher frequency power law as was seen in Figures 5.18 to 5.24, some appreciable energy still exists before it reaches the level of background noise. The trend of this overall variation of leak noise energy is investigated in this section. Following an identical procedure to the one described in Chapter 4, Section 4.4.8, the leak noise is plotted as a function of flow velocity and frequency for the different leak sizes. A typical example is shown in Figure 5.28 for the 2 mm leak. The maximum frequency shown is 4 kHz because, as was seen in Figures 5.18 to 5.24, most of the leak noise energy is concentrated at frequencies lower than 4 kHz. A high pass filter with cut-off frequency at 50 Hz was applied to the signal to remove the low frequency background noise. The two black dashed lines represent the critical Strouhal number $St_c$ as evaluated in Section 5.7 and shown in Figure 5.27, and the critical Strouhal number $St_g$ which depicts the overall limit below which most of the leak energy concentrates. Although this limit depends on the level of the background noise is used in this case to demonstrate how it varies for the different leak sizes assuming that the background noise does not change significantly.

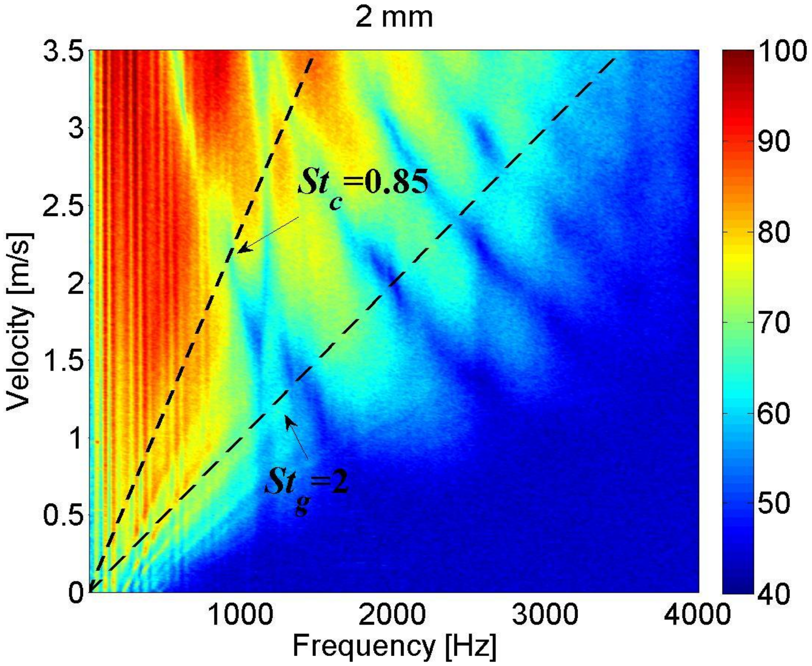

Figure 5.28. Leak noise as a function of flow velocity and frequency for 2 mm diameter leak; Units of colorbar are in dB re 1 μPa$^2$/Hz.

Figure 5.28 suggests that the notion of a critical frequency is a soft limit, shown with the black dashed line $St_g$, above which there remains some pressure fluctuations. This frequency limit is also of the form of a constant Strouhal number $fL/V = \text{const}$ where $L$, as mentioned before, is some characteristic dimension associated with the turbulence generation in the leak hole.

Note also, that instability waves cannot be now seen as clearly as for the case shown in Chapter 4, Section 4.4.9 where the leak was drilled into the clear pipe section. The reason for this is not known at the present time. It is speculated that the appearance of them could be affected by the roughness of the leak hole. A rougher hole will lead to the onset of a turbulent jet much closer to the leak hole than a smooth hole making it more difficult for the instability waves to be discerned.

In Figure 5.29 the leak noise of the 2 mm hole is plotted as a function of Strouhal number $fd/V$, and flow velocity. The two black dashed lines indicate as before the characteristic Strouhal numbers $St_c$ and $St_g$.

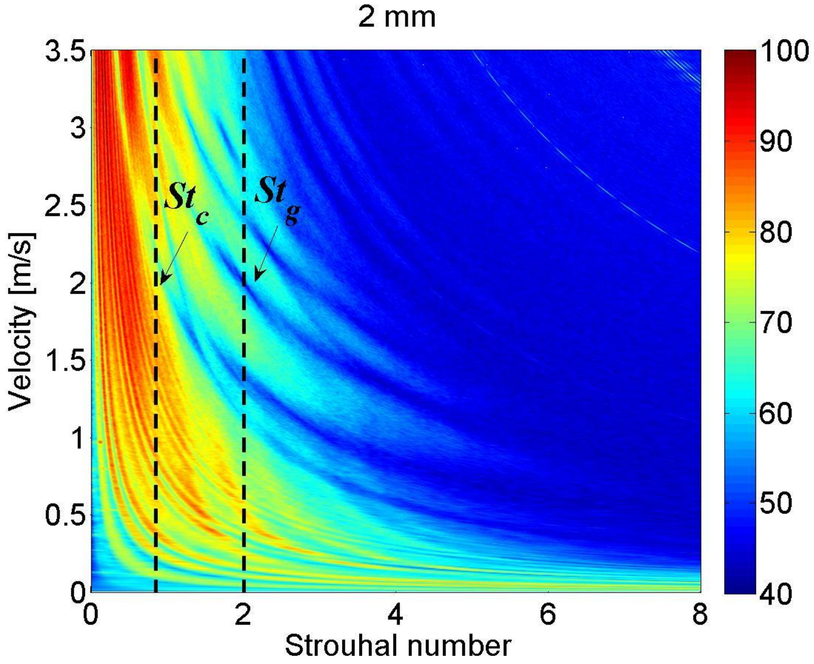

Figure 5.29. Leak noise as a function of flow velocity and Strouhal number for 2 mm diameter leak; Units of colorbar are in dB re 1 μPa$^2$/Hz.

Figure 5.29 suggests that for this leak of 2 mm diameter most of the leak noise energy is concentrated at Strouhal numbers lower than approximately 2 as indicated from the $St_g$ dashed black line. This figure shows again that the Strouhal number is a soft limit since there is appreciable energy at Strouhal numbers greater than 2.

Following a similar as before procedure, leak noise is plotted in Figure 5.30 as a function of flow velocity and frequency for the other leak sizes.

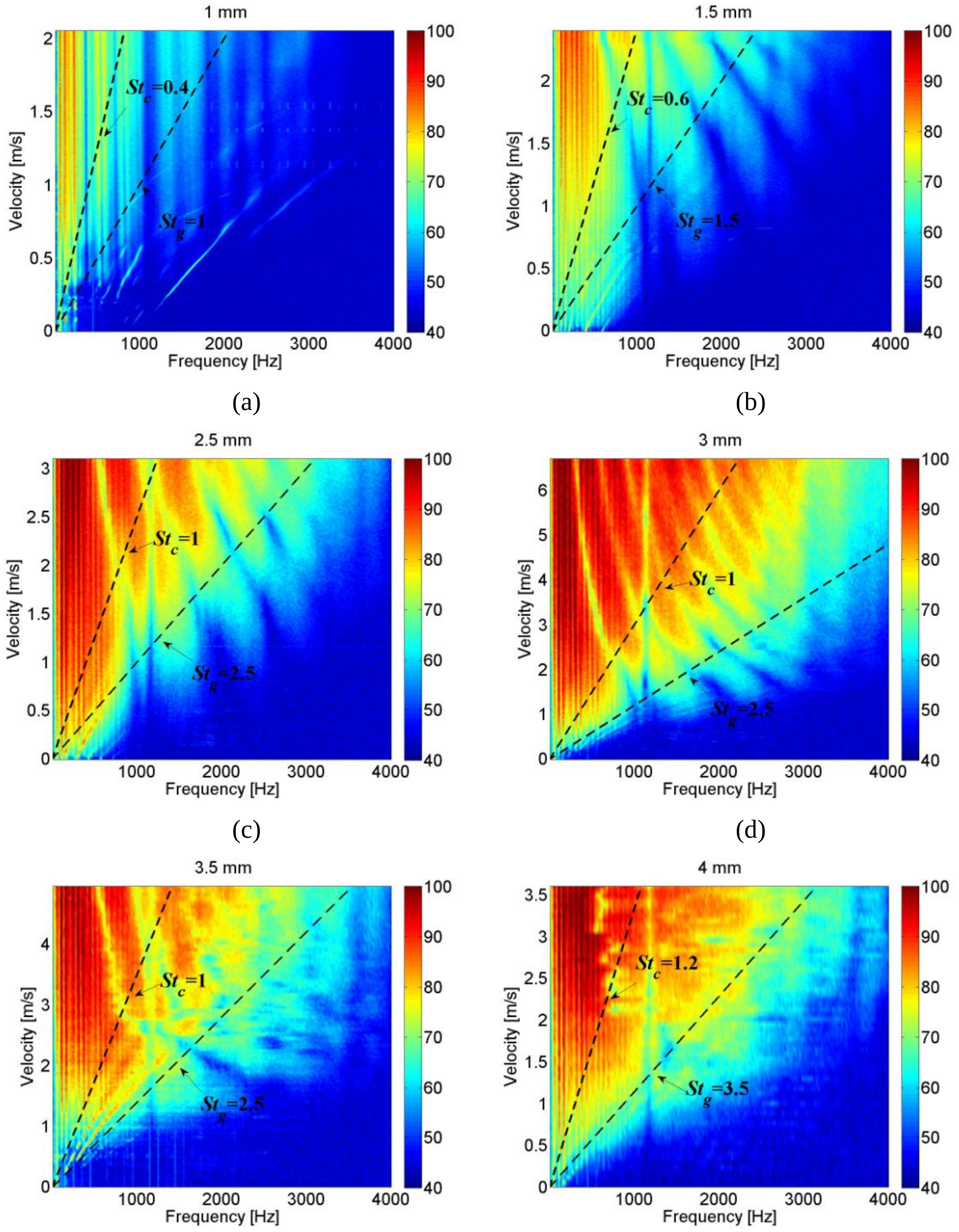

(a) (b)

(c) (d)

(e) (f)

Figure 5.30. Leak noise versus flow velocity and frequency for different leak sizes; (a) 1 mm; (b) 1.5 mm; (c) 2.5 mm; (d) 3 mm; (e) 3.5 mm; (f) 4 mm; Units of colorbar are in dB re 1 μPa$^2$/Hz.

Figure 5.30 suggests that the soft limit, described by $St_g$, below which most of the leak noise energy concentrates varies between 1 and 4 for the different leaks. This is further evidence that there is not a unique Strouhal number that describes the flow fluctuations for all the leak sizes. This will be further investigated in Section 5.9. In Figure 5.31 the variation of Strouhal number $St_g$ for increasing leak diameter is shown.

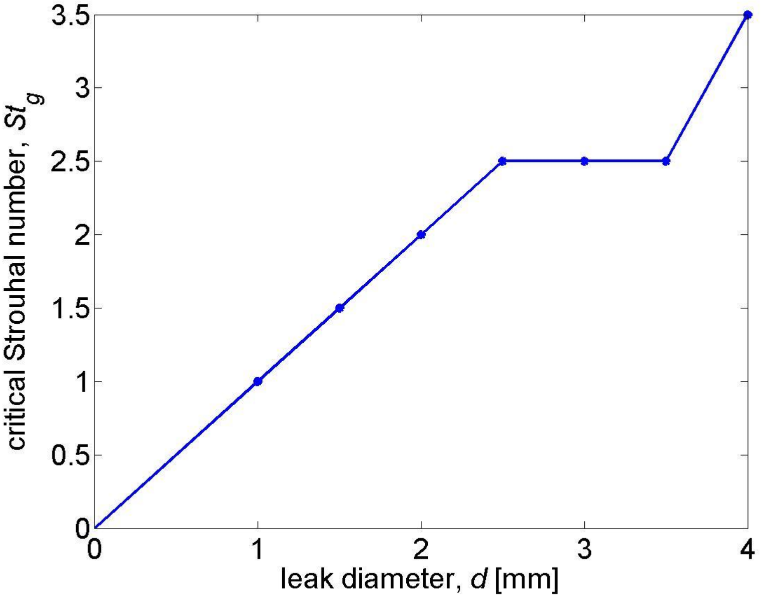

Figure 5.31. Strouhal number $St_g$, variation for increasing leak diameter.

Figures 5.31 and 5.27 suggest that the Strouhal numbers $St_g$ and $St_c$ vary with leak diameter with a very similar way.

## 5.9 Procedure for the estimation of the characteristic length for the evaluation of a leak size-independent Strouhal number

As mentioned in Sections 5.7 and 5.8, and can also be seen in Figures 5.27 and 5.31, the leak flow from all the different leak sizes cannot be described by a unique Strouhal number defined by $St_c = f_c L/V$ with $L$ = $d$ the leak diameter. In order to determine the variation of $L$ with $d$ that gives a $d$-independent Strouhal number, say $St_{c,o}$, we define a non-dimensional scaling factor $F(d)$ on $d$ as,

$$F(d) = L(d)/d \tag{5.14}$$

such that $St_c$ is constant for all $d$ and $V$. Thus,

$$St_{c,o} = f_c(d)L(d)/V = \text{const} \tag{5.15}$$

where $St_{c,o}$ is independent of $d$ and $V$. Substituting $L(d) = F(d)d$ in Eq.(5.15) gives,

$$St_{c,o} = f_c(d)F(d)d/V \tag{5.16}$$

Thus,

$$F(d) = St_{c,o}V/f_c(d)d = St_{c,o}/St_c(d) \tag{5.17}$$

We choose $St_{c,o}$ arbitrarily but with condition that $F(d) < 1$ as must be physically the case, since the turbulence generating region $L$ must be within the water jet and hence $L < d$ and therefore $F(d) < 1$.

The variation of $F(d)$ with $d$ obtained from Eq.(5.17) using $St_c(d)$ from Figure 5.27 is shown in Figure 5.32. A good fit to $F(d)$ for $d < 2.5$ mm is provided by the red dashed line representing the ratio 0.25/$d$ and is plotted for comparison.

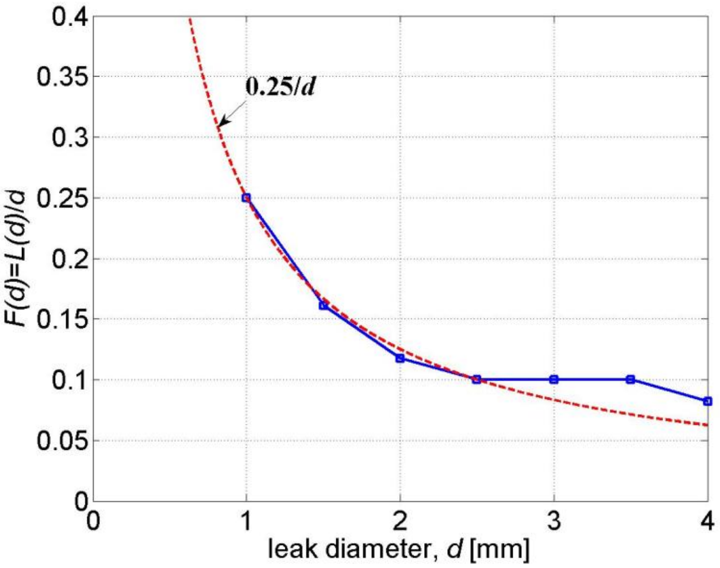

Figure 5.32. Function of leak diameter for the estimation of Strouhal number.

Figure 5.32 shows that $F(d)$ decreases as the leak diameter increases and varies as $d^{-1}$ with some deviations occurring for the case of 3, 3.5 and 4 mm leak sizes. The latter suggests that the characteristic length $L$ does not vary significantly for the different leak sizes. The variation of $L$ with $d$ computed from $F(d)d$, is shown in Figure 5.33.

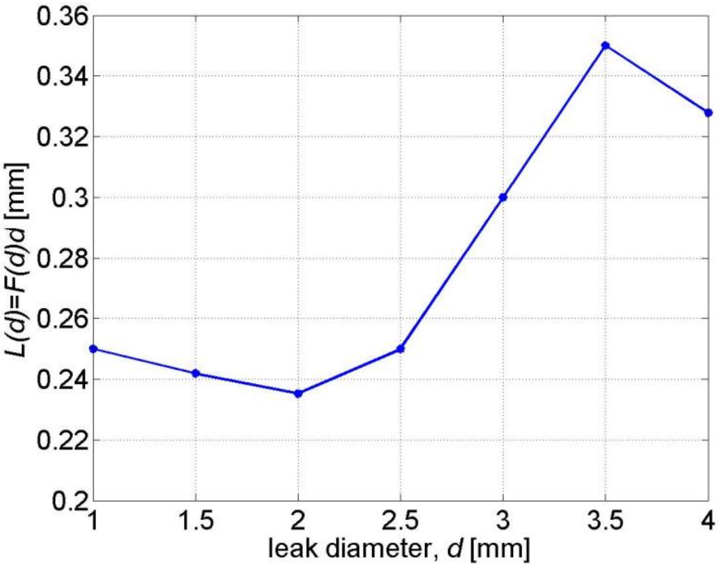

Figure 5.33. Variation of the characteristic length *L* for the different leak sizes.

Figure 5.33 suggests that *L* is very nearly constant and almost independent of the leak diameter. We speculate that the turbulent sources occur in the shear layer of the jet of thickness $\delta$. This implies that the characteristic length *L* is connected with this layer rather than the actual leak diameter. Note that the shear layer is defined as the distance from the surface to the point where viscosity has no effect and the local velocity equals 99% of the free stream velocity [37]. A schematic of the shear layer thickness of a water jet discharging into air is shown in Figure 5.34.

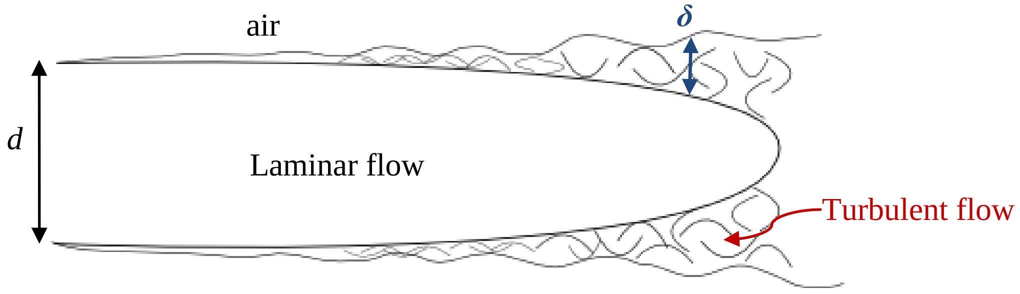

Figure 5.34. Schematic of the shear layer thickness of a water jet discharging into air.

Although the experimental results in our rig showed that the characteristic length *L* and hence $\delta$, is almost independent of the leak diameter *d*, in previous works [47-49] carried out with air jets, it was found that the shear layer thickness is proportional to the jet diameter, thus, $\delta \cong 0.003d$. It is likely that this discrepancy is due to the different flow mechanisms that exist between the water jets and the air jets.

## 5.10 Critical Strouhal number obtained by using the new characteristic length

In this section the results presented in Sections 5.7 and 5.8 are plotted again by using the new characteristic length $F(d)d$, for the estimation of the critical Strouhal number. In Figure 5.35 the critical Strouhal number $St_c$, is plotted for different flow velocities for each different leak size.

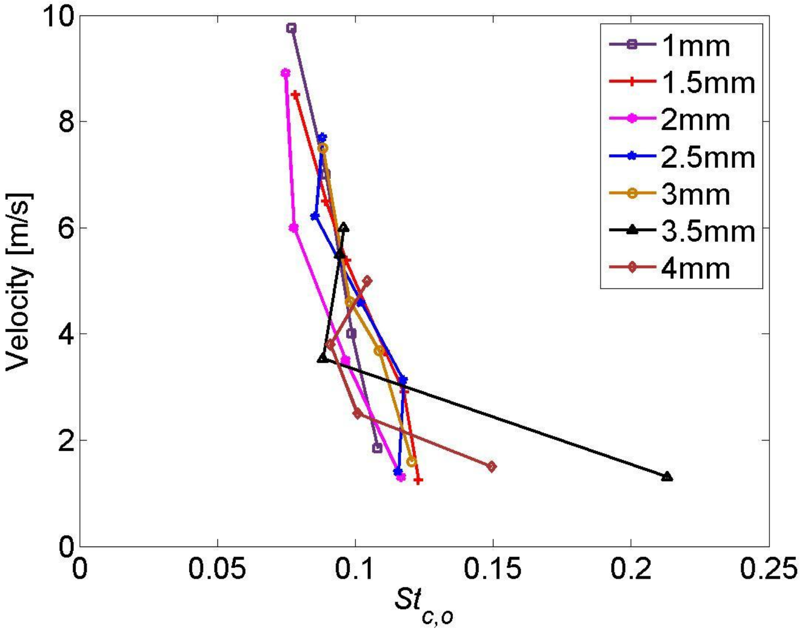

Figure 5.35. Critical Strouhal number variation with flow velocity for the different leaks. The characteristic length is the product of $F(d)d$.

Figure 5.35 suggests that by using the characteristic length defined as in Eq.(5.14) the data are collapse reasonably well around the value of critical Strouhal number $St_{c,o} = 0.1$ although it exhibits a weak variation with velocity. Comparison can be made with Figure 5.27 where the leak diameter is used as the characteristic length.

## 5.11 General shape of leak noise spectrum

Since there is poor SNR below around 50 Hz, we assume that the leak noise spectrum continues to vary as $\omega^{-1}$ as $\omega \to 0$. The results from the 1st rig shown in Chapter 3 confirm this assumption. Thus, the proposed leak noise spectrum will have the form,

$$S_{ll}(\omega) = \begin{cases} \dfrac{\mathrm{A}(V,d)}{\omega} & \omega \leq \omega_c \\ \dfrac{\mathrm{A}(V,d)\omega_c{}^{n-1}}{\omega^n} & \omega_c \leq \omega \leq \infty \end{cases} \tag{5.18}$$

where $\mathrm{A}(V,d)$ is a measure of the leak source strength, which varies with $d$ and $V$ and which has units of squared pressure and

$$\omega_c = 2\pi \frac{St_{c,o}V}{L} = 2\pi \frac{0.1V}{L} \tag{5.19}$$

with $L$ defined by Eq.(5.14). The form of Eq.(5.18) is chosen to ensure continuity at $\omega = \omega_c$. The value of $n$ is between 6 and 16. However, in most of the cases $n$ = 8 as Figures 5.18 to 5.24 suggest. An estimate of $\mathrm{A}(V,d)$ will be presented in Section 5.13.

Note that the leak noise spectrum cannot continue to increase on $\omega^{-1}$ for $\omega \approx 0$ since the overall mean square pressure $\int_0^\infty S_{ll}(\omega)d\omega$, will not be finite.

In Figure 5.36 a schematic of the leak noise spectrum is shown on a log-log scale.

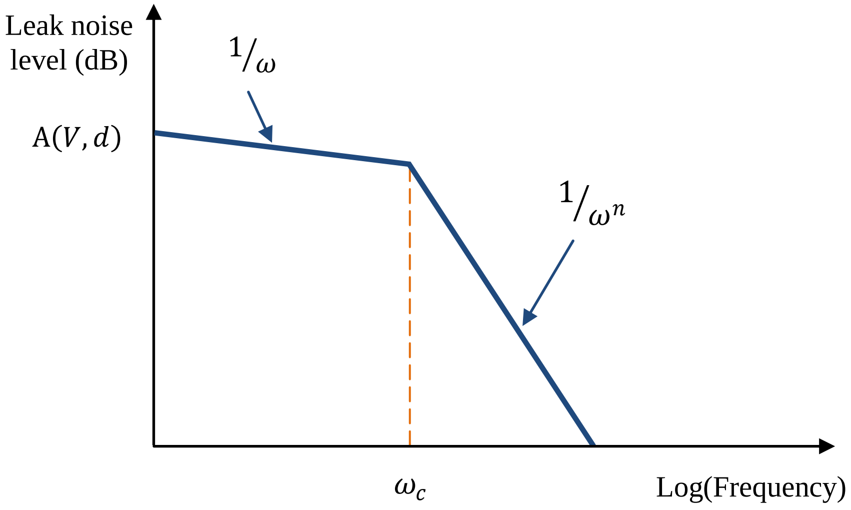

Figure 5.36. Schematic of leak noise spectrum plotted on a log-log scale.

## 5.12 Mean square pressure for different leak sizes and different flow velocities

In this section the relationship between mean square pressure and flow velocity is established for each different leak size as well as the relationship between mean square pressure and leak diameter for different flow velocities. The mean square pressure was calculated in the frequency band between 50 Hz to 4 kHz where the SNR is high. In Figures 5.37 and 5.38 the mean square pressure due to the leak is plotted versus velocity for the 1-3 mm and 3.5-4 mm leaks respectively. The reason for plotting the results in two separate figures is because the 3.5 and 4 mm leaks exhibit a different behaviour. Dashed lines of $V^2$ and $V^8$ that match the trend of the results are also plotted for comparison.

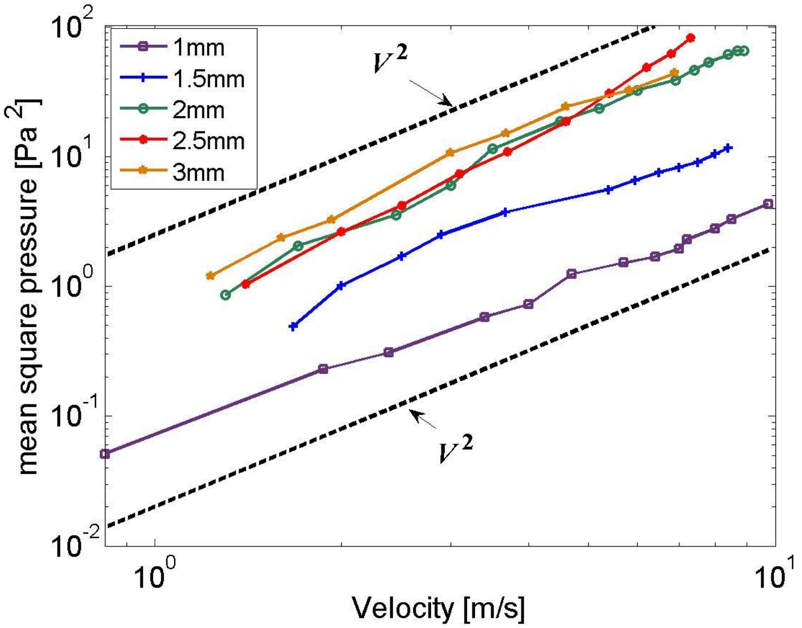

Figure 5.37. Mean square pressure as a function of jet velocity for leaks between 1-3 mm diameter and $V^2$ line.

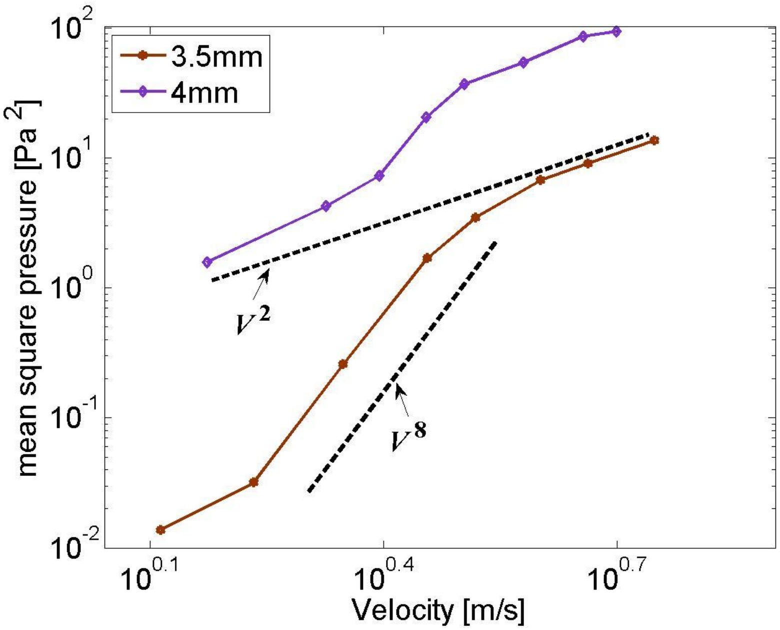

Figure 5.38. Mean square pressure as a function of jet velocity for leaks with 3.5, 4 mm diameter and $V^2$, $V^8$ lines for comparison.

Figure 5.37 suggests that the mean square pressure for the leak sizes between 1 mm and 3 mm has a flow velocity dependency of approximately $V^2$, assuming an integer power law. However, the results for the 3.5 mm and 4 mm shown in Figure 5.38 reveal a much higher flow dependence. The mean square pressure for these leaks does not follow a single power law of velocity but it varies between $V^2$ and $V^8$. The sudden change to a different flow speed power law suggests the onset of a different noise generation mechanism. A velocity power law between 7 and 8 is indicative of the noise generated by free turbulence, as predicted by the classical jet noise theory of Lighthill [38] in which the noise is attributed to volumetric quadrupoles, which are very inefficient at low flow velocities.

In Figure 5.39 the mean square pressure is plotted versus leak size for a number of constant flow velocities. Lines proportional to $d^3$ are also plotted for comparison.

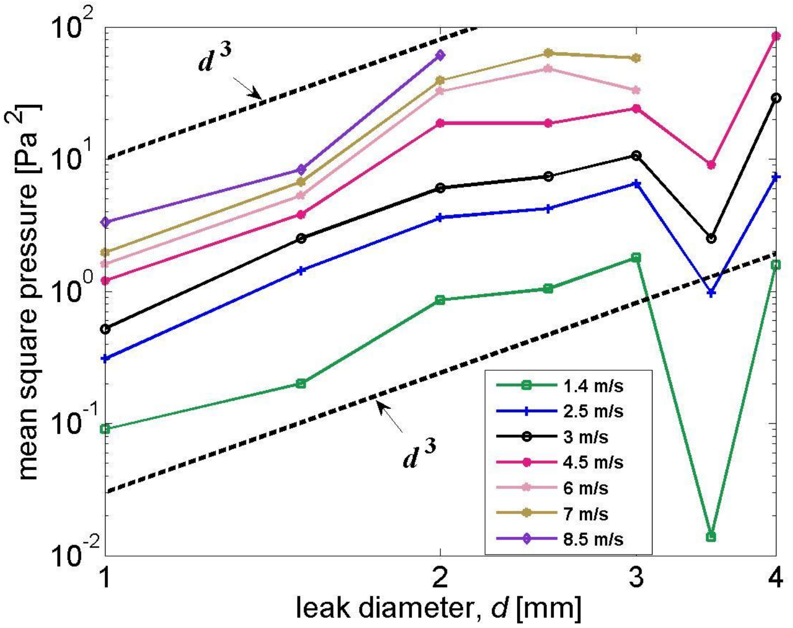

Figure 5.39. Mean square pressure variation with leak size for a number of different constant velocities and $d^3$ line plotted for comparison.

Figure 5.39 suggests that the mean square pressure increases as approximately $d^3$ for all the different flow velocities, apart from the results of the 3.5 mm leak. This indicates that the noise sources connected with the turbulent flow generated in the shear layer of the jet, scale with volume proportional to $d^3$. This suggests that $d$ determines the extent of the turbulent generating region in all 3 dimensions. The drop in noise by nearly 10 dB for the 3.5 mm is in agreement with the results shown in Figure 5.38 where the mean square pressure of the 3.5 leak varies with $V^8$ indicating noise from volumetric quadrupoles which are very inefficient. The reason why the 3.5 mm leak does not follow the same trend as the other leak sizes is not clear at the present time but may be related to the small details of the leak hole caused by non-uniform drilling of the hole.

The proportionality of mean square pressure with $V^2$ and $d^3$ will be used to estimate the leak noise source level A$(V, d)$.

## 5.13 Estimate of the leak noise source level

The results in Sections 5.11 and 5.12 show that $A(V, d)$ can be written in the form,

$$A(V,d) = A_o\left(d/d_{ref}\right)^3\left(V/V_{ref}\right)^2\left(D_{ref}/\mathrm{D}\right)^2 \tag{5.20}$$

where $A_o$ is a constant with dimensions [$\text{Pa}^2$] and is independent of $d$ and $V$, $d_{ref}$ and $D_{ref}$ is a reference leak and pipe diameter taken equal to 1m and $V_{ref}$ is a reference velocity taken equal to 1 m/s. The factor $\left(D_{ref}/\mathrm{D}\right)^2$ has been included to allow for the effect of pipe diameter $D$, since in the plane wave region the mean square pressure equals $\overline{p^2} = W\rho c/\left({}^1\!/_4\,\pi D^2\right)$, where $W$ is the leak sound power and $\rho c$ is the characteristic acoustic impedance. Thus, $A_o$ is given by,

$$A_o = \frac{A(V,d)\left(D/D_{ref}\right)^2}{\left(d/d_{ref}\right)^3\left(V/V_{ref}\right)^2} \tag{5.21}$$

Eq.(5.21) suggests that the leak noise source level $A_o$ may be interpreted as the leak spectrum at unit (radian) frequency, unit leak and pipe diameter and unit velocity.

From above, the leak noise spectrum may be expressed in the form,

$$S_{ll}(\omega) = \begin{cases} \dfrac{A_o}{\omega}\left(\dfrac{d}{d_{ref}}\right)^3\left(\dfrac{V}{V_{ref}}\right)^2\left(\dfrac{D_{ref}}{D}\right)^2 & \omega \le \omega_c \\ \dfrac{A_o {\omega_c}^{n-1}}{\omega^n}\left(\dfrac{d}{d_{ref}}\right)^3\left(\dfrac{V}{V_{ref}}\right)^2\left(\dfrac{D_{ref}}{D}\right)^2 & \omega_c \le \omega \le \infty \end{cases} \tag{5.22}$$

where $\omega_c$ defined by Eq.(5.19) and $A_o$ may be deduced from,

$$A_o = \frac{S_{ll}(\omega)\omega\left(D/D_{ref}\right)^2}{\left(d/d_{ref}\right)^3\left(V/V_{ref}\right)^2} \tag{5.23}$$

for $\omega \le \omega_c$.

In Figure 5.40, $A_o$ calculated from Eq.(5.23) is plotted for four representative leak diameters. A value of $A_o$ that provides a good estimate of the source level in the 40 mm diameter pipe averaged over frequency is,

$$A_o = 10^4\ \text{Pa}^2 \tag{5.24}$$

as shown in Figure 5.40 as a straight dashed line.

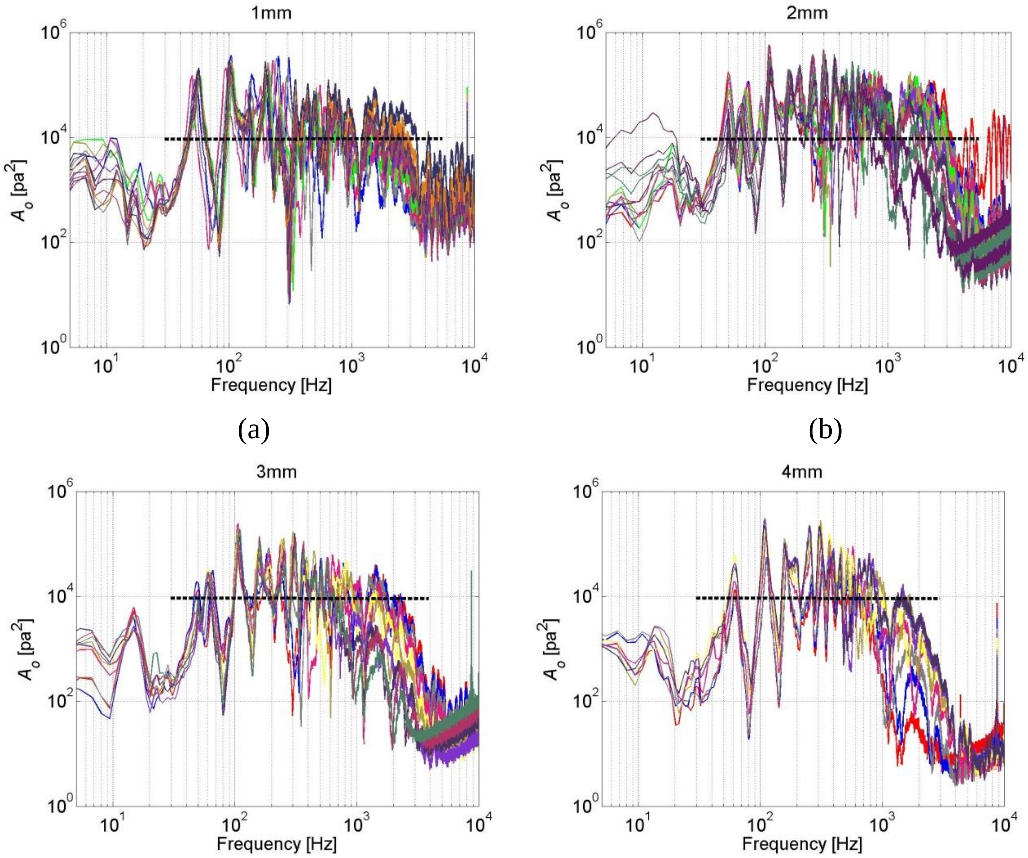

(a) (b)

(c) (d)

Figure 5.40. Constant $A_o$ for different leak sizes; (a) 1 mm; (b) 2 mm; (c) 3 mm; (d) 4 mm.

It is useful for practical purposes to express the leak noise spectrum in dB (re 1 μPa$^2$/Hz.). Thus, for $\omega \leq \omega_c$,

$$SPL_{ll} = 160 - 10\log_{10}(\omega) + 30\log_{10}(d/d_{\text{ref}}) + 20\log_{10}(V/V_{\text{ref}}) - 20\log_{10}(D/D_{\text{ref}}) \tag{5.25}$$

where, $160 = 10\log_{10}(10^4) + 120$ is the contribution of the logarithm of $A_o$ and the reference pressure.

## 5.14 Normalized leak spectrum versus Strouhal number

In this section, we use Eq.(5.22) to collapse and normalize the data for all the different leak sizes and flow velocities around the value of 1. In Figure 5.41 the leak spectrum normalized on $V^2$, $d^3$, $D^2$ and $A_o$ is plotted versus Strouhal number for all the leak sizes. The critical Strouhal number $St_{c,o}$ is also indicated.

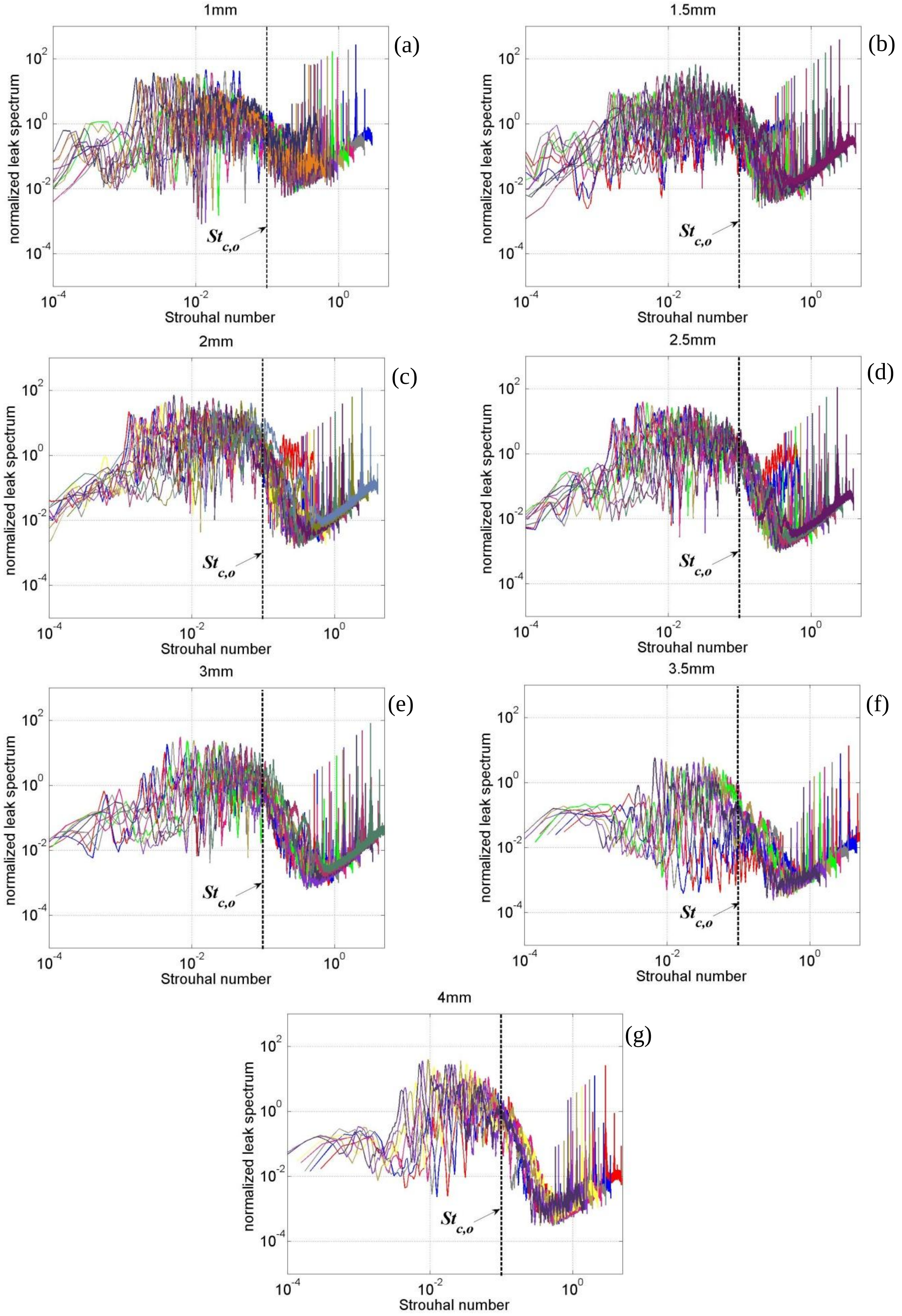

Figure 5.41. Leak spectrum normalized on $V^2$, $d^3$, $D^2$ and $A_o$ versus Strouhal number for the different leak sizes (a) 1 mm; (b) 1.5 mm; (c) 2 mm; (d) 2.5 mm; (e) 3 mm; (f) 3.5 mm; (g) 4 mm.

Figure 5.41 suggests that normalizing the pressure spectrum on $V^2$, $d^3$, $D^2$ and $A_o$ provides a reasonable collapse of data for all the different leaks, apart from the 3.5 mm leak, which as mentioned before shows behaviour that is relatively inconsistent with the other leak holes. Although the pipe resonances have a strong effect on the appearance of leak spectrum the general trend can be clearly seen.

## 5.15 Additional analysis of the results from the preliminary experimental rig

In this section an analysis of the results obtained from the preliminary test rig presented in Chapter 3 is made to investigate the characteristics in the leak spectrum common to both the first and the final rig. The preliminary experimental rig indicated two critical frequencies that characterize the shape of the PSD of the measured acoustic pressure signals. Their variation with flow velocity is initially examined. Finally, the empirical model for the leak noise spectrum that was developed in this chapter is applied to these results to investigate its level of agreement.

### 5.15.1 Critical frequencies and Strouhal number versus flow velocity

It was seen in Chapter 3 that for the preliminary rig two critical frequencies $f_{c1}$ and $f_{c2}$ characterize the shape of the PSD of the measured acoustic pressure signal. In Figure 5.42, $f_{c1}$ and $f_{c2}$ are plotted as a function of flow velocity for each leak size.

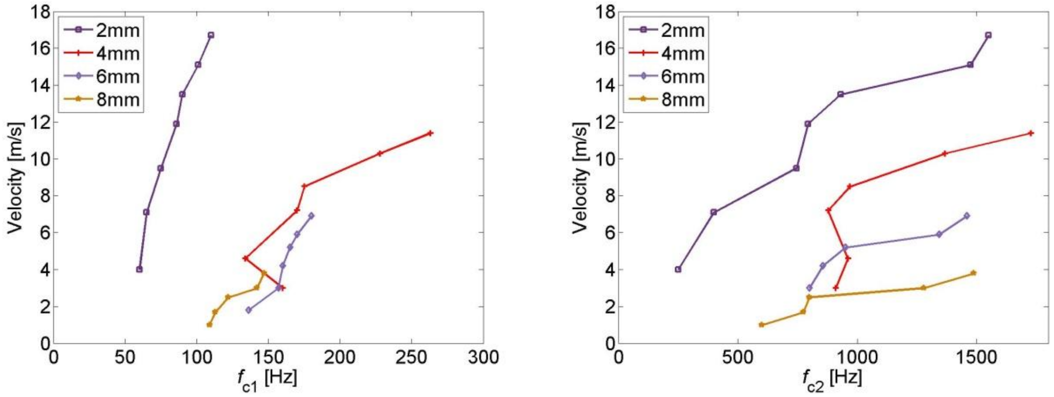

(a) (b)

Figure 5.42. Critical frequency variation with flow velocity; (a) First critical frequency, $f_{c1}$; (b) Second critical frequency $f_{c2}$.

Figure 5.42 suggests that the critical frequencies $f_{c1}$ and $f_{c2}$ increase almost linearly with velocity for all the leak sizes apart from the 4 mm leak hole for low flow velocities. This linear behaviour suggests a Strouhal number relationship as deduced from the data obtained in the final rig.

In Figure 5.43 the critical frequencies $f_{c1}$ and $f_{c2}$ are re-plotted in terms of the corresponding critical Strouhal number $St_{c1} = f_{c1}d/V$ and $St_{c2} = f_{c2}d/V$ where $d$ is the leak hole diameter.

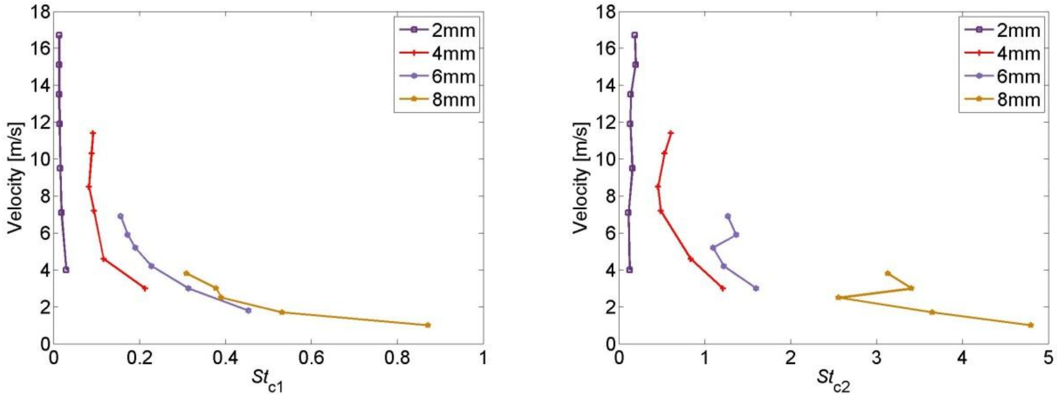

(a) (b)

Figure 5.43. Critical Strouhal number variation with flow velocity; (a) First critical Strouhal number $St_{c1}$; (b) Second critical Strouhal number $St_{c2}$.

Figure 5.43 suggests that the critical Strouhal numbers $St_{c1}$ and $St_{c2}$ defined with respect to leak hole diameters are weakly dependent upon velocity for all the different leaks apart from the 8 mm leak. The reason for this deviation for the 8 mm leak is not known at the present time. However, there is a significant dependency of $St_{c1}$ and $St_{c2}$ with leak diameter. This variation of the critical frequencies of the noise signals with $V$ and $d$ obtained from the preliminary rig are in satisfactory agreement with those obtained from the final rig showing that the critical frequencies increase with an increase in the flow velocity for a constant leak hole diameter and that the leak hole diameter is not the appropriate length-scale to establish a universal critical Strouhal number. However, the actual values of the Strouhal numbers for the 2 and 4 mm leaks obtained from the two different rigs do not match. For example, for the 2 mm leak $St_{c1} = 0.01$ and $St_{c2} = 0.15$ as Figure 5.43 suggests whereas the critical Strouhal number obtained from the final rig is close to 0.7 (Figure 5.26). This discrepancy could be due to different flow mechanisms existing in the preliminary rig.

### 5.15.2 Application of the empirical model of leak noise spectrum on the results from the preliminary test rig

In this section the empirical model for the leak noise spectrum (Eqs. (523)-(5.25)) is applied to the results obtained from the preliminary test rig for all the different leak sizes and flow velocities. Although as it was seen in Section 5.15.1 the critical frequencies of the PSD of the noise signals from the two rigs do not match, it is interesting to see how the model applies on the results from the preliminary rig which is a completely different rig. In Figure 5.44 the leak spectrum of the noise signals from the preliminary rig normalized on $V^2$, $d^3$, $D^2$ and $A_o$ is plotted versus Strouhal number for all the leak sizes and flow velocities. The horizontal black dashed lines that are drawn indicate the shape that the normalized leak spectrum should have (1 until $St_c = 0.1$ and decay with a higher frequency rate for $St_c > 0.1$).

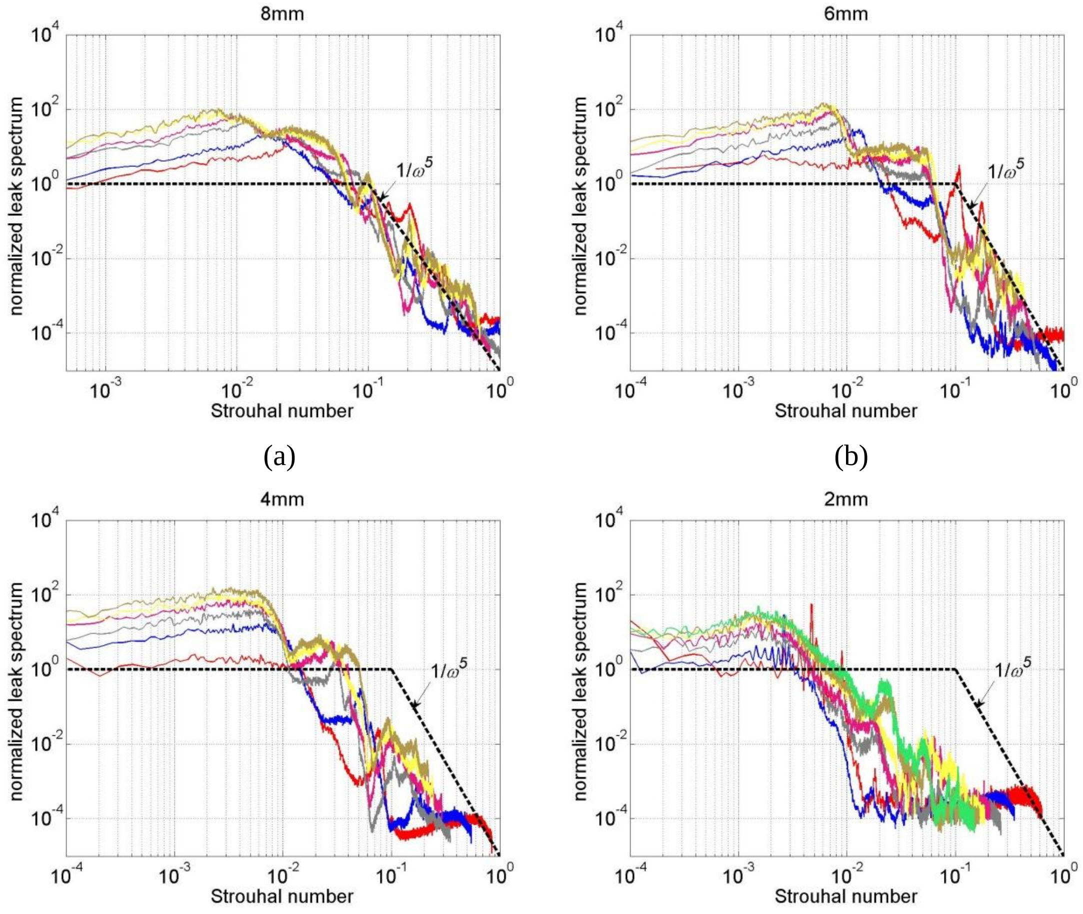

(a) (b)

(c) (d)

Figure 5.44. Normalized leak spectrum versus Strouhal number for the different leak sizes; (a) 8 mm; (b) 6 mm; (c) 4 mm; (d) 2 mm.

Figure 5.44 suggests that the leak spectral model, calculated from Eq.(5.22) and shown with the black dashed lines, provides an under prediction of 10 to 20 dB when compared with the level of the normalized leak spectrum. Furthermore, the spectrum starts to decay for Strouhal numbers smaller than 0.1 for all the leak sizes apart from the 8 mm leak. Overall, the empirical model that was developed does not give a perfect match to the results from the preliminary experimental rig but gives a rough estimate of the level of leak noise spectrum. We should note that the two rigs are completely different, for example in the first rig the leak hole was on the end of the pipe whereas in the final rig was on the side, and it is possible that different flow mechanisms exist in each rig and hence the noise spectra are different.

# 5.17 Discussion

The aim of this rig was to derive information about the leak noise spectrum and how it is affected by leak size and water flow velocity. The clear plastic section in the previous rig that was responsible for the broad peak in the frequency range of 750 Hz was now removed and the leak was drilled directly to the MDPE pipe. Good coherence between the signals was achieved in the frequency range between 50 Hz to 4 kHz. At lower frequencies the background noise was too high and no information about the shape of leak spectrum was possible. Thus, in this low frequency range, it was assumed that the leak noise spectrum continues to vary with the same frequency power law $\omega^{-1}$.

A procedure for estimating the leak noise spectrum was developed by inverting the pipe response using a theoretical model for calculating the cross-spectrum of two signals in a finite-length pipe [44]. Uncertainty about the pipes loss factor was shown not to affect the results because in the specific rig the hydrophones were placed close to the leak to prevent any significant attenuation of the signals before they reached the hydrophones.

The noise measurements showed that the leak noise spectrum decays with a frequency power law of $\omega^{-1}$ until a specific critical frequency $\omega_c$. Above this frequency it decays with a higher power law of $\omega^{-n}$ where $n$ takes values between 6 and 16 with $n = 8$ seen most common. Although strong resonances were apparent in the results due to the finite pipe length, this general trend of the leak noise spectrum was clearly revealed.

Plotting the critical frequency $f_c$ versus flow velocity for all the different leaks revealed a linear relationship between them suggesting a Strouhal number dependency. However, the critical Strouhal number expressed as $St_c = f_c L/V$ with $L$ equal to pipe diameter did not collapse the results to a unique critical Strouhal number (Figure 5.27). This was evidence that the characteristic length $L$ taken equal to the leak diameter was not correct and $L$ should be a function of the leak diameter $F(d)$ instead of the leak diameter itself. An expression of $F(d)$ was determined based on the physical assumption that it should be smaller than 1. It was speculated that this characteristic length $L$ could be connected with the shear layer thickness $\delta$ where the turbulent sources occur. This new definition of $L$ gave good collapse of data and the critical frequency $f_c$ was expressed by a unique critical Strouhal number $St_{c,o} = 0.1$. The proposed model of the leak noise spectra was expressed in terms of the new characteristic dimension $L$, flow velocity *V* and leak noise source level $A(V, d)$.

Plotting the mean square pressure as a function of flow velocity for the different leaks and as a function of leak diameter for different velocities revealed a $V^2$ and $d^3$ dependency. Using this information an estimate of the leak noise source level $A(V, d)$ was found and a complete model that describes the leak noise spectrum in terms of leak and pipe diameter *d*, *D* and flow velocity *V* was predicted. The model came in agreement with the data from the preliminary rig of between 10 and 20 dB.

# 5.18 Conclusions

This final rig gave us information for the leak noise spectrum and how is affected by leak size and flow velocity. Although high resonances were apparent in the spectrum due to the finite length of the pipe the general trend was clear. Results showed that until a critical frequency $f_c = 0.1V/L$ the spectrum decays with a frequency power law of $\omega^{-1}$ followed by a sharper drop of $\omega^{-n}$ with $n$ ≈8 seen most common. An estimate of the leak noise source level was determined and an empirical model that describes the leak noise spectrum in terms of $d$, *D* and *V* was established.

# CHAPTER 6

# TIME DELAY ESTIMATION USING MATCHED FIELD PROCESSING

## 6.1 Introduction

In this chapter, a form of matched field processing (MFP) that is widely used for source localization in underwater acoustics is described and is applied to the leak detection problem. This processor involves correlating the measurements of the acoustic pressure with a model of the signal due to an assumed leak position in the frequency domain. This is in contrast to the common correlation technique that correlates sensor signals in the time domain. The main advantage of this processor, over the correlation techniques commonly used for leak detection, is that it allows the use of more than two sensors which can lead to a sharper peak and a better estimation of the leak position.

It is shown in this chapter that the conventional form of the MFP (Bartlett processor) gives reasonable results only in the case of equidistant sensors and not for the general case of unequal sensor distances. The reason why this happens is explained. An alternative form of Bartlett processor, (ABP), is therefore proposed and compared to the Basic Cross Correlator (BCC) that is widely used in leak detection problems and also to the Phase Transform processor (PHAT) that has found to give a much sharper peak at the leak location. The effect of background noise and the frequency bandwidth on the proposed correlator is also investigated. Finally, the proposed form of MFP is applied to experimental data obtained from the test rig presented in Chapter 5. It is shown that the new processor gives better performance than the BCC and comparable performance to the PHAT correlator. However, specific advantages of this processor make it more useful in practical situations, as it will be discussed below.

## 6.2 General description of the linear, Bartlett processor

The linear MFP, also referred to as the Bartlett or conventional processor, is the most widely used matched field processor for source detection in underwater acoustics [50]. This processor directly correlates the vector of measured data $\mathbf{p_m}$,

$$\mathbf{p_m}(\omega) = [p_1(\omega), p_2(\omega), \dots, p_N(\omega)]^{\mathrm{T}} \tag{6.1}$$

where $p_i(\omega)$ is the Fourier transform of the pressure measurement at the $i$ sensor, with the vector of modelled data $\widehat{\mathbf{p}}_{\mathrm{m}}$,

$$\widehat{\mathbf{p}}_{\mathrm{m}}(\omega, \mathbf{d}) = [\hat{p}_1(\omega, \mathbf{d}), \hat{p}_2(\omega, \mathbf{d}), \dots, \hat{p}_N(\omega, \mathbf{d})]^{\mathrm{T}} \tag{6.2}$$

in the frequency domain, where $N$ is the number of sensors that are used which as mentioned before, can be greater than two, and $\mathbf{d}$ is the vector of assumed, trial distances of each sensor from the leak position $d_1, d_2, \dots, d_N$ given by,

$$\mathbf{d}^{\mathrm{T}} = [d_1, d_2, \dots, d_N] \tag{6.3}$$

Note that in the final form of Bartlett processor, $\mathbf{p_m}$ and $\widehat{\mathbf{p}}_{\mathrm{m}}$ are normalized as $\|\mathbf{p}\| = 1$ and $\|\widehat{\mathbf{p}}\| = 1$ where $\| \quad \|$ is the norm of the vector and $\mathbf{p}$ and $\widehat{\mathbf{p}}$ are given by,

$$\mathbf{p}(\omega) = \frac{\mathbf{p_m}(\omega)}{\|\mathbf{p_m}(\omega)\|} = \frac{[p_1(\omega), p_2(\omega), \dots, p_N(\omega)]^{\mathrm{T}}}{\sqrt{|p_1(\omega)|^2 + |p_2(\omega)|^2 + \cdots + |p_N(\omega)|^2}} \tag{6.4}$$

and

$$\widehat{\mathbf{p}}(\omega, \mathbf{d}) = \frac{\widehat{\mathbf{p}}_{\mathrm{m}}(\omega, \mathbf{d})}{\|\widehat{\mathbf{p}}_{\mathrm{m}}(\omega, \mathbf{d})\|} = \frac{[\hat{p}_1(\omega, \mathbf{d}), \hat{p}_2(\omega, \mathbf{d}), \dots, \hat{p}_N(\omega, \mathbf{d})]^{\mathrm{T}}}{\sqrt{|\hat{p}_1(\omega, \mathbf{d})|^2 + |\hat{p}_2(\omega, \mathbf{d})|^2 + \cdots + |\hat{p}_N(\omega, \mathbf{d})|^2}} \tag{6.5}$$

The elements $p_1(\omega), p_2(\omega), \dots, p_N(\omega)$ of $\mathbf{p}$ are Fourier transforms of the pressure measurements $p_1(t), p_2(t), \dots, p_N(t)$ according to,

$$p(\omega) = \int_{-T/2}^{T/2} p\,(t)\mathrm{e}^{-j\omega t}\,\mathrm{d}t \tag{6.6}$$

The processor output is formed by correlating the Fourier transformed data **p** at each sensor with the noise free model $\widehat{\mathbf{p}}$ of the acoustic pressure at each sensor location, at each frequency, summing and squaring [50],

$$\mathrm{P_M}(\omega, \mathbf{d}) = \mathrm{E}\{|\widehat{\mathbf{p}}(\omega, \mathbf{d})^{+}\mathbf{p}(\omega)|^2\} = \mathrm{E}\left\{\left|\frac{\sum_{n=1}^{N}\hat{p}_n^*(\omega, \mathbf{d})p_n(\omega)}{\sqrt{\sum_{n=1}^{N}|p_n(\omega)|^2\sum_{n=1}^{N}|\hat{p}_n^*(\omega, \mathbf{d})|^2}}\right|^2\right\} \tag{6.7}$$

where '+' is the Hermitian operator.

The expectation operator in Eq. (6.7) is used because $\mathbf{p}(\omega)$ is a random function of time. Expanding Eq.(6.7) gives,

$$\begin{aligned}\mathrm{P_M}(\omega, \mathbf{d}) = \mathrm{E}\{|\widehat{\mathbf{p}}(\omega, \mathbf{d})^{+}\mathbf{p}(\omega)|^2\} &= \mathrm{E}\left\{\left(\widehat{\mathbf{p}}(\omega, \mathbf{d})^{+}\mathbf{p}(\omega)\right)\left(\widehat{\mathbf{p}}(\omega, \mathbf{d})^{+}\mathbf{p}(\omega)\right)^*\right\} \\ &= \mathrm{E}\{\widehat{\mathbf{p}}(\omega, \mathbf{d})^{+}\mathbf{p}(\omega)\mathbf{p}(\omega)^{+}\widehat{\mathbf{p}}(\omega, \mathbf{d})\}\end{aligned} \tag{6.8}$$

Because $\widehat{\mathbf{p}}(\omega, \mathbf{d})^{+}$ and $\widehat{\mathbf{p}}(\omega, \boldsymbol{d})$ are deterministic processes and $\mathbf{p}(\omega)$ and $\mathbf{p}(\omega)^{+}$ are random measured data Eq.(6.8) becomes,

$$\mathrm{P_M}(\omega, \mathbf{d}) = \widehat{\mathbf{p}}(\omega, \mathbf{d})^{+}\mathrm{E}\{\mathbf{p}(\omega)\mathbf{p}(\omega)^{+}\}\widehat{\mathbf{p}}(\omega, \boldsymbol{d}) = \widehat{\mathbf{p}}(\omega, \mathbf{d})^{+}\mathbf{K}(\omega)\widehat{\mathbf{p}}(\omega, \boldsymbol{d}) \tag{6.9}$$

where **K** is the measured covariance matrix $\mathbf{K} = \mathrm{E}\{\mathbf{p}(\omega)\mathbf{p}(\omega)^{+}\}$ with elements $\mathrm{K}_{ij} = \mathrm{E}\{(p_i^* p_j)/||\mathbf{p_m}||\,||\widehat{\mathbf{p}}_\mathrm{m}||\}$ which comprise contributions from both signal and noise.

Finally, Eq.(6.9) is integrated over a frequency range and the final form of the Bartlett processor gives,

$$\mathrm{P_M}'(\mathbf{d}) = \frac{1}{\omega_2 - \omega_1}\int_{\omega_1}^{\omega_2} \mathrm{P_B}(\omega, \mathbf{d})\,d\omega \tag{6.10}$$

The location of the leak is detected by determining **d** that maximizes $\mathrm{P_M}'(\mathbf{d})$.

# 6.3 Theoretical prediction of the Bartlett processor for leak detection using two sensors

With reference to Figure 6.1, for two sensors, $N$=2 located either side of the leak at distance $d$ between them, the pressure signal measured at each of the sensor is given by [9],

$$p_1(\omega, d_1) = p_l(\omega) e^{-\beta\omega d_1} e^{-jk d_1} + n_1(\omega) \tag{6.11}$$

$$p_2(\omega, d_2) = p_l(\omega) e^{-\beta\omega d_2} e^{-jk d_2} + n_2(\omega) \tag{6.12}$$

where $d_1$ is the distance of sensor 1 from the leak, $d_2 (= d' - d_1)$ is the distance of sensor 2 from the leak, $k = \omega / c$ is the wavenumber, $c$ the wavespeed, $\beta$ quantifies the rate of decay along the pipe, $n_1(\omega)$, $n_2(\omega)$ is the background noise measured at sensor 1 and 2 respectively and $p_l(\omega)$ is the spectrum of the acoustic pressure measured at the leak location.

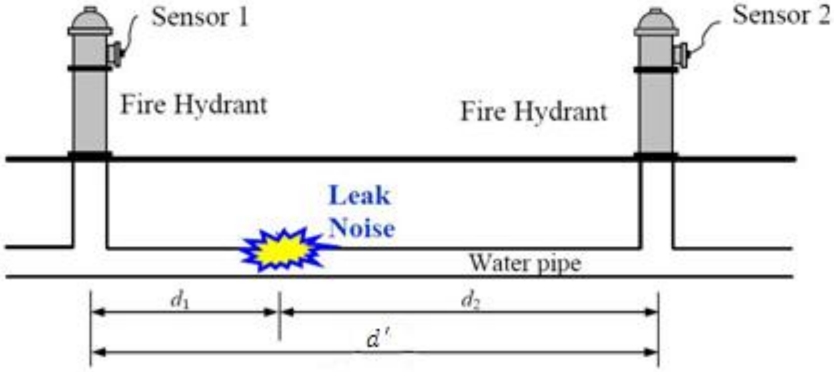

Figure 6.1. Schematic of a pipe with a leak bracketed by two sensors.

The modelled data is assumed to be of an identical form to Eqs.(6.11) and (6.12) but noise free and hence,

$$\hat{p}_1(\omega, \hat{d}_1) = e^{-\hat{\beta}\omega \hat{d}_1} e^{-j\hat{k}\hat{d}_1} \tag{6.13}$$

$$\hat{p}_2(\omega, \hat{d}_2) = e^{-\hat{\beta}\omega \hat{d}_2} e^{-j\hat{k}\hat{d}_2} \tag{6.14}$$

where $\hat{d}_1$ , and $\hat{d}_2 (= d' - \hat{d}_1)$ are the assumed trial distances of sensor 1 and 2 respectively from the leak, $\hat{\beta}$ is the assumed attenuation factor of the pipe and $\hat{k}$ is the assumed wavenumber. Note that the model does not require a leak pressure amplitude term because of the normalization in Eq.(6.5). When $\hat{d}_1$ matches with the actual distance $d_1$ from the leak, $\hat{d}_1 = d_1$ and $\hat{d}_2 = d_2$, in the noise-free case, the Bartlett processor gives the maximum value $\mathrm{P_M}' = 1$.

Using Eqs.(6.11) to (6.14), the Bartlett processor given by Eq.(6.7) for *N*=2 may be expressed as,

$$\mathrm{P_M}(\omega,\mathbf{d}) = \mathrm{E}\left\{\frac{\left|\sum_{i=1}^{2} p_i(\omega)\hat{p}_i^*(\omega,\mathbf{d})\right|^2}{\sum_{i=1}^{2}|p_i(\omega)|^2\sum_{i=1}^{2}|\hat{p}_i(\omega,\mathbf{d})|^2}\right\} \tag{6.15}$$

which may be expressed more fully as,

$$\begin{aligned}&\mathrm{P_M}(\omega,\mathbf{d})\\ &= \mathrm{E}\left\{\frac{\left|\sum_{i=1}^{2}\left(\left(p_l(\omega)e^{-\beta\omega d_i}e^{-jk d_i}+n_i(\omega)\right)e^{-\hat{\beta}\omega\hat{d}_i}e^{jk\hat{d}_i}\right)\right|^2}{\left[\sum_{i=1}^{2}\begin{pmatrix}\left(p_l(\omega)e^{-\beta\omega d_i}\cos(kd_i)+n_i(\omega)\right)^2+\\ \left(p_l(\omega)e^{-\beta\omega d_i}\sin(kd_i)\right)^2\end{pmatrix}\right]\left[\sum_{i=1}^{2}\left(e^{-2\beta\omega d_i}\right)\right]}\right\}\end{aligned} \tag{6.16}$$

Note that at this stage it is not possible to make any further simplifications to Eq.(6.16) because it involves the expectation of a quotient of random variables. In order to derive an analytical solution to Eq.(6.16), we define a slightly different form to Eq.(6.16) that will allow further simplifications to be made without altering the fundamental function of the Bartlett processor, which is the correlation between measurement data and a model of the leak spectrum in the frequency domain.

Thus, we now define a slightly different form to Eq.(6.15), in which the processor $\mathrm{P_M}$ is the quotient of the expectations,

$$\mathrm{P_B}(\omega,\mathbf{d}) = \frac{\mathrm{E}\left\{\left|\sum_{i=1}^{2} p_i(\omega)\hat{p}_i^*(\omega,\mathbf{d})\right|^2\right\}}{\mathrm{E}\{\sum_{i=1}^{2}|p_i(\omega)|^2\}\sum_{i=1}^{2}|\hat{p}_i(\omega,\mathbf{d})|^2} \tag{6.17}$$

Substituting Eqs.(6.11)-(6.14) to Eq.(6.17), after simplifications and assuming that the background noise has zero mean value, Eq.(6.17) gives,

$$\mathrm{P_B}(\omega, \mathbf{d}) = \frac{2S_{ll}(\omega)e^{-(\beta\omega d' + \hat{\beta}\omega\hat{d})}\left(\cosh\left(\beta\omega\Delta d + \hat{\beta}\omega\Delta\hat{d}\right) + \cos\left(k\Delta d - \hat{k}\Delta\hat{d}\right)\right) + S_{n_1n_1}(\omega)e^{-\hat{\beta}\omega\hat{d}_1} + S_{n_2n_2}(\omega)e^{-\hat{\beta}\omega\hat{d}_2}}{2S_{ll}(\omega)e^{-(\beta\omega d' + \hat{\beta}\omega\hat{d})}\left(\cosh\left(\beta\omega\Delta d + \hat{\beta}\omega\Delta\hat{d}\right) + \cosh\left(\beta\omega\Delta d - \hat{\beta}\omega\Delta\hat{d}\right)\right) + \left(e^{-\hat{\beta}\omega\hat{d}_1} + e^{-\hat{\beta}\omega\hat{d}_2}\right)\left(S_{n_1n_1}(\omega) + S_{n_2n_2}(\omega)\right)} \tag{6.18}$$

where, $\Delta d = d_1 - d_2$, $\Delta\hat{d} = \hat{d}_1 - \hat{d}_2$, $S_{ll}$ is the PSD of the leak noise and $S_{n_1n_1}$, $S_{n_2n_2}$ are the PSD of the background noise at sensors 1 and 2 respectively.

Assuming that noise can be neglected, Eq.(6.18) may be written as,

$$\mathrm{P_B}(\omega, \mathbf{d}) = \frac{\cosh\left(\beta\omega\Delta d + \hat{\beta}\omega\Delta\hat{d}\right) + \cos\left(k\Delta d - \hat{k}\Delta\hat{d}\right)}{\cosh\left(\beta\omega\Delta d + \hat{\beta}\omega\Delta\hat{d}\right) + \cosh\left(\beta\omega\Delta d - \hat{\beta}\omega\Delta\hat{d}\right)} \tag{6.19}$$

which is independent of the PSD of the leak noise spectrum.

### 6.3.1 Application of the Bartlett processor on signals measured with equidistant sensors from the leak

In the special but unlikely case where the two sensors are of equal distance from the leak, $d_1 = d_2$, the results from the Bartlett processor computed from Eq.(6.18) versus $\hat{d}_1/d_1$ are shown in Figure 6.2 for a frequency bandwidth 5-1000 Hz. For simplicity, the leak spectrum is assumed to be flat over the bandwidth of interest [9]. Three different signal to noise ratios (SNR) are considered, 40 dB, 5 dB and -5 dB. These simulations assume values of $\beta$, $c$ estimated from theoretical expressions based on the material properties and characteristic dimensions of the pipe that was used for our experiment [9]. It is assumed in this simulation that $\hat{\beta} = \beta$ and $\hat{c} = c$.

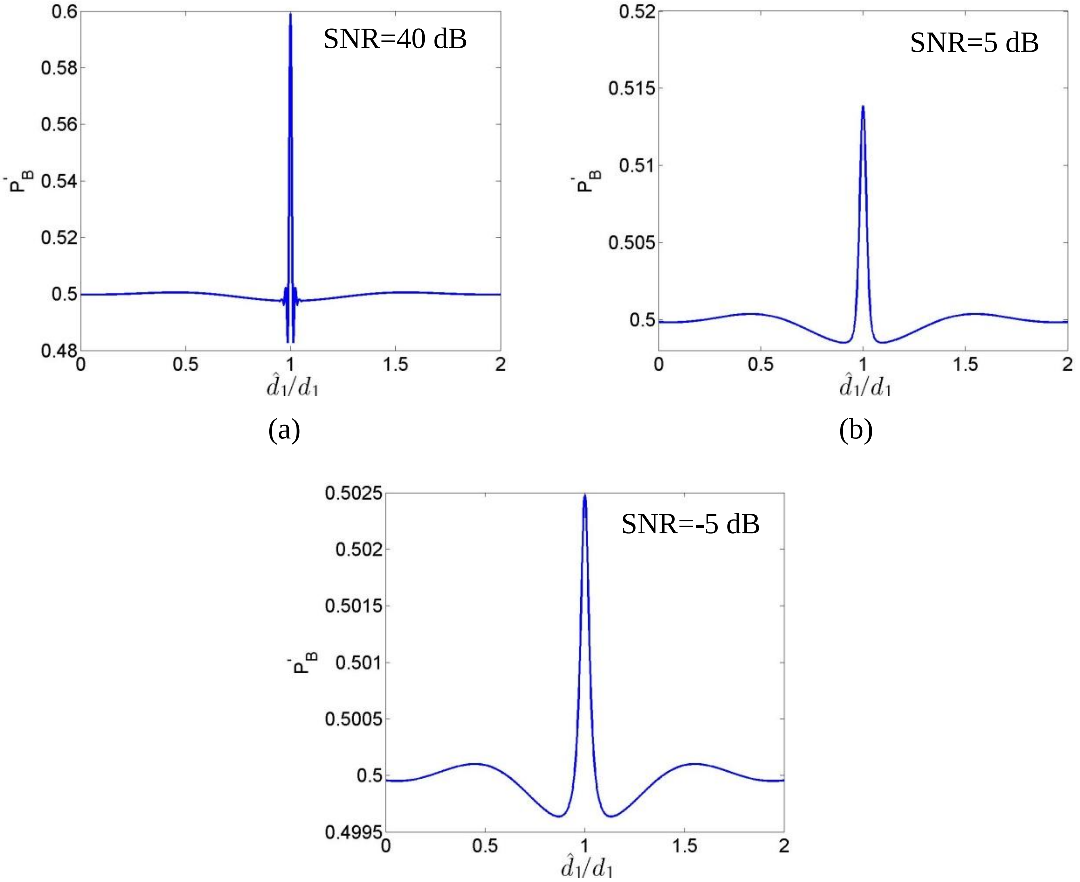

(a)

(b)

(c)

Figure 6.2. Bartlett processor for equidistant sensors $d_1 = d_2 = 50$ m and for frequency bandwidth 5-1000 Hz. The values for the attenuation factor and wavespeed for both measurement and model were taken $\beta = \hat{\beta} = 7.25\text{x}10^{-5}$ s/m, $c = \hat{c} = 385$ m/s; (a) SNR=40 dB; (b) SNR=5 dB; (c) SNR=-5 dB.

Figure 6.2 shows the presence of a sharp peak at the leak location, $\hat{d}_1 = d_1$. Although for negative SNR the peak in Figure 6.2(c) is very small it can still be distinguished. This peak becomes sharper as SNR increases. Note also that when $\hat{d}_1 \neq d_1$ the Bartlett processor tends to ½ and not to 0 as in the conventional correlators. This happens because as $\hat{d}_1 \to 0$, $\hat{d}_2 \to d$ and taking into account that $d_1 = d_2 = d/2$, Eq.(6.19) gives,

$$\mathrm{P_B}(\omega, \mathbf{d}) = \frac{\cosh(\hat{\beta}\omega d) + \cos(\hat{k}d)}{\cosh(\hat{\beta}\omega d) + \cosh(\hat{\beta}\omega d)} \approx \frac{1}{2} \tag{6.20}$$

### 6.3.2 Application of the Bartlett processor on signals measured with non-equidistant sensors from the leak

In practice of course, the sensors are usually non-equidistant, $d_1 \neq d_2$. In this general case, the Bartlett processor is plotted in Figure 6.3 versus $\hat{d}_1/\, d_1$ for three different values of SNR and for an extreme case of unequal sensors, $d_1 = 95$ m, $d_2 = 5$ m and in Figure 6.4 for $d_1 = 70$ m, $d_2 = 30$ m.

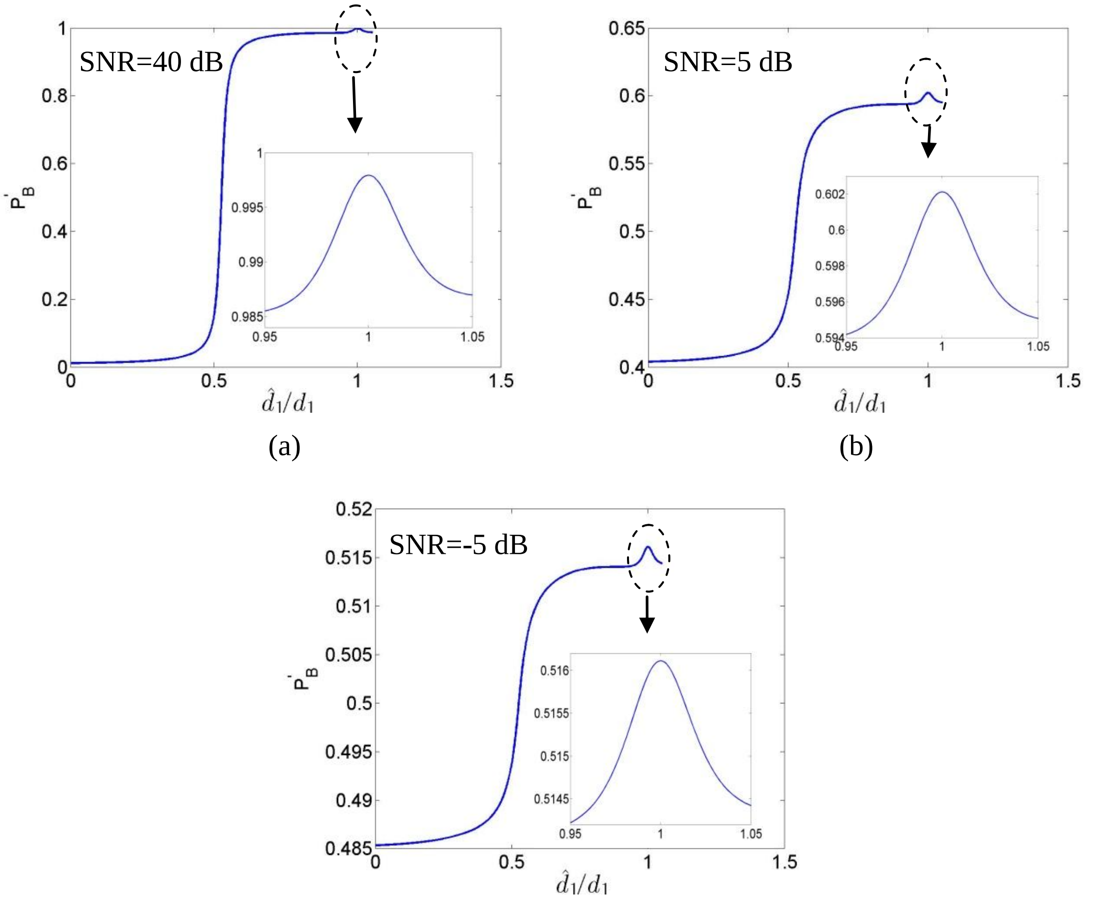

(a)

(b)

(c)

Figure 6.3. Bartlett processor for $d_1 = 95$ m, $d_2 = 5$ m and for frequency bandwidth 5-1000 Hz; $\beta = \hat{\beta} = 7.25\text{x}10^{-5}$ s/m, $c = \hat{c} = 385$ m/s; (a) SNR=40 dB, (b) SNR=5 dB, (c) SNR=-5 dB.

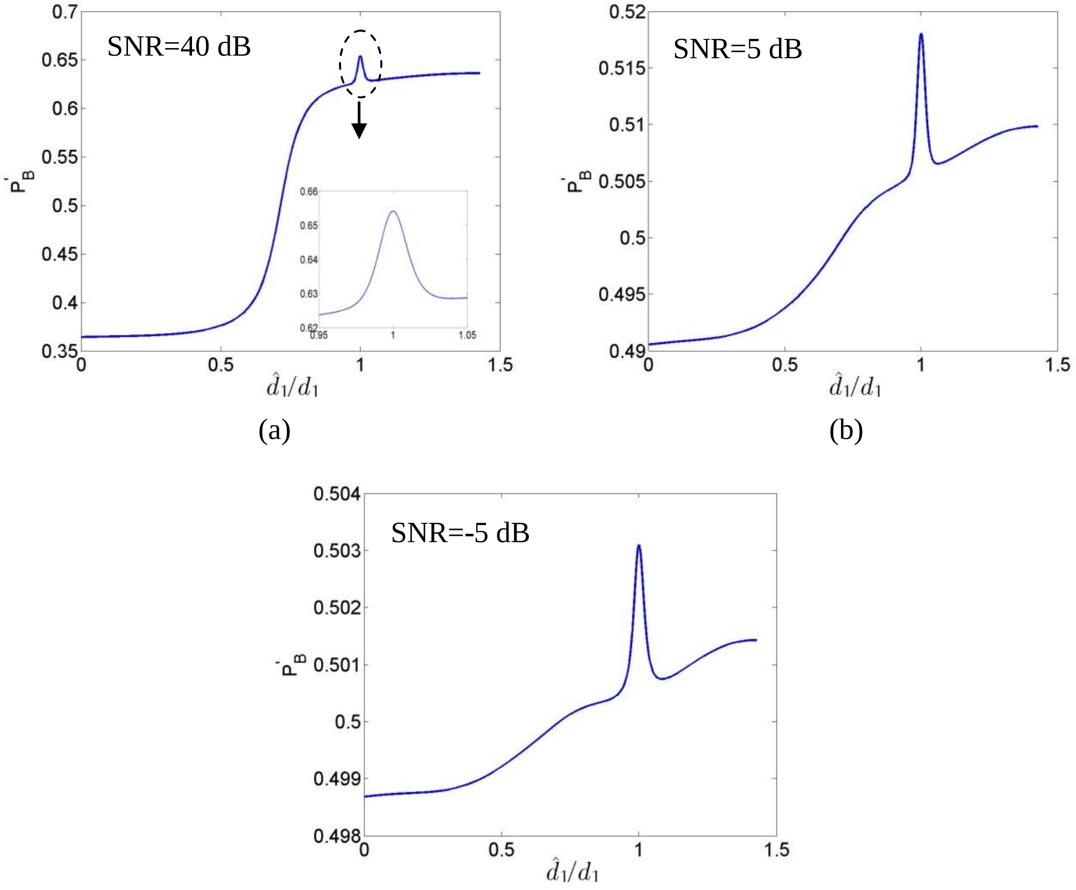

(a) (b)

(c)

Figure 6.4. Bartlett processor for $d_1 = 70$ m, $d_2 = 30$ m and for frequency bandwidth 5-1000 Hz; $\beta = \hat{\beta} = 7.25\text{x}10^{-5}$ s/m, $c = \hat{c} = 385$ m/s; (a) SNR=40 dB, (b) SNR=5 dB, (c) SNR=-5 dB.

Figure 6.3 shows that for this general case, a very small and broad peak is observed at all SNRs when $\hat{d}_1 = d_1$. This peak becomes smaller for decreasing values of SNR as the expanded figures in Figure 6.3 suggest. For this reason the results cannot be considered satisfactory. This behaviour occurs because when $d_1 \gg d_2$, one sensor is much further from the leak than the other, which results in one sensor receiving a highly attenuated signal compared to the other signal. Therefore, the information from the sensor furthest from the leak is excluded in the correlation and the correlation is formed between only one sensor and the model thereby leading to weak sensitivity to the assumed leak position. This problem arises from the frequency decay $e^{-\beta\omega d'}$ of the measured and modelled pressure. As the difference in the distances $d_1$ and $d_2$ between the sensors and the leak decreases a sharper peak in the leak location is observed as Figure 6.4 suggests as in this case more information from the furthest sensors is included.

To explain the shape of the Bartlett processor in Figure 6.3 when $\hat{d}_1 \neq d_1$, two cases are considered, when $\hat{d}_1 \approx d$ and when $\hat{d}_1 \approx 0$.

When $\hat{d}_1 \approx d^{'}$ and $d_1 \gg d_2$, Eq.(6.18) gives,

$$\mathrm{P_B}(\omega) \approx \frac{S_{ll}(\omega) + S_{n_2 n_2}(\omega)}{S_{ll}(\omega) + S_{n_1 n_1}(\omega) + S_{n_2 n_2}(\omega)} \tag{6.21}$$

Assuming that $S_{n_1 n_1}(\omega) \approx S_{n_2 n_2}(\omega) \neq 0$, for a case of low SNR Eq.(6.21) will give,

$$\mathrm{P_B}(\omega) \approx \frac{1}{2} \tag{6.22}$$

whereas for a case of high SNR Eq.(6.21) will give,

$$\mathrm{P_B}(\omega) \approx 1 \tag{6.23}$$

Therefore, $\mathrm{P_B}^{'} \rightarrow 1/2$ as SNR→0 and $\mathrm{P_B}^{'} \rightarrow 1$ as SNR→ ∞ as can be seen in Figures 6.3.

Similarly, when $\hat{d}_1 \approx 0$ and $d_1 \gg d_2$, Eq.(6.18) becomes,

$$\mathrm{P_B}(\omega) \approx \frac{S_{n_1 n_1}(\omega)}{S_{ll}(\omega) + S_{n_1 n_1}(\omega) + S_{n_2 n_2}(\omega)} \tag{6.24}$$

As before, assuming that $\mathrm{S}_{n_1 n_1}(\omega) \approx \mathrm{S}_{n_2 n_2}(\omega) \neq 0$, $\mathrm{P_B}^{'} \rightarrow 0$ as SNR→ ∞ and $\mathrm{P_B}^{'} \rightarrow 1/2$ as SNR→0 as can be also seen in Figures 6.3.

## 6.4 Bartlett processor with more than two sensors

The form of the Bartlett processor of Eq.(6.17) readily generalizes to more than two sensors. Thus, in this section the effect of using multiple sensors (more than two) on the Bartlett processor is quantified. In Figure 6.5 the Bartlett processor is plotted for an increasing number of sensors.

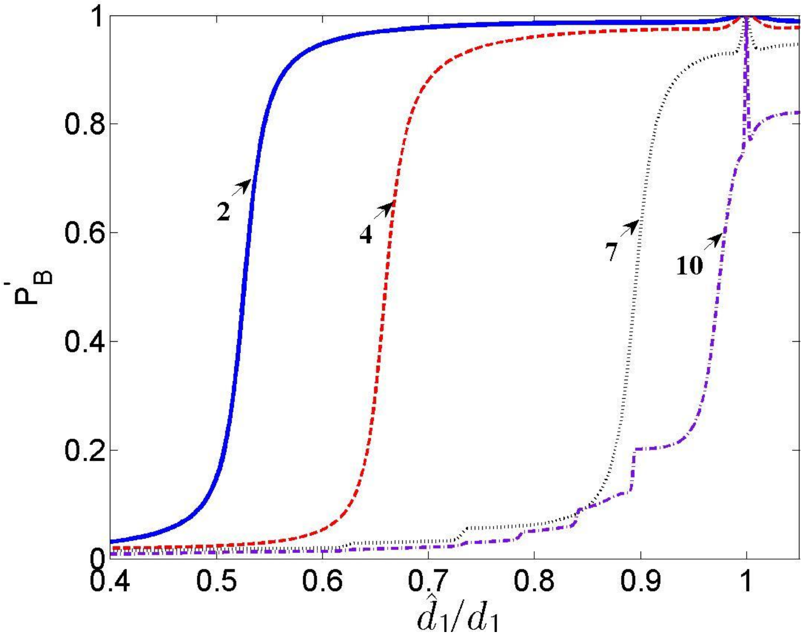

Figure 6.5. Effect of increasing the number of sensors on the Bartlett processor for frequency bandwidth 5-1000 Hz; $d_1 = 95$ m, $d_2 = 5$ m, $\beta = \hat{\beta} = 7.25\text{x}10^{-5}$ s/m, $c = \hat{c} = 385$ m/s SNR=40 dB.

Figure 6.5 suggests that by increasing the number of sensors the peak in the Bartlett processor output significantly sharpens. By using an increasing number of sensors therefore, more signals are correlated which leads to more information being included in the correlator. Note also that as in the case of two sensors, in the case of multiple sensors, there is always just one unknown, the distance of one sensor from the leak $\hat{d}_1$. The rest of the unknowns (distances of the other sensors from the leak) can be expressed in terms of $\hat{d}_1$ and the distances between the sensors. However, in practice using many sensors may not always be convenient or possible.

## 6.5 Alternative form of the Bartlett processor (ABP)

In the previous section it was shown that the conventional Bartlett processor does not give satisfactory results in the general case of non-equidistant sensors from the leak. The reason why this occurs was investigated. In an attempt to improve the performance and achieve a sharper peak in the processor output an alternative form of the Bartlett processor is proposed based on the square of the real part of $\hat{\mathbf{p}}^{+}\mathbf{p}$. Thus, the proposed new form of this processor may be written more fully as,

$$\mathrm{P_{ABP}}\,(\omega,\mathbf{d}) = \left(\frac{\mathrm{Re}\left\{\mathrm{E}\{\sum_{i=1}^{2} p_i(\omega)\hat{p}_i^*(\omega,\mathbf{d})\}\right\}}{\mathrm{E}\left\{\sqrt{\sum_{i=1}^{2}|p_i(\omega)|^2 \sum_{n=1}^{2}|\hat{p}_i(\omega,\mathbf{d})|^2}\right\}}\right)^2 \tag{6.25}$$

Combining Eqs.(6.11)-(6.14) and Eq.(6.25) and after simplifying the ABP gives,

$$\mathrm{P_{ABP}}\,(\omega,\mathbf{d}) = \frac{\sum_{i=1}^{2}\left[S_{ll}(\omega)\left[e^{-\left(\beta\omega d_i+\hat{\beta}\omega\hat{d}_i\right)}\cos\left(kd_i-\hat{k}\hat{d}_i\right)\right]^2 + S_{n_in_i}(\omega)e^{-2\hat{\beta}\omega\hat{d}_i}\cos^2\left(\hat{k}\hat{d}_i\right)\right]}{\left(S_{ll}(\omega)\sum_{i=1}^{2}e^{-2\beta\omega d_i}+\sum_{i=1}^{2}S_{n_in_i}(\omega)\right)\sum_{i=1}^{2}e^{-2\hat{\beta}\omega\hat{d}_i}} \tag{6.26}$$

By taking the real part we can eliminate the problem encountered in the Bartlett processor in the general case of non-equidistant sensors because more phase information between the measurements and the model prediction is now taken into account as can be seen in Eq.(6.26).

In Figure 6.6, Eq.(6.26) is plotted after integration over the frequency range 5 Hz to 1 kHz. The sensor positions were chosen as before to be $d_1 = 95$ m, and $d_2 = 5$ m. For this simulation it was assumed that $\beta = \hat{\beta}$ and $c = \hat{c}$.

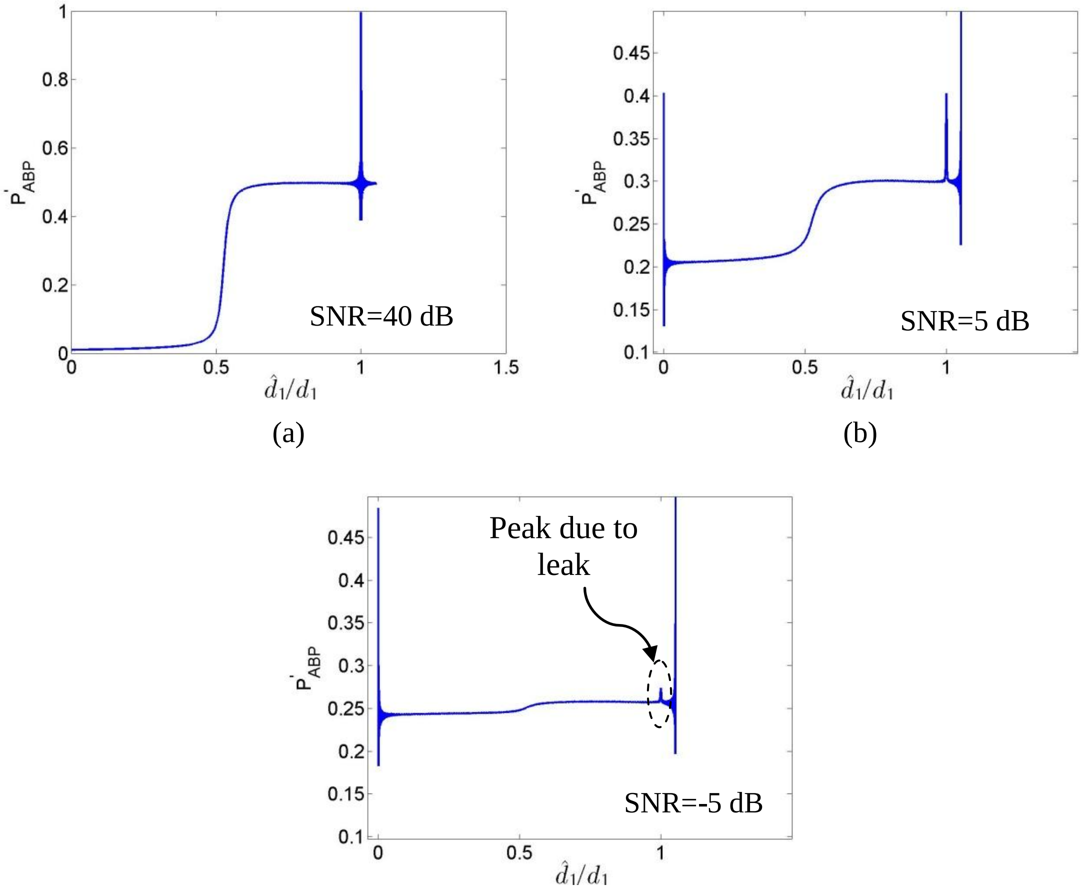

(a) (b)

(c)

Figure 6.6. ABP for $d_1 = 95$ m, $d_2 = 5$ m and for frequency bandwidth 5-1000 Hz. The values for attenuation factor and wavespeed for both measurement and model were taken $\beta = \hat{\beta} = 7.25\text{x}10^{-5}$ s/m, $c = \hat{c} = 385$ m/s; (a) SNR=40 dB, (b) SNR=5 dB, (c) SNR=-5 dB.

Figure 6.6 suggests that the ABP gives a much sharper peak when $\hat{d}_1 = d_1$ in the case of non-equidistant sensors compared with the conventional Bartlett processor shown in Figures 6.3. However, in Figure 6.6(b,c) where the SNR is low (less than 5 dB), two additional sharp peaks can be seen when $\hat{d}_1 = 0$ and when $\hat{d}_1 = d^{'}$. This occurs because when, for example $\hat{d}_1 = 0$, (and therefore $\hat{d}_2 = d^{'}$), Eq.(6.26) gives,

$$\mathrm{P_{ABP}}\,(\omega, \mathbf{d}) \approx \frac{S_{ll}(\omega)\left[e^{-(\beta\omega\, d_1)}\cos(kd_1) + e^{-(\beta\omega\, d_2 + \hat{\beta}\,\omega\, \hat{d}_2)}\cos\!\left(kd_2 - \hat{k}\hat{d}_2\right)\right]^2 + S_{n_1 n_1}(\omega)}{\left(S_{ll}(\omega)(e^{-2\beta\omega\, d_1} + e^{-2\beta\omega\, d_2}) + S_{n_1 n_1}(\omega) + S_{n_2 n_2}(\omega)\right)} \tag{6.27}$$

Thus, when the SNR is low, the noise terms $S_{n_1n_1}(\omega)$ and $S_{n_2n_2}(\omega)$ in Eq.(6.27) dominate suppressing the exponentials terms, which results in a peak at $\hat{d}_1 = 0$. Thus, knowing that this effect occurs at $\hat{d}_1 = 0$ (and $\hat{d}_1 = d'$ ), the ABP is therefore not evaluated at these points.

Figure 6.7 shows a plot of the ABP for $\hat{\beta} = 10\beta$ and for three different values of SNR.

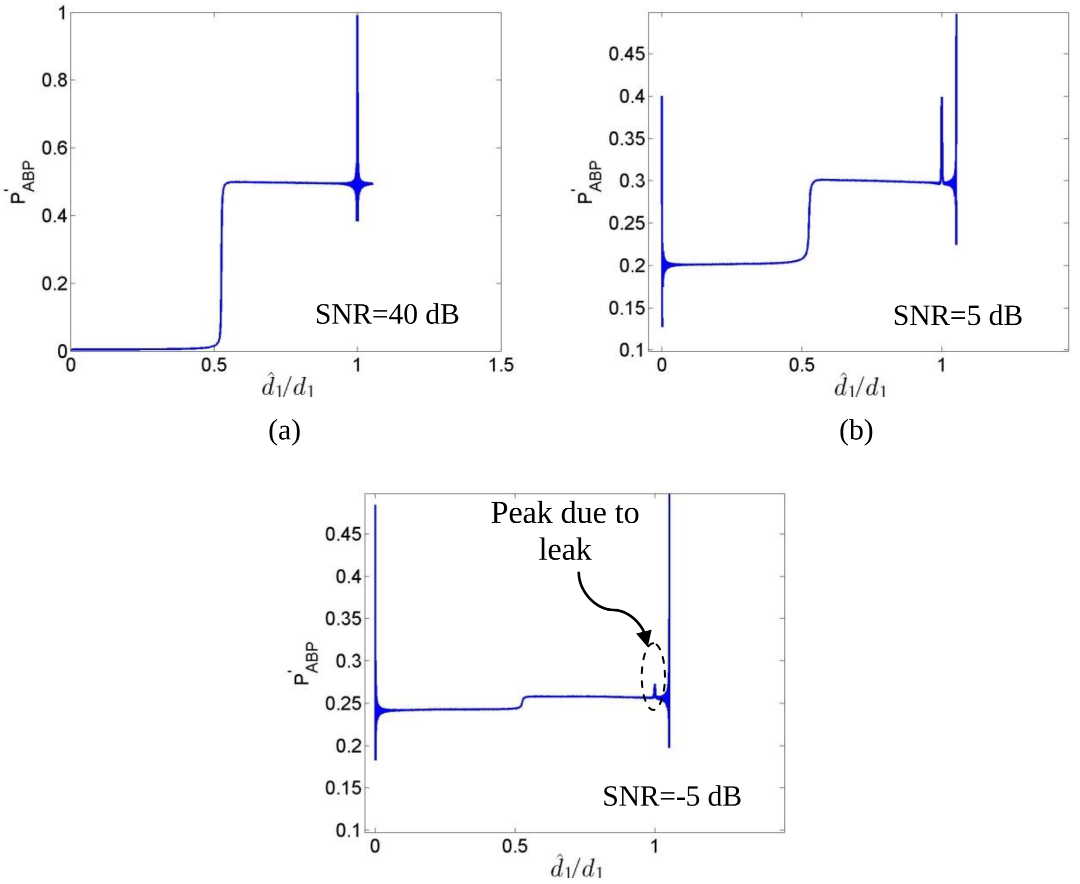

(a) (b)

(c)

Figure 6.7. ABP for $d_1 = 95$ m, $d_2 = 5$ m and for frequency bandwidth 5-1000 Hz. The values for attenuation factor and wavespeed for both measurement and model were taken $\hat{\beta} = 10\beta = 7.25\text{x}10^{-4}$ s/m, $c = \hat{c} = 385$ m/s; (a) SNR=40 dB, (b) SNR=5 dB,(c) SNR=-5 dB.

It can be seen that an incorrect choice of decay rate $\beta$ has no effect on the correct estimation of the leak location which, as in the standard correlator, depends on the propagation wavespeed.

## 6.6 Comparison of the ABP with the BCC and PHAT correlator

In this section the correlator proposed in this chapter is compared with the Basic Cross Correlator (BCC) and the Phase Transform correlator (PHAT) for different values of SNR. The BCC is widely used for leak detection in plastic water pipes and its effectiveness is found to be affected by several factors, including the selection of either acoustic or vibration sensors and the cut-off frequencies of the high and low-pass digital filters used to remove noise in the frequency range in which the signal is weak [51].

In previous work the PHAT correlator was found to give a sharper peak in the leak location compared to BCC by pre-whitening the measured cross-spectral density (CSD) for performing time delay estimation [51]. For the case of the PHAT processor, the correlation between two sensor signals $x_1(t)$, $x_2(t)$ is given by,

$$R_{x_1x_2}(\tau) = F^{-1}\left\{\Psi_p(\omega)S_{x_1x_2}(\omega)\right\} \tag{6.28}$$

where $F^{-1}\{\quad\}$ denotes the inverse Fourier transform, $S_{x_1x_2}$ is the CSD and $\Psi_p(\omega)$ is the PHAT frequency weighting function given by,

$$\Psi_p(\omega) = 1/\left|S_{x_1x_2}(\omega)\right| \tag{6.29}$$

In this way, the effects of propagation along the pipe, the amplitude dependence of the distance between the sensors and also the effects of leak spectrum are effectively removed by the pre-whitening procedure. However, whitening the modulus of the CSD, results in a spurious peak in the correlation function at zero time lag, due to the background noise outside the frequency bandwidth of our interest [51]. It is possible that the peak in the cross-correlation function due to the time delay may be masked by the oscillatory behaviour of the spurious peak. In order to remove the possibility of these peaks it is necessary to pass the signals through a band-pass filter prior to using the PHAT correlator [51].

The comparison of the ABP with the BCC and the PHAT correlator is shown in Figures 6.8, 6.9 and 6.10 for different values of SNR equal to 40, 5 and -5 dB respectively. The results are normalized to their peak correlation value. The values for $\beta$, $\hat{\beta}$, $c$,and $\hat{c}$ used in these simulations are the same as the ones used in the previous sections (Sections 6.3.1-6.5).

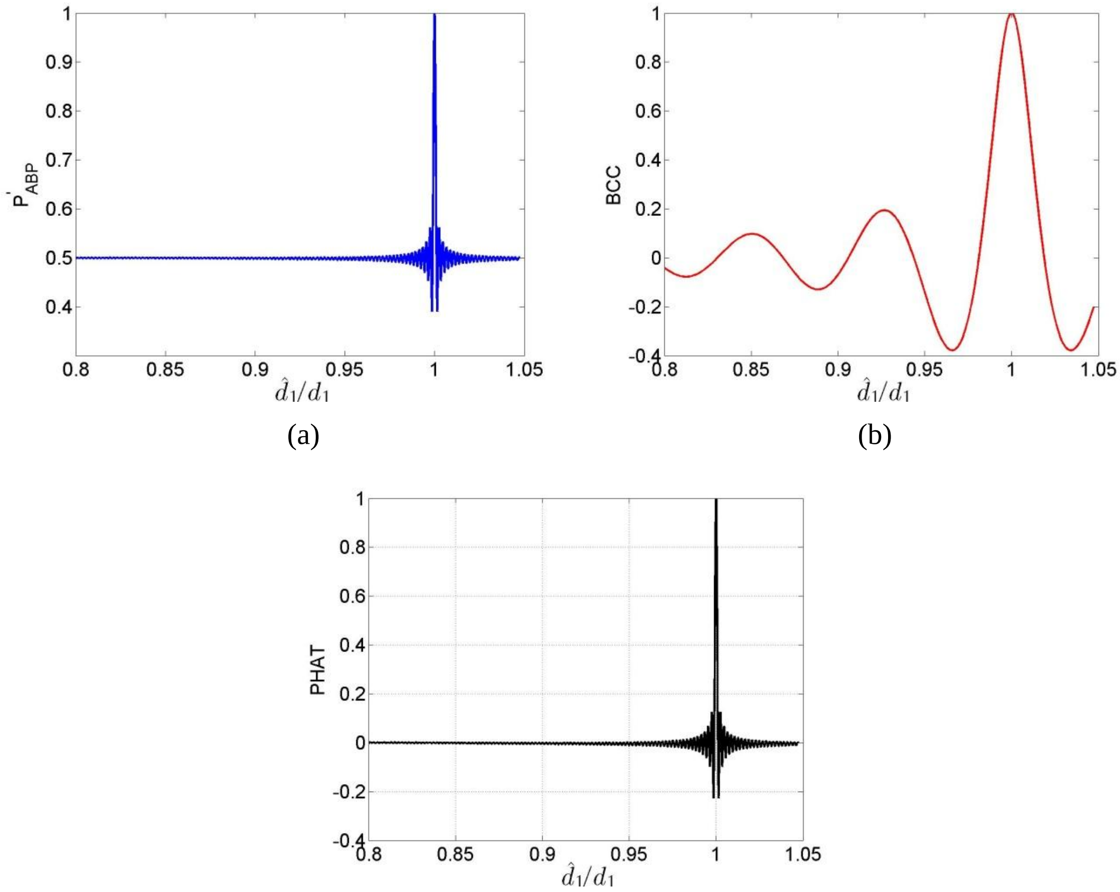

(a) (b)

(c)

Figure 6.8. Comparison of the ABP with the BCC and PHAT for $d_1 = 95$ m, $d_2 = 5$ m and for frequency bandwidth 5-1000 Hz; $\beta = \hat{\beta} = 7.25\text{x}10^{-5}\ \text{s/m},\ c = \hat{c} = 385$ m/s, SNR=40 dB; (a) ABP; (b) BCC; (c) PHAT correlator.

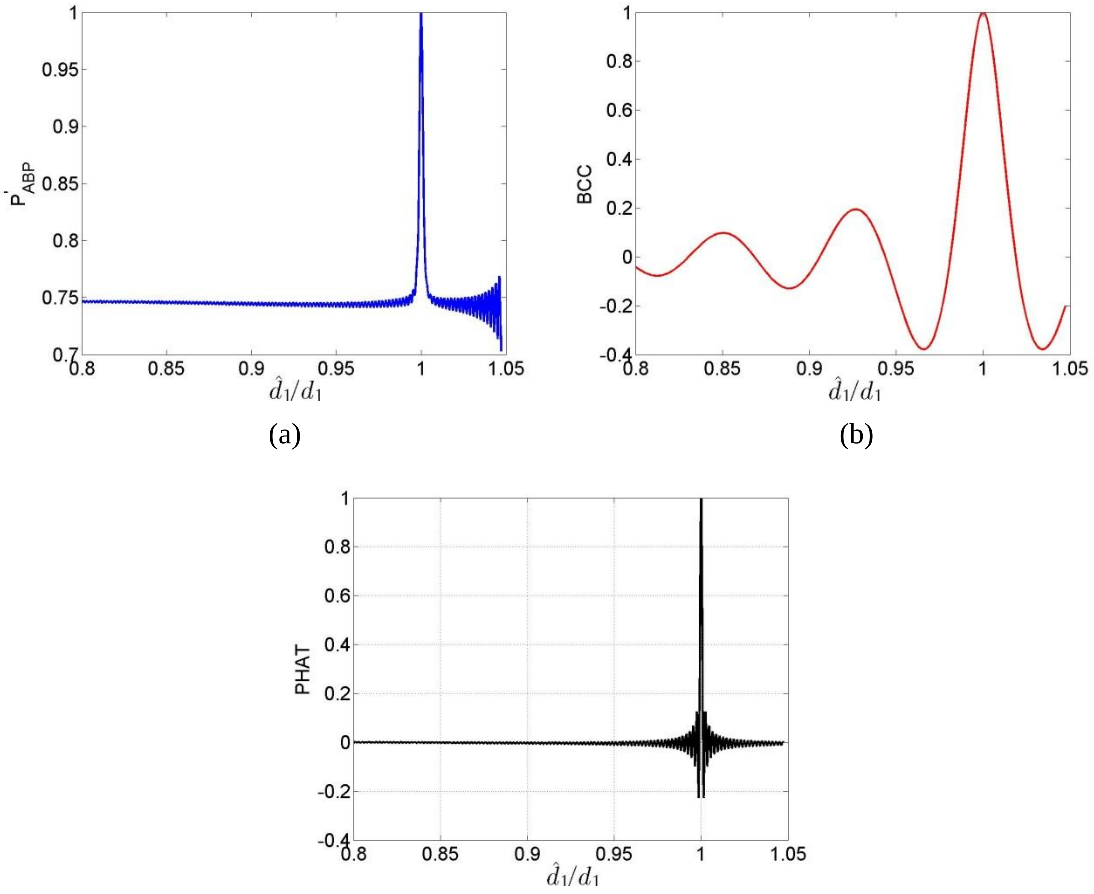

(a) (b)

(c)

Figure 6.9. Comparison of the ABP with the BCC and PHAT for $d_1 = 95$ m, $d_2 = 5$ m and for frequency bandwidth 5-1000 Hz; $\beta = \hat{\beta} = 7.25\text{x}10^{-5}$ s/m, $c = \hat{c} = 385$ m/s, SNR=5 dB; (a) ABP; (b) BCC; (c) PHAT correlator.

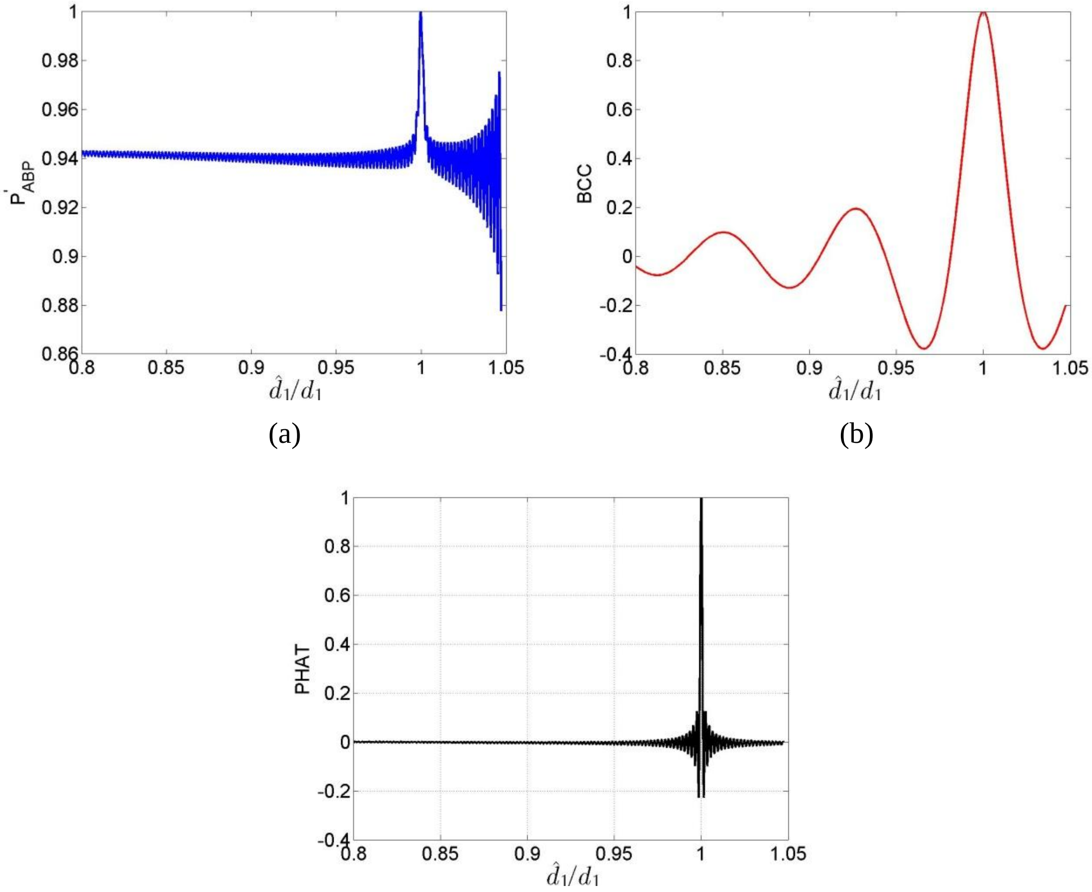

(a) (b)

(c)

Figure 6.10. Comparison of the ABP with the BCC and PHAT for $d_1 = 95$ m, $d_2 = 5$ m and for frequency bandwidth 5-1000 Hz; $\beta = \hat{\beta} = 7.25\text{x}10^{-5}$ s/m, $c = \hat{c} = 385$ m/s, SNR=-5 dB; (a) ABP; (b) BCC; (c) PHAT correlator.

Figures 6.8, 6.9 and 6.10 suggest that for high SNR both the ABP and the PHAT correlator give a very sharp peak at the leak location in contrast to the BCC which gives a much broader peak. For lower values of SNR, the performance of the PHAT and the BCC does not change because, as mentioned previously, the effect of the uncorrelated background noise in both correlators can be removed when correlating the two sensor signals. However, even for negative values of SNR the ABP still gives a sharp and distinctive peak. It can be seen that while the SNR decreases, the amplitude of the oscillations of the side lobes close to the peak decreases. This occurs because in this case the denominator of Eq.(6.28) increases so that the cosine term in the numerator which is responsible for the oscillatory behaviour is suppressed. Note however, that due to the effect of noise the amplitude of oscillations close to the limit point $\hat{d}_1 = d'$ increases as SNR decreases. Thus, in this case the ABP cannot be evaluated close to these points.

### 6.6.1 Effect of band-pass filtering on the ABP, BCC and PHAT

In this section, the effect of band-pass filtering on the ABP is investigated and is compared with the effect of band-pass filtering on the BCC and PHAT correlator for $d_1 = 95$ m, $d_2 = 5$ m. In Figures 6.11, 6.12 and 6.12 the effect of the lower frequency of the band-pass filter is investigated. The upper frequency of the filter is fixed to 1000 Hz and the lower one varies between 20 to 80 Hz.

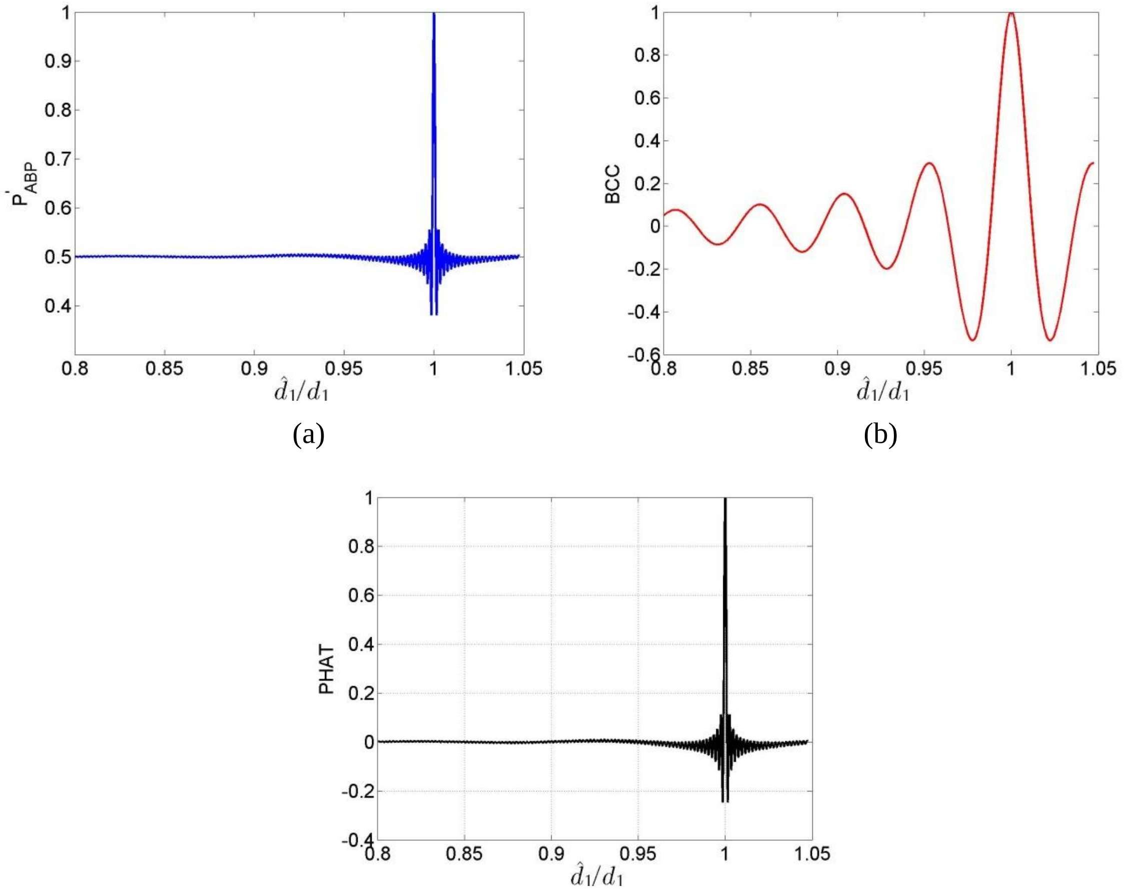

(a)

(b)

(c)

Figure 6.11. Effect of the lower frequency of the band-pass filter on the ABP, BCC and PHAT correlator for SNR=40 dB. The upper frequency of the filter is fixed to 1000 Hz. The lower frequency is set to 20 Hz.

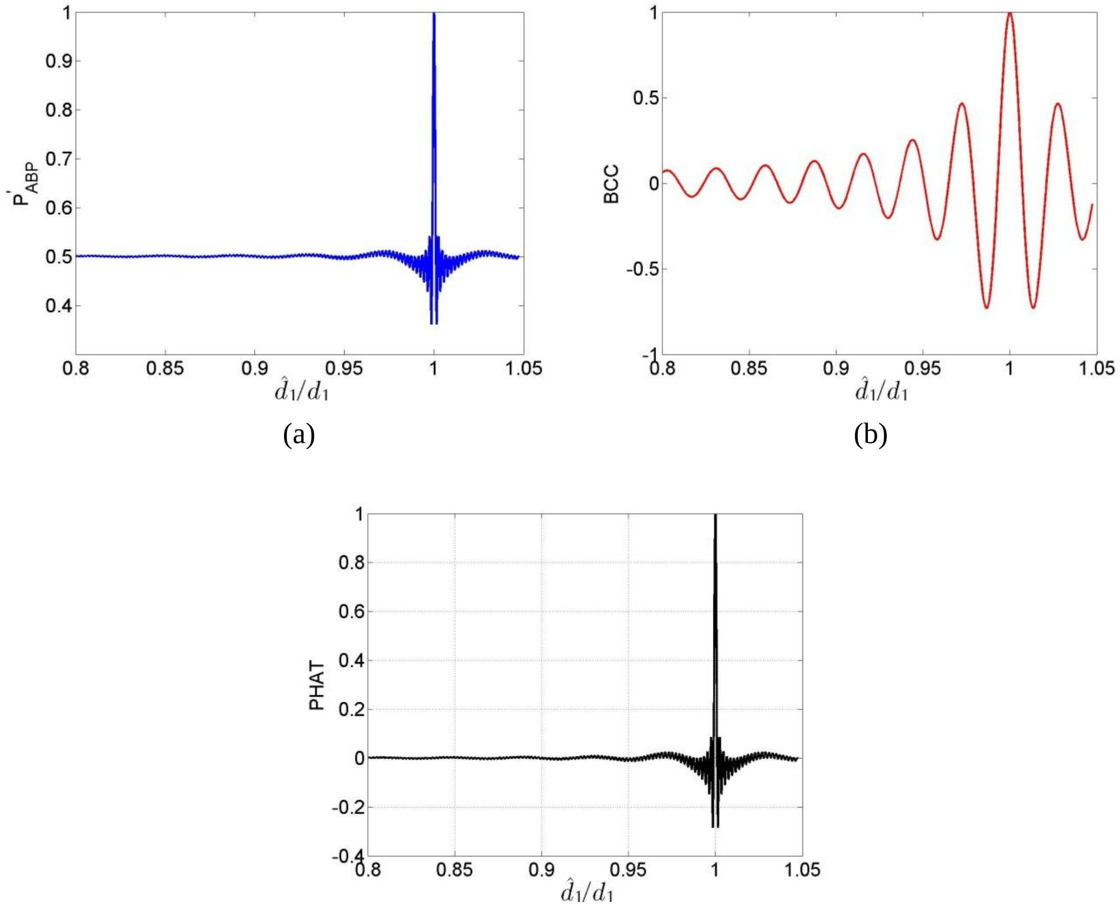

(a)

(b)

(c)

Figure 6.12. Effect of the lower frequency of the band-pass filter on the ABP, BCC and PHAT correlator for SNR=40 dB. The upper frequency of the filter is fixed to 1000 Hz. The lower frequency is set to 50 Hz.

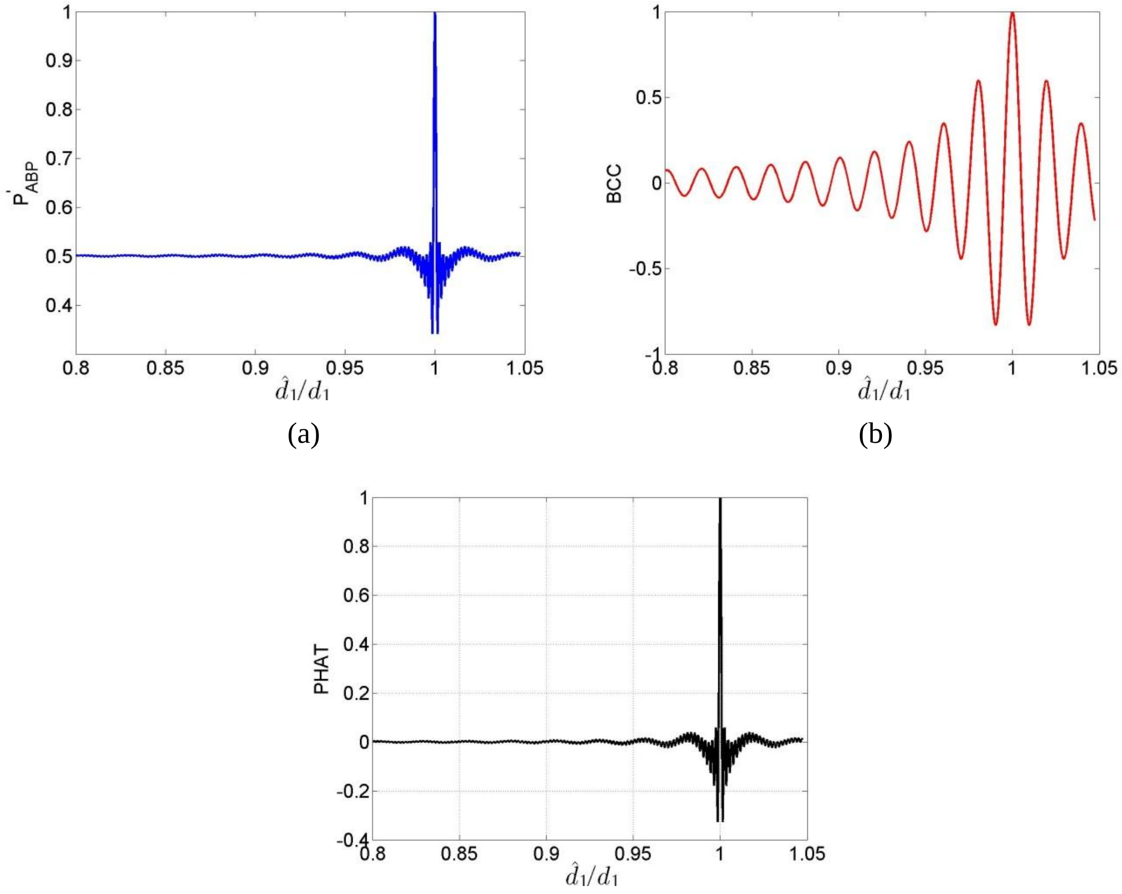

(a) (b)

(c)

Figure 6.13. Effect of the lower frequency of the band-pass filter on the ABP, BCC and PHAT correlator for SNR=40 dB. The upper frequency of the filter is fixed to 1000 Hz. The lower frequency is set to 80 Hz.

Figures 6.11, 6.12 and 6.12 suggest that the ABP and PHAT correlator are not significantly affected by increasing the lower frequency of the band-pass filter whereas for the BCC function the amplitude of the oscillations is highly dependent upon the lower frequency of the filter. In Figures 6.14, 6.15 and 6.16 the effect of the upper frequency of the band-pass filter is investigated while the lower frequency of the filter is set to 5 Hz.

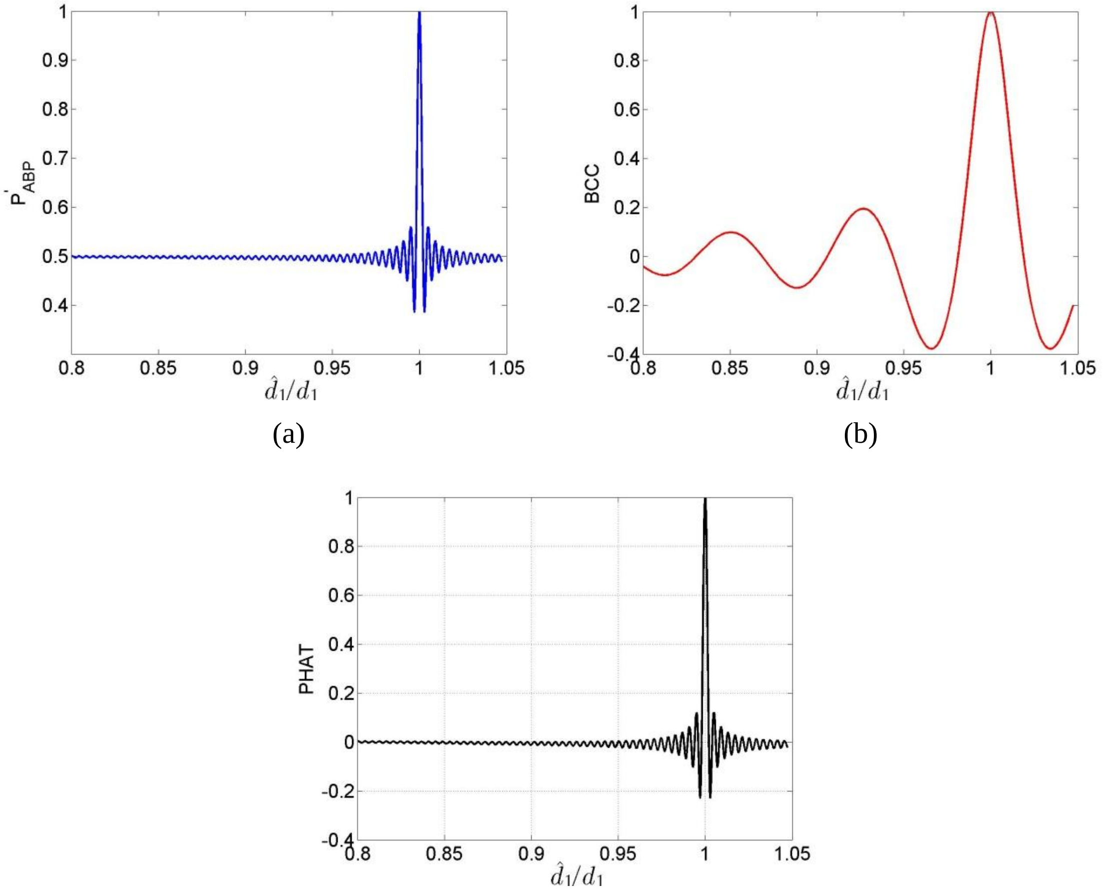

(a) (b)

(c)

Figure 6.14. Effect of the upper frequency of the band-pass filter on the ABP, BCC and PHAT correlator for SNR=40 dB. The lower frequency of the filter is fixed to 5 Hz. The upper frequency is set to 500 Hz.

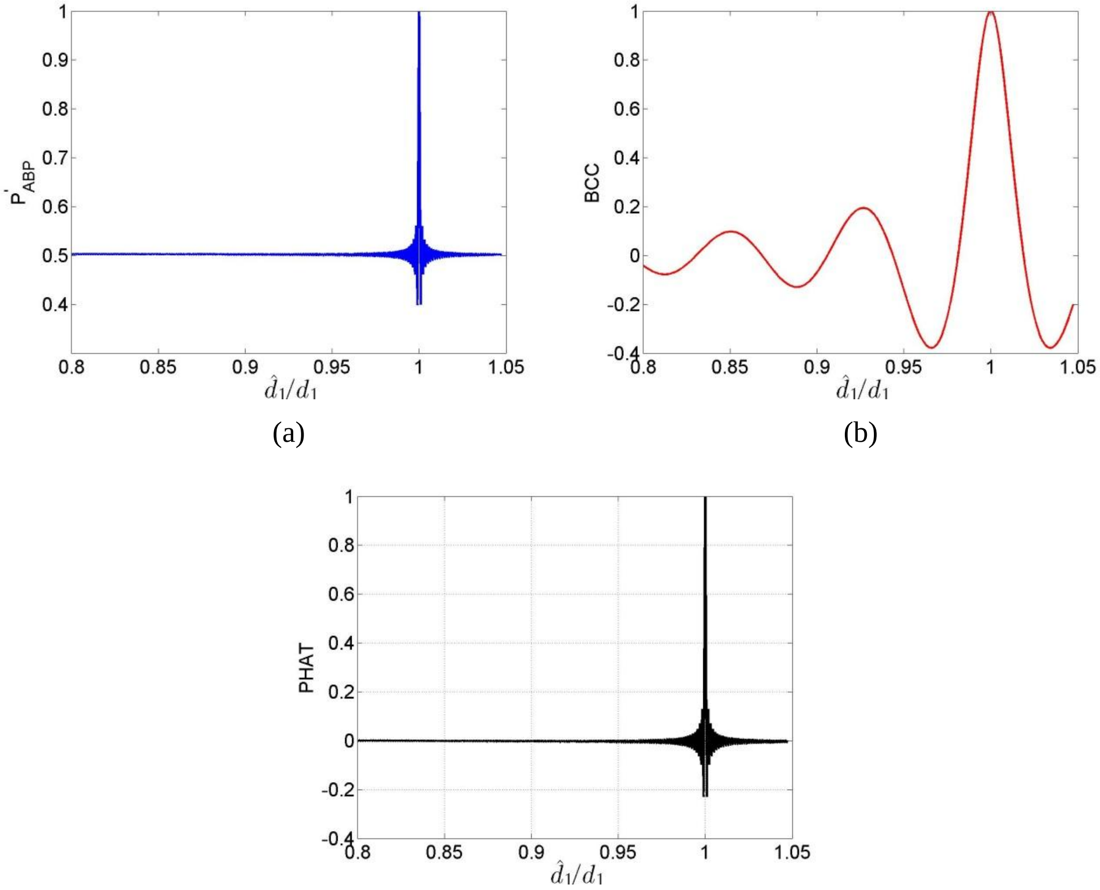

(a) (b)

(c)

Figure 6.15. Effect of the upper frequency of the band-pass filter on the ABP, BCC and PHAT correlator for SNR=40 dB. The lower frequency of the filter is fixed to 5 Hz. The upper frequency is set to 1500 Hz.

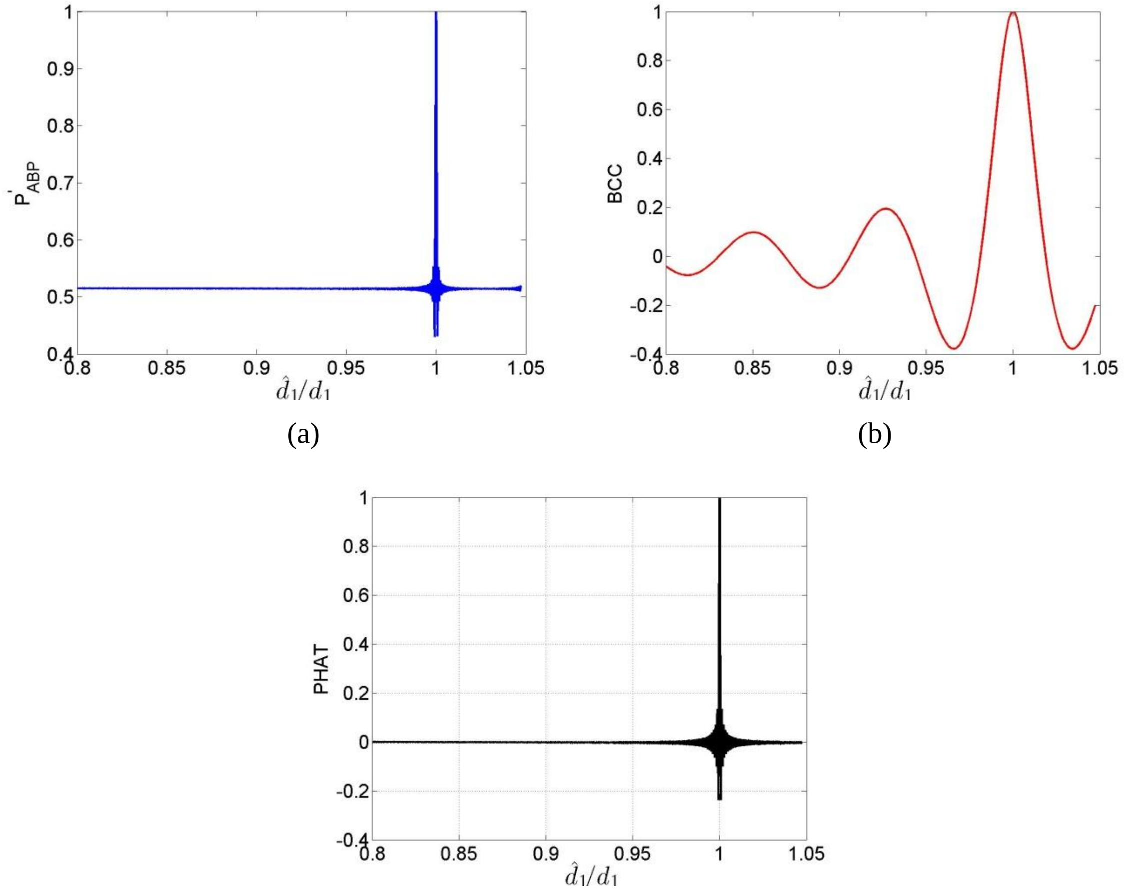

(a) (b)

(c)

Figure 6.16. Effect of the upper frequency of the band-pass filter on the ABP, BCC and PHAT correlator for SNR=40 dB. The lower frequency of the filter is fixed to 5 Hz. The upper frequency is set to 2000 Hz.

Figures 6.14, 6.15 and 6.16 suggest that by increasing the upper frequency of the band-pass filter and hence the frequency bandwidth, the performance of the ABP and PHAT correlator is improved as it reduces the amplitude of the oscillations around the peak value. No effect is observed on the performance of the BCC function which remains unaffected by changes in the upper frequency of the band-pass filter.

In practice, background noise is generally high at frequencies of up to about 50 Hz as seen in Chapter 5. Thus, the lower frequency of the band-pass filter should be set no lower than 50 Hz, which for the BCC produces a rather oscillatory behaviour. The upper frequency of the band-pass filter can be set in the range of 1-2 kHz.

## 6.7 Application of the ABP to experimental data and comparison with the BCC and PHAT correlator

In this section the ABP is applied to the experimental data obtained from the test rig presented in Chapter 5 for a leak of 2 mm diameter and 8.7 m/s jet flow velocity. The results are compared with those obtained from the BCC and PHAT correlator applied to the same set of data. In Figure 6.17 the theoretical prediction and the experimental results obtained from the ABP are plotted over a frequency bandwidth of 50 Hz to 3 kHz where, as seen in Chapter 5, the SNR is high. For the simulations, the values of the variables that were used are, $d_1 = 0.7$ m, $d_2 = 0.3$ m, $c$ = 375 m/s, $\eta$ = 0.008 and SNR=40 dB.

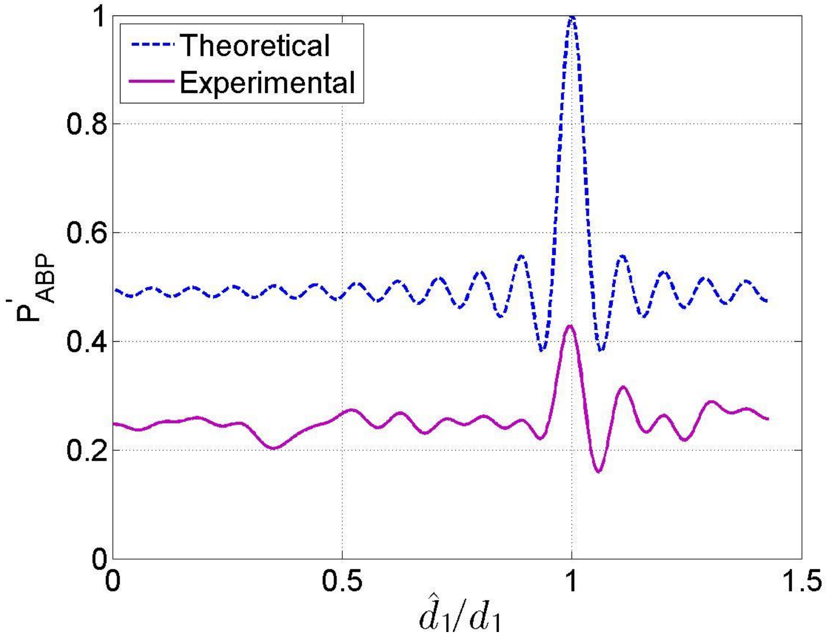

Figure 6.17. Comparison of the theoretical estimation of ABP with the experimental results obtained from a 2 mm leak with jet flow velocity 8.7 m/s. For the simulations, $d_1 = 0.7$ m, $d_2 = 0.3$ m, $c$ = 375 m/s, $\eta$ = 0.008 and SNR=40 dB. The frequency bandwidth is 50 Hz-3 kHz.

Figure 6.17 suggests a difference in the overall level of the ABP between the theoretical estimation and the experimental results. Possible reason for this difference could be the reflections due to the finite length of the pipe which are not taken into account in the expression of the theoretical model and which could affect the level of the ABP of the experimental results. Nevertheless, a clear peak is observed at the leak position when the APB is applied to the measured data.

To allow easier comparison of the results shown in Figure 6.17 the level of the experimental results of the ABP was adjusted to give the same correlation value with the theoretical estimation for $\hat{d}_1 = 0$ when normalized to their peak correlation values. This is shown in Figure 6.18.

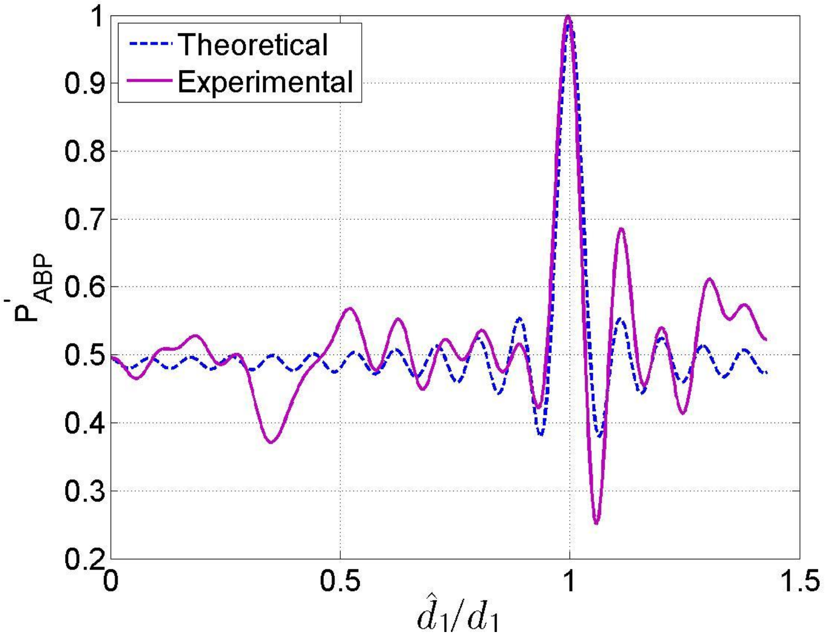

Figure 6.18. Comparison of the theoretical estimation of ABP with the experimental results when the results are normalized to their peak correlation values. For the simulations, $d_1 = 0.7$ m, $d_2 = 0.3$ m, $c$ = 375 m/s, $\eta$ = 0.008 and SNR=40 dB. The frequency bandwidth is 50 Hz-3 kHz.

Figure 6.18 suggests that the experimental results now match well with the theoretical predictions giving a peak with similar bandwidth in the leak position. In Figures 6.19 and 6.20 the ABP is compared with the results obtained from the PHAT correlator and the BCC respectively. Note that the BCC is now normalized over the square root of the product of the maximum values of the auto-correlation of each sensor signals in order to give values between -1 and 1. This is the cross-correlation coefficient as defined in Chapter 1, Eq.(1.12).

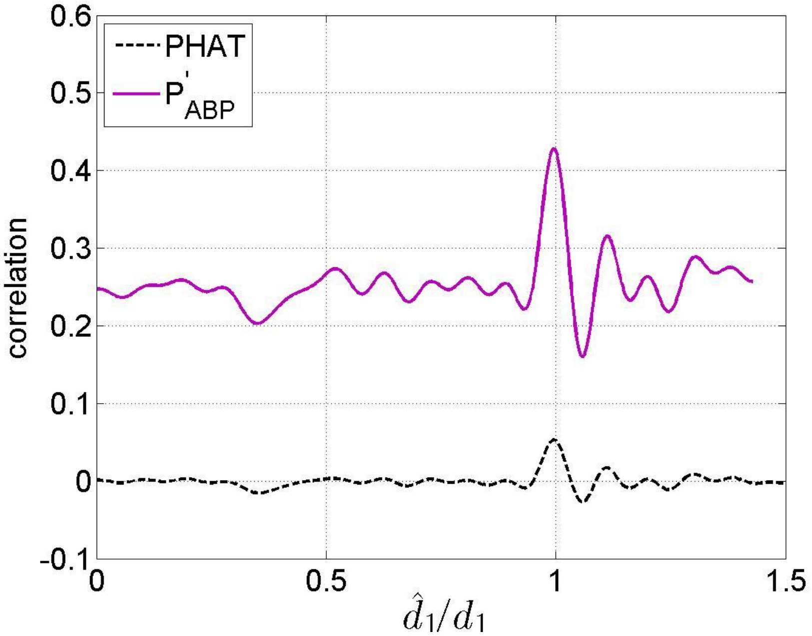

Figure 6.19. Comparison of the PHAT correlator and the ABP when applied to experimental data. For the simulations, $d_1 = 0.7$ m, $d_2 = 0.3$ m, $c$ = 375 m/s, $\eta$ = 0.008 and SNR=40 dB. The frequency bandwidth is 50 Hz-3 kHz.

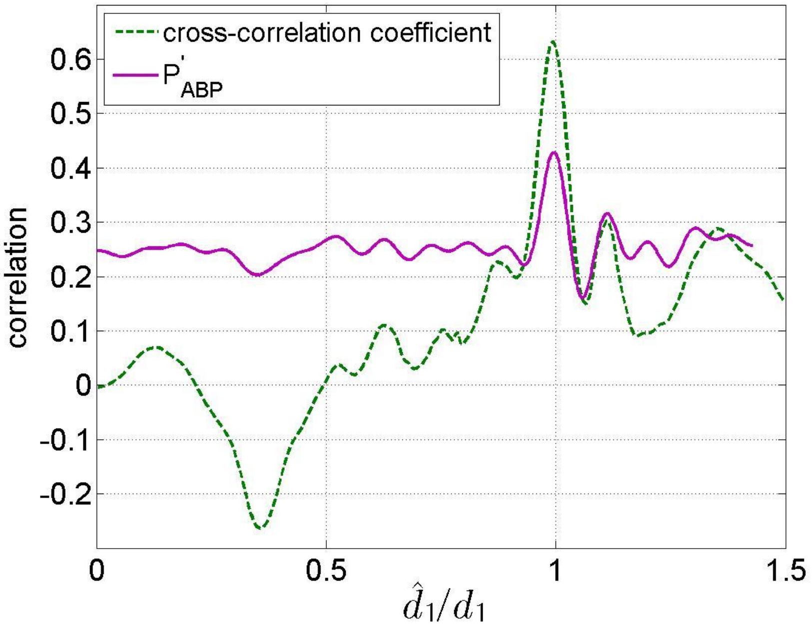

Figure 6.20. Comparison of the cross-correlation coefficient and the ABP when applied to experimental data. For the simulations, $d_1 = 0.7$ m, $d_2 = 0.3$ m, $c$ = 375 m/s, $\eta$ = 0.008 and SNR=40 dB. The frequency bandwidth is 50 Hz-3 kHz.

As before, to allow easier comparison the level of the ABP was adjusted to give the same correlation values with the PHAT and BCC for $\hat{d}_1 = 0$ when normalized to their peak correlation values.

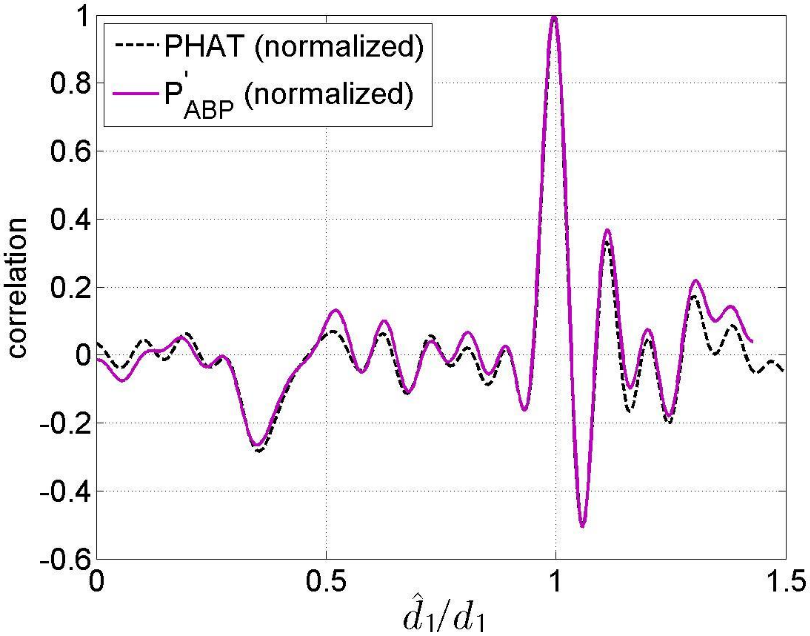

Figure 6.21. Comparison of the PHAT correlator and the ABP when applied to experimental data. The results are normalized to their peak correlation values.

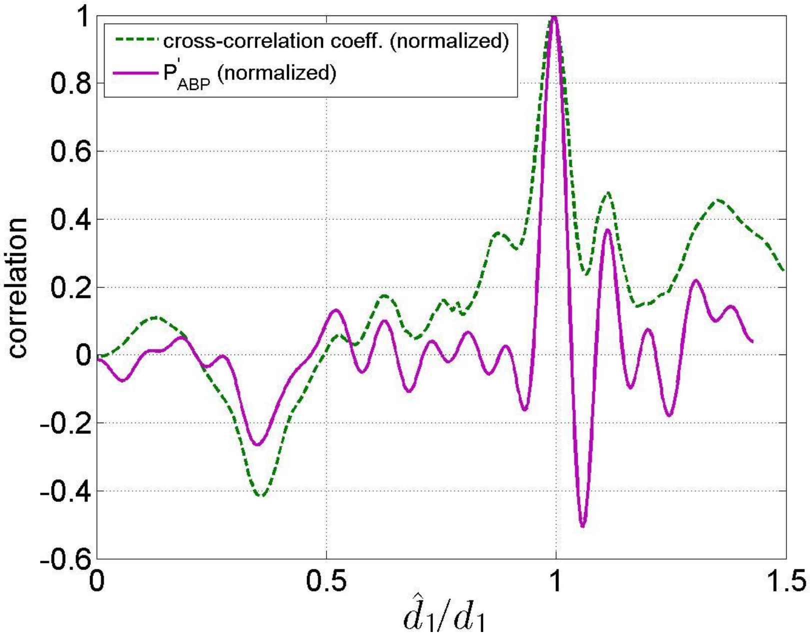

Figure 6.22. Comparison of the cross-correlation coefficient and the ABP when applied to experimental data. The results are normalized to their peak correlation values.

Figure 6.21 shows a nearly identical performance for both the ABP and PHAT correlator giving a clear peak of similar bandwidth at the leak location. The reason for this level of agreement is because the PHAT processor explicitly pre-whitens the cross spectrum prior to inverse Fourier transformation, while the ABP implicitly pre-whitens the signal by normalising the measurement vectors by their norms and finally integrating the results over frequency. In both cases the frequency dependence of the pipe and the leak is removed in this pre-whitening procedure and therefore, both correlators appear to give similar performance.

Figure 6.22 shows the ABP has a much better performance when compared to the cross-correlation coefficient which gives a broader peak at the leak location.

## 6.8 Discussion

In this chapter the linear Bartlett processor that is widely used in underwater acoustics for source localization was applied to the leak detection problem. Although this processor gives a sharp peak at the leak position in the case of equidistant sensors in the general case, where the two sensors are unequal distant it fails. The reason why this happens was explained. Results can be improved by increasing the number of sensors but this may not always be feasible. Thus, an alternative form of the Bartlett processor (ABP) was proposed which was found to give a sharp peak at the leak position regardless the distance between the sensors and the leak. Comparing theoretically the ABP with the BCC and the PHAT processor, ABP was found to have a very similar behaviour with the PHAT both giving a sharper peak in the leak position compared to that of the BCC. However, one disadvantage of the PHAT is that it takes no account of the coherence between the signals which means that in practical situations where the SNR is low, the effects of noise may be enhanced by pre-whitening the signals and thus, lead to erroneously conclusions about the leak location.

An advantage of the BCC is that it is not affected by the un-correlated background noise. However, it was shown that the BCC is sensitive to the lower frequency of the band-pass filter and becomes more oscillatory as this frequency, and thus the frequency bandwidth, increases whereas the ABP and PHAT correlator remain unaltered. In practical situations and as seen in Chapter 5 the background noise is quite high for frequencies up to 50 Hz. Therefore, the lower frequency of the band-pass filter should be set at frequencies no less than 50 Hz which means that the BCC will have a rather oscillatory behaviour.

The proposed estimator was applied to experimental data and results compared with the ones obtained from the BCC and the PHAT correlator. It was found that the proposed correlator gives a much better performance compared to the BCC and a similar performance compared to the PHAT correlator.

However, one advantage of the ABP over the PHAT correlator is that information from more than 2 sensors can be used which can lead to a better estimation of the leak location. Improvement of the results can also be achieved by modifying the model so to include reflections and offer other aspects of the propagation. Another advantage of the ABP is that it can be applied in the case where correlated background noise exists in the sensors positions. This is because the ABP correlates the measured signal with a noise free model. In general, the ABP is more tolerant to background noise compared to the PHAT correlator that gives equal weight to all frequencies without taking into account the background noise. These features make the ABP more useful in practical situations.

## 6.9 Conclusions

The proposed correlator (ABP) was found to give better performance than the BCC when applied to experimental data. Its performance was found to be similar when compared to the PHAT processor. However, the ABP has as advantages that more than two sensors can be used for the leak localization and also that it can be used in the case when correlated background noise exists at the sensor position, making it more useful than the PHAT correlator in practical situations.

# CHAPTER 7

# EFFECT OF THE LEAK NOISE SPECTRUM ON THE PEAK OF THE CROSS-CORRELATION COEFFICIENT

## 7.1 Introduction

In this chapter the effect of the shape of the leak noise spectrum on the peak of the cross-correlation coefficient, $\rho_{peak}$ , is investigated. The reason for this comparison is that in a previous work, [9] the cross-correlation coefficient was estimated assuming a flat leak spectrum over the frequency bandwidth of interest. However, the measurement results presented in Chapter 5 showed that the leak spectrum is not flat but rolls off with a relationship of $\omega^{-1}$ until a specific critical frequency $\omega_c$. Thus, the aim of this chapter is to compare the two models and see how much this roll off affects the $\rho_{peak}$ . In Figure 7.1 the leak noise spectrum of the two models is shown, with dashed line representing Model I (flat leak spectrum) and with solid line representing Model II ($\omega^{-1}$ trend).

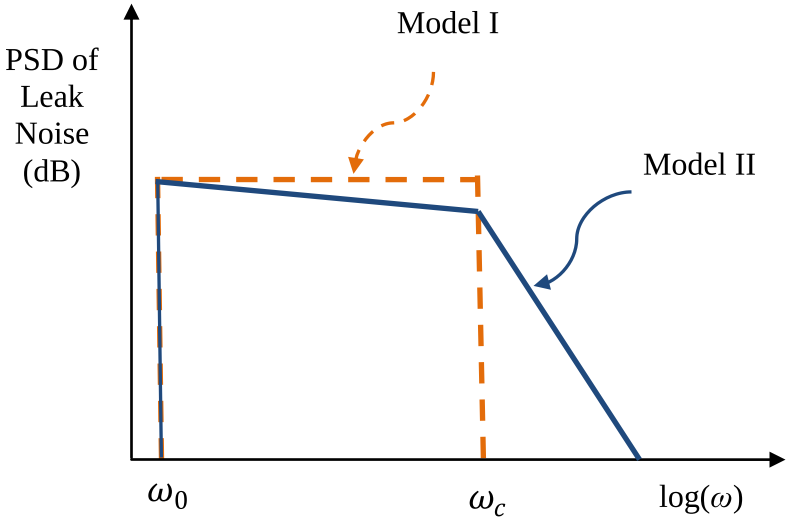

Figure 7.1. Shape of the leak noise spectrum for the two models.

Note that possible differences in the leak noise source levels of the two models cannot affect the comparison of the peak of the cross-correlation coefficient because in each case the $\rho_{peak}$ is independent of the leak source level due to the normalization.

## 7.2 Models I and II of the leak noise spectrum

In Chapter 1, Section 1.4.1, a model developed by Gao *et al.* to predict the cross-correlation function and thus the cross-correlation coefficient of leak signals in plastic water pipes was presented [9]. The model was based on a theoretical formulation of wave propagation in a fluid-filled pipe *in vacuo* and the assumption that the leak sound at source has a flat spectrum over the bandwidth of interest. The leak signals were passed through a band-pass filter before calculating the cross-correlation function and the analysis showed that the cross-correlation is mostly affected by the lower frequency of the band-pass filter while it is insensitive to the higher one. The reason for that is that the pipe acts as a low pass filter and attenuates quickly the high frequencies.

The PSD $S_{ll}(\omega)$, of the leak signal representing Model I is given by,

$$S_{ll_1}(\omega) = \begin{cases} S_0 & \omega_0 \le |\omega| \le \omega_c \\ 0 & \text{otherwise} \end{cases} \tag{7.1}$$

where $\omega_0$ and $\omega_c$ are the lower and upper frequencies of the band-pass filter respectively. It was mentioned in Chapter 1 and is repeated here for convenience that the peak of the cross-correlation coefficient is given by [9],

$$\rho_{x_1x_2}(\tau_{peak}) = \frac{2\sqrt{d_1d_2}}{d'}\frac{1-e^{-\Delta\omega\beta\,d'}}{(1-e^{-2\Delta\omega\beta\,d_1})^{1/2}(1-e^{-2\Delta\omega\beta\,d_2})^{1/2}} \tag{7.2}$$

where $d_1, d_2$ are the distances of sensor 1 and 2 from the leak and $\Delta\omega = \omega_c - \omega_0$ is the frequency bandwidth.

The model of the leak noise spectrum developed in Chapter 5 (Model II) is described by,

$$S_{ll_{\mathrm{II}}}(\omega) = \begin{cases} \dfrac{\mathrm{A}(V,d)}{\omega} & \omega_0 \le |\omega| \le \omega_c \\ \dfrac{\mathrm{A}(V,d){\omega_c}^{n-1}}{\omega^n} & \omega_c \le |\omega| \le \infty \end{cases} \tag{7.3}$$

With reference to Figure 1.1 for two signals $x_1(t)$, $x_2(t)$ measured at positions $d_1, d_2$ respectively from the leak the cross-spectral density (CSD) is given by [9],

$$S_{x_1x_2}(\omega) = S_{ll}(\omega)e^{-\beta|\omega|d'}e^{j\omega T_0} \tag{7.4}$$

where $T_0$ is the time shift given by $T_0 = -(d_2 - d_1)/c$ and $d' = d_1 + d_2$. Thus,

$$R_{x_1x_2}(\tau) = F^{-1}\{S_{x_1x_2}(\omega)\} = \frac{1}{2\pi}\int_{-\infty}^{+\infty} S_{ll}(\omega)e^{-\beta|\omega|d'}e^{j\omega T_0}e^{j\omega\tau}d\omega \tag{7.5}$$

Substituting Eq.(7.3) for the leak noise spectrum in Eq.(7.5) and due to the symmetry of the cross-correlation function around zero, $R_{x_1x_2}$ will be given by,

$$R_{x_1x_2}(\tau) = 2\left[\frac{1}{2\pi}\int_{\omega_0}^{\omega_c}\frac{S_0}{\omega}e^{-\beta\omega\,d'}e^{j\omega\,(\tau+T_0)}d\omega + \frac{1}{2\pi}\int_{\omega_c}^{\infty}\frac{S_0{\omega_c}^{n-1}}{\omega^n}e^{-\beta\omega\,d'}e^{j\omega\,(\tau+T_0)}d\omega\right] \tag{7.6}$$

Following a similar procedure the auto-correlation function of $x_1(t),\ x_2(t)$ will be given by,

$$R_{x_1x_1}(\tau) = 2\left[\frac{1}{2\pi}\int_{\omega_0}^{\omega_c}\frac{S_0}{\omega}e^{-2\beta\omega d_1}e^{j\omega\tau}d\omega + \frac{1}{2\pi}\int_{\omega_c}^{\infty}\frac{S_0{\omega_c}^{n-1}}{\omega^n}e^{-2\beta\omega d_1}e^{j\omega\tau}d\omega\right] \tag{7.7}$$

and

$$R_{x_2x_2}(\tau) = 2\left[\frac{1}{2\pi}\int_{\omega_0}^{\omega_c}\frac{S_0}{\omega}e^{-2\beta\omega d_2}e^{j\omega\tau}d\omega + \frac{1}{2\pi}\int_{\omega_c}^{\infty}\frac{S_0{\omega_c}^{n-1}}{\omega^n}e^{-2\beta\omega d_2}e^{j\omega\tau}d\omega\right] \tag{7.8}$$

Thus, the cross-correlation coefficient, given by Eq.(1.2) becomes,

$$\rho_{x_1x_2}(\tau) = \frac{\int_{\omega_0}^{\omega_c}\frac{1}{\omega}e^{-\beta\omega d'}e^{j\omega(\tau+T_0)}d\omega + \int_{\omega_c}^{\infty}\frac{{\omega_c}^{n-1}}{\omega^n}e^{-\beta\omega d'}e^{j\omega(\tau+T_0)}d\omega}{\sqrt{\left(\int_{\omega_0}^{\omega_c}\frac{e^{-2\beta\omega d_1}}{\omega}d\omega + \int_{\omega_c}^{\infty}\frac{e^{-2\beta\omega d_1}{\omega_c}^{n-1}}{\omega^n}d\omega\right)}\ \text{x}\ \sqrt{\left(\int_{\omega_0}^{\omega_c}\frac{e^{-2\beta\omega d_2}}{\omega}d\omega + \int_{\omega_c}^{\infty}\frac{e^{-2\beta\omega d_2}{\omega_c}^{n-1}}{\omega^n}d\omega\right)}} \tag{7.9}$$

At $\tau = -T_0$ the peak value of the cross-correlation coefficient is given by,

$$\rho_{x_1x_2}(-T_0) = \frac{\int_{\omega_0}^{\omega_c}\frac{1}{\omega}e^{-\beta\omega d'}d\omega + \int_{\omega_c}^{\infty}\frac{{\omega_c}^{n-1}}{\omega^n}e^{-\beta\omega d'}d\omega}{\sqrt{\left(\int_{\omega_0}^{\omega_c}\frac{e^{-2\beta\omega d_1}}{\omega}d\omega + \int_{\omega_c}^{\infty}\frac{e^{-2\beta\omega d_1}{\omega_c}^{n-1}}{\omega^n}d\omega\right)}\ \text{x}\ \sqrt{\left(\int_{\omega_0}^{\omega_c}\frac{e^{-2\beta\omega d_2}}{\omega}d\omega + \int_{\omega_c}^{\infty}\frac{e^{-2\beta\omega d_2}{\omega_c}^{n-1}}{\omega^n}d\omega\right)}} \tag{7.10}$$

To allow some simplifications to Eq.(7.10), we note that the second term of the numerator of Eq.(7.10) is much smaller than the first one due to the decaying behaviour of the $e^{-\beta\omega d'}$ term and also due to the value of *n* which as seen in Chapter 5, varies between 6 and 16 and can therefore be neglected. Following a similar procedure for the denominator, Eq.(7.10) can be re-written without significant loss of accuracy as,

$$\rho_{x_1x_2}(-T_0) \cong \frac{\int_{\omega_0}^{\omega_c} \frac{1}{\omega} e^{-\beta\omega d'} d\omega}{\sqrt{\left(\int_{\omega_0}^{\omega_c} \frac{e^{-2\beta\omega d_1}}{\omega} d\omega\right)\left(\int_{\omega_0}^{\omega_c} \frac{e^{-2\beta\omega d_2}}{\omega} d\omega\right)}} \tag{7.11}$$

where the second integrals between $\omega_c$ and $\infty$ have been ignored.

Equation (7.11) can be evaluated as series expansion by expanding the term $e^{-\beta\omega d'}$ as,

$$e^{-\beta\omega d'} = \sum_{k=0}^{\infty} \frac{\left(-\beta\omega d'\right)^{\mathrm{k}}}{k!} \tag{7.12}$$

valid for all $\beta\omega d'$ [52].

Recognizing that $\beta d' \ll 1$ (as seen in Chapter 5, $\beta \approx 10^{-5}\ \mathrm{s/m}$ and in practical cases $d' \leq 100$ m) and for $\omega \leq \omega_c$ the sum in Eq.(7.12) converges rapidly using only the first five terms . Thus,

$$\int_{\omega_0}^{\omega_c} \frac{1}{\omega} e^{-\beta\omega d'} d\omega = \sum_{k=0}^{m} \left[\frac{\left(-\beta d'\right)^k}{k!} \int_{\omega_0}^{\omega_c} \omega^{k-1} d\omega\right] = \int_{\omega_0}^{\omega_c} \frac{1}{\omega} d\omega + \sum_{k=1}^{m} \left[\frac{\left(-\beta d'\right)^k}{k!} \left(\frac{\omega_c^k}{k} - \frac{{\omega_0}^k}{k}\right)\right] \tag{7.13}$$

where $m$ is sufficiently large to ensure convergence. But, as mentioned above, $\omega_0$ is small compared to $\omega_c$ and hence, Eq.(7.13) reduces to,

$$\int_{\omega_0}^{\omega_c} \frac{1}{\omega} e^{-\beta\omega d'} d\omega \approx \int_{\omega_0}^{\omega_c} \frac{1}{\omega} d\omega + \sum_{k=1}^{m} \left[\frac{\left(-\beta d'\right)^k}{k!} \frac{\omega_c^k}{k}\right] = \ln\left(\frac{\omega_c}{\omega_0}\right) + \sum_{k=1}^{m} \left[\frac{\left(-\beta d'\right)^k}{k!} \frac{\omega_c^k}{k}\right] \tag{7.14}$$

In a similar way,

$$\int_{\omega_0}^{\omega_c} \frac{1}{\omega} e^{-2\beta\omega\, d_1} d\omega \approx \ln\left(\frac{\omega_c}{\omega_0}\right) + \sum_{k=1}^{m}\left[\frac{(-2\beta d_1)^k}{k!}\frac{\omega_c^k}{k}\right] \tag{7.15}$$

and

$$\int_{\omega_0}^{\omega_c} \frac{1}{\omega} e^{-2\beta\omega\, d_2} d\omega \approx \ln\left(\frac{\omega_c}{\omega_0}\right) + \sum_{k=1}^{m}\left[\frac{(-2\beta d_2)^k}{k!}\frac{\omega_c^k}{k}\right] \tag{7.16}$$

Thus the peak of the cross-correlation coefficient can be approximated by,

$$\rho_{x_1x_2}(-T_0) \cong \frac{\ln\left(\frac{\omega_c}{\omega_0}\right) + \sum_{k=1}^{m}\left[\frac{\left(-\beta\omega_c d'\right)^k}{kk!}\right]}{\sqrt{\ln\left(\frac{\omega_c}{\omega_0}\right) + \sum_{k=1}^{m}\left[\frac{(-2\beta\omega_c d_1)^k}{kk!}\right]}\sqrt{\ln\left(\frac{\omega_c}{\omega_0}\right) + \sum_{k=1}^{m}\left[\frac{(-2\beta\omega_c d_2)^k}{kk!}\right]}} \tag{7.17}$$

Eq.(7.17) suggests that the peak of the cross-correlation coefficient is defined in terms of the distance between the sensors $d'$, the distance between the sensors and the leak, $d_1$ and $d_2$, the frequencies $\omega_c$ and $\omega_0$ and the measure of loss in the pipe $\beta$.

## 7.3 Comparison of Model I and II for the cross-correlation coefficients

In this section the peak values of the cross-correlation coefficient for Model I and II obtained from Eqs.(7.2) and (7.11) respectively are plotted for comparison for different values of critical frequency $f_c$.

To support the assumption that the contribution of the leak noise spectrum above $\omega_c$ is not significant to the estimation of the cross-correlation coefficient, $\rho_{peak}$ of Model II given by Eq.(7.10) is plotted in Figure 7.2 for two different values of *n*, which as mentioned earlier defines the slope of the leak noise spectrum ($\omega^{-n}$) for frequencies greater than $f_c$, in order to verify that it does not affect the $\rho_{peak}$ . As seen in Chapter 5, *n* varies between 6 and 16 and for this reason $\rho_{peak}$ is plotted for these two limit values. For the simulations, $\omega_0 = 0.2\pi$ rads/s, $d^{'} = 100$ m and $\beta = 7.25\text{x}10^{-5}$ s/m (Chapter 6).

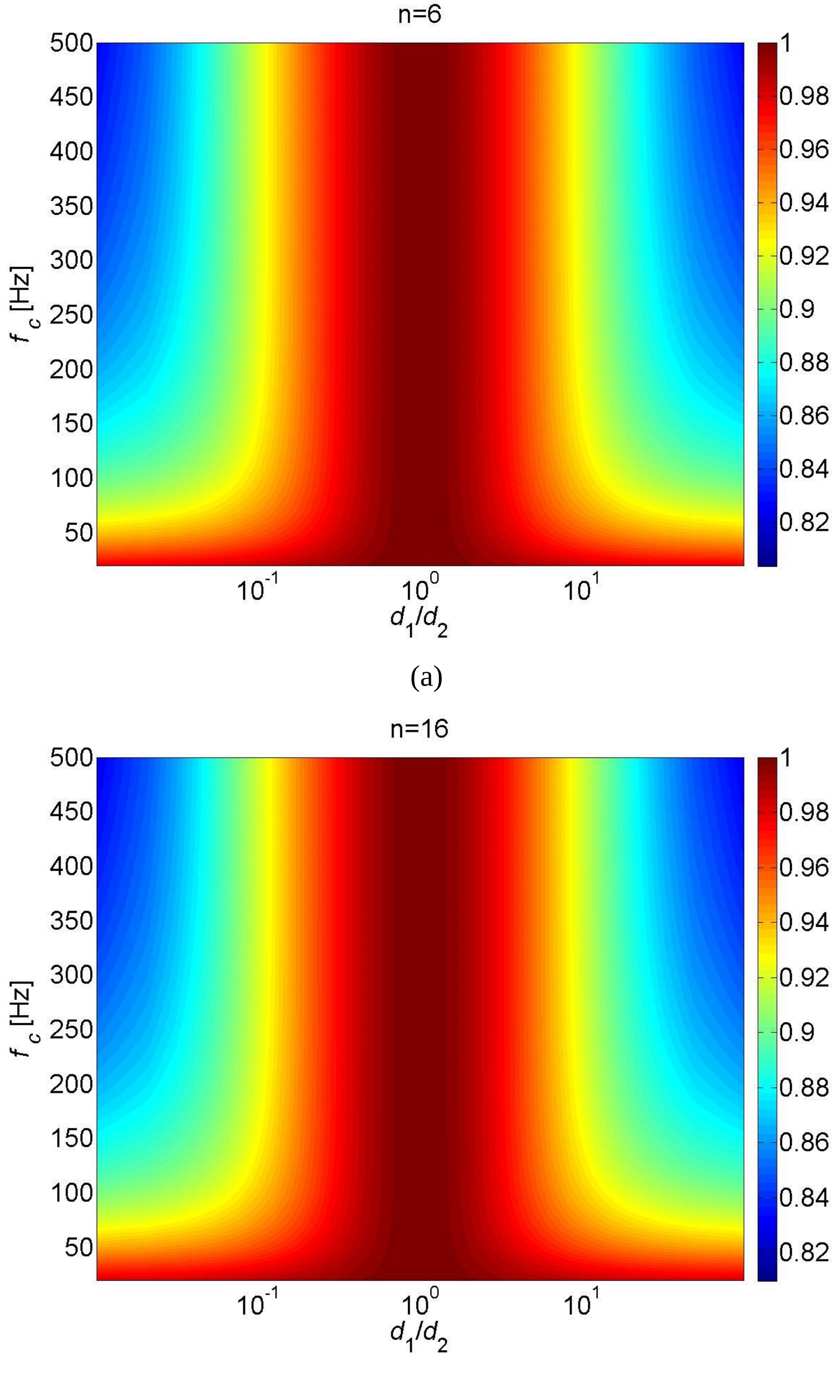

(a)

(b)

Figure 7.2. Peak value of the cross-correlation coefficient of Model II versus the critical frequency $f_c$ and the ratio $d_1/d_2$ for two values of *n*; (a) *n*=6; (b) *n*=16. For the simulations $\omega_0 = 0.2\pi$ rads/s, $d^{'} = 100$ m and $\beta = 7.25\text{x}10^{-5}$ s/m.

Figures 7.2 suggest that variations of $n$ do not affect the peak of the cross-correlation coefficient. This was expected due to the filtering effect of the pipe that attenuates the high frequencies and is consistent with the work of Gao *et al.* [9] for Model I.

In Figure 7.3 the $\rho_{peak}$ of Model I, estimated from Eq.(7.2) is plotted versus $d_1/d_2$ for different values of $f_c$ that expresses the upper limit of the band-pass filter. The lower limit is set to zero. As before, $d^{'} = 100$ m and $\beta = 7.25\text{x}10^{-5}$ s/m.

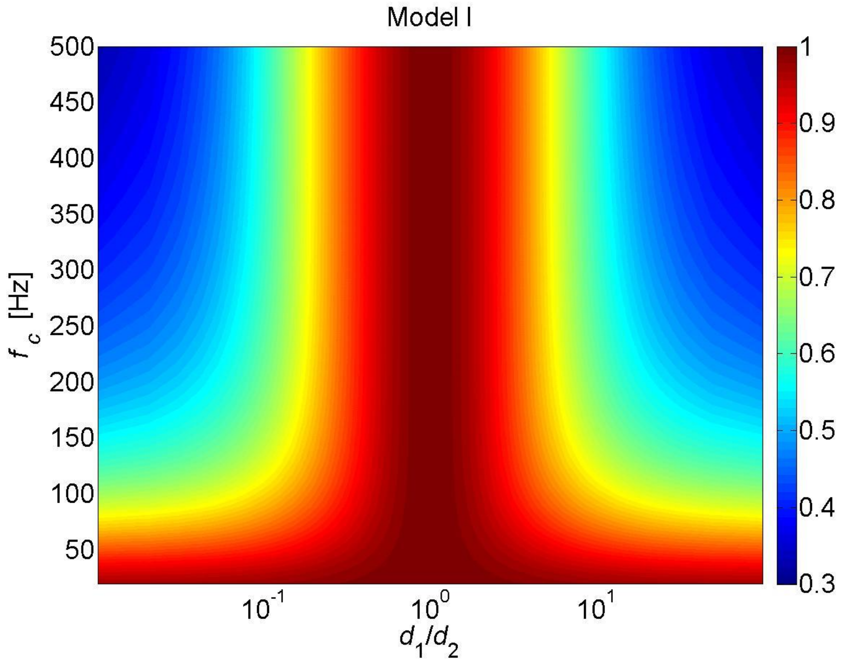

Figure 7.3. Peak value of the cross-correlation coefficient of Model I versus critical frequency $f_c$ and ratio $d_1/d_2$.

Comparing Model I and Model II from Figures 7.3 and 7.2 respectively it can be seen that both models, as expected, give a value of 1 for equidistant sensors. $d_1/d_2 = 1$. However, for different values of ratio $d_1/d_2$, Model I gives significantly lower values of $\rho_{peak}$ compared to those of Model II. These values decrease as $f_c$ increases. To allow an easier comparison, the $\rho_{peak}$ of the two models is plotted in Figure 7.4 for four different values of $f_c$.

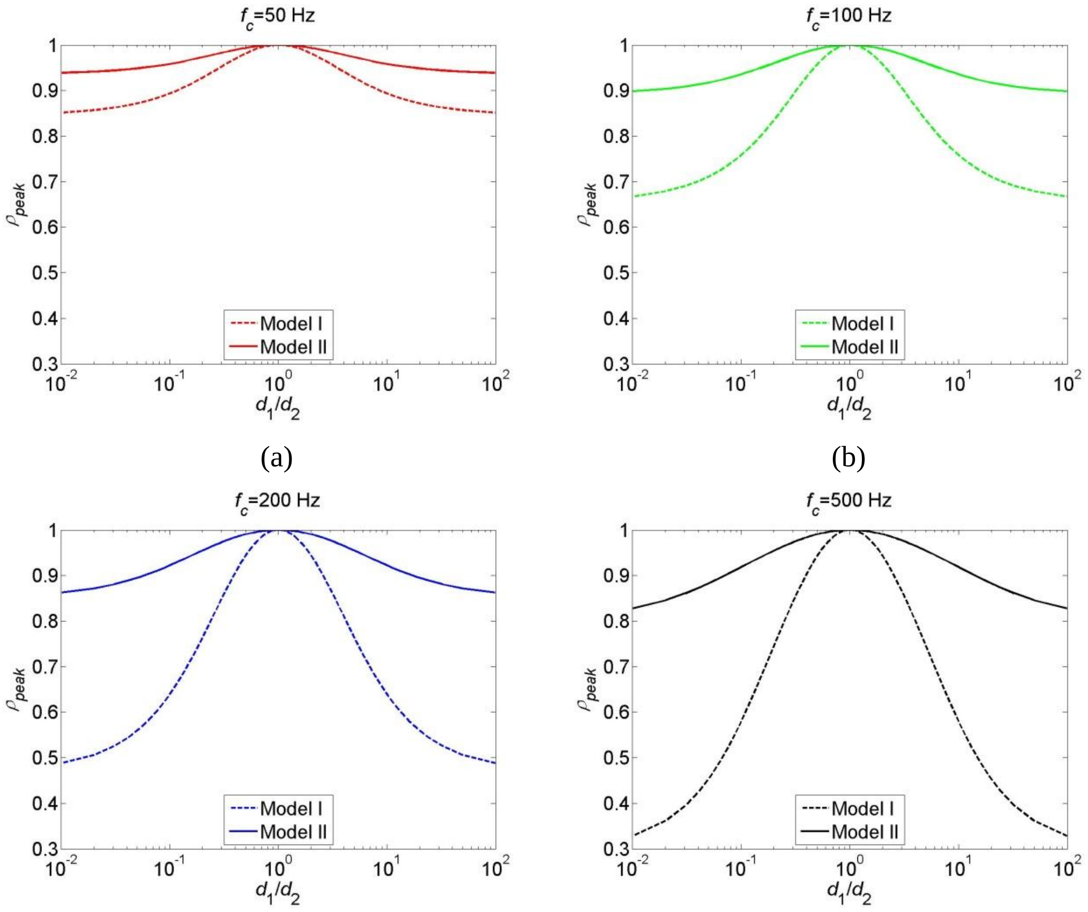

(a) (b)

(c) (d)

Figure 7.4. Comparison of the peak values of the cross-correlation coefficient between Model I and II for different critical frequencies; (a) $f_c = 50$ Hz; (b) $f_c = 100$ Hz; (c) $f_c = 200$ Hz; (d) $f_c = 500$ Hz.

Figure 7.4 suggests that Model I is more sensitive to $f_c$ and decreases significantly while $f_c$ increases that corresponds to an increase in the filter bandwidth. This happens because when for example $d_1$ is very small such that $d^{'} \approx d_2$ and assuming that $\Delta\omega = 2\pi(f_c - f_0)$ is still sufficiently large so that $e^{-2\Delta\omega\beta\, d_2} \ll 1$, but $1 - e^{-2\Delta\omega\beta\, d_1} \approx 2\Delta\omega\beta d_1$ Eq.(7.2) reduces to [9],

$$\rho_{x_1x_2}(-T_0) = \sqrt{\frac{2}{\beta d_2 \Delta\omega}} \tag{7.18}$$

which decreases as $\Delta\omega$ increases. From Eq.(7.11) when $d_1$ is very small such that $d^{'} \approx d_2$ the $\rho_{peak}$ is,

$$\rho_{x_1x_2}(-T_0) \approx \frac{\int_{\omega_0}^{\omega_c} \frac{1}{\omega} e^{-\beta\omega\, d'}\, d\omega}{\sqrt{\left(\int_{\omega_0}^{\omega_c} \frac{e^{-2\beta\omega\, d_1}}{\omega}\, d\omega\right)}} \approx \frac{\ln\left(\frac{\omega_c}{\omega_0}\right) + \sum_{k=1}^{m}\left[\frac{(-\beta\omega_c d')^k}{kk!}\right]}{\sqrt{\ln\left(\frac{\omega_c}{\omega_0}\right) + \sum_{k=1}^{m}\left[\frac{(-2\beta\omega_c d_1)^k}{kk!}\right]}} \tag{7.19}$$

which shows a much weaker dependence on the frequencies $\omega_c$ and $\omega_0$.

# 7.4 Conclusions

In this chapter the effect of the shape of the leak noise spectrum, determined in Chapter 5, on the peak of the cross-correlation coefficient was investigated. It was seen that the $\omega^{-n}$ trend of the spectrum model (Model II) for frequencies higher than the critical frequency $\omega_c$ does not affect the $\rho_{peak}$ which is basically influenced by the behaviour of $\omega^{-1}$ for $\omega \leq \omega_c$. This happens due to the filtering effect of the pipe that acts as a low pass filter. Comparing the results of the $\rho_{peak}$ with those obtained from previous work [9] where a flat leak spectrum (Model I) was assumed, it was found, as expected, that both spectrum models give a $\rho_{peak}$ equal to 1 for ratios of sensor distances from the leak close to 1 ($d_1/d_2 \approx 1$). However, for different ratios $d_1/d_2$ the $\rho_{peak}$ calculated with Model I is highly affected by the frequency bandwidth $\Delta\omega$ and decreases as $\Delta\omega$ increases whereas the $\rho_{peak}$ calculated with Model II is not affected by the frequencies $\omega_c$ and $\omega_0$ and gives higher values of $\rho_{peak}$ .

# CHAPTER 8

# CONCLUSIONS AND FUTURE WORK

## 8.1 Conclusions

This chapter contains the general conclusions of this thesis and also some recommendations for future work. Detailed conclusions are included at the end of each chapter so only the most important points are presented here. Throughout this thesis, work has been focused on characterizing the physical mechanisms of leak noise generation and investigating how it is affected by leak size and flow velocity. The main conclusions can be summarized as follows,

1. The rig described in Chapter 4 gave important information about the mechanism of leak noise generation, which is shown to be connected with turbulent flow in the water jet and not with cavitation, as no bubbles were observed in the vicinity of the leak. Furthermore, the general shape of the measured leak spectrum had many differences from a typical cavitation spectrum shown in Chapter 2.

2. Measurements on the 2 mm leak for low flow velocities revealed flow activity with a Strouhal number dependency. This flow activity is most likely related to axisymmetric instability waves in the jet, which according to Hoyt *et al.*, appear after less than one diameter of air travel. For higher flow velocities instability waves were not visible, possibly due to masking by the strong pipe resonances.

3. A procedure for estimating the leak noise spectrum was developed by inverting the pipe response using a theoretical model for calculating the cross-spectrum of

two signals in a finite-length pipe. Uncertainty about the pipe's loss factor was shown not to affect the results because in the specific rig the hydrophones were placed close to the leak to prevent any significant attenuation of the signals before they reached the hydrophones.

4. The final rig described in Chapter 5 gave significant information about the leak noise spectrum and how it is affected by leak size and flow velocity. Although large resonances were apparent in the spectrum due to the finite length of the pipe the general trend was clear enough to enable conclusions to be drawn. Measurement results revealed that below a critical frequency $\omega_c$ the spectrum decays with a frequency power law of $\omega^{-1}$ followed by a sharper drop of $\omega^{-n}$ with $n \approx 8$ appear to be most common. However, $\omega_c$ varied with leak size and flow velocity.

5. The critical frequency $\omega_c$ appeared to have a linear relationship with flow velocity for all the different leaks suggesting a Strouhal number dependency. However, the critical Strouhal number expressed as $St_c = f_c L/V$, with $L$ equal to pipe diameter, did not collapse the results to a unique critical Strouhal number. It was speculated that this characteristic length $L$ could be connected with the shear layer thickness $\delta$ where the turbulent sources occur. This new definition of $L$ gave good collapse of data and the critical frequency $f_c$ was expressed by a unique critical Strouhal number $St_{c,o} = 0.1$.

6. Plotting the mean square pressure as a function of flow velocity for the different leaks and as a function of leak diameter for different velocities revealed a $V^2$ and $d^3$ dependency. Using this information an estimate of the leak noise source level was found and a complete empirical model that describes the leak noise spectrum in terms of leak diameter $d$ and flow velocity $V$ was proposed.

7. A matched field processor was applied to experimental data presented in Chapter 5 and it was found to give better performance than the BCC and similar to the PHAT processor. However, this processor has the advantage that more than two

sensors can be used, which can lead to greater information about the leak position. Also, this processor can be used in the case when correlated background noise exists at the sensors positions because with this correlator the measurement data are correlated with a noise-free model. This feature makes it more useful in practical situations than the PHAT as the latter does not take into account the noise in the signals and requires an effective band-pass filtering to remove the frequencies where the SNR is low.

8. The effect of the shape of the leak noise spectrum on the peak of the cross-correlation coefficient ($\rho_{peak}$) was investigated. Two spectrum models were compared, a flat leak spectrum (Model I) and a spectrum that decays with a frequency power law of $\omega^{-1}$ until a frequency $\omega_c$ and with a frequency power law of $\omega^{-n}$ at higher frequencies (Model II). It was seen that both models give, as expected, $\rho_{peak} = 1$ when sensors are equidistant, but for all the other cases, Model I is highly affected by the frequency bandwidth and gives smaller values of $\rho_{peak}$ compared to Model II.

## 8.2 Recommendations for future work

This research work has been focused on leak noise signals produced by circular leaks discharging into air. Therefore, research into different shapes of orifices could be conducted in further studies discharging into different environments (porous soil for example) to investigate their effect on the leak noise specra.

Also, the effect of leak position on the measured signal could be examined. Tests can be conducted with leaks located at different positions on the pipe, so as the water jet points vertically, horizontally or with a different angle, to investigate any variations at the leak noise spectra.

Furthermore, experiments could be conducted on a full-scale rig with a long underground water filled pipe which represents real situations. A variety of different leak sizes can be tested for a greater variety of flow velocities in order to verify the empirical model that has been developed for the prediction of the leak noise spectrum.

Computational fluid dynamics methods (CFD) could be applied to investigate the leak flow pattern in the vicinity of the leak and just before it escapes from the leak hole. The CDF solution would be useful to validate some of the findings made in this thesis regarding the relationship between shear layer thickness, length scale, jet velocity and leak diameter.

Finally, measurements could be carried out using more than two sensors and investigate in practice how the alternative Bartlett processor improves its performance.

# REFERENCES

[1] O. Hunaidi, W. Chu, A. Wang, W. Guan, 'Detecting Leaks in Plastic Water Distribution Pipes', *Journal of the American Water Works Association*, vol. 92, pp. 88-94, 2000.

[2] M. Fantozzi, G. D. Chirico, E. Fontana, F. Tonolini, 'Leak inspection on water pipelines by acoustic emission with cross-correlation method', *Journal of the American Water Works Association,* pp. 609-621, 1993.

[3] H. V. Fuchs, R. Riehle, 'Ten Years of Experience with Leak Detection by Acoustic Signal Analysis', *Applied Acoustics*, vol. 33, pp. 1-19, 1991.

[4] D. A. Liston, J. D. Liston, 'Leak Detection Techniques', *Journal of the New England Water Works Association,* vol. 106, pp. 103-108, 1992.

[5] G. J. Weil, 'Non contact, remote sensing of buried water pipeline leaks using infrared thermography', *Water Resources Planning and Management and Urban Water Resources,* pp. 404-407, 1993.

[6] R. S. Pudar, J. A. Liggett, 'Leaks in Pipe Networks', *Journal of Hydraulic Engineering*, American Society of Civil Engineers, vol. 118, pp. 1031-1046, 1992.

[7] K. W. Sneddon, G. R. Olhoeft, M. H. Powers, 'Determining and Mapping DNAPL saturation values from noninvasive GPR measurements', *Symposium on the Application of Geophysics to Environment and Engineering Problems*, Arlington, Virginia, pp. 293-302, 2000.

[8] O. Hunaidi, P. Giamou, 'Ground-penetrating radar for detection of leaks in buried plastic water distribution pipes', *Seventh International Conference on Ground-Penetrating Radar*, Lawrence, Kansas, USA, 1998.

[9] Y. Gao, M. J. Brennan, P. F. Joseph, J. M. Muggleton, O. Hunaidi, ‘A model of the correlation function of leak noise in buried plastic pipes’, *Journal of Sound and Vibration*, vol. 277, pp. 133-148, 2004.

[10] A. V. Oppenheim, *Signals & Systems*, 2nd edition, London: Prentice-Hall International, 1997.

[11] J. M. Muggleton, M. J. Brennan, P. W. Linford, ‘Axisymmetric wave propagation in fluid-filled pipes: Measurements in *in-vacuo* and buried pipes’, *Journal of Sound and Vibration*, vol. 270, pp. 171-190, 2004.

[12] J. M. Muggleton, M. J. Brennan, R. J. Pinnington, ‘Wavenumber prediction of waves in buried pipes for water leak detection’, *Journal of Sound and Vibration*, vol. 249, pp. 939-954, 2002.

[13] O. Hunaidi, W. Chu, ‘Acoustical Characteristics of Leak Signals in Plastic Water Distribution Pipes’, *Applied Acoustics*, vol. 58, pp. 235-254, 1999.

[14] Y. Gao, M. J. Brennan, P. F. Joseph, J. M. Muggleton, O. Hunaidi, ‘On the selection of acoustic/vibration sensors for leak detection in plastic water pipes’, *Journal of Sound and Vibration*, vol. 283, pp. 927-941, 2005.

[15] S. Markus, *The mechanics of vibrations of cylindrical shells: Studies in Applied Mechanics*, vol. 17, Elsevier 1988.

[16] R. J. Pinnington, A. R. Briscoe, ‘Externally applied sensor for axisymmetric waves in a fluid filled pipe’ *Journal of Sound and Vibration*, vol. 173, pp. 503-516, 1994.

[17] C. R. Fuller, F. J. Fahy, ‘Characteristics of wave propagation and energy distributions in cylindrical elastic shells filled with fluid’, *Journal of Sound and Vibration*, vol. 81, pp. 501-518, 1982.

[18] J. M. Muggleton, M. J. Brennan, ‘Axisymmetric wave propagation in buried, fluid-filled pipes: effects of wall discontinuities’, *Journal of Sound and Vibration*, vol. 281, pp. 849-867, 2005.

[19] I. L. Ver, L. L. Beranek, *Noise and Vibration Control Engineering Principles and Applications*, 2nd edition, John Wiley & Sons, Inc., Hoboken, New Jersey, 2006.

[20] R. H. Sabersky, A. J. Acosta, E. G. Hauptman, *Fluid Flow A first course in fluid mechanics*, 3rd edition, Macmillan Publishing Company, London, 1989.

[21] S. J. Michell, *Fluid and Particle Mechanics*, 1st edition, Pergamon Press, 1970.

[22] R. L. Daugherty, J. B. Franzini, E. J. Finnemore, *Fluid Mechanics with Engineering Applications*, 8th edition, McGraw-Hill Book company, USA, 1985.

[23] F. C. Johansen, Flow through Pipe Orifices at Low Reynolds Number, *Proceedings of the Royal Society of London*, vol. 126, pp. 231-245 1930.

[24] A. A Draad, G. D. C. Kuiken, F. T. M. Nieuwstadt, Laminar-turbulent transition in pipe flows for Newtonian and non-Newtonian fluids, *Journal of Fluid Mechanics*, vol. 377, pp. 267-312, 1998.

[25] L. Prandtl, J. P. Den Hartog, *Applied Hydro- and Aeromechanics*, Dover Publications, New York, 1957.

[26] V. C. Patel, M. R. Head, Reversion of turbulent to laminar flow, *Journal of Fluid Mechanics*, vol. 34, pp. 371-392, 1968.

[27] M. A. B. Narayanan, V. Ramjee, On the criteria for reverse transition in a two-dimensional boundary layer flow, *Journal of Fluid Mechanics*, vol. 35, pp. 225-241, 1969.

[28] M. Ichimiya, I. Nakamura, S. Yamashita; Properties of a relaminarizing turbulent boundary layer under a favourable pressure gradient, *Experimental Thermal and Fluid Science*, vol. 17, pp. 37-48, 1998.

[29] R. Narasimha, K. R. Sreenivasan; Relaminarization in highly accelerated turbulent boundary layers, *Journal of Fluid Mechanics*, vol. 61, pp. 417-447, 1973.

[30] D. Ross, *Mechanics of Underwater Noise*, Pergamon Press, 1976.

[31] M. T. Landahl, Wave mechanisms of breakdown, *Journal of Fluid Mechanics*, vol. 56, pp.775-802, 1972.

[32] J. W. Hoyt, J. J. Taylor, C. D. Runge, The structure of jets of water and polymer solution in air, *Journal of Fluid Mechanics*, vol. 63, pp. 635-640, 1974.

[33] J. W. Hoyt, J. J. Taylor, Waves on water jets, *Journal of Fluid Mechanics*, vol. 83, pp. 119-127, 1977.

[34] J. W. Hoyt, J. J. Taylor, Turbulence structure in a water jet discharging in air, *The Physics of Fluids*, vol. 20, pp. S253-S257, 1977.

[35] B. H. K. Lee, Some measurements of spatial instability waves in a round jet, *Journal of American Institute of Aeronautics and Astronautics*, vol. 14, pp. 348-351, 1975.

[36] G. E. Mattingly, C. C. Chang, Unstable waves on an axisymmetric jet column, *Journal of Fluid Mechanics*, vol. 65, pp. 541-560, 1974.

[37] M. E. Goldstein, S. J. Leib, The role of instability waves in predicting jet noise, *Journal of Fluid Mechanics*, vol. 525, pp. 37-72, 2005.

[38] M. Thompson, D.J. Allwright, C. J. Chapman, S. D. Howison, J. R. Ockendon, Noise generation by water pipe leaks, *Study report of 40th European Study group with industry*, pp. D1-D6, 2001.

[39] F. R. Young, *Cavitation*, McGraw-Hill, London 1989.

[40] H. C. Pumphrey, J. E. Ffowcs Williams, Bubbles as Sources of Ambient Noise, *IEEE Journal of Oceanic Engineering*, vol. 15, pp. 268-274, 1990.

[41] J. F. Douglas, J. M. Gasiorek, J. A. Swaffield, L. B. Jack, *Fluid Mechanics*, 5th edition, Pearson, Prentice Hall, 2005.

[42] M. J. Lighthill, ‘On Sound Generated Aerodynamically’, *Proceedings of the Royal Society of London*, A 211, pp. 564-587, 1952.

[43] R. G. White, J. G. Walker, *Noise and Vibration*, Ellis Horwood-Publishers 1986.

[44] R. H. Self, ‘Jet Noise Prediction Using the Lighthill Acoustic Analogy ’, *Journal of Sound and Vibration*, vol. 275, pp. 757-768, 2004.

[45] Y. Gao, M. J. Brennan, P. F. Joseph, On the effects of reflections on time delay estimation for leak detection in buried plastic water pipes, *Journal of Sound and Vibration*, vol. 325, pp. 649-663, 2009.

[46] L. E. Kinsler, A. R. Frey, A. B. Coppens, J. V. Sanders, *Fundamental of Acoustics*, 4th edition, John Wiley & Sons, Inc, 2000.

[47] K. B. M. Q. Zaman, Effect of initial conditions on subsonic jet noise, *AIAA*, vol. 23, pp. 1370-1373, 1985.

[48] J. E. Bridges, A. K. M. F. Hussain, Roles of initial conditions and vortex pairing in jet noise, *Journal of Sound and Vibration* vol. 117, pp. 289-311, 1987.

[49] C. Bogey, C. Bailly, Influence of the nozzle-exit boundary-layer thickness on the flow and acoustic fields of initially laminar jets, *AIAA/CEAS Aeroacoustics Conference*, Miami, FL, 11-13 May 2009.

[50] A.Tolstoy, *Matched Field Processing for Underwater Acoustics*, World Scientific, Singapore, 1993.

[51] Y.Gao, M.J. Brennan, P.F. Joseph, A comparison of time delay estimators for the detection of leak noise signals in plastic water distribution pipes, *Journal of Sound and Vibration* vol. 292, pp. 552-570, 2006.

[52] I. S. Ģradshteyn, I.M. Ryzhik, *Tables of Integrals Series and Products*, 6th edition, Academic Press, London, 2000.